Experimental Investigation of Residential Cogeneration Devices and Calibration of Annex 42 Models

A Report of Subtask B of FC+COGEN-SIM
The Simulation of Building-Integrated
Fuel Cell and Other Cogeneration Systems

Annex 42 of the International Energy Agency
Energy Conservation in Buildings and Community Systems Programme
First published: December 2007

REPORT AUTHORS:
Ulli Arndt (Research Institute for Energy Economy, FfE)
Ian Beausoleil-Morrison (Natural Resources Canada)
Mark Davis (National Institute of Standards and Technology)
William D'haeseleer (Catholic University of Leuven)
Viktor Dorer (Swiss Federal Laboratories for Materials Testing and Research, EMPA)
Evgeuniy Entchev (Natural Resources Canada)
Alex Ferguson (Natural Resources Canada)
John Gusdorf (Natural Resources Canada)
Nick Kelly (University of Strathclyde)
Marianne Manning (National Research Council Canada)
Leen Peeters (Catholic University of Leuven)
Maurizio Sasso (University of Sannio)
Daniel Schreiber (Swiss Federal Laboratories for Materials Testing and Research, EMPA)
Sergio Sibilio (Second University of Napoli)
Kathleen Siemens (Natural Resources Canada)
Mike Swinton (National Research Council Canada)

REPORT EDITOR & ANNEX 42 OPERATING AGENT:
Ian Beausoleil-Morrison (Natural Resources Canada)

ANNEX 42 SUBTASK B LEADER:
Nick Kelly (University of Strathclyde)

CITATION

Ian Beausoleil-Morrison (Natural Resources Canada). Experimental Investigation of Residential Cogeneration Devices and Calibration of Annex 42 Models. A Report of Subtask B of FC+COGEN-SIM The Simulation of Building-Integrated Fuel Cell and Other Cogeneration Systems. Annex 42 of the International Energy Agency Energy Conservation in Buildings and Community Systems Programme. (255 pages).

Copies of this report may be obtained from the Annex 42 web site at: www.cogen-sim.net or from the IEA/ECBCS Bookshop at: www.ecbcs.org.

DISCLAIMER

This report is distributed for information purposes only and does not necessarily reflect the views of the Operating Agent (Government of Canada through the Department of Natural Resources Canada) nor does it constitute an endorsement of any commercial product or person. All property rights, including copyright, are vested in the Operating Agent on behalf of the International Energy Agency Energy Conservation in Buildings and Community Systems Programme (IEA/ECBCS) for the benefits of the Annex 42 Participants provided, however, that the Participants may reproduce and distribute such material, but if it shall be published with a view to profit, permission should be obtained from the IEA/ECBCS. In particular, no part of this publication may be reproduced, stored in a retrieval system or transmitted in any form or by any means, electronic, mechanical, photocopying, recording or otherwise, without the prior written permission of the Operating Agent. Neither the International Energy Agency (IEA), Canada, its ministers, officers, employees nor agents make any warranty or representation, expressed or implied, with respect to the use of any information, apparatus, method, process or similar items disclosed in this report, that such use does not infringe on or interfere with the privately owned rights, including any party's intellectual property or assume any liability or responsibility arising out of this report.

Participating countries in ECBCS:

Australia, Belgium, CEC, Canada, Czech Republic, Denmark, Finland, France, Germany, Greece, Israel, Italy, Japan, the Netherlands, New Zealand, Norway, Poland, Portugal, Sweden, Switzerland, Turkey, United Kingdom and the United States of America.

© Her Majesty the Queen in Right of Canada, 2007
ISBN No. 978-0-662-47523-1
Catalogue No.: M154-14/4-2007E-PDF

Preface

International Energy Agency

The International Energy Agency (IEA) was established in 1974 within the framework of the Organisation for Economic Co-operation and Development (OECD) to implement an international energy programme. A basic aim of the IEA is to foster co-operation among the twenty-four IEA participating countries and to increase energy security through energy conservation, development of alternative energy sources and energy research, development and demonstration (RD&D).

Energy Conservation in Buildings and Community Systems

The IEA sponsors research and development in a number of areas related to energy. The mission of one of those areas, the ECBCS - Energy Conservation for Building and Community Systems Programme, is to facilitate and accelerate the introduction of energy conservation, and environmentally sustainable technologies into healthy buildings and community systems, through innovation and research in decision-making, building assemblies and systems, and commercialisation. The objectives of collaborative work within the ECBCS R&D programme are directly derived from the on-going energy and environmental challenges facing IEA countries in the area of construction, energy market and research. ECBCS addresses major challenges and takes advantage of opportunities in the following areas:

- exploitation of innovation and information technology;
- impact of energy measures on indoor health and usability;
- integration of building energy measures and tools to changes in lifestyles, work environment alternatives, and business environment.

The Executive Committee

Overall control of the programme is maintained by an Executive Committee, which not only monitors existing projects but also identifies new areas where collaborative effort may be beneficial. To date the following projects have been initiated by the executive committee on Energy Conservation in Buildings and Community Systems (completed projects are identified by (*)):

Annex 1: Load Energy Determination of Buildings (*)
Annex 2: Ekistics and Advanced Community Energy Systems (*)
Annex 3: Energy Conservation in Residential Buildings (*)
Annex 4: Glasgow Commercial Building Monitoring (*)
Annex 5: Air Infiltration and Ventilation Centre
Annex 6: Energy Systems and Design of Communities (*)
Annex 7: Local Government Energy Planning (*)
Annex 8: Inhabitants Behaviour with Regard to Ventilation (*)
Annex 9: Minimum Ventilation Rates (*)
Annex 10: Building HVAC System Simulation (*)
Annex 11: Energy Auditing (*)
Annex 12: Windows and Fenestration (*)

Annex 13: Energy Management in Hospitals (*)
Annex 14: Condensation and Energy (*)
Annex 15: Energy Efficiency in Schools (*)
Annex 16: BEMS 1- User Interfaces and System Integration (*)
Annex 17: BEMS 2- Evaluation and Emulation Techniques (*)
Annex 18: Demand Controlled Ventilation Systems (*)
Annex 19: Low Slope Roof Systems (*)
Annex 20: Air Flow Patterns within Buildings (*)
Annex 21: Thermal Modelling (*)
Annex 22: Energy Efficient Communities (*)
Annex 23: Multi Zone Air Flow Modelling (COMIS) (*)
Annex 24: Heat, Air and Moisture Transfer in Envelopes (*)
Annex 25: Real time HEVAC Simulation (*)
Annex 26: Energy Efficient Ventilation of Large Enclosures (*)
Annex 27: Evaluation and Demonstration of Domestic Ventilation Systems (*)
Annex 28: Low Energy Cooling Systems (*)
Annex 29: Daylight in Buildings (*)
Annex 30: Bringing Simulation to Application (*)
Annex 31: Energy-Related Environmental Impact of Buildings (*)
Annex 32: Integral Building Envelope Performance Assessment (*)
Annex 33: Advanced Local Energy Planning (*)
Annex 34: Computer-Aided Evaluation of HVAC System Performance (*)
Annex 35: Design of Energy Efficient Hybrid Ventilation (HYBVENT) (*)
Annex 36: Retrofitting of Educational Buildings (*)
Annex 37: Low Exergy Systems for Heating and Cooling of Buildings (LowEx) (*)
Annex 38: Solar Sustainable Housing
Annex 39: High Performance Insulation Systems
Annex 40: Building Commissioning to Improve Energy Performance
Annex 41: Whole Building Heat, Air and Moisture Response (MOIST-ENG)
Annex 42: The Simulation of Building-Integrated Fuel Cell and Other Cogeneration Systems (FC+COGEN-SIM)
Annex 43: Testing and Validation of Building Energy Simulation Tools
Annex 44: Integrating Environmentally Responsive Elements in Buildings
Annex 45: Energy Efficient Electric Lighting for Buildings
Annex 46: Holistic Assessment Tool-kit on Energy Efficient Retrofit Measures for Government Buildings (EnERGo)
Annex 47: Cost-Effective Commissioning for Existing and Low Energy Buildings
Annex 48: Heat Pumping and Reversible Air Conditioning
Annex 49: Low Exergy Systems for High Performance Buildings and Communities
Annex 50: Prefabricated Systems for Low Energy Renovation of Residential Buildings

Working Group - Energy Efficiency in Educational Buildings (*)
Working Group - Indicators of Energy Efficiency in Cold Climate Buildings (*)
Working Group - Annex 36 Extension: The Energy Concept Adviser (*)

(*) - Completed

Annex 42

The objectives of Annex 42 were to develop simulation models that advance the design, operation, and analysis of residential cogeneration systems, and to apply these models to assess the technical, environmental, and economic performance of the technologies. This was accomplished by developing and incorporating models of cogeneration devices and associated plant components within existing whole-building simulation programs. Emphasis was placed upon fuel cell cogeneration systems and the Annex considered technologies suitable for use in new and existing single and low-rise-multi-family residential buildings. The models were developed at a time resolution that is appropriate for whole-building simulation.

To accomplish these objectives Annex 42 conducted research and development in the framework of the following three Subtasks:

- Subtask A : Cogeneration system characterization and characterization of occupant-driven electrical and domestic hot water usage patterns.
- Subtask B : Development, implementation, and validation of cogeneration system models.
- Subtask C : Technical, environmental, and economic assessment of selected cogeneration applications, recommendations for cogeneration application.

Annex 42 was an international joint effort conducted by 26 organizations in 10 countries:

Belgium	▪ University of Liège / Department of Electrical Engineering and Computer Science ▪ COGEN Europe ▪ Catholic University of Leuven
Canada	▪ Natural Resources Canada / CANMET Energy Technology Centre ▪ University of Victoria / Department of Mechanical Engineering ▪ National Research Council / Institute for Research in Construction ▪ Hydro-Québec / Energy Technology Laboratory (LTE)
Finland	▪ Technical Research Centre of Finland (VTT) / Building and Transport
Germany	▪ Research Institute for Energy Economy (FfE)
Italy	▪ National Agency for New Technology, Energy and the Environment (ENEA) ▪ University of Sannio ▪ Second University of Napoli
Netherlands	▪ Energy Research Centre Netherlands (ECN) / Renewable Energy in the Built Environment
Norway	▪ Norwegian Building Research Institute (NBRI) ▪ Telemark University College
United Kingdom	▪ University of Strathclyde / Energy Systems Research Unit (ESRU) ▪ Cardiff University / Welsh School of Architecture
United States of America	▪ Penn State University / Energy Institute ▪ Texas A&M University / Department of Architecture ▪ National Institute of Standards and Technology ▪ National Renewable Energy Laboratory

	▪ National Fuel Cell Research Center of the University of California-Irvine
Switzerland	▪ Swiss Federal Laboratories for Materials Testing and Research (EMPA) / Building Technologies Laboratory ▪ Swiss Federal Institute of Technology (EPFL)/ Laboratory for Industrial Energy Systems ▪ Hexis AG (Hexis) ▪ Siemens Switzerland AG (Siemens)

Table of Contents

Section I : Introduction

Section II : Annex 42 Experimental Protocol

Section III : Description of Experimental Facilities

III-1 Technical University of Munich

III-2 Catholic University of Leuven

III-3 Canadian Centre for Housing Technology

III-4 Fuel Cell Technologies Ltd.

III-5 National Institute of Standards and Technology

III-6 Napoletanagas

Section IV : Experimental Investigations of Residential Cogeneration Devices

IV-1 Investigation of a WhisperGen SE device at the Catholic University of Leuven

IV-2 Investigation of a WhisperGen SE device at the Canadian Centre for Housing Technology

IV-3 Investigation of a Solo SE device at the Technical University of Munich

IV-4 Investigation of a Senertec ICE device at the Technical University of Munich

IV-5 Investigation of an Ecopower ICE device at the Technical University of Munich

IV-6 Investigation of a Senertec ICE device at the Catholic University of Leuven

IV-7 Investigation of a Senertec ICE device at Swiss Federal Laboratories for Materials Testing and Research

IV-8 Investigation of an AISIN ICE device at Napoletanagas

IV-9 Investigation of a PEMFC (System A) Device at the National Institute of Standards and Technology

IV-10 Investigation of a PEMFC (System B) Device at the National Institute of Standards and Technology

IV-11 Investigation of a Vaillant PEMFC device at the Technical University of Munich

IV-12 Investigation of a FCT SOFC at the Canadian Centre for Housing Technology

IV-13 Investigation of a FCT SOFC at Fuel Cell Technologies

Section V : Calibration of the Annex 42 combustion cogeneration model to the Whisper-Gen SE device

Section VI : Calibration of the Annex 42 combustion cogeneration model to the Senertec ICE device

Section VII : Calibration of the Annex 42 fuel cell cogeneration model to the FCT SOFC device

Section I

Introduction

AUTHORS:

Nick Kelly (University of Strathclyde)

Ian Beausoleil-Morrison (Natural Resources Canada)

The Need for Calibration

Annex 42 has developed two models for simulating the performance of residential-scale cogeneration devices (Kelly and Beausoleil-Morrison, 2007). One of these models treats fuel cell systems while the other treats combustion-based systems (Stirling engines and internal combustion engines).

These models were developed using a "grey box" approach, wherein the structure of the model is roughly related to the basic underlying physical processes. However, many of the characteristic equations used in the models take the form of parametric equations describing the relationships between key input and output parameters. One of the models also features equations that describe time-varying characteristics such as dynamic heat exchange. Each of these parametric equations requires the input of empirical constants that characterize the performance of subsystems of specific cogeneration devices. The establishment of these empirical constants is known as the process of model *calibration*.

Annex 42 Experimental Work and Calibration

With regard to model calibration, a review of available experimental data was undertaken within Annex 42. It was apparent from this review that few existing datasets had data suitable for model calibration purposes. It was therefore extremely important that, given the lack of data in the literature, any experimental data collected during Annex 42's experimental testing programme should be of sufficient detail and breadth to facilitate model calibration. To this end, an experimental protocol was developed for experimental work conducted within Annex 42.

Seven Annex 42 participants from six countries conducted experiments with prototype or early market residential cogeneration devices. In total, 13 separate investigations were conducted on devices of the following types:

- Solid oxide fuel cell (SOFC);
- Polymer exchange membrane fuel cell (PEMFC);
- Stirling engine (SE);
- Internal combustion engine (ICE);

In some cases these experimental programmes were conducted prior to the establishment of the experimental protocol, but where possible the protocol was adhered to for the purposes of collecting data suitable for model calibration purposes.

Report Outline

This report documents the experimental investigations of residential cogeneration systems conducted within Annex 42 and the subsequent calibration of the Annex 42 models using these data.

Section II of the report documents the experimental protocol discussed above. Section III then describes the laboratory and field test facilities used to conduct the experimental investigations. A separate subsection is provided for each facility. Following this, Section IV describes the 13 experimental investigations of SOFC, PEMFC, SE, and ICE cogeneration devices, each in a separate subsection.

The calibration of the Annex 42 models using some of these data are then detailed in Sections V through VII. Examples are provided for SE, ICE, and SOFC cogeneration devices.

References

Kelly N. and Beausoleil-Morrison I., Editors (2007), *Specifications for Modelling Fuel Cell and Combustion-Based Residential Cogeneration Devices within Whole-Building Simulation Programs*, IEA/ECBCS Annex 42 Report, ISBN No. 978-0-662-47116-5.

Section II

Experimental Protocol

AUTHORS:

Nick Kelly (University of Strathclyde)

Ian Beausoleil-Morrison (Natural Resources Canada)

WITH INPUT FROM:

Ernst-Jan Bakker (Energy Research Centre Netherlands)

Ulli Arndt (Research Institute for Energy Economy)

Evgueniy Entchev (Natural Resources Canada)

Mike Swinton (National Research Council of Canada)

Dave Thompson (Penn State University)

Mark Davis (National Institute of Standards and Technology)

The protocol takes a pragmatic approach to data capture, recognizing that different laboratories will be equipped to different levels and be able to capture different types of data. With this in mind the protocol divides the data requirements for calibration into two categories: *critical* data and *desired* data.

Critical Data

This is the basic data needed to calibrate any of the device models and is in-turn subdivided into static and time-varying data. Static data can be collected prior to any experiment commencing. For example the mass of components can be measured; this data is useful in developing dynamic performance equations.

Time varying measurements are those that would be collected during an experiment and mainly consist of temperatures and flow rates.

Table II.1 : Essential data for model calibration

Static Measurements	*Time-varying Measurements*
1. Mass of cogeneration device, not including the balance of plant components (e.g. pumps, storage). 2. Empty and charged mass of heat exchanger (exhaust-gas-to-air or water-to-water) used for capturing thermal output. 3. Total mass of cogeneration device. 4. Composition of fuel (molar fractions of CH_4, C_2H_6 C_3H_8, higher hydrocarbons, N_2, CO_2).	1. Electrical demand placed upon cogeneration device (W) 2. Net AC electrical output from cogeneration device (after parasitic losses, battery losses, and losses from power conditioning unit) (W) 3. Natural gas consumption rate (m^3 /s at standard temperature and pressure). 4. Air supply rate to cogeneration device (kg/s). 5. Temperature of air supplied to cogeneration device (^oC). 6. Humidity of air supplied to cogeneration

	device (RH or T_{dp}) 7. Flow rate of liquid water supplied to cogeneration device (kg/s) 8. Flow rate of exhaust gases through gas-to-water heat exchanger or flow rate of water on cogeneration side of water-to-water heat exchanger (kg/s). 9. Temperature of exhaust gases as they enter gas-to-water heat exchanger or temperature of entering water on cogeneration side of water-to-water heat exchanger (^{o}C). 10. Temperature of exhaust gases as they exit gas-to-water heat exchanger or temperature of exiting water on cogeneration side of water-to-water heat exchanger (^{o}C). 11. Flow rate of water on plant side of gas-to-water or water-to-water heat exchanger (kg/s) 12. Temperature of entering water on plant side of gas-to-water or water-to-water heat exchanger (^{o}C). 13. Temperature of exiting water on plant side of gas-to-water or water-to-water heat exchanger (^{o}C). 14. Exhaust gas composition (molar fractions of CO_2, N_2, Ar, O_2, H_2O, CH_4, H_2, CO, etc). 15. Ambient air temperature (^{o}C). 16. Ambient air humidity (RH or T_{dp}).

Desired Data

This is data that would enhance a calibration exercise, i.e. allowing a more detailed model to emerge, but which is not essential.

Table II.2 : non-essential data for calibration

Desired Data
1. Gross DC electrical production from cogeneration device prior to power conditioning (W)
2. Cogeneration device parasitic electrical draws (e.g. fans, controls) (W)
3. DC electrical input to battery storage[1] (W)
4. DC electrical output from battery storage to power conditioning unit (PCU) (W)
5. Net AC electrical output from PCU (W)
6. Temperature of fuel supplied to cogeneration device (^{o}C)
7. Pressure of fuel supplied to cogeneration device (kPa)
8. Pressure of air supplied to cogeneration device (kPa)
9. Parasitic thermal losses from cogeneration device, either directly measured or deduced from skin measurements, infrared camera scans, or a room energy balance (W).
10. Fuel consumption, exhaust-gas temperature, electrical output during start-up period (relevant only for start-up test described in "Tests appropriate for parameter identification" section). Duration of start-up period also to be measured
11. Fuel consumption (if any), exhaust-gas temperature (if any), and solid-component temperatures during shut-down period
12. Duration of period until unit can be restarted.

Testing Specifications

In addition to the data that should be captured, the Protocol also highlights the type of tests that should be undertaken on the cogeneration devices. Ideally, the data captured from these tests should be sampled at a time interval of 1 minute or less (ideally 10 seconds), in order to capture some of the higher-frequency thermal and control phenomena occurring within the test.

[1] Where applicable: some cogeneration devices place batteries between the DC power generator and the power conditioner. This is used to respond to short-term electrical demands in electric load following control strategies.

A complete description of the methods used to collect, integrate and report data should be provided. The nature of each measurement (spot, integrated or averaged, etc.) should be specified. It is also be important to record the precise point in time that the data acquisition equipment registers each sensor's measurement.

Three types of tests are specified: parameter identification, algorithm calibration, and whole model validation-type tests. The Protocol categorises the first two types as those tests that are performed in laboratories and can be used to characterise all or part of a model. The latter are classed as those tests that can be conducted in less controlled situation (e.g. a test house) which could be used for whole-model validation.

Except where noted, all the tests described here are applicable for all the cogeneration technologies considered by Annex 42 (SOFC, PEMFC, Stirling engine, ICE). It is recognized that not all experimental facilities will be able to run all tests on all available cogeneration devices. Indeed, some customization of the test programme laid out here will be necessary for each device and circumstance.

Parameter Identification

This uses test data to identify specific parameters within a model. The types of tests that could be used for this function include step and ramp tests and cold-start and cool down sequences.

Specific tests that could be undertaken are as follows.

Table II.3 : parameter identification tests

1. Dynamic step tests (particularly valuable for SOFC): the cogeneration device is started from cold and monitored until steady-state operation is obtained.
2. The cogeneration device is shut down but the flow rate and temperature of the water on the plant side of the heat exchanger remains constant. The cooling characteristics of cogeneration device are measured.

Algorithm Calibration

These tests would be used for calibration or validation of specific algorithms within models. Examples of the type of test include: variation in coolant supply and flow rate over several steady state tests and variations in loading. Where this data is being used for calibration, it could be used to develop maps of a component's performance over a finite range of operating conditions.

Specific tests to undertake are as follows.

Table II.4 : algorithm calibration tests

1. While the cogeneration device is operating with a constant electrical output, the temperature of the water supplied by the plant (or the experimental facility) to the cogeneration device's heat exchanger is varied from 10°C to 90°C in approximately 5°C steps (or over the range that can be achieved given the constraints of the experimental set-up and the operational requirements of the cogeneration device, e.g. minimum turn-down-ratio). Sufficient time is allowed for conditions to stabilize between each step change. The flow rate of the water through the heat exchanger remains constant at the manufacturer's (or experimentalist's) recommended flow rate. The test is repeated at the minimum and maximum recommended flow rates.
2. While the cogeneration device is operating with a constant electrical output, the flow rate of the water supplied by the plant to the cogeneration device's heat exchanger is varied from 50% of the manufacturer's (or experimentalist's) recommended flow rate to 200% in approximately 10% steps (or over the range that can be achieved given the constraints of the experimental set-up and the operational requirements of the cogeneration device, e.g. pump control and flow rate and temperature restrictions). Sufficient time is allowed for conditions to stabilize between each step change. The temperature of the water supplied to the heat exchanger remains constant at 50°C. The test is repeated for a supply water temperature of 5°C and again for a supply water temperature of 80°C.
3. If feasible, the above two test sequences are repeated at other constant electrical outputs. This will provide a "performance map" over the full range of cogeneration device outputs and thermal boundary conditions.

4. While the cogeneration device is operating with a constant electrical output, the temperature of the water supplied by the plant to the cogeneration device's heat exchanger is varied in a ramp with a given time period from 10°C to 90°C (or over the range that is feasible given the constraints of the experimental set-up and the operational requirements of the cogeneration device). The flow rate of the water through the heat exchanger remains constant.
5. The electrical load placed upon the cogeneration device is varied in a ramp over a given time period from no load to full load, subject to the restrictions of the experimental set- up and the operational requirements of the cogeneration device.
6. The electrical load placed upon the cogeneration device is varied in steps (approximately 10%, 25%, 50%, 75%, and 100% of full load, subject to the same constraints as above) and the cogeneration device is allowed to reach steady-state at each step.

Whole Model Validation

These tests record operating conditions that would be more akin to what the unit would experience in reality. Suggestions for tests are as follows.

Table II.5 : whole model verification tests

1. The cogeneration device follows the house's electric load, which varies according to the "typical" behaviour of occupants and electrical draws of HVAC equipment. The range of electrical draws should vary from 5% to 100% of the device's rated net output (or over its full safe operating range).
2. The cogeneration device is modulated to maintain the temperature of the water in the buffering tank within a pre-defined control range. The hot water draws from the buffering tank are consistent with "typical" DHW and space- heating needs.
3. The cogeneration device is modulated to respond to "typical" varying electrical and thermal loads and analysed in both electrical and thermal tracking control regimes (useful for control optimization analysis).

Section III

Description of Experimental Facilities

III-1 : Description of the Experimental Facilities at the Technical University of Munich[1]

In the framework of the project *Innovative CHP-Systems for energy supply of residential buildings* the Research Institute for Energy Economy in Munich has cooperated with the Institute for Energy Economy and Application Technology at the Technical University of Munich, which has built a test rig for heat generation.

Description of the test rig

The test rig allows the analysis of heat generators under real conditions such as those experienced on a typical winter or summer day, including all of its dynamic load changes. It is validated, tested and suitable for further system tests such as CHP systems. Figure III-1.1 illustrates the "central heating room" with the usual equipment of central heating systems. The connections of the boiler on the left side of this figure are used for the peak load boiler in the CHP system. Connected to the boiler are distribution pipelines for space heating and domestic hot water with controls, pumps, measuring devices for flow rate and temperature.

Figure III-1.2 shows the heat storage integrated in the system and the facilities for domestic hot water supply. For the testing of various CHP systems for the energy supply of residential buildings, the test rig had to be modified in terms of hydraulics and technical measurements. The planning criteria for the hydraulic composition were based on the suggested connections of particular project partners. The variety of manufacturers' ideas to integrate their equipment under test in existing systems is remarkable.

[1] Authored by Ulli Arndt (Research Institute for Energy Economy, FfE, Munich, Germany)

Figure III-1.1 : Test rig for heat generation

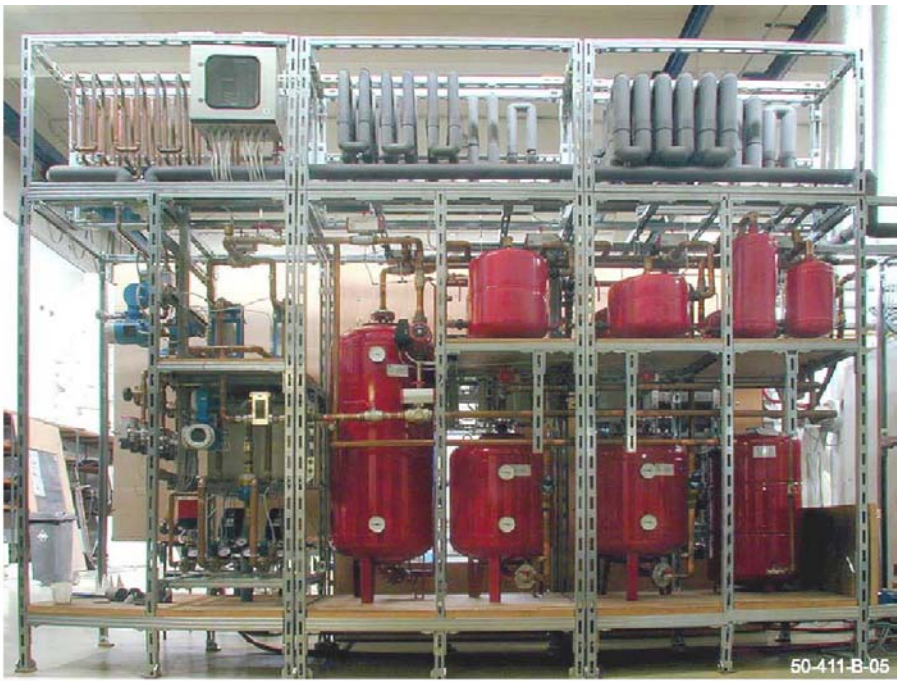

Figure III-1.2 : Side elevation of the test rig for heat generation

The developed schematic of the plant is illustrated in Figure III-1.3. The CHP plant under test is embedded with the "peak load boiler" in the heat generation balance. The components "heating circuit for space heating" and "domestic hot water supply" are incorporated as heat sinks. (Refer to the legend in the figure to relate these items to the German text within the figure.)

It can affect the heat sinks directly or can be integrated in the supply via heating or hot water storage. The actual design of the CHP upgrade includes two 1 000 L and one 500 L heating buffer vessels and 1 000 L and 500 L for domestic hot water storage.

To guarantee an efficient provision of space heating and domestic hot water of a residential building with a CHP system, the CHP plant has to provide the supply primarily if necessary by inclusion of heat storage, in doing so the electrical network supply is always guaranteed. Only when the CHP plant cannot provide sufficient required thermal energy, the peak load boiler will start to operate.

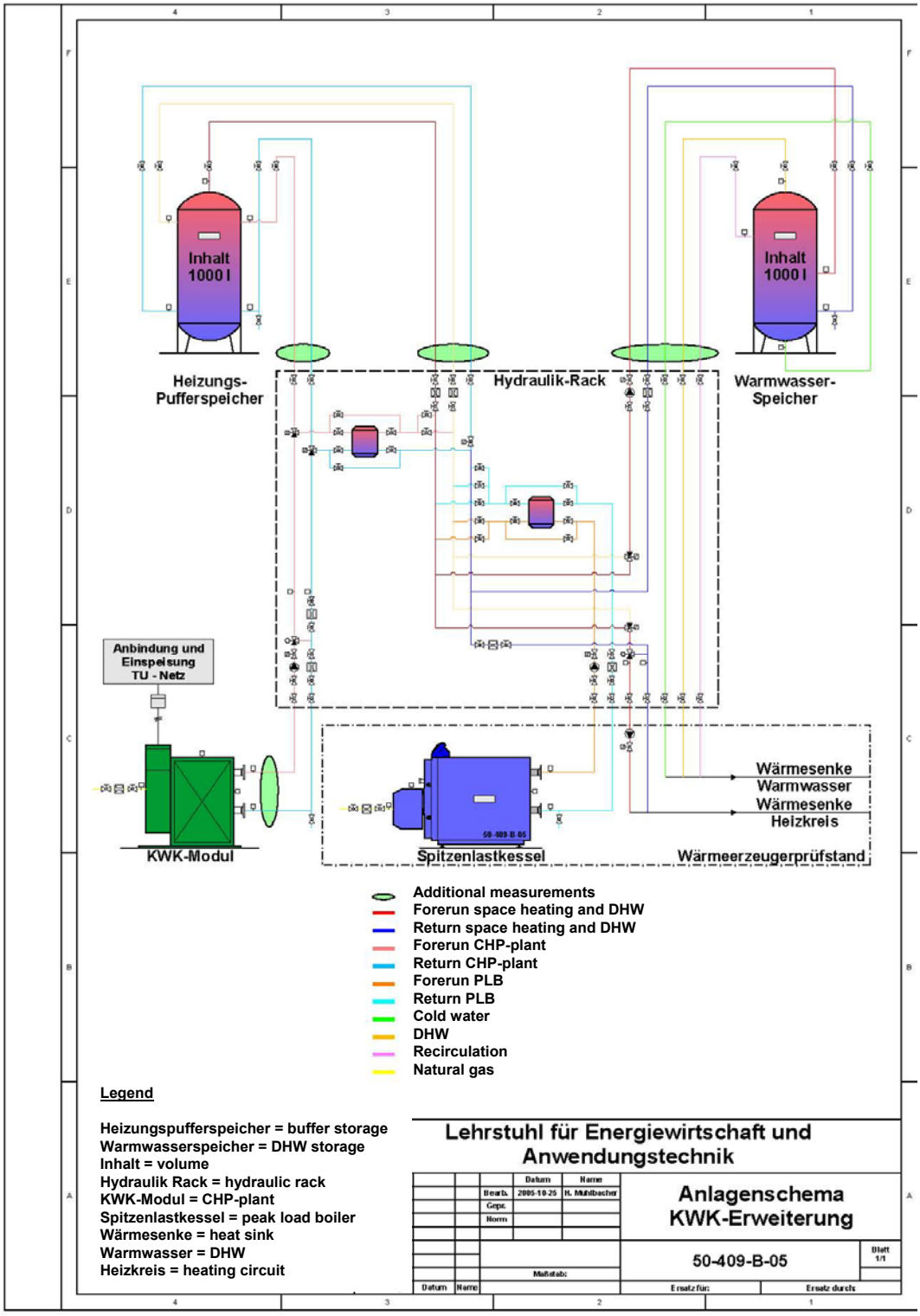

Figure III-1.3 : Plant design for the CHP upgrade

Different options were recommended by respective manufacturers for this plant design. To enable the measurement of all equipment without elaborate hydraulic conversion, a hydraulic rack was developed (see Figure III-1.4). Many plant schemes are possible but this one was chosen to be the most favourable with regard to complexity, costs and technical measurement reasons. Flexible stainless steel pipes connect the rack with the CHP plant and the hydraulic rack. The rack has ball valves that enable the desired hydraulic control. The CHP-plant can be operated

- directly on the buffer storage (alternative 1)
- directly on the heating circuit (alternative 2)
- directly on the domestic hot water storage (alternative 3)
- as preheating of return temperature (alternative 4) for the peak boiler

Figure III-1.4 : Equipment under test and hydraulic rack

To ensure a constant flow in the CHP plant for the alternative 2 and 4, a hydraulic switch was placed. This switch can be by-passed by means of two ball valves in case the CHP plant does not have an own pump.

The supply of the buffer and domestic hot water storage load circuit can happen by heat generators (CHP plant and peak load boiler) as well as by the buffer storage. The operation of the three replaceable buffer storages can take place individually or in series. Should the buffer storage have five connections, the "hot" connection (on top of the buffer vessel) can be used for e.g. domestic hot water load and the "warm" connection to supply the space heating circuit.

The supply of the space heating circuit can happen directly or via a motor controlled mixer. Similar to the buffer storages, up to two hot water storages can be operated serially. The required heat quantities for domestic hot water draw and circulation losses are covered by the domestic hot water storage. The flow measurement devices which are necessary for the balance were also integrated in the rack. Ball valves that are controlled by compressed air were built in where switching during test rig trials should be possible and after circulation pumps respectively to avoid residual flows. Where heating and hot water leave the rack, the incorporation to the existing test rig takes place.

Measuring points

The measured data of the test rig are shown in Table III-1.1 with respective position and type of measuring head.

- The temperatures are measured by means of a PT-100 resistance thermometer and an additional thermal element NiCR in the exhaust pipe. The calibration of respective sensors is carried out by a calibrator.

- The measurement of particular flows is realised by magnetic inductive measurement devices

- To determine electrical variables of the CHP plant, configurable multifunctional transducers are used for the measurement of effective power, idle power and respective voltages.

- To reduce faults, various transducer variables can be introduced depending on the power.

- The consumption of auxiliary power of the CHP plant can be determined by subtraction of generator and energetic recovery system power.

The compilation of the fuel consumption happens via an experimental gas meter with 1 dm^3/impulse inside of the gas pipe.

As respective equipment is operated by different gas pressure, a connection of 50 mbar was installed; another connection was installed via a gas pressure control which permits a pressure between 20 mbar and 50 mbar.

Table III-1.1 : Overview of test points of the CHP-test rig

Number	Position	Measuring device
CHP-plant		
1	Gas temperature	Pt-100
2	Gas consumption	Gas meter
3	Temperature of combustion air	Pt-100
4	Exhaust gas temperature	Pt-100
5	Temperature of cooling water (if possible)	Pt-100
6	Forerun temperature	Pt-100
7	Return temperature	Pt-100
8	Flow CHP-plant	MID
9	Power measurement generator	Active energy meter
10	Power measurement feeding / backup power	Active energy meter
Peak load boiler		
11	Gas temperature	Pt-100
12	Gas consumption	Gas meter
13	Temperature of combustion air	Pt-100
14	Exhaust gas temperature	Pt-100
15	Temperature of cooling water (if possible)	Pt-100
16	Forerun temperature	Pt-100
17	Return temperature	Pt-100
18	Flow peak load boiler	MID
Buffer storage I to III		
19-21	Forerun temperature of buffer storage load	Pt-100
22-24	Return temperature of buffer storage load	Pt-100
25-27	Forerun temperature of buffer storage draw	Pt-100
28-30	Return temperature of buffer storage draw	Pt-100
31-33	Buffer storage temperature	Pt-100
34	Flow buffer storage load	MID
35	Flow buffer storage draw	MID
Domestic hot water storage I to II		
36-37	Forerun temperature of DHW-storage load	Pt-100
38-39	Return temperature of DHW-storage load	Pt-100
40-41	Domestic hot water storage temperature	Pt-100
42-43	Cold water temperature	Pt-100
44-45	Domestic hot water temperature	Pt-100
46-47	Circulation return temperature	Pt-100
48	Flow DHW storage load	MID
49	Flow domestic hot water draw	MID
50	Flow circulation loop	MID
Heating circuit		
51	Forerun temperature	Pt-100
52	Return temperature	Pt-100
53	Flow heating circuit	MID

References

Mühlbacher, H.; Geiger, B.: Innovative CHP-systems for the energy supply of residential buildings - Progress report Phase I / Modification of the test rig, Institute for Energy Economy and Application Technology, Technical University of Munich, October 2005

III-2 : Description of the Catholic University of Leuven's Experimental Facilities[1]

A schematic overview of the KULeuven test set-up is shown in Figure III-2.1

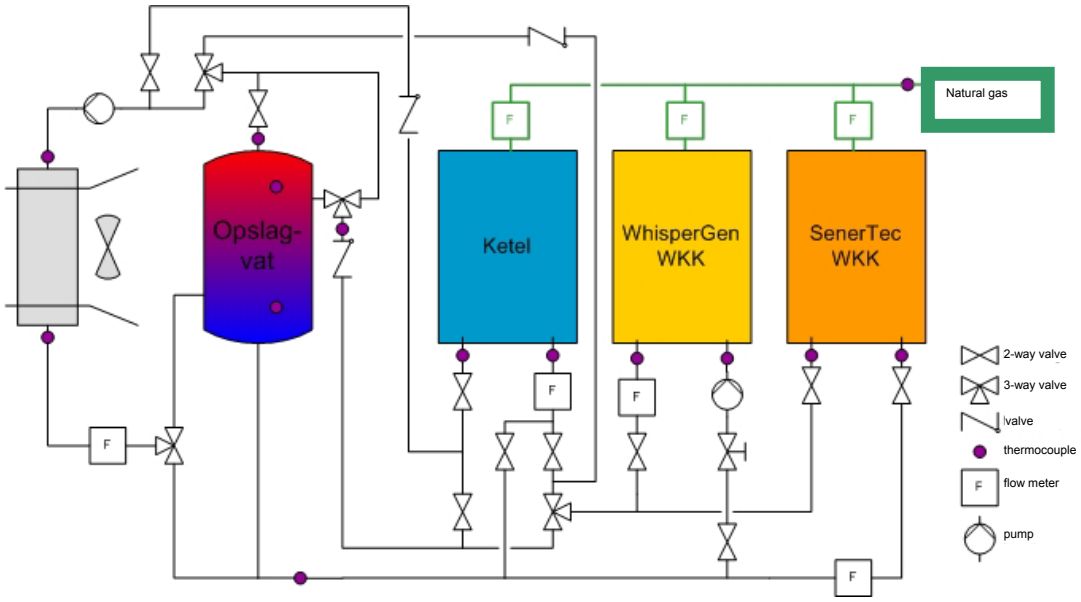

Figure III-2.1 : Schematic overview of experimental set-up at KULeuven

Heat can be produced by the Senertec CHP (Senertec WKK), the WhisperGEN CHP (WhisperGEN WKK) or the Viessmann boiler (ketel). The boiler is used as back up in case of a failure of a CHP or in case the produced heat is not sufficient to cover the heat demand. Production and emission of heat can be coupled directly by using the convector. By using the storage tank (opslagvat), production and emission can be decoupled. It is a stratified storage tank and thus hot water will leave or enter the tank at the top. Cold water coupling is at the bottom.

[1] Authored by Leen Peeters and William D'haeseleer (Catholic University of Leuven)

Both the boiler and the Senertec have an internal pump. The WhisperGEN has an external pump that is controlled by this Stirling CHP. Both CHP's can be connected in series with the boiler. Natural gas consumption and electricity consumption or production, are measured for each heat production system separately.

Tests were conducted both for the dynamic behaviour and the stationary properties. Dynamic behaviour is measured by direct coupling of CHP and convector. The water flow rate varied from 3 to 8 L/min. To test the impact of a warm or cold start up, different starting conditions were measured: cold start and starts after 1 hr, 2 hrs and 4 hrs shut down time.

Tests on the stationary behaviour were conducted by using the convector for direct emission of heat. Different electrical output power levels were defined and measured once in steady state. This was only done for the WhisperGEN. The Senertec could only be measured for the set value of electrical and thermal power.

The WhisperGEN's performance was also tested for a variation in water inlet temperature, to check on the performances with and without condensation.

III-3 : Description of the Canadian Centre for Housing Technology Experimental Facilities[1]

CCHT Twin-House Facility

Built in Ottawa in 1998, the Canadian Centre for Housing Technology (CCHT) is jointly operated by the National Research Council, Natural Resources Canada and Canada Mortgage and Housing Corporation. CCHT features twin research houses to evaluate the whole-house performance of new technologies in side-by-side testing (see Figure III-3.1). These houses were designed and built by a local builder with the same crews and techniques normally used by the builder on other sites in Ottawa. The CCHT twin houses are fully instrumented and are unoccupied. To simulate the normal internal heat gains of lived-in houses, these houses feature identical 'simulated occupancies'. The simulated occupancy strategy is described in the next section.

Originally designed as passive solar houses, the CCHT houses have been run under different configurations to suit the experiment. For the Stirling engine experiment, the houses were operated in their original passive solar configuration (no shades). For the fuel cell CHP experiment, a conventional house design was chosen for the experiment rather than a passive solar design. To accommodate this requirement, large shades were deployed on two south windows to achieve a more balanced solar gain profile for the houses (see Figure III-3.1).

[1] Authored by Mike Swinton and Marianne Manning (National Research Council Canada) and Evgeuniy Entchev and John Gusdorf (Natural Resources Canada)

Figure III-3.1 : CCHT Twin-House Facility - with 2 south windows shaded to reduce passive solar gains.

Simulated occupancy deployed at the Canadian Centre for Housing Technology

The twin-houses at the Canadian Center for Housing Technology feature an identical "simulated occupancy system" in each house. It is based on home automation technology, which simulates human activity by operating major appliances (stove, dishwashers, washer and dryer), lights, water valves, fans, and a host of other sources simulating typical heat gains. The schedule is typical of activities that would take place in a home with a family of two adults and two children. Electrical consumption is typical for a family of four and hot water draws are set in accordance with ASHRAE standards for sizing hot water heaters. The heat given off by humans is simulated by two 60 W (2 adults) and two 40 W (2 children) incandescent bulbs at various locations in the house. The accompanying table records the simulated occupancy schedule used in the CHP experiments.

CCHT Simulated Occupancy Schedule

Note: Water draws shown here are for hot water only, in litres.

Overnight				
Device	Water Utility	Draw	Time	Duration
Bedroom 2 humans		66.4 W	0:00	6 hrs 45 min
Master bedroom humans		99.6 W	0:00	6 hrs 45 min
Morning				
Device	Water Utility	Draw	Time	Duration
2nd floor lights		410 W	6:45	60.0 min
	1. Master bedroom shower	36 L	6:50	10.2 min
Family room humans		166 W	7:00	60.0 min
Main floor lights		200 W	7:00	60.0 min
Kitchen products		450 W	7:30	10.2 min
Kitchen fan		80 W	7:30	10.2 min
Kitchen stove (intermittent)		1600 W	7:30	20.0 min
	2. Kitchen tap	13 L	7:45	3.0 min
Afternoon				
Device	Water Utility	Draw	Time	Duration
Kitchen fan		80 W	12:00	15.0 min
Kitchen stove (intermittent)		1600 W	12:00	15.0 min
Family room humans		166 W	12:00	30.0 min
Kitchen products		450 W	12:00	10.2 min
Main floor lights		200 W	12:00	15.0 min
	3. Kitchen tap	13 L	12:30	3.0 min
Evening				
Device	Water Utility	Draw	Time	Duration
	4 & 5. Clothes washer (46L)	400 W	17:00	60.0 min
Main floor lights		200 W	17:00	2 hrs 30 min
Kitchen fan		80 W	17:30	3.6 min
Kitchen stove (intermittent)		1600 W	17:30	30.0 min
Family room humans		166 W	17:30	2 hrs 30 min
Kitchen products		450 W	17:30	10.2 min
Dining room products		225 W	18:00	2 hrs
2nd floor lights		410 W	18:00	5 hrs

	6. Kitchen tap	27 L	18:30	6.0 min
	7 & 8. Dishwasher	650 W	19:00	60.0 min
Dryer		2250 W	19:00	25.2 min
Living room humans		166 W	19:00	2 hrs
Bedroom 2 humans		66 W	21:00	3 hrs
	9. Main bathroom bath	41 L	21:05	4.8 min
	10. Master bedroom shower	55 L	22:30	15 min
Master Bedroom Humans		100 W	23:00	60 min

III-4 : Description of Fuel Cell Technologies' Experimental Facilities [1]

An experimental programme was configured and executed at Fuel Cell Technologies' (FCT) facilities in Kingston (Canada) in collaboration with Natural Resources Canada to perform the tests of the Annex 42 experimental protocol. The experimental set-up is shown schematically in Figure III-4.1.

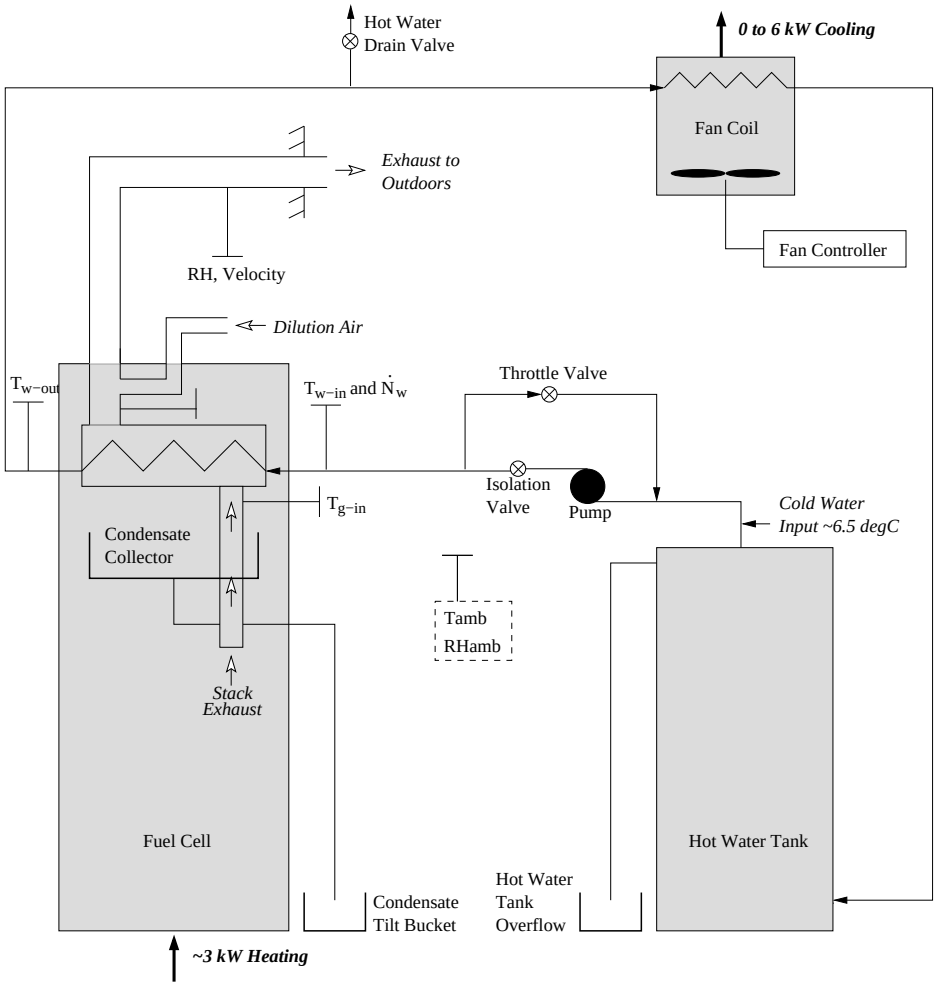

Figure III-4.1: Experimental configuration to control flow rate and temperature of water entering the heat exchanger

Many of the tests required control over the water flow rate through the cogeneration device's heat exchanger and the water inlet temperature. Water was pumped from a storage tank to the

[1] Authored by Ian Beausoleil-Morrison and Kathleen Siemens (Natural Resources Canada)

cogeneration device's heat exchanger. From there the water flowed through a fan-coil before returning to the storage tank. As the circulating pump was operated at constant speed, the flow rate of water through the cogeneration device's heat exchanger was controlled by manually setting a throttling valve. An isolation valve downstream of the pump was manually controlled to increase back pressure, enabling a further reduction in the water flow rate through the heat exchanger. The lowest steady water flow rate through the heat exchanger that could be be achieved was 4 L/min. The highest flow rate was limited by the pump's capacity and was approximately equal to 12 L/min.

The fan-coil was used to dissipate heat from the loop when the desired water temperature was greater than that of the room air. An on-off controller with a 0.2°C dead-band cycled the fan-coil on when necessary to achieve the desired water inlet temperature at the cogeneration device's heat exchanger. This resulted in a small degree of oscillation although the control was mostly satisfactory. When the desired water temperature was below that of the room air, warm water was drained downstream of the cogeneration device. This volume of water was replenished by adding cold water from the mains to the tank. The minimum heat exchanger water inlet temperature was thus regulated by the temperature of the water mains (approximately 6°C). The maximum temperature was restricted to 60°C in order to protect the circulating pump.

Once steady conditions were achieved, measurements were logged to file for a period of time to provide sufficient data to analyze the statistical variation of the measured and derived quantities for each test. Figure III-4.2 illustrates the flow rate and heat exchanger water inlet temperature for the test that was configured to supply 30°C water to the heat exchanger at the lowest flow rate possible. As can be seen from the graph, ideal steady conditions could not be maintained over the duration of the test. Control over the water flow rate was found to be more stable than that over the water inlet temperature. In general, steady thermal conditions were more difficult to achieve at lower entering water temperatures. Notwithstanding, the variations in the water inlet temperature were deemed to be acceptable.

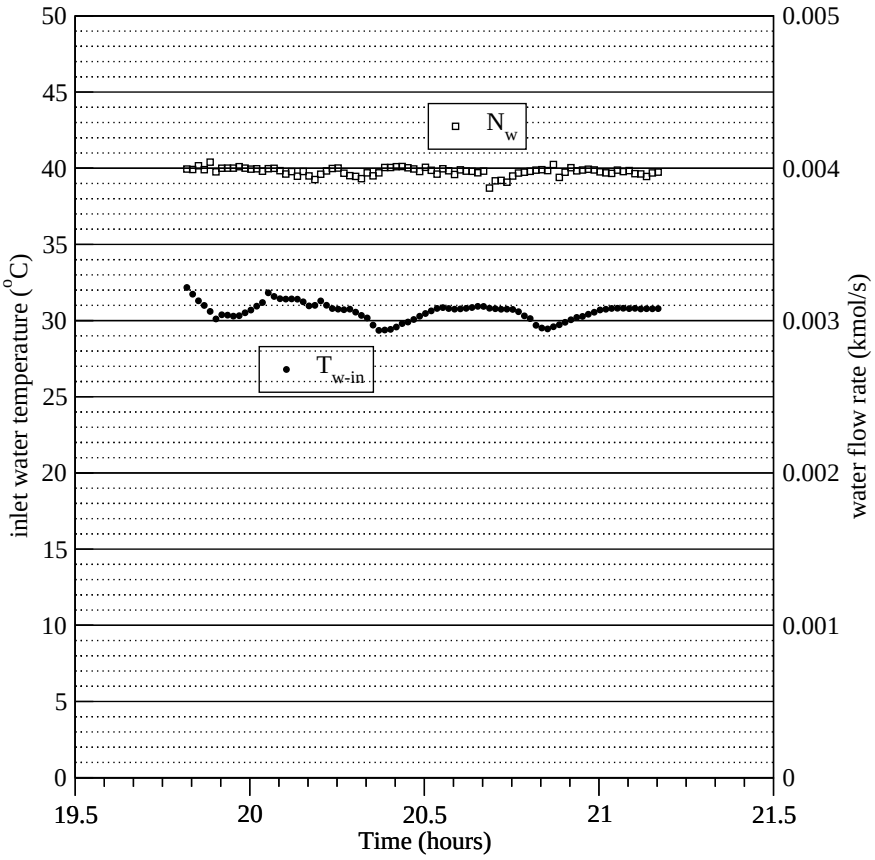

Figure III-4.2: T_{w-in} and $\dot{N}_w$ over duration of one test

III-5 : Description of the National Institute of Standards and Technology's Experimental Facilities[1]

All tests were performed in the NIST Residential Fuel Cell Test Facility as part of an effort to develop a consumer-oriented rating methodology for residential fuel cell systems. The facility (Figure III-5.1) was constructed to test residential-scale fuel cell systems over a wide range of environmental, electrical, and thermal loads. The test facility permits the measurement of a system's fuel consumption, fuel energy content, electrical energy output, and thermal energy output. Operational parameters that can be controlled during a test include: the temperature and relative humidity of the air surrounding the fuel cell, the electrical output of the fuel cell, and the flow rate and temperature of the fluid used to extract the thermal load from the fuel cell. As shown in Figure III-5.1, the fuel cell unit was installed in the test chamber that mimics outdoor weather conditions.

[1] Authored by Mark Davis (National Institute of Standards and Technology)

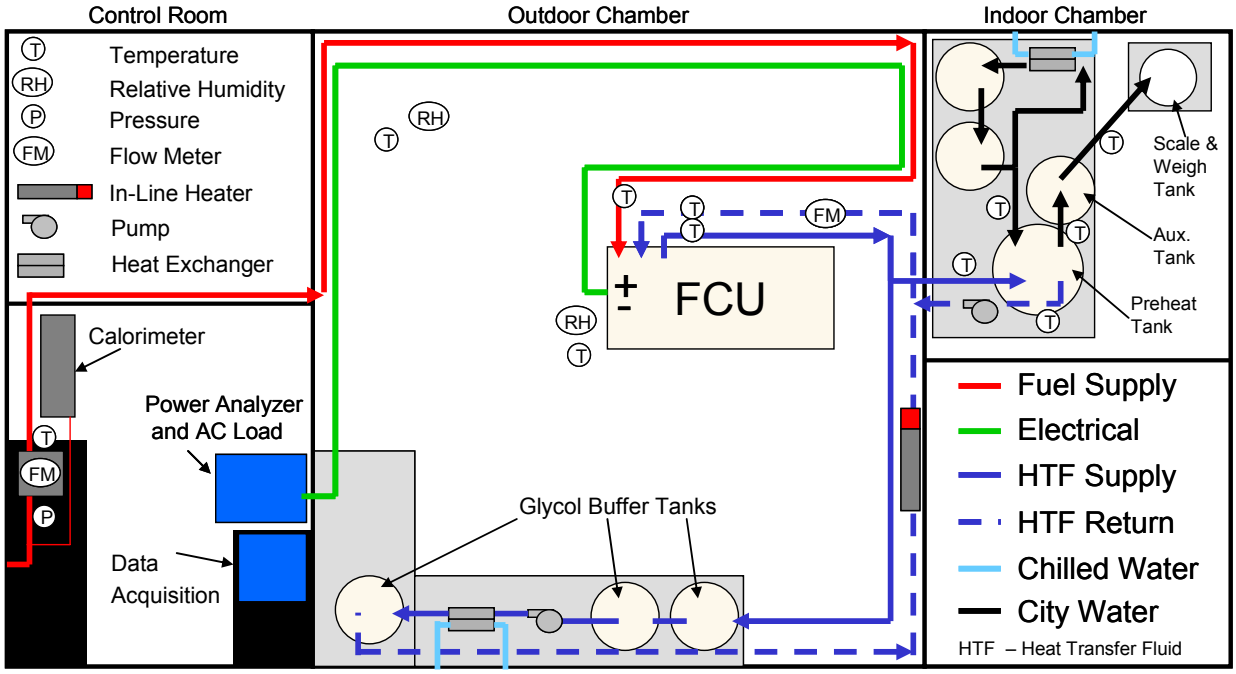

Figure III-5.1 : Schematic of NIST Residential Fuel Cell Test Facility

Table III-5.1 : Control Parameter Ranges

Control Parameter	Minimum	Maximum
Ambient Temperature	-10 °C	40 °C
Relative Humidity	25 %	75 %
Electrical Power	0.1 kW	6.0 kW
Fluid Flow Rate	5 L/min	30 L/min
Fluid Inlet Temperature	8 °C	65 °C

Control

The facility allows the range of control that is listed in Table III-5.1. The electrical load can be supplied to a bank of computer-controlled AC loads or to the local utility grid. When the electrical load is directed to the AC loads, the output power, current, or resistance and the power factor or crest factor are user-selectable. To maintain a steady ambient environment, the fuel cell system is installed within an environmental chamber, which controls both the relative humidity and ambient temperature. The thermal energy produced by the fuel cell is extracted using a mixture of 35 % propylene glycol and 65 %

water by volume fraction as a heat transfer fluid, which allows for testing at ambient temperatures below freezing. The heat transfer fluid flow rate is controlled using two variable-speed pumps in series. Two chilled-water cooled, flat plate heat exchangers and a 3 kW in-line heater control the heat transfer fluid temperature in a fluid conditioning loop.

In lieu of controlling the heat transfer fluid temperature, the fluid can be diverted from the fluid conditioning loop to a simulated residential domestic hot water system. In this arrangement, the fluid transfers heat to a 300 L preheat tank through an integral heat exchanger. When a hot water load is imposed, water is withdrawn from the preheat tank through a 190 L auxiliary electric water heater into a weigh tank and scale, which records the water volume drawn. Water is withdrawn in accordance with the United States Department of Energy's (DOE) residential water heater test procedure. Make-up water into the preheat tank is also temperature controlled.

Measurement

The test facility measures the fuel energy consumed and the electrical and thermal energy produced by the fuel cell. The uncertainties for each measurement and the associated instruments are shown in Table III-5.2. Each uncertainty represents a 95 % confidence interval with the inclusion of a coverage factor of k=2. The fuel energy consumption is measured using a dry-type natural gas meter. A calorimeter continually measures the energy content of the gas. The electrical energy output is measured directly with a power analyzer. For the thermal energy output, the flow rate of the heat transfer fluid is measured with both a turbine and magnetic flow meter for redundancy. The temperature difference imparted to the fluid by the fuel cell is measured using a pair of platinum-resistance thermometers (PRT). The density and specific heat of the glycol-water mixture are calculated using previously derived correlations between these properties and the fluid temperature.

Equations III-5.1 through III-5.6 relate individual measurements with the energy flows to/from the fuel cell and the respective efficiencies. All efficiencies reported in this paper are calculated using the higher heating value (HHV) of natural gas, which is consistent with other appliance rating procedures.

The fuel energy is defined as the summation over the test period of the fuel energy measured at each scan,

$$E_{fuel} = \sum_{i}^{N} \left(V_{fuel,i} \cdot \frac{298.15\ K}{101325\ Pa} \cdot \frac{P_{fuel,i}}{T_{fuel,i}} \cdot e_{fuel,i} \right) \qquad \text{[III-5.1]}$$

Where $V_{fuel,i}$ is volume of natural gas consumed by fuel cell system at each measurement scan (m^3).

Table III-5.2 : Measurement Uncertainties

Measurement	Expanded Uncertainty (k=2)
Fuel	
Energy	0.6 %
Natural gas flow meter	0.2 %
Calorimeter	0.55 %
Fuel temperature	0.3 °C
Fuel Pressure	0.8 %
Electrical	
Energy	0.7 %
Voltage – AC Output	0.5 %
Current – AC Output	0.5 %
Efficiency	0.2 % (i.e. 20 % ± 0.2 %)
Thermal	
Energy	3.5 %
Magnetic flow meter	1.2 %
Temperature	0.1 °C
Density	1.0 %
Specific heat	3.0 %
Efficiency	4.0 % (i.e. 35 % ± 4.0 %)
Environmental	
Ambient temperature	0.3 °C
Relative humidity	1.4 %
Barometric pressure	0.8 %
Exhaust	
Temperature	0.3 °C
Flow rate*	3 %
CO2 concentration*	3 %
Thermal Storage Tank	
Tank inlet and outlet	0.3 °C
HX inlet and outlet	0.3 °C
Tank draw flow rate	2 %

* Exhaust flow rate and carbon dioxide concentration measurements are only available on data recorded after June 2006 (after the 2nd system was installed)

$P_{fuel,i}$ is the pressure of natural gas at the gas meter (Pa)

$T_{fuel,i}$ is the temperature of natural gas at the gas meter (K)

$e_{fuel,i}$ is the energy content of natural gas (kJ/m^3)

The electrical energy over the test period is simply the summation of the electrical energy exported at each measurement scan,

$$E_{electrical} = \sum_{i}^{N} \left[E_{electrical,i} \right] \quad \text{[III-5.2]}$$

Where $E_{electrical,i}$ is the exported electrical energy at each measurement scan.

The thermal energy provided by the fuel cell system over the testing period is the summation of the thermal energy at each measurement scan,

$$E_{thermal} = \sum_{i}^{N} \left[V_{HTF,i} \cdot \rho_{T_{avg,i}} \cdot c_{p,T_{avg,i}} \cdot \left(T_{outlet,i} - T_{inlet,i} \right) \right] \quad \text{[III-5.3]}$$

Where $V_{HTF,i}$ is the volume of heat transfer fluid that passed through the fuel cell system at each measurement scan (m^3)

$\rho_{T_{avg,i}}$ is the density of the heat transfer fluid, which is calculated at the average fluid temperature (kg/m^3)

$c_{p,T_{avg,i}}$ is the specific heat of the heat transfer fluid, which is calculated at the average fluid temperature (kJ/kg)

$T_{outlet,i}$ is the temperature of the heat transfer fluid at the outlet of the fuel cell system (°C)

$T_{inlet,i}$ is the temperature of the heat transfer fluid at the outlet of the fuel cell system (°C)

The electrical and thermal efficiencies over the testing period are calculated as the quotient of the electrical and thermal energy, respectively and the fuel energy.

$$\eta_{electrical} = \frac{E_{electrical}}{E_{fuel}} \cdot 100\% \qquad \text{[III-5.4]}$$

$$\eta_{thermal} = \frac{E_{thermal}}{E_{fuel}} \cdot 100\% \qquad \text{[III-5.5]}$$

The overall efficiency is the sum of the electrical and thermal efficiencies.

$$\eta_{overall} = \eta_{electrical} + \eta_{thermal} \qquad \text{[III-5.6]}$$

III-6 : Description of Napoletanagas Experimental Facilities[1]

A test facility has been built at the gas utility Napoletanagas in Naples, Italy, in order to evaluate the performances of gas-fuelled micro-CHP devices for domestic and light commercial applications. It is possible to simulate electric and thermal demands in this test facility (M. Dentice d'Accadia, M. Sasso, S. Sibilio, R. Vanoli, 2000). For residential and light commercial applications, and referring to the demand profile of an Italian user, the simulation system has been planned to follow the electric demand in the range 0–10 kW and the heat demand in the range 0–30 kW.

The test station (Figure II-6.1) consists of two different sectors: the external part where the micro-CHP device is located and the internal part that contains the components to simulate the electric and thermal load (household appliances), and the relative sensors for measuring electrical, thermal and flow quantities.

The test station has been designed to simulate both the operation of micro-CHP connected in parallel with the electrical grid and the stand-by operation mode. At the early stage the electrical load has been simulated by the employment of a resistor bank, based on three pure electrical resistance (3.4 Ω and 750 W each), connected in parallel; each resistance had an applied voltage of 220 V, the maximum electrical load is 6.75 kW (3x2250 W). To closely follow the electrical profile, one resistor was connected to a voltage transformer with an appropriate transformation ratio. The system was also designed to supply electrical power to the electrical resistances of both storage heaters; at the present an Electric Heat Pump contributes to the electric load considered.

[1] Authored by Sergio Sibilio (Second University of Napoli) and Maurizio Sasso (University of Sannio)

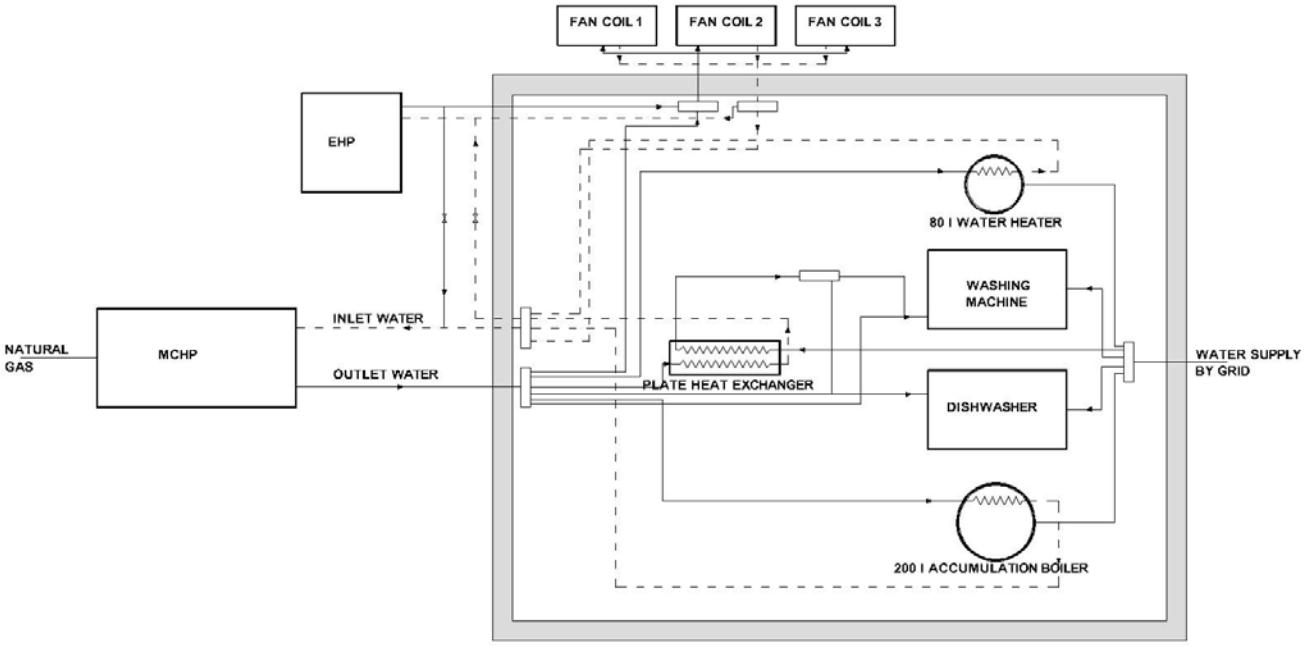

Figure II-6.1 : Test facility hydronic layout

The simulation of thermal load is accomplished by means of two hydraulic circuits (open and closed loop water circuit) respectively. The closed loop water circuit recovers heat from heat exchangers and then diverts it, using a circulation pump, to the systems that simulate users demands; to this aim, by means of a suitable manifolds, it is possible to supply heat to:

- Washing machines and dishwashers that have, not only the typical cold water supply, but also a suitable input for preheated water by thermal recovery of the micro-CHP;
- 80 L water heater and 200 L accumulation boiler, both with electric resistances and internal coil heat exchanger for thermal recovery of the micro-CHP hot water;

- 3 fan coils, each one with 3 velocity levels setting;
- Heat exchanger to use the thermal energy of micro-CHP modules recovery circuit in the various thermal users' simulation components.

The open water circuit may accomplish several goals to actually simulate a domestic heat demand; it is possible, by suitable closing/opening of manifold valves, to fill both accumulation systems, to recovery heat from the closed loop circuit by means of the plate heat exchanger, and finally to feed directly the domestic appliances and the tap.

Some of experimental activities were performed with the micro-CHP devices coupled with an electric vapour compression type heat pump (EHP) of air/water type equipped with a four way valve for functioning in cooling and heating modes with on/off regulation.

Attention is paid to the system micro-CHP/EHP both for its application in gas-cooling field as a thermally activated heat pump and for a "trigeneration" use able to satisfy electric, thermal and cooling energy requirements. The station arrangement allows to test two operating modes:

1. in the winter working mode the secondary fluid is preheated in the heat pump condenser and subsequently completes the thermal recovery in the micro-CHP recovery system; In heating mode has been made experimental tests at two different mass flow-rates 0.333 kg /s and 0.167 kg /s that are representative of volumetric requirements of a domestic user;
2. in the summer working mode the water cooled by the EHP evaporator is sent to the fan coils in the simulation station; so are satisfied both the cooling and heating loads. In this case, the proposed system configures itself as a tri-generation system (Possidente, R., Roselli, C., Sasso, M., Sibilio S., 2004). In this operating mode the tests have been made ranging the mass flow-rate of the micro-CHP thermal recovery to the following values: 0.217 kg/s and 0.108 kg/s; for the cooling

circuit, instead, has been considered a nominal water mass flow-rate of 0.250 kg/s constant.

In both operating conditions the electric power that exceeds the needs of EHP is supplied to end-user.

References

M. Dentice d'Accadia, M. Sasso, S. Sibilio, R. Vanoli, 2000 "A test facility for technical assessment of Micro CHP feasibility in residential and light commercial applications", Proc. V° International Conference on Industrial Thermal Engineering, renewable Energy and Environment COMEC 2000, Las Villas, Cuba, 8-10 Novembre.

Possidente, R., Roselli, C., Sasso, M., Sibilio S., 2004, *On Site Analysis Of A Gas Driven Microcogenerator Incorporating Heat Pump*, Proc. International Gas Research Conference, Vancouver, pp.100-116.

Section IV

Experimental Investigations of Residential Cogeneration Devices

IV-1 : Investigation of a WhisperGen SE Device at the Catholic University of Leuven[1]

The tests on the WhisperGen CHP were conducted in 2005, in the framework of an Electrabel, the main electricity supplier in Belgium research on the feasibility of small Stirling CHP's in Belgian residential buildings. The WhisperGen MK4 has two programmed thermal and electrical output levels, but can, when adapting the control, also be tested on intermediate level

To gain insight in the performances of the WhisperGEN for residential applications, its transient and stationary behaviour were tested. The aim was to check the efficiencies of the CHP and the overall system (including emission and/or storage) starting from different conditions: cold start-up (at least 5 hours shut down), warm start-up (1, 2 and 4 hours shut down before restarting) and steady state (measured after at least one hour on). A variation in inlet water temperature was used to gather information on the effect of the recuperation of latent heat.

Direct coupling with the heat demand often leads to frequent on/off cycling due to fluctuations in the heat demand. Therefore the performances are also tested for use with a storage tank. (For the tests of which the data have been used within Annex 42, the WhisperGen was coupled directly with the convector).

Besides temperatures, pressures, flow rates, gas consumption and electricity consumption and production were measured. The electrical outputs, as well as the gas consumption, are measured automatically. The former has an accuracy of 2% on the measured value. The gas meter has an accuracy of 1% on the measured value. Thermocouples type K measure temperatures at different points. An electromagnetic flow meter is installed on the cold water side. Gas temperatures are measured using a meter fixed to the wall at a certain distance from the set-up. Therefore the error margin on this temperature measurement is rather high.

[1] Authored by Leen Peeters and William D'haeseleer (Catholic University of Leuven)

In order to minimize the errors, thermocouples and flow meters were calibrated. These calibrations were effected by comparing instrument readings to reference instruments and then adjusting offset and slope parameters to adjust the translation of voltage signals to measured quantities.

The sample frequency during tests is set equal to 4/min.

The energetic value of natural gas is calculated as:

$$\dot{F} = \dot{q}_{gas} \cdot \frac{p_{gas}}{p_N} \cdot \frac{T_N}{T_{gas}} \cdot LHV$$

$\dot{F}$: the natural gas power [W]
$\dot{q}_{gas}$: the measured flow rate [m³/s]
p_{gas} : the absolute pressure in the gas supply pipes [Pa]
p_N : the pressure in standard atmospheric conditions [101325 Pa and 273.15K]
T_{gas} : the temperature of the gas in the supply pipes [K]
T_N : the temperature in standard atmospheric conditions [101325 Pa and 273.15K]
LHV : the lower heating value of natural gas [J/Nm³]

The natural gas network delivers low caloric gas of which the average composition is given in Table IV-1.1.

Component	Molar fraction [%]
CH_4	83,2
C_2H_6	3,80
C_3H_8	0,839
C_4H_{10}	0,302
C_{4+}	0,1619
N_2	10,28
CO_2	1,400

Table IV-1.1: composition of L-gas

The corresponding heating value results in 33.7 MJ/Nm³. The pressure in the gas supply pipes is supposed to have a constant value of 104200 Pa.

Uncertainty analysis

As the data is used for the model calibration and validation, the calculation of the derived parameters and their associated uncertainties is described here. However, when using the KULeuven data, care should be taken as the experiments were not performed following the Annex 42 experimental protocol (refer to section II of this report).

As an example the bias and precision errors of the temperatures and flow rates in steady period are calculated here. Bias errors are assigned to primary measurements only. They further propagate, combined with the precision errors, into the derived quantities.

In case of the gas and electricity consumption, as well as the energetic value of the natural gas, additional bias errors were assigned upon judgment. The reason being that for these measurements, the values have to be read from the meter and written to the file. Besides a delay, the introduction of an error is of high risk compared to electronic data reading and writing.

Bias error and precision errors of the flow rates and temperatures measured during a 34 minute steady period, are summarized in Table IV-1.2. The aim of the KULeuven tests was to check the performance on system level; temperatures were therefore measured on the inlet and outlet of the heat production systems.

B indicates the total bias, calculated from the individual bias errors for that sensor, using the root-sum-square method. The precision index S is calculated based on the average value of that parameter during the test and the number of logged readings.

	Total bias B	Precision index S	$U_{95\%}$	Average
T_{in_CHP}	0.1 °C	0.36 °C	0.47 °C	44.68 °C
T_{out_CHP}	0.2 °C	0.28 °C	0.41 °C	32.67 °C
$T_{in\_Convector}$	0.2 °C	0.40 °C	0.55 °C	45.61 °C
$T_{out\_convector}$	0.1 °C	0.25 °C	0.34 °C	32.43 °C
Water flow rate	8.7 kg/hr	2.38 kg/hr	9.1 kg/hr	387.11 kg/hr
Gas flow rate	0.013 Nm^3	0.01 Nm^3	0.02 Nm^3	0.883 Nm^3
Net electricity production	12.04 W	10.42 W	17.97 W	675.83 W

Table IV-1.2 : bias errors, precision indices, uncertainty at 95% and average value of primary parameters.

The bias errors and precision indices are combined to express the uncertainty in a measured quantity, U95%, the measured uncertainty at the 95 percent confidence level. T_{in_CHP}, T_{out_CHP} and $T_{in\text{-}convector}$ and $T_{out\_convector}$ represent the inlet and outlet temperatures of CHP and convector respectively.

The estimated error values for gas and electricity consumption/production can be summarized as follows:

- Uncertainty on electricity measurements is 2%
- Uncertainty on gas meter measurements is 1%
- Uncertainty on gas temperature measurement +/- 2°C
- Uncertainty on pressure ‘measurement’ +/- 2%
- Uncertainty on specific heat constant at constant pressure for water is, based on the variation in the values of this constant within the temperature range considered here, 1%

The energetic value of natural gas is calculated, as described above, expressed by:

$$\dot{F} = \dot{q}_{gas} \cdot \frac{p_{gas}}{p_N} \cdot \frac{T_N}{T_{gas}} \cdot LHV$$

And thus the introduced error for this derived quantity results in:

$$\left(\frac{\Delta \dot{F}}{\dot{F}}\right)^2 = \left(\frac{\Delta \dot{q}_{gas}}{\dot{q}_{gas}}\right)^2 + \left(\frac{\Delta p_{gas}}{p_{gas}}\right)^2 + \left(\frac{\Delta T_{gas}}{T_{gas}}\right)^2$$

$$\left(\frac{\Delta \dot{F}}{\dot{F}}\right) = 0.13$$

The uncertainty on the LHV, due to small fluctuations in composition is limited to 2% of the measured value[2].

[2] Personal communication with Fluxys, Belgian gas transmission system operator.

IV-2 : Investigation of a WhisperGen SE Device at the Canadian Centre for Housing Technology[1]

In 2003, the Canadian Centre for Housing Technology (CCHT) incorporated the capability of assessing residential micro combined heat and power (CHP) systems under real-world conditions. The intent of the project was to adapt one of two existing research houses at CCHT to integrate a prototype CHP unit that would provide some electricity and heat to the house, and supply surplus electricity back to the grid. Documentation of the adaptation and CHP operation, including building integration issues and CHP performance characteristics, were key objectives, with the intent of providing valuable information to CHP manufacturers and researchers alike.

The CHP unit chosen for this demonstration was the Whisper Tech Ltd. WhisperGen Stirling engine, fuelled by natural gas. This was a pre-production Mark 0 unit. The unit had a small electrical capacity (750 W nominal) and a larger thermal output (6.5 kW nominal). It was designed to be 'heat-driven'- controlled according to heat demand of the residence, so that electricity generation is a by-product. The unit was installed as a grid-connected device, with local electrical inspections performed.

The Test House at CCHT, a fully automated and monitored house, was adapted to allow waste heat from the CHP unit to be collected, stored and used to meet space and water heating loads of the house. This portion of the CHP system was referred to as the 'Balance of Plant' (BOP). As well, the house's electrical wiring was reconfigured to permit the CHP generator to provide electricity to both the house, addressing a portion of the house's electrical needs, and to the electrical power grid, on occasions where the house loads were less than the CHP unit electrical output.

The CHP unit was then installed in the basement of the Test House and connected to thermal and electrical systems. The existing house thermostat on the main floor wall, and

[1] Authored by Mike Swinton and Marianne Manning (National Research Council Canada) and Evgeuniy Entchev and John Gusdorf (Natural Resources Canada)

the programmed demand for hot water ultimately controlled the CHP's BOP by calling for heat from the system. Controls in the BOP signalled a need for heat from the CHP unit when heat stores were being depleted. The CHP generated electricity simultaneously whenever there was a demand for heat. Installed meters kept track of how much electricity was being generated and where it was going, whether to the house, to the grid or both.

Operation of the house with the CHP unit occurred between March and June 2003. Both the house performance and the CHP system were monitored extensively. Outdoor conditions ranged from late winter to summer conditions in the Ottawa area. This allowed the CHP unit performance to be assessed under a range of space heating loads, as well as a daily profile of water heating loads associated with the CCHT Test House operation.

The CHP - Stirling Engine

The prototype Stirling engine was purchased prior to the start of this project for $12k US - current models are available at time of report writing for $7.5k US. The unit was installed at CCHT as a residential micro combined heat and power (micro CHP) device. A Stirling engine is an external combustion device and can burn many different fuels (diesel, NG, propane, biogas, kerosene, and solid fuels) providing the heat exchanger is specifically designed for the selected fuel and sufficient temperatures can be reached (700 to 1 000^{o}C).

Natural Resources Canada purchased this unit and completed lab testing at the Natural Gas Technology Centre (NGTC) with a natural gas industry partner, as a separate project preceding this one. The manufacturer's specification is 750We, 230V AC grid connected, continuous duty, with 6.5kW of co-generated water heating. The fuel is natural gas and the control is by heat demand (heat-led) rather than electrical demand. It performed well in the previous lab tests, producing 750We gross (with net output of 575We once

parasitic electrical consumption of the CHP was subtracted) and produced 6.5kW of heat. The results of the lab tests were made available to funding partners of this CHP project.

Balance of Plant Design and Installation

The Balance of Plant consists of the storage tank (ST), the hot water tank (HWT), the air handler (AH), and 3 pumps and a mixing valve as illustrated in Figure IV-2.1.

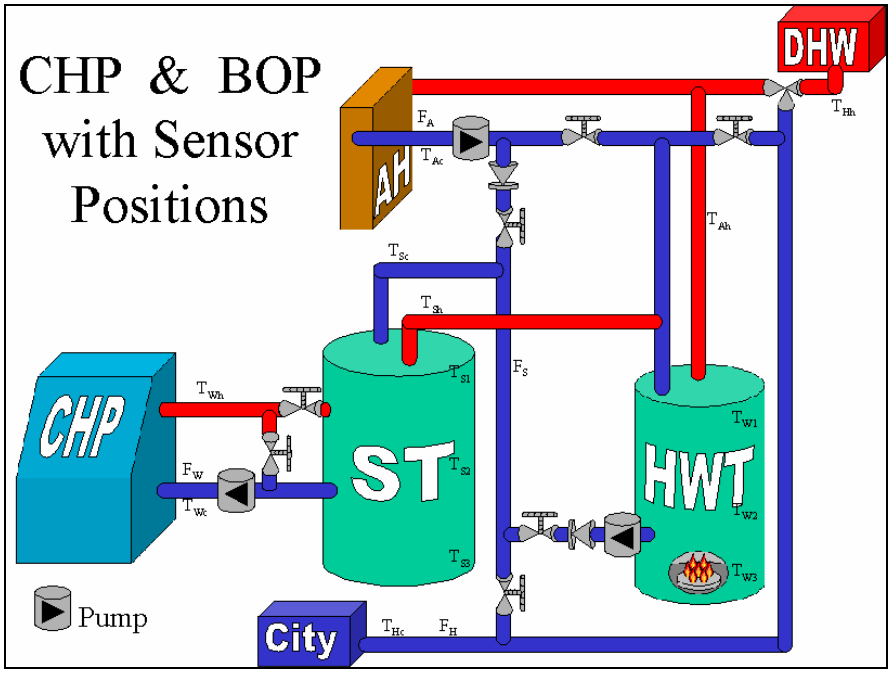

Figure IV-2.1 : Schematic Diagram of The Balance of Plant and Sensors

The existing hot water tank (HWT), as well as the air handler (AH), were already in the house as a result of a previous experiment. The HWT was already hooked-up to the house, providing a means of domestic hot water and space heating distribution. The burner on the HWT served as a backup or top-up burner in instances where the CHP unit could not supply all of the heat requirements, either due to heavy demand or shut down of the CHP unit.

The storage tank, three pumps, mixing valve and piping connections were specified and installed to complete the Balance of Plant.

Setups of the Balance of Plant

The experimental nature of this project afforded the opportunity to configure the same BOP components in two different ways to investigate whether the strategy for directing heated water and cooler return water had an impact on the operating efficiency of the CHP and the BOP, as well as that of the overall system. These approaches are described below.

- Setup 1: The Storage tank ST is used as a supplementary heater to the HWT (warm water in storage circulated to HWT, and cooler HWT water back to storage. HWT gets the fresh water supply)

- Setup 2: ST is in series with the HWT (hot water from the hot water storage tank circulated to HWT and then to space heat load and back to ST, or to water heating, with fresh water into ST)

In both configurations, the CHP unit is the heating source to the storage (ST), with a closed loop and heat exchangers linking the CHP unit to the storage.

Electrical Modifications

The modifications were made to accommodate the installation of combined heat and power (CHP) systems having a generating capacity up to 40 kWe, for either grid-dependent operation (this project) or stand-alone, grid-independent operation (possible future projects).

The following wiring and metering changes were made to the test house for the Stirling Engine experiment:

- Three additional bi-directional, pulse generating kilowatt-hour meters, and an additional power quality meter were added for monitoring purposes.

- A weatherproof, padlockable disconnect switch was installed on the exterior of each house to meet requirements of rule 84-028 of the Canadian Electrical Code.

- A four-pole transfer switch was installed to allow various generator configurations without re-wiring.

- A 100-amp disconnect / isolating switch with 20-amp fuses was installed to protect and isolate the CHP generator under test.

A schematic diagram of the integration of these elements to the Test house is shown in Figure IV-2.2.

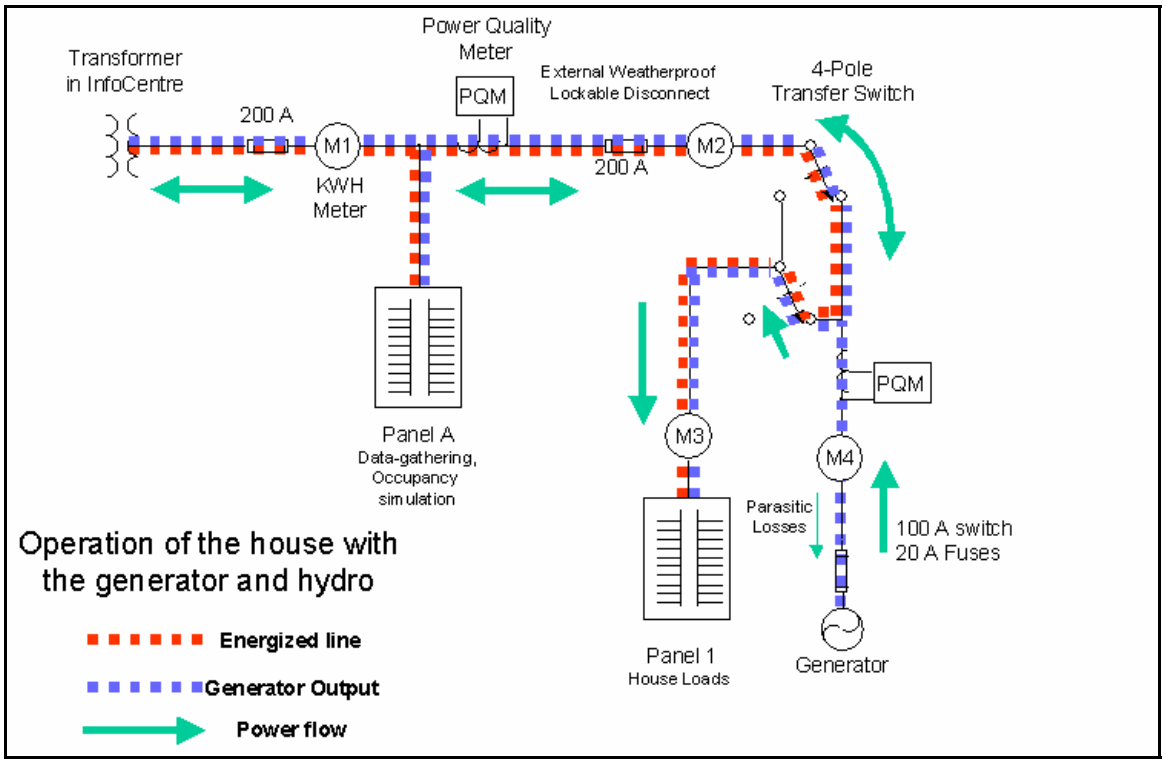

Figure IV-2.2 : Schematic Diagram of the Upgraded Wiring and Metering in the CCHT Houses.

Monitoring

Each of the CCHT houses has a permanently installed data collection system with over 250 points of temperature, relative humidity, moisture content and flow rates that are read every five minutes and stored every hour. It also has 18 meters to monitor electrical consumption of various appliances, lighting and other devices. These are read and stored every five minutes. Three of the kWh meters (two of which are bi-directional) were used in the CHP experiments.

Power Quality Meters

The house in which the CHP was installed has two power quality monitoring systems, one that monitors power from the grid, and one that monitors the power produced by the CHP. Electric utilities and CHP manufacturers were especially interested in the power quality of the power generator. The following describes the power quality meter set-up:

- The two 7600 ION power quality meters (PQM) were installed and tested. The first was located between the grid and the house, and the second between the CHP generator under test and the house circuits and grid.

- The PQMs were configured according to the type of installation involved in our project. A simplified version of the PQMs' software was set up on a dedicated computer, to allow the team to familiarize itself with the outputs.

- Purchased and setup the PQM "Ion Enterprise" software, for more complete access to data being monitored by the PQMs.

- Contacted the PQM manufacturer and secured the name of a qualified programmer, if more refined analysis should be of interest.

- Files with power data (power, voltage and current) were recorded every 15 minutes and a variety of power quality data were recorded at one-hour intervals.

Instrumentation of the BOP

Each heat transfer loop of the BOP had 2 thermocouples and a flow meter. The loops are:

- from the CHP unit to the Storage Tank (ST),
- from the ST to the Hot Water Tank (HWT),
- from the HWT to the Air Handler (AH), and
- from the HWT to hot water taps.

Data were collected, and heat flows were calculated every 10 seconds.

Two existing natural gas meters were used to monitor the gas consumption of the CHP unit and that of the HWT back-up burner. Averages of temperatures and totals of heat flows and natural gas were saved every minute.

Stirling Engine Experimental Period

The CHP unit was installed at CCHT in February 2003, and was operated and monitored between March 13 and June 10 2003. For analysis purposes, the overall monitoring period was split up into 39 individual 'runs' for which energy balances and system efficiencies were calculated. In essence, each 'run' can be viewed as an individual experiment. Some of the characteristics of these runs include:

- The duration of each run ranged from 23 to 65 hours, with an average of 40 hours per run. The duration of runs varied due to CHP unit problems and changes from one Set-up to another.

- 11 runs (497 hours) were in Setup #1.
- 16 runs (594 hours) were in Setup #2.
- 3 additional runs occurred during which the CHP unit failed, and were not analyzed with the others. These 'failed' runs demonstrated that the gas burner in the HWT serves as a backup, supplying all space heat and HW demands when the CHP had failed.
- In all runs, the house space heat and hot water demands were met.
- 8 runs used additional heat from the HWT gas burner. This was due to the control strategy and HWT setting, not to lack of available heat from the CHP. For these cases, the gas use by the HWT was 6% or less of total gas use.

The experimental period preceded the development of the IEA Annex 42 experimental protocol for CHP testing (refer to section II of this report) and therefore did not adhere to it. Key datasets were collected at the desired 5-minute time interval, but some elements of the protocol were not met, notably measurements of performance parameters inside the Stirling engine unit. This made model benchmarking and validation a challenging exercise. Nevertheless, the data were used to guide Stirling engine model benchmarking in one instance.

References

Bell, M., Swinton, M.C., Entchev, E., Gusdorf, J., Kalbfleisch, W., Marchand, R.G., Szadkowski, F., Development of Micro Combined Heat and Power Technology Assessment Capability at the Canadian Centre for Housing Technology, December 08, 2003 (B6010). URL: http://irc.nrc-cnrc.gc.ca/pubs/fulltext/b6010/

Bell, M., Swinton, M.C., Entchev, E., Gusdorf, J., Kalbfleisch, W., Marchand, R.G.,

Szadkowski, F., "Testing Residential Combined Heat and Power Systems at the Canadian Centre for Housing Technology," *Proceedings 2004 ACEEE Summer Study on Energy Efficiency in Buildings,* August 2004, American Council for an Energy-Efficient Economy, Washington, DC.

IV-3 : Investigation of an Solo Stirling Device at the Technical University of Munich[1]

Technical data and system integration

The analysed CHP-system is a Stirling engine 161 microKWK-Modul manufactured by SOLO STIRLING GmbH. The device allows continuously variable power modulation between minimal and nominal power. The technical data (manufacturer's data) are listed in Table IV-3.1. Current systems of the combined heat and power plants show 9.5 kWel und 26 kWth with a system pressure of 150 bar.

Table IV-3.1 : Technical manufacturer data of the Solo Stirling engine

Name	Unit	
Fuel	-	natural gas
Electrical power	kW	2 – 7.5
Thermal power	kW	8 – 22
Operating gas	-	Helium
Operating pressure	bar	30 – 130

The hydraulic integration of the individual components is illustrated in Figure IV-3.1. The built-in peak load boiler is a gas condensing boiler type ecotec VC 466-E manufactured by Vaillant with a rated heating output of 45 kW.

[1] Edited by Ulli Arndt (Research Institute for Energy Economy, FfE, Munich, Germany)

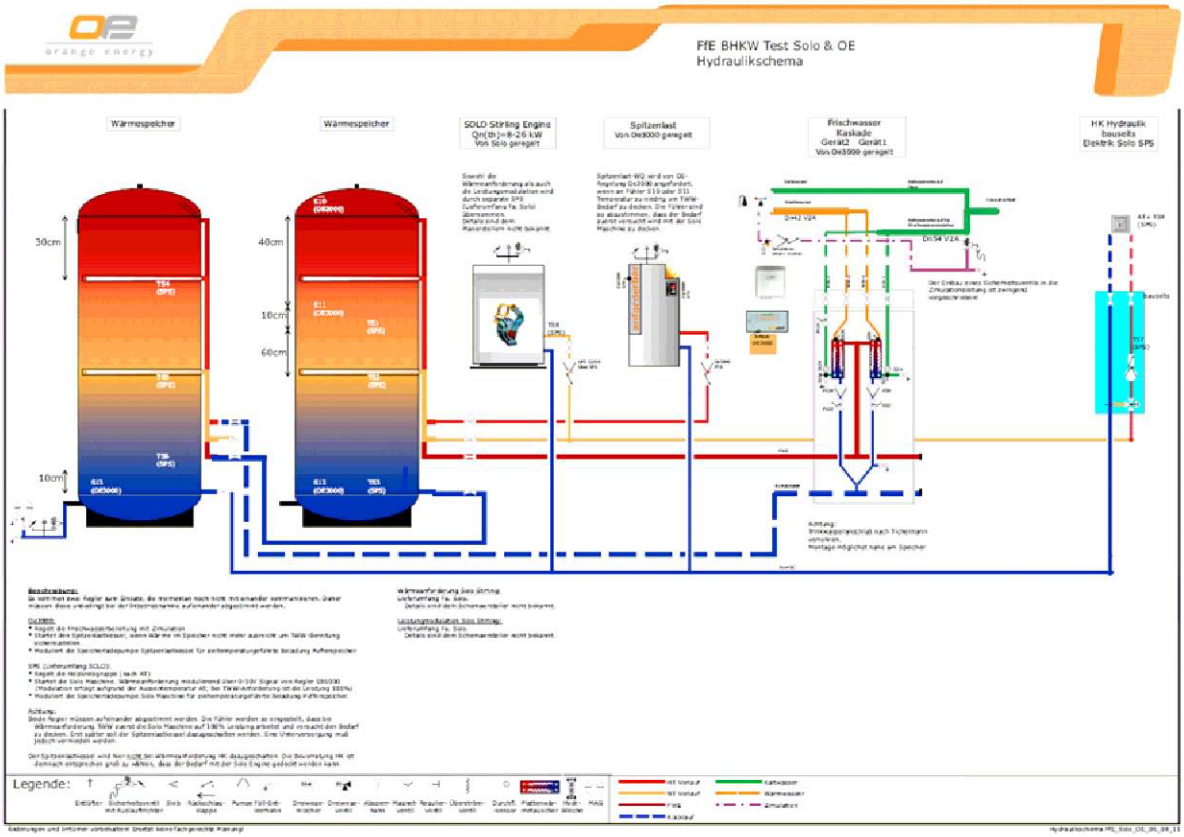

Figure IV-3.1 : Hydraulic integration of the Solo module, peak load boiler and two heating buffer storages into the test rig

The forerun of the CHP plant enters the forerun of the heating circuit. Depending on the flow rate inside of the heating circuit, the CHP plant serves as a temperature increase for the forerun and the loading of the heating buffer vessel respectively. Two 1000 liters heating buffer storages in series were applied as heating buffers. The domestic hot water generation results from a fresh water cascade manufactured by Orange Energy. The control of the components such as the heating circulation pump, heating circuit mixer and peak load boiler was adopted by a recently programmed control of the manufacturer.

Measurements

For the assessment of the CHP plant's energetic performance, the following tests were conducted which are described subsequently:

- Steady state operation with different pressures of the operating gas
- Cold and warm start tests
- Day in winter
- Transition day
- Day in summer

Steady state tests

Table IV-3.2 shows the measured data, its energy quantities (fuel quantity, heat quantity, electricity generation) and related efficiencies with different pressures of helium (130 bar and 30 bar). All efficiencies are relative to the fuel's LHV.

Table IV-3.2 : Balance results of the steady state rig testing

Name	Unit	Test 1	Test 2
Operating pressure	bar	130	30
Forerun/ return temperature	°C	52/33	42/36
Balance period	h	1	1
Q_{fuel}	kWh	34.1	9.6
Q_{el}	kWh	8.0	1.3
Q_{th}	kWh	24.3	6.9
η_{th}	**%**	**71.2**	**71.9**
η_{el}	**%**	**23.6**	**13.8**
η_{total}	**%**	**94.8**	**85.7**

When the steady state condition is reached, the balancing for steady state operating performance took place for one hour. The measured forerun and return temperatures at the

CHP-module added up to 52/33 °C and 42/36 °C respectively. The thermal efficiencies of the measured test series were between 71.2 % and 71.9 % and the electrical overall efficiencies (energetic recovery system) between 23.6 % and 13.8 %. The overall efficiency of the CHP-module for steady state conditions adds up to 94.8 % and 85.7 %.

Cold start test

Figure IV-3.2 shows the start-up from cold state (temperature 20 °C, gas pressure 130 bar). The CHP-module is started at 08:27h and the gas release happens two minutes after that event. During the heat-up phase between 08:29 and 08:36h, the average fuel power was in the range of 19 kW. From 08:36 onwards, the production of electricity starts, fuel power and electrical power increase to 36 kW and 8 kW respectively. After a transition time of around 25 minutes, the combined heat and power plant runs in steady state. At 08:55h forerun and return temperature reach constant values of 54 °C and 47 °C.

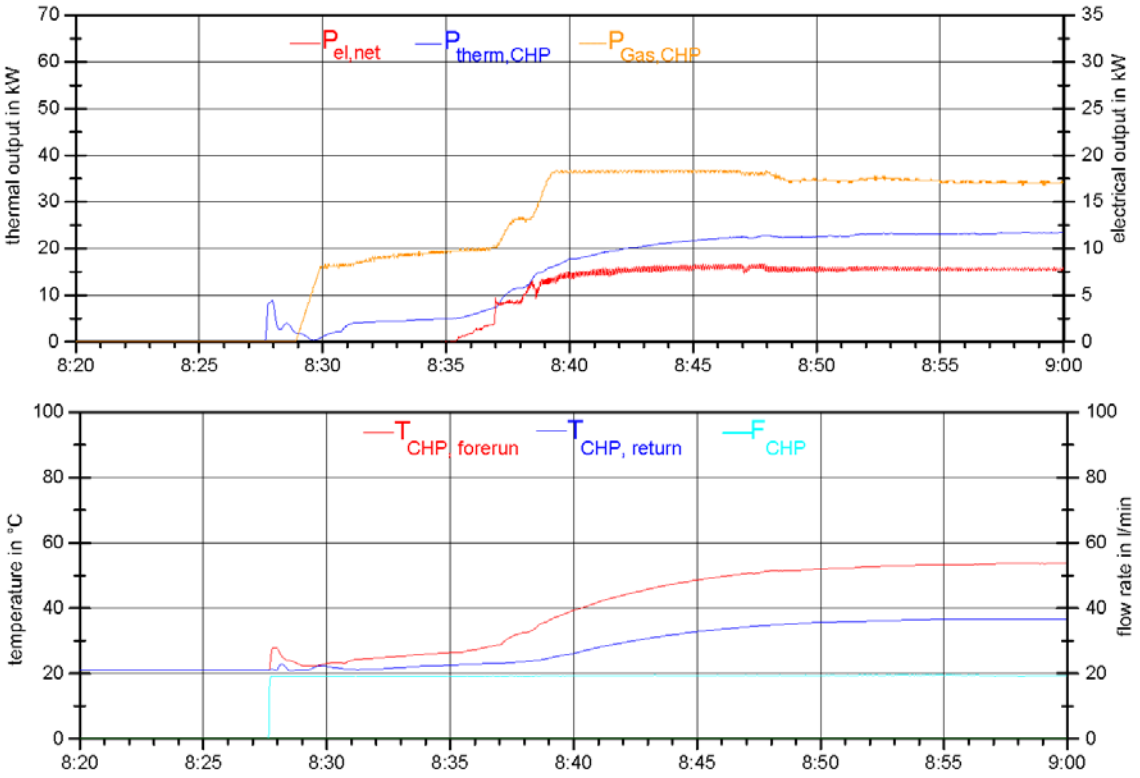

Figure IV-3.2 : Course of temperature, flow rate and power during cold start test

Warm start test

The start-up in warm state (forerun temperature of around 75 °C, gas pressure of 130 bar) is illustrated in Figure IV-3.3. At 23:08h it is being stopped and the fuel supply terminated; during a period of five minutes the released heat quantity drops down to naught. In-between 23:15 and 23:34 the circulation pump of the CHP-module is switched on temporary every five minutes by the control of the combined heat and power plant. At the same time, the return temperature drops down to around 50 °C.

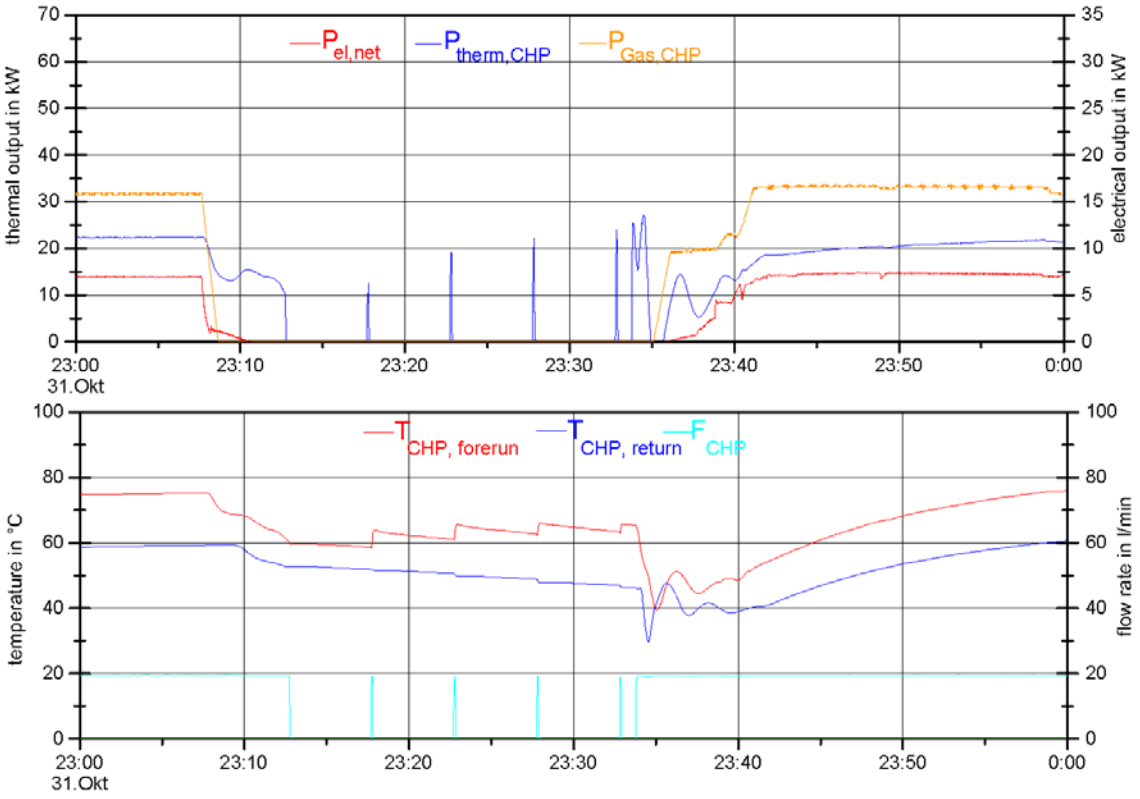

Figure IV-3.3 : Course of temperature, flow rate and power during warm start test

The warm start occurs at 23:34h. The circulation pump starts to operate resulting in a thermal power output of around 20 kW (residual heat in the CHP-module). In doing so forerun and return temperature decrease. At 23:35h, the thermal power output drops to naught as forerun and return temperature are on the same level at that moment. Subsequently, the return temperature exceeds the forerun temperature temporary resulting in a momentary heat flow from the heating buffer storage in the CHP-module. At 23:35h the gas valve opens, the fuel power increases in two steps from 20 kW to 32 kW. At the same time, thermal power, forerun and return temperature rise. The electricity production starts about one minute after fuel supply and reaches a power output of 7.5 kW after six minutes. Within 20 minutes the forerun's initial temperature of around 75 ºC and the return temperature of around 60 ºC are obtained.

Day in winter

Figure IV-3.4 illustrates the measurements relevant for heat generated by the CHP-module and the peak load boiler. Just less than 19 hours of operating time was determined for this type of day. Due to the great heating- and domestic hot water demand, the peak load boiler conducts seven start activities during the day.

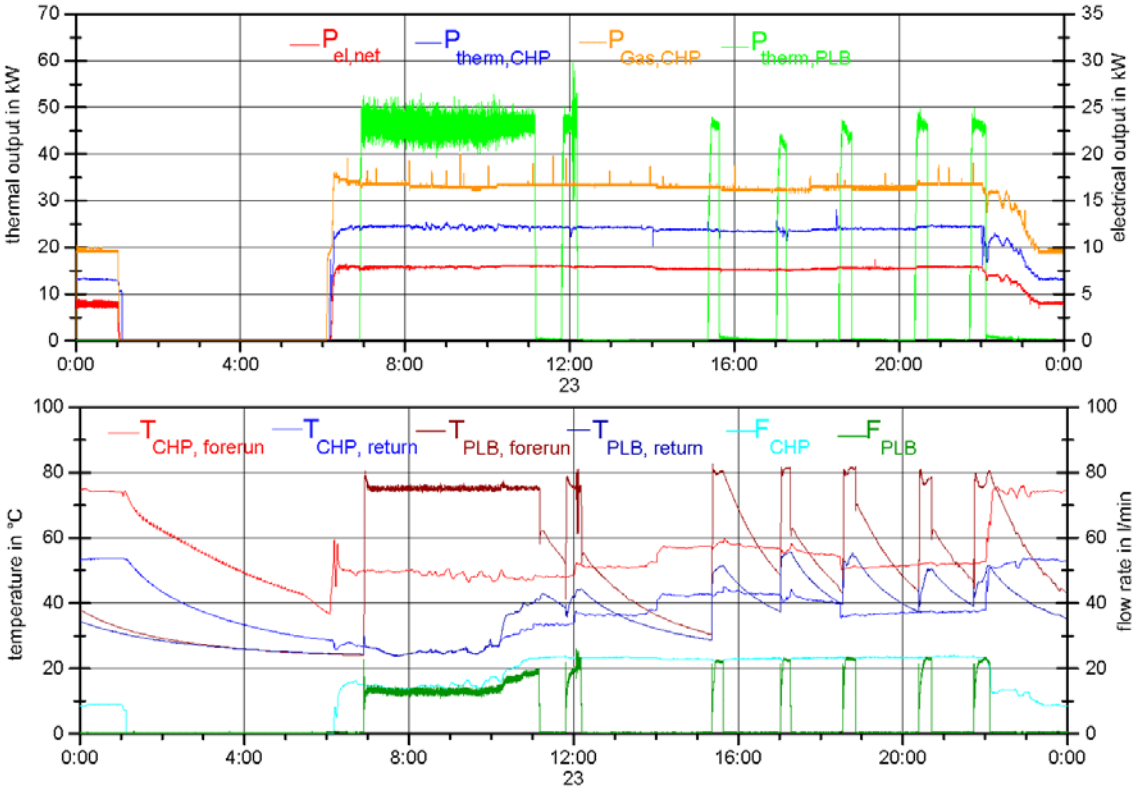

Figure IV-3.4 : Course of temperature, flow rate and power of the CHP-module and peak load boiler (day in winter)

Balance results day in winter

The balance results of the performed tests for the day in winter are shown in Table IV-3.3.

Table IV-3.3 : Balance results day in winter

Name	Unit	Day in winter
CHP plant		
$Q_{fuel,CHP}$	kWh/d	596.5
$Q_{el,CHP}$	kWh/d	138.6
$Q_{th,CHP}$	kWh/d	420.3
cos φ	-	0.67
t_{CHP}	h/d	18.9
$\eta_{th,CHP}$	**%**	**70.5**
$\eta_{el,CHP}$	**%**	**23.2**
$\eta_{total,CHP}$	**%**	**93.7**
Peak load boiler		
$Q_{fuel,PLB}$	kWh/d	281.5
$Q_{th,PLB}$	kWh/d	268.9
t_{PLB}	h/d	6.2
$\eta_{th,PLB}$	**%**	**95.5**

The CHP-module's thermal overall efficiency accounted for 70.5 %, the electrical overall efficiency for 23.2 %. The overall efficiency of the system is therefore 93.7 %. The peak load boiler's thermal overall efficiency comes up to 95.5 %.

Transition day

Figure IV-3.5 illustrates the representative measurements for the heat generation (CHP-module and peak load boiler) on a transition day. During the day, four start activities of the combined heat and power plant can be observed and seven start-up processes. The forerun temperatures at the Solo lies in the range of 40 ºC and around 80 ºC and the return temperatures between 30 ºC and 50 ºC.

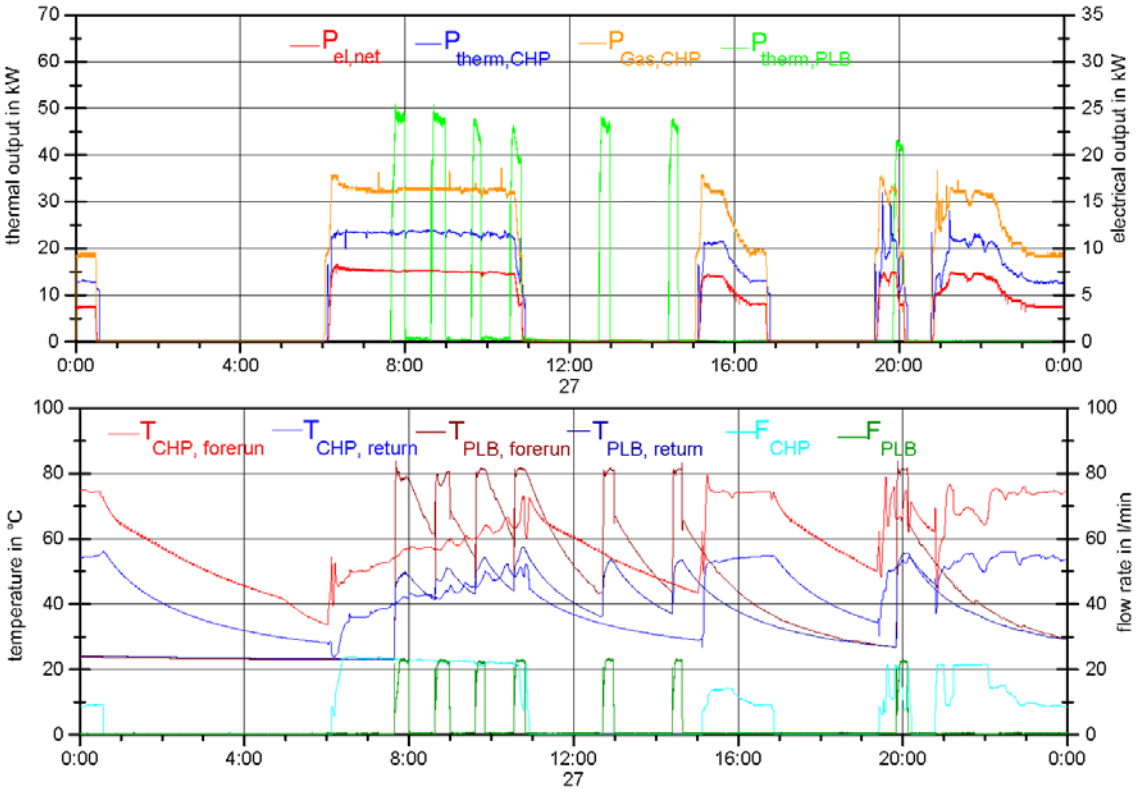

Figure IV-3.5 : Course of temperature, flow rate and power of the CHP-module and the peak load boiler (transition day)

Balance results transition day

Table IV-3.4 demonstrates the balance results for the transition day.

For a fuel input of around 307 kWh (CHP plant) and 86 kWh (peak load boiler) the overall efficiency accounts to 88.3 % (CHP plant) and 92.1 % (peak load boiler). The electrical efficiency of the CHP-module reaches 21.6 %. The operating time of the combined heat and power plant comes up to around eleven hours per day, the peak load boiler is being operated for more than two hours.

Table IV-3.4 : Balance results transition day

Name	Unit	Transition day
CHP plant		
$Q_{fuel,CHP}$	kWh/d	306,9
$Q_{el,CHP}$	kWh/d	66,5
$Q_{th,CHP}$	kWh/d	204,5
cos φ	-	0,62
t_{CHP}	h/d	10,9
$\eta_{th,CHP}$	**%**	**66,7**
$\eta_{el,CHP}$	**%**	**21,6**
$\eta_{total,CHP}$	**%**	**88,3**
Peak load boiler		
$Q_{fuel,PLB}$	kWh/d	86,0
$Q_{th,PLB}$	kWh/d	79,2
t_{PLB}	h/d	2,1
$\eta_{th,PLB}$	**%**	**92,1**

Day in summer

Figure IV-3.6 illustrates the courses of temperature, flow rate, thermal and electrical output of the CHP-module. During the night, the combined heat and power plant switches off due to the small heat consumption for domestic hot water generation. Solo starts to operate at 06:45 as a result of a falling temperature in the buffer storage. Most of the day, the module is being operated on the minimum power level with two time-outs each with 2.5 hours. Due to the relatively low heat demand for domestic hot water generation, the peak load boiler does not operate on the day in summer.

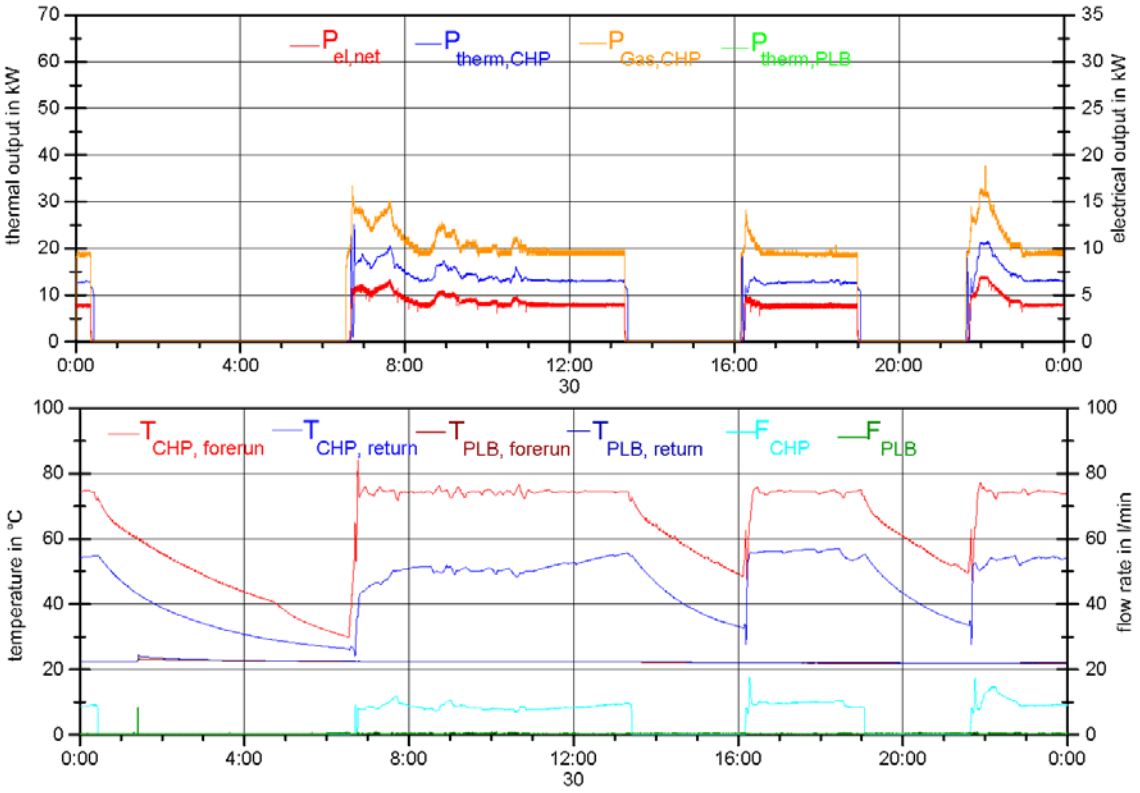

Figure IV-3.6 : Course of temperature, flow rate and power of the CHP-module and the peak load boiler (day in summer)

Balance result day in summer

Table IV-3.5 shows the balance results of the day in summer test.

During summer days a further decrease to 84.8 % of the CHP-module's overall efficiency occurs when comparing them with winter and transition days. This is down to the operation with mainly a minimum of power. In doing so, operating times of the combined heat and power plant of around 12.3 hours and a fuel demand of 258.4 kWh could be determined for the type day in summer.

Table IV-3.5 : Balance results day in summer

Name	Unit	Day in summer
CHP plant		
$Q_{fuel,CHP}$	kWh/d	258,4
$Q_{el,CHP}$	kWh/d	52,2
$Q_{th,CHP}$	kWh/d	167,0
cos φ	-	0,52
t_{CHP}	h/d	12,3
$\eta_{th,CHP}$	**%**	**64,6**
$\eta_{el,CHP}$	**%**	**20,2**
$\eta_{total,CHP}$	**%**	**84,8**
Peak load boiler		
$Q_{fuel,PLB}$	kWh/d	0
$Q_{th,PLB}$	kWh/d	0
t_{PLB}	h/d	0
$\eta_{th,PLB}$	**%**	**-**

References

Mühlbacher, H.; Geiger, B.: Innovative CHP-systems for the energy supply of residential buildings - Final report Phase II, Institute for Energy Economy and Application Technology, Technical University of Munich, May 2007

IV-4 : Investigation of a Senertec ICE Device at the Technical University of Munich[1]

Technical data and system integration

The analysed CHP-plant is a Senertec Dachs HKA G 5.5. It is equipped with an additional condensation exhaust gas heat exchanger (condenser) to increase heat recovery and hence improve the efficiency. The technical data of the CHP-plant and the condenser are listed in Table IV-4.1.

A standard buffer tank with four connections and a capacity of 1 000 litres acts as a buffer storage. The installed peak load boiler is a condensing gas boiler type ecotec VC 466-E from Vaillant with a rated thermal output of 45 kW.

Table IV-4.1 : Technical manufacturer data for Senertec Dachs HKA G 5.5

Name	Unit	
Dachs HKA G 5.5		
Fuel	-	natural gas
Electrical power	kW	5.5
Thermal power	kW	12.5
Condenser		
Return temperature 20 C / exhaust temperature 40 C		
Thermal power	kW	3.0
Degree of condensation	%	80
Return temperature 60 C / exhaust temperature 85 C		
Thermal power	kW	0.8
Degree of condensation	%	0

[1] Edited by Ulli Arndt (Research Institute for Energy Economy, FfE, Munich, Germany)

The hydraulic integration of the individual components and the balance boundaries necessary for the balance are illustrated in Figure IV-4.1. The forerun of the CHP-plant runs to the connection at the top third of the buffer storage. The return runs from the lower connection of the buffer storage via the condenser, where it is heated, back to the CHP-plant. The forerun to the heating circuit and the domestic hot water storage are fed from the top side of the buffer storage and can get additional heating from the peak load boiler if required. The return from the heating circuit and the domestic hot water storage runs back to the buffer storage in the lower third. The domestic hot water distribution system is carried out as a circulation system and the domestic hot water draw temperature was adjusted to 38°C.

Measurements

To evaluate the energetic performance of the CHP-plant, the following tests were conducted which will also be described consecutively and documented by measurements:

- Day in winter
- Transition day
- Day in summer

All efficiency values are referred to the lower heating Value (LHV).

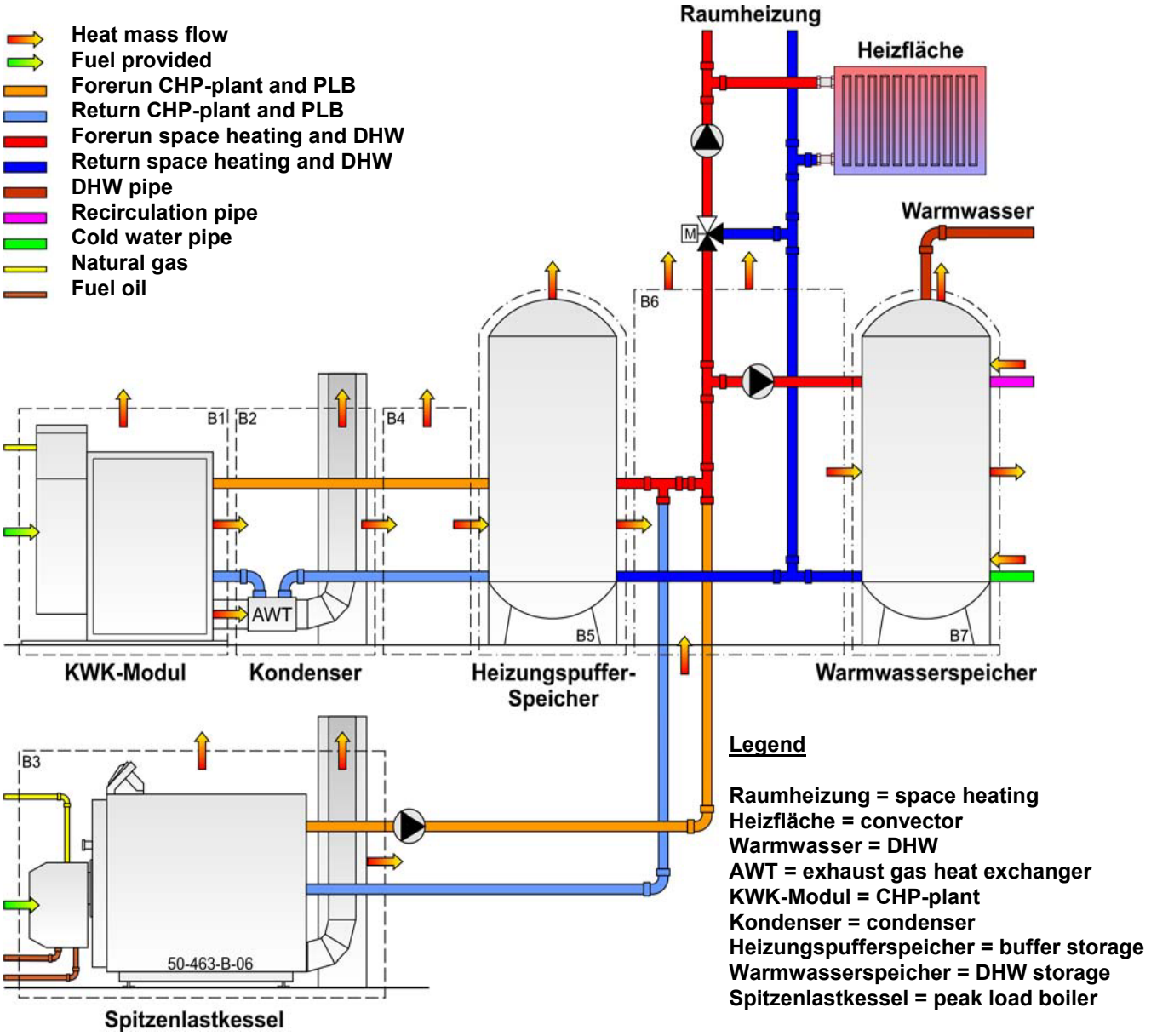

Figure IV-4.1 : Hydraulic schematic with heat- and fuel mass flow

Day in winter

The loading of the buffer storage occurs solely via the CHP-plant. In principle, the CHP-plant starts operating at 5 am, to raise the temperature in the buffer storage and therefore to cope with the heating and domestic hot water peaks in the morning. The temperature of the buffer storage drops due to the great power demand when switching to day operation at 6 am. The relevant readings for the heat generation by the CHP-plant and the peak load boiler are illustrated in Figure IV-4.2. For this day, an operating time of the CHP-plant of over 18 hours was determined.

The electrical power $P_{el.net}$ is below the power generated as a result of the auxiliary energy demand of around 120 W. The thermal power of the CHP-plant with condenser $P_{th,CHP,incl.\ HEX}$ is more than the thermal power of the CHP-plant due to the energy taken from the exhaust. The difference between $P_{th,CHP,incl.\ HEX}$ and $P_{th,CHP}$ increases the more the return temperature $T_{CHP,return\ to\ HEX}$ drops.

The peak load boiler operates consistently throughout the day due to a great heating and domestic hot water demand. Depending on the flow temperature of the combined heat and power system, the peak load boiler switches on and off. The peak load boiler only increases the forerun temperature because of its hydraulic bonding. Therefore, low flow rates result in a rapid increase of the forerun temperature $T_{PLB,forerun}$ which causes the stopping of the peak load boiler through the control of the CHP-plant. The consequence is a frequent chopping during certain working conditions. The flow control of the CHP-plant happens with a thermostatic pump, integrated in the forerun by the manufacturer.

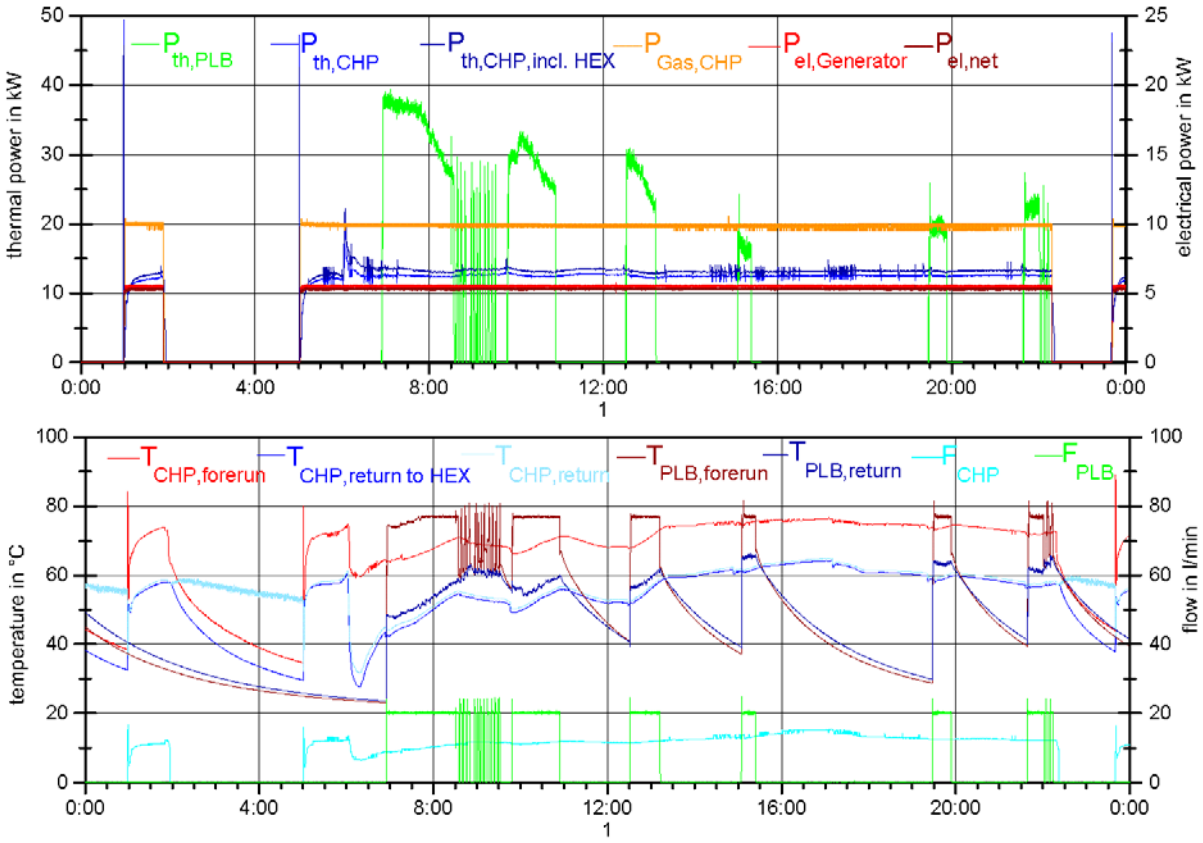

Figure IV-4.2 : Temperature-, flow- and power characteristics of the CHP-plant and the peak load boiler (day in winter)

The balance results of the measured winter day are listed in Table IV-4.2. The CHP-plant runs longer than the operation time of the space heating system from 6 am to 10 pm. The peak load boiler assists the heat production in the morning and at several times in the evening.

Table IV-4.2 : Balance results of the day in winter

Name	Unit	Day in winter
CHP-plant		
$Q_{CHP,Gas}$	kWh/d	363.6
$Q_{el.\ Generator}$	kWh/d	101.4
$Q_{el.\ net}$	kWh/d	97.2
$Q_{CHP,\ excl.\ condenser}$	kWh/d	222.9
$Q_{CHP,\ incl.\ condenser}$	kWh/d	235.6
cos φ	-	0.89
t_{CHP}	h/d	18.5
$g_{th,CHP,\ excl.\ condenser}$	%	61.3
$g_{th,CHP,\ incl.\ condenser}$	%	64.8
$g_{el,CHP,net}$	%	26.7
$g_{el,CHP,Generator}$	%	27.9
$g_{CHP,total,\ excl.\ condenser}$	%	88.0
$g_{CHP,total,\ incl.\ condenser}$	%	91.5

Transition day

The measurements taken from the heat generators are shown in Figure IV-4.3. During a day's operation on this specific transition day, the CHP-plant switches consistently off due to a very low thermal space heating demand. When loading the domestic hot water storage, the CHP-plant starts operating because of the default high temperature set point. On this day, eight start-up procedures take place. The criteria for switching off the CHP-plant are the measured buffer storage temperature, the temperature of the heating circuit forerun and the domestic hot water storage temperature. The thermal power of the CHP-plant suffices to cover the total space heating and domestic hot water demand. This results in a non-operational mode of the peak load boiler. Due to the rather high return temperature at the CHP-plant $T_{CHP,return\ to\ HEX}$ only a small temperature increase of the return water $T_{CHP,return}$ occurs in the condenser. The flow rate in the heating circuit is also influenced by the domestic hot water storage load as mentioned for the day in winter. The peaks in the course of the buffer storage draw are caused by the domestic hot water storage loads.

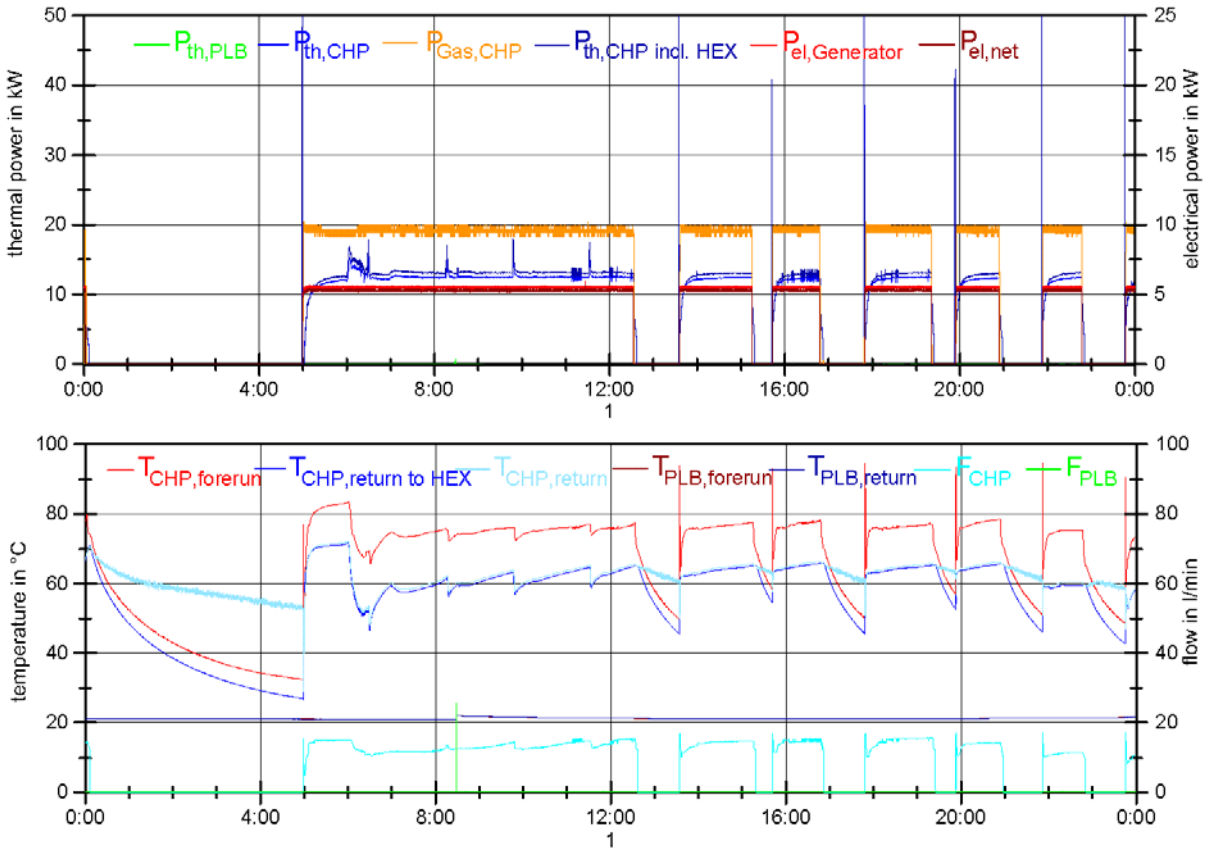

Figure IV-4.3 : Temperature-, flow- and power characteristics of the CHP-plant and the peak load boiler (shoulder day)

The balance results of the measured shoulder day are listed in Table IV-4.3. The heat supply of the building was possible without the peak load boiler on the transition day with and without the heating circuit mixer

Table IV-4.3 : Balance results of the shoulder day

Name	Unit	Transition day
CHP-plant		
$Q_{CHP,Gas}$	kWh/d	284.3
$Q_{el,\ Generator}$	kWh/d	80.4
$Q_{el.\ net}$	kWh/d	76.9
$Q_{CHP,\ excl.\ condenser}$	kWh/d	176.2
$Q_{CHP,\ incl.\ condenser}$	kWh/d	184.5
cos φ	-	0.88
t_{CHP}	h/d	14.7
$g_{th,CHP,\ excl.\ condenser}$	%	62.0
$g_{th,CHP,\ incl.\ condenser}$	%	64.9
$g_{el,CHP,net}$	%	27.1
$g_{el,CHP,Generator}$	%	28.3
$g_{CHP,total,\ excl.\ condenser}$	%	89.0
$g_{CHP,total,\ incl.\ condenser}$	%	91.9

Day in summer

The temperature, flow, and power characteristics at the buffer storage are shown in Figure IV-4.4. Due to the long operational hours of the CHP-plant during the morning, the domestic hot water storage loads could be covered by the buffer storage at 1 pm and 3 pm. For the remaining loadings, the CHP-plant started operating after a short while as a result of the temperature drop of the buffer storage.

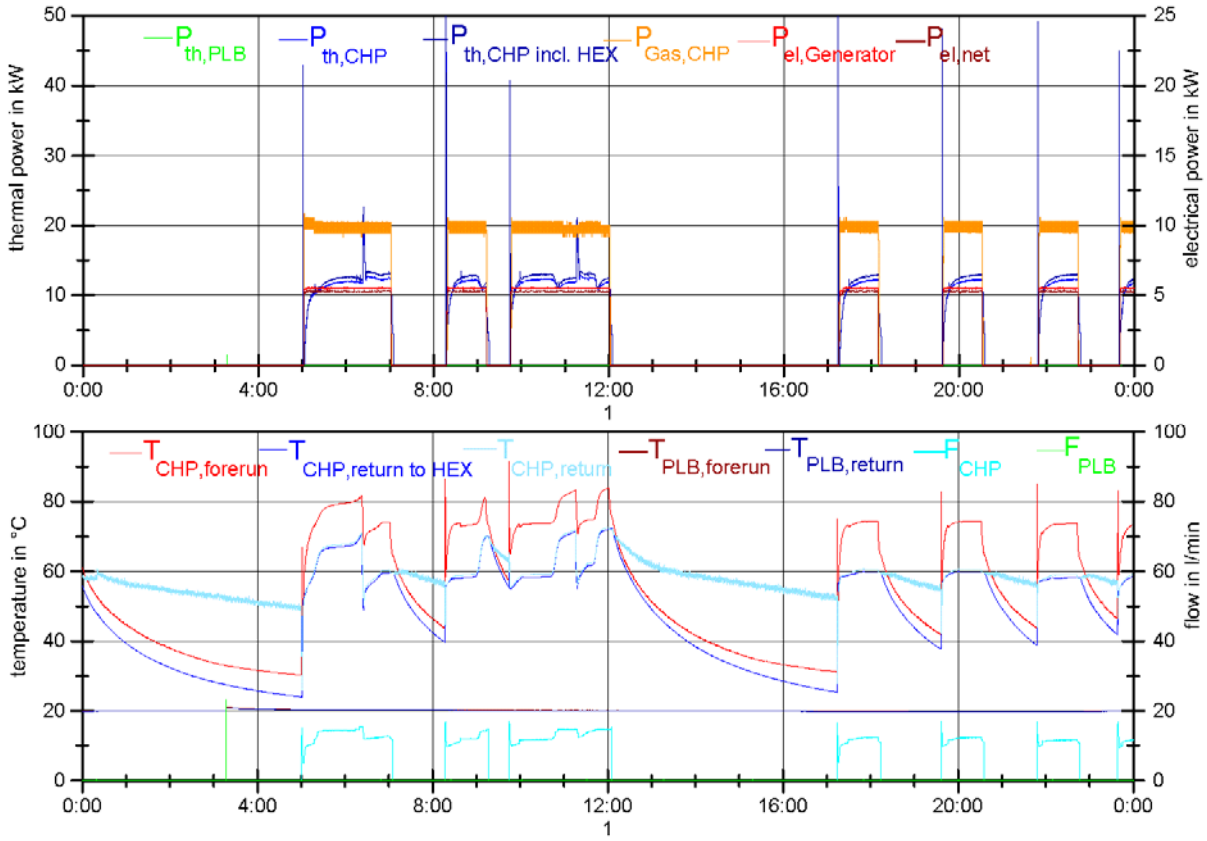

Figure IV-4.4 : Temperature-, flow- and power characteristics of the CHP plant and the peak load boiler

The balance results of the tests during summer days with buffer storage are listed in Table IV-4.4. The operation with the buffer storage and a fuel demand of 172.0 kWh/d resulted in degrees of efficiency of 86.0 % before and 88.6 % after the condenser.

Table IV-4.4 : Balance results for day in summer with buffer storage

Name	Unit	Day in summer with buffer storage
CHP-plant		
$Q_{CHP,Gas}$	kWh/d	172.0
$Q_{el, Generator}$	kWh/d	48.0
$Q_{el. net}$	kWh/d	45.7
$Q_{CHP, excl. condenser}$	kWh/d	102.2
$Q_{CHP, incl. condenser}$	kWh/d	106.6
cos φ	-	0.88
t_{CHP}	h/d	8.8
$g_{th,CHP, excl. condenser}$	%	59.4
$g_{th,CHP, incl. condenser}$	%	62.0
$g_{el,CHP,net}$	%	26.6
$g_{el,CHP,Generator}$	%	27.9
$g_{CHP,total, excl. condenser}$	%	86.0
$g_{CHP,total, incl. condenser}$	%	88.6

References

Mühlbacher, H.; Geiger, B.: Innovative CHP-systems for the energy supply of residential buildings - Final report Phase II, Institute for Energy Economy and Application Technology, Technical University of Munich, May 2007

IV-5 : Investigation of an PowerPlus Ecopower ICE Device at the Technical University of Munich[1]

Technical data and system integration

The analysed CHP-plant is an Ecopower Mini-CHP-plant from PowerPlus Technologies GmbH. It is equipped with a continuous modulation of the motor rotation speed and hence a power modulation. The technical data of the CHP-plant are listed in Table IV-5.1.

Table IV-5.1 : Technical manufacturer data of the Ecopower-CHP-plant

Name	Unit	
Fuel	-	natural gas
Thermal power	kW	4.0 – 12.5
Electrical power	kW	1.3 – 4.7
Range of speeds	rpm	1,200 – 3,600

An extra storage provided by the manufacturer (see Figure IV-5.1) with eight connections and a capacity of 1 000 litres acts as a buffer storage.

[1] Edited by Ulli Arndt (Research Institute for Energy Economy, FfE, Munich, Germany)

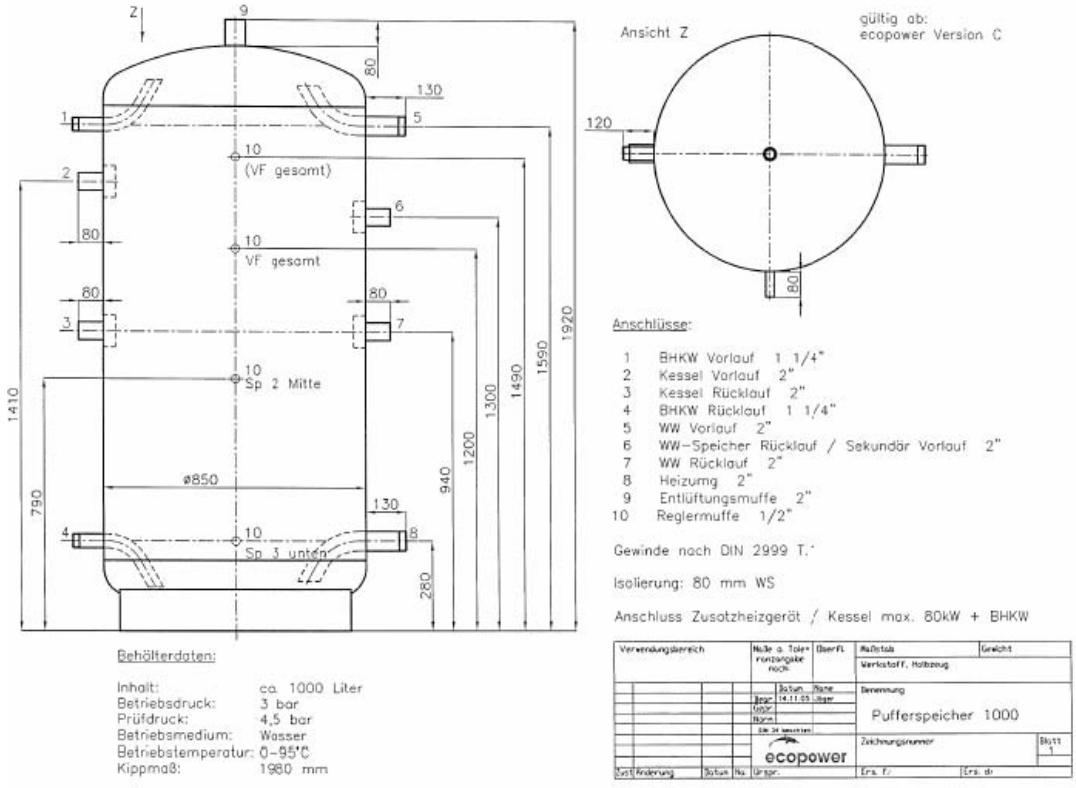

Figure IV-5.1 : Buffer storage

The installed peak load boiler is a condensing gas boiler from Vaillant type ecotec VC 466-E with a rated heating power of 45 kW. The hydraulic integration of the particular components is shown in Figure IV-5.2. To guarantee a certain return temperature at the CHP-plant, an additional distribution valve was installed at the discharge. For an efficient loading of the buffer storage, the CHP's forerun was connected to the top connection and the return to the bottom one of the vessel. The integration of the peak load boiler in the system occurs at two connections of the buffer storage which are located between the forerun and return connections of the CHP-plant. The supply of the domestic hot water storage also happens via the buffer storage. The connections are located on top and at the middle of the buffer storage. The control of respective components such as heating circulation pumps, heating circuit mixer and modulation of the peak load boiler is taken over by the control of the CHP.

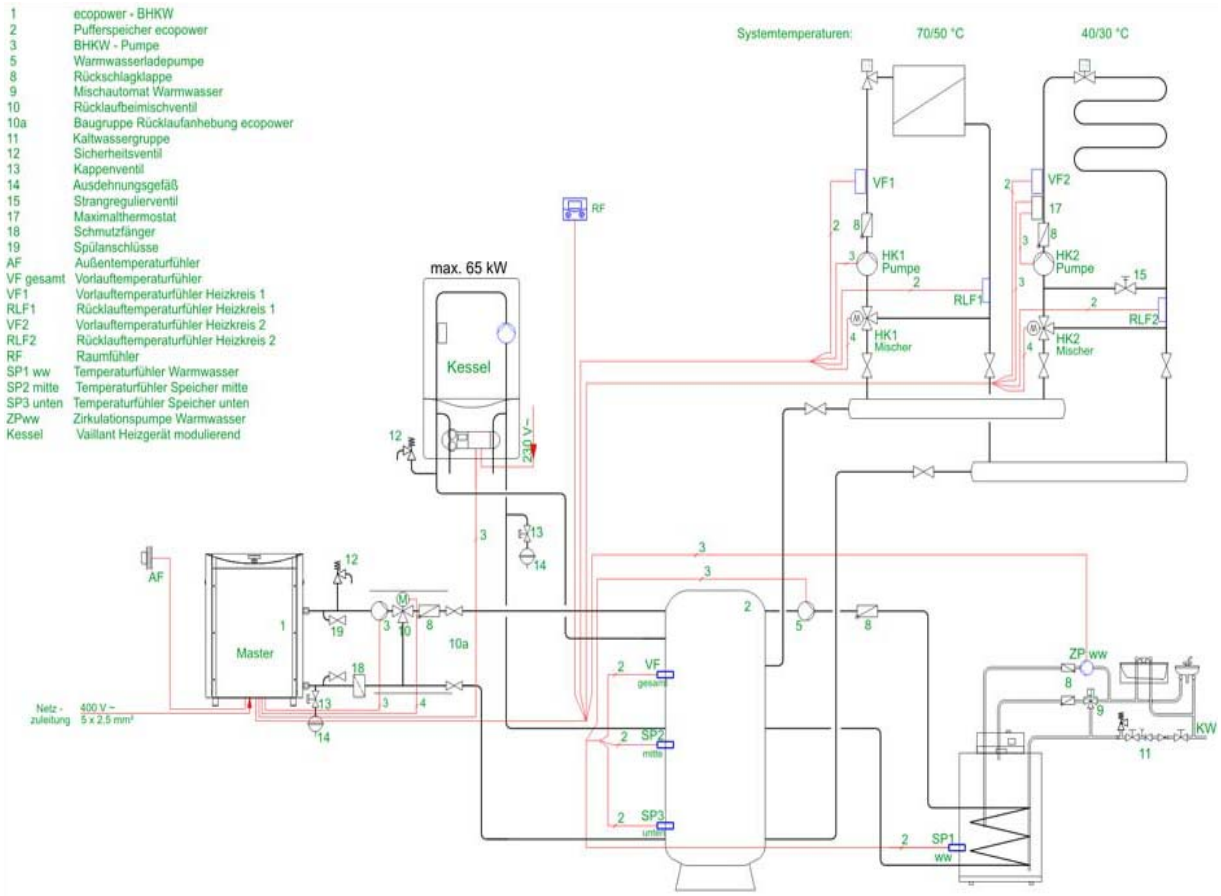

Figure IV-5.2 : Hydraulic integration of the CHP-plant with peak load boiler and buffer storage at the test rig

Measurements

To determine the energetic performance of the CHP-plant, the following tests were performed which will also be described consecutively and validated by measurements:

- Stationary operation at varied rotation speed
- Cold- and warm start
- Day in winter
- Transition day
- Day in summer

All efficiency values are referred to the lower heating value (LHV).

Stationary tests

Table IV-5.2 includes the performance data taken at various alternator RPM and the energy flux and efficiency determined by the data. The selected alternator RPM are the minimum speed of 1 200 rpm and the maximum speed of 3 600 rpm. An extra test with an average speed of 2 400 rpm was conducted. According to the measurements the temperature difference between forerun and return at the CHP-plant was in the range of 40 K and 45 K. To obtain significant test results, a balance took place for at least one hour after the stationary condition was reached. The thermal efficiency of the collection of test data was between 66.5 % and 68.2 % and the electrical efficiency of the generator was in the range of 23.8 % and 25.8 %. The overall efficiency of the CHP-plant hence is between 89.8 % and 92.1 % at stationary conditions.

Table IV-5.2 : Balance results of stationary testing

Name	Unit	Test 1	Test 2	Test 3
revolution speed	rpm	1,200	2,400	3,600
Forerun- and return temperature	°C	70/25	70/30	70/30
Balance period	h	1.0	1.0	1.0
Q_{Gas}	kWh	5.5	11.9	18.0
$Q_{electrical,Generator}$	kWh	1.3	3.1	4.6
$Q_{electrical,net}$	kWh	1.2	2.9	4.4
$Q_{thermal}$	kWh	3.8	7.9	12.1
cos φ	-	0.92	0.97	0.98
$g_{thermal,CHP}$	%	68.2	66.5	67.4
$g_{electrical,CHP,net}$	%	21.6	24.5	24.7
$g_{electrical,CHP,Generator}$	%	23.8	25.8	25.8
$g_{overall,CHP}$	%	89.8	91.0	92.1

Cold and warm start tests

The cold start of the CHP-plant is illustrated in Figure IV-5.3. It starts to operate at 6:39 am and the generator starts around one minute later than that with 2.5 kWel. After five minutes, the engine switches to maximum speed which is being reached at around seven minutes after the start-up signal. When reaching a certain return or engine temperature, the distribution valve opens and thermal power is being input in the heating buffer load circuit. After a transient period of around 25 minutes, the CHP-plant reaches a steady state. The difference between the electrical power at the generator and the net power results in the electrical auxiliary energy demand; it is around 200 W.

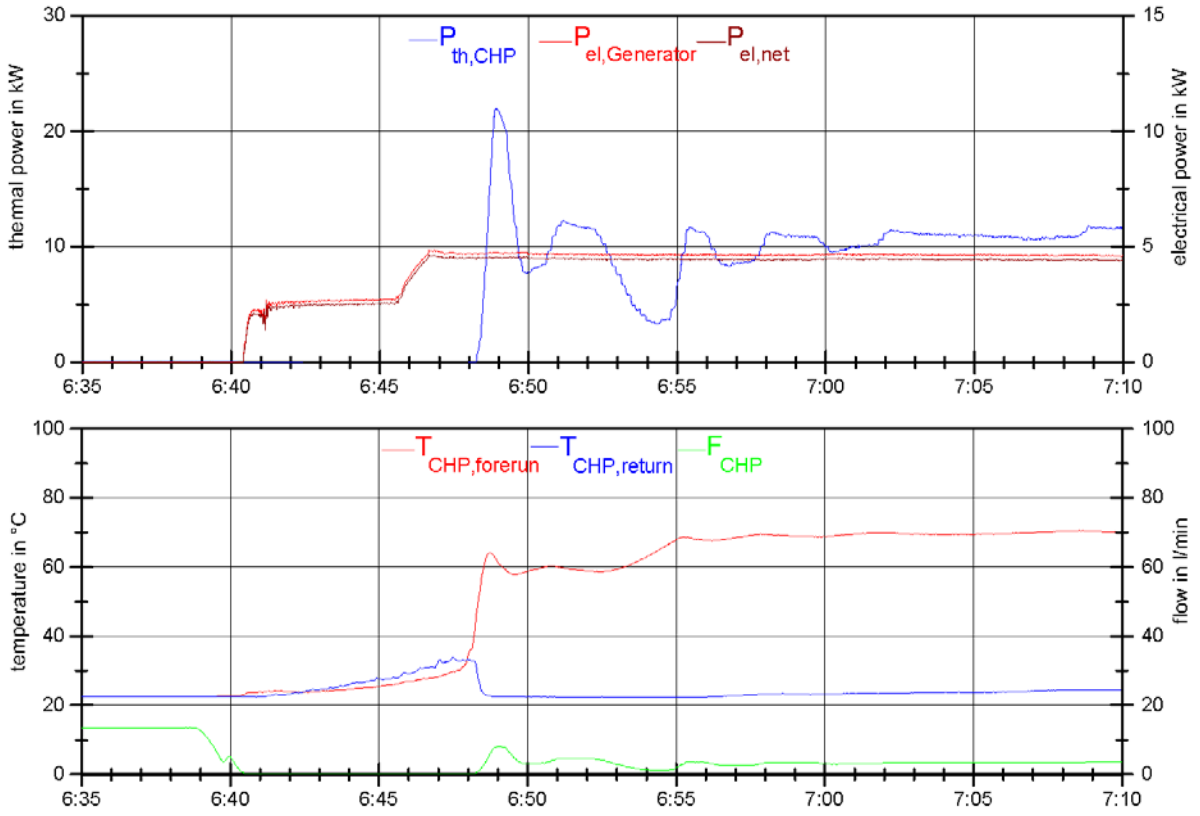

Figure IV-5.3 : Temperature-, flow- and power curve during cold start

Figure IV-5.4 shows the warm start test. At 6:35 am the shut down process is initiated. The CHP-plant operates at medium engine speed and switches off after around two minutes. At the same time, the distribution valve opens to avoid the engine from overheating and to inject the residual heat of the engine into the heat distribution system. During the start-up, the distribution valve shuts again and the engine operates at medium speed. Unlike the cold start test, the engine switches to the maximum speed after two minutes already. After around ten minutes, the CHP-plant runs steady state again.

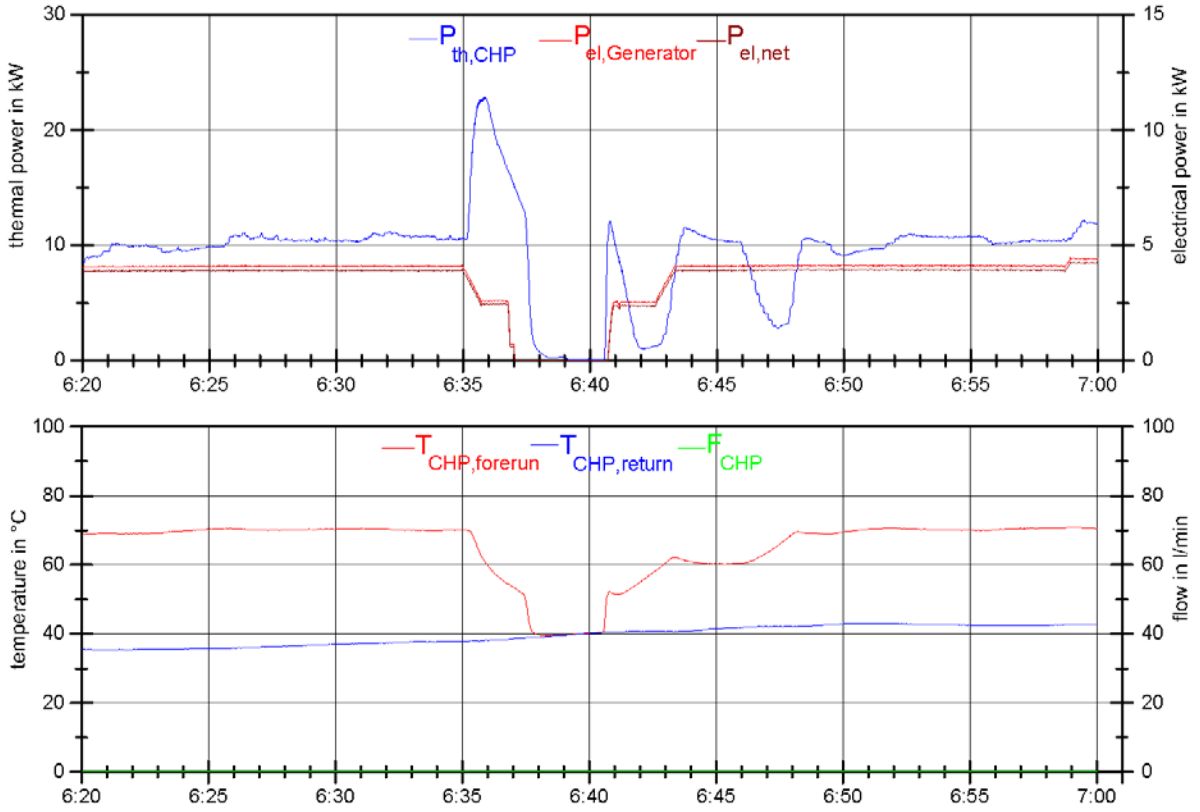

Figure IV-5.4 : Temperature-, flow- and power curve during warm start test

Day in winter

The relevant readings for the heat generation by the CHP-plant and the peak load boiler are illustrated in Figure IV-5.5. For this type of day, running-times of around 24 hours could be identified. Only at 5:15 am the CHP-plant was shut down for a short period and restarted again due to the daily compulsory shut down. The electrical power Pelectri-cal,net is below the power produced at the generator due to an auxiliary energy demand of around 170 W. The fluctuation of the thermal power at the CHP-plant traces back to flow variation in the CHP-plant resulting from the control of the distribution valve. The peak load boiler starts eight times throughout the day due to the high heating- and domes-tic hot water demand.

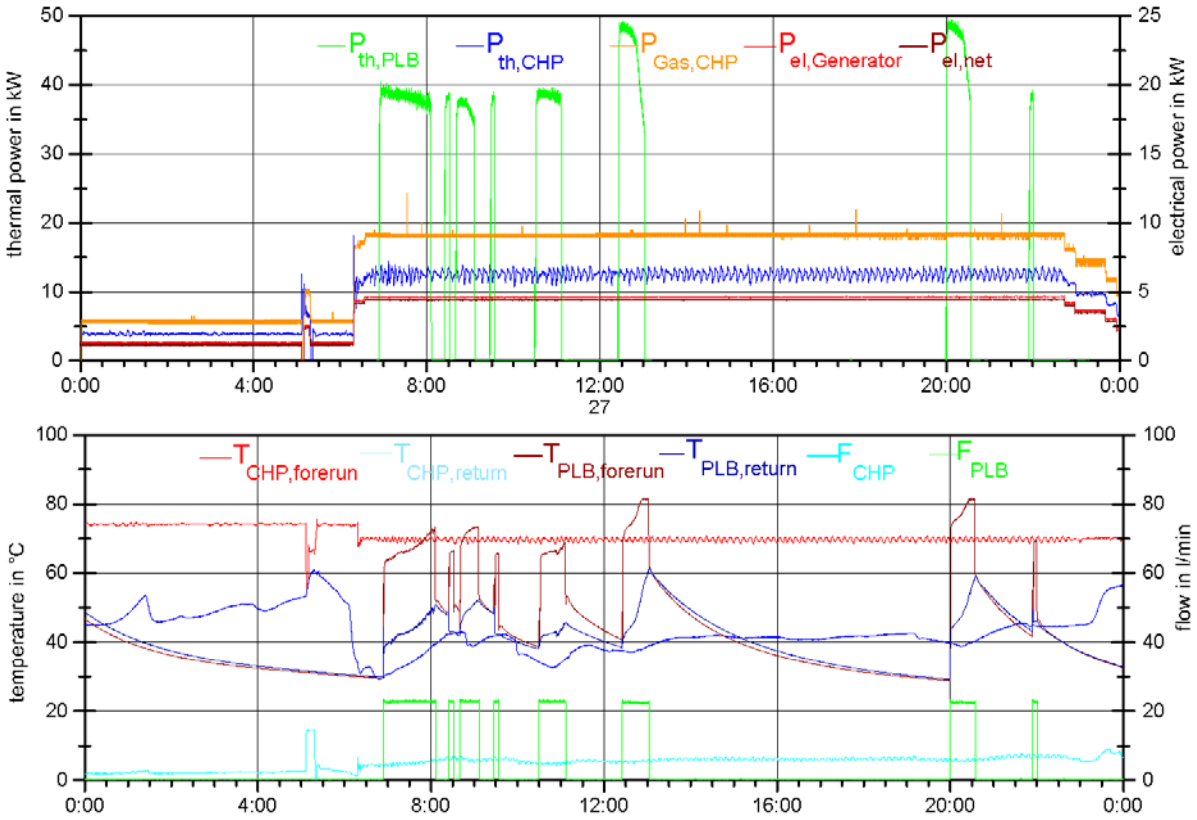

Figure IV-5.5 : Temperature-, flow- and power curve of the CHP-plant and the peak load boiler (day in winter)

The balance results of the tests carried out for a day in winter are shown in Table IV-5.3. The thermal efficiency of the CHP-plant was 66.9 %. During the measuring of the generator, the inverter was measured too as a result of technical measurement reasons. This resulted in an electrical efficiency of the generator including the inverter of 25.2 %. The overall efficiency of the system is therefore 90.9 %. Despite of the relatively short running time of the peak load boiler, its efficiency is still 97.8 %.

Table IV-5.3 : Balance results day in winter

Name	Unit	Day in winter
CHP-plant		
Q_{Gas}	kWh/d	351.3
$Q_{electrical,Generator}$	kWh/d	88.6
$Q_{electrical,net}$	kWh/d	84.5
$Q_{thermal}$	kWh/d	234.9
cos φ	-	0.98
t_{CHP}	h/d	23.9
$g_{thermal,CHP}$	%	66.9
$g_{electrical,CHP,net}$	%	24.0
$g_{electrical,CHP,Generator}$	%	25.2
$g_{overall,CHP}$	%	90.9

Transition day

The measured data taken from the heat generators are illustrated in Figure IV-5.6. The CHP-plant was in operation throughout the whole day for this day type also. During night operation, the CHP-plant mainly runs at minimum power level. It is only interrupted at the time when the domestic hot water storage loading takes place as the CHP-plant needs to switch to another power level for the heat supply. At the start of the day operation at 6:00 am, the CHP-plant runs with maximum power due to the peak power demand for the heating circuit in the morning and its related rapid drop of the heating buffer storage temperature. At 10:00 am, the peak load boiler is being switched on as a result of the decreased buffer storage temperature. The very low heating demand from 11:00 am onwards allows the CHP-plant to heat up the buffer storage to the desired temperature level again. Subsequently, a constant power reduction takes place until 3:00 pm, when the minimum engine speed is being reached to extend the running time of the plant. Between 3:00 pm and 10:00 pm, a power increase of the CHP-plant only happens during domestic hot water storage loading.

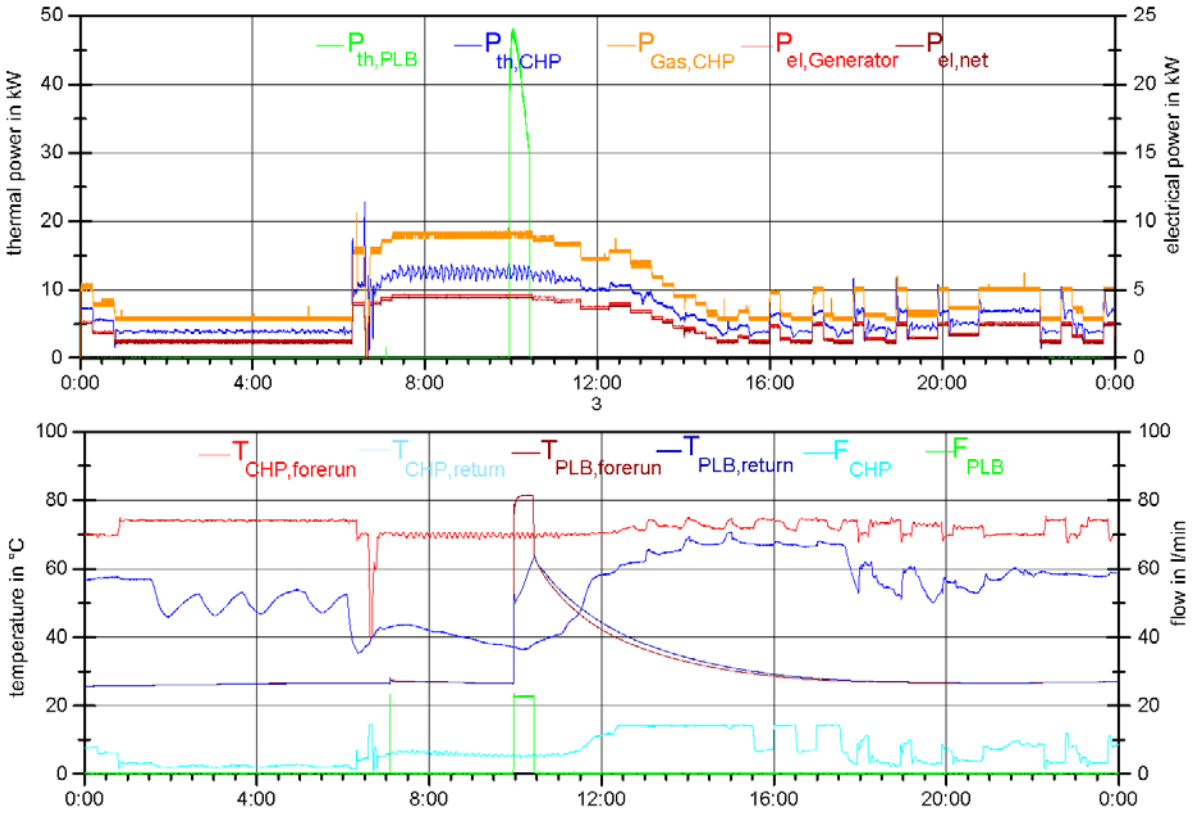

Figure IV-5.6 : Temperature-, flow- and power curve of the CHP-plant and the peak load boiler (transition day)

The balance results of the transition day are listed in Table IV-5.4. The overall efficiency of the CHP-plant is 90.0 % with an input heat of 57.6 kWh into the heating circuit and 66.1 kWh into the domestic hot water storage. A reduction of the electrical overall efficiency gelectrical,CHP of one per cent could be identified. The thermal efficiency goverall,CHP was around the same as for the day type: day in winter. This is due to the fact that the plant was being operated over a long period of time with reduced power. The net electricity production during the balance period added up to 55.3 kWh. An efficiency of 93,8 % for this particular type of day could be established, although the peak load boiler's running time tPLB was only 0.5 h.

Table IV-5.4 : Balance results for the transition day

Name	Unit	Transition day
CHP-plant		
Q_{Gas}	kWh/d	237.1
$Q_{electrical,Generator}$	kWh/d	58.8
$Q_{electrical,net}$	kWh/d	55.3
$Q_{thermal}$	kWh/d	158.0
cos φ	-	0.97
t_{CHP}	h/d	23.9
$g_{thermal,CHP}$	%	66.7
$g_{electrical,CHP,net}$	%	23.3
$g_{electrical,CHP,Generator}$	%	24.8
$g_{overall,CHP}$	%	90.0

Day in summer

The relevant curves for the balance i.e. temperature, flow and power of the CHP-plant and peak load boiler are shown in Figure IV-5.7. During the night the CHP-plant switches off due to the low energy demand for domestic hot water production. At the same time as the domestic hot water storage loading, at 6:30 am, the CHP-plant starts to cover the domestic hot water demand. For the most time of the day, the plant is being operated on the lowest power level. In Figure IV-5.7, the power increase during domestic hot water storage loading can be identified.

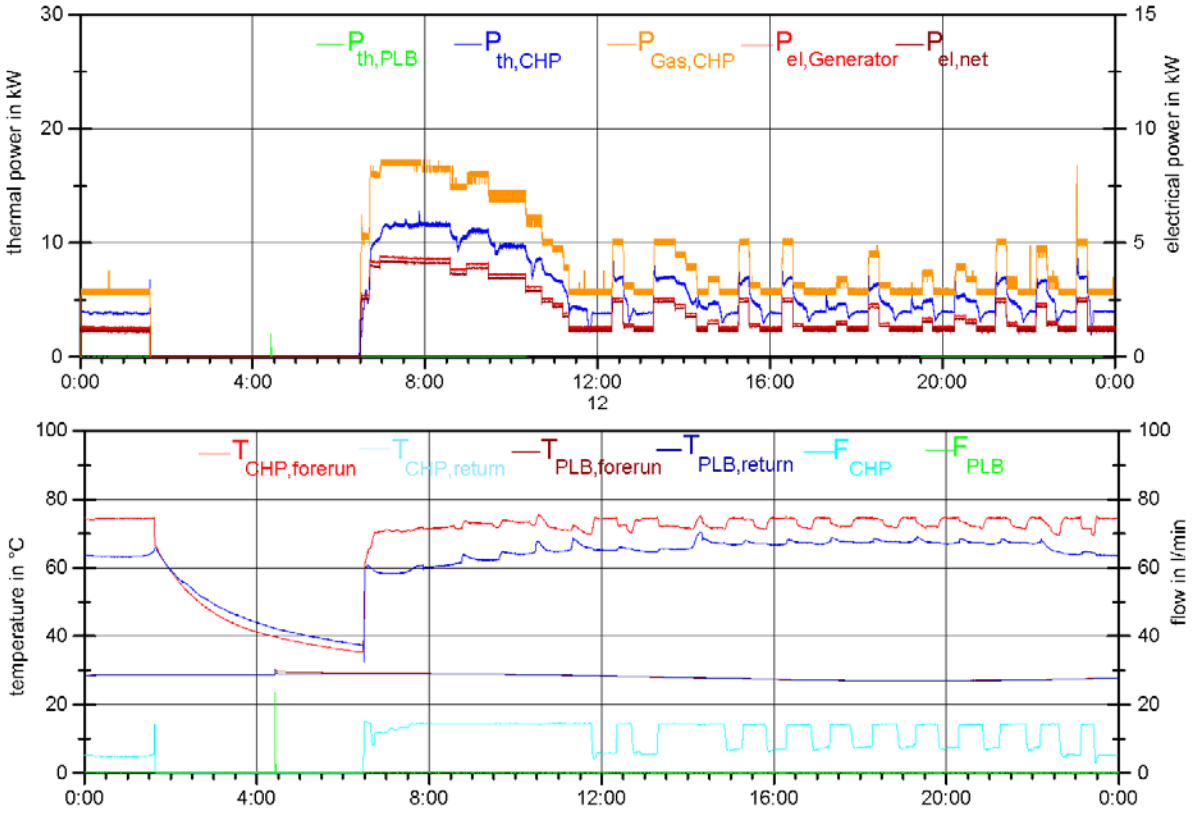

Figure IV-5.7 : Temperature-, flow- and power curves of the CHP-plant and the peak load boiler (day in summer)

The balance results of the test for the day in summer are listed in Table IV-5.5. During summer days a further reduction to 89.4 % of the CHP's overall efficiency $g_{overall,CHP}$ occurs in comparison the winter- and transition days. This is due to the operating mostly at minimum power. Although running times tCHP of the CHP of around 19 hours at a fuel consumption QGas of 164.6 kWh could be determined for the day in summer.

Table IV-5.5 : Balance results for day in summer

Name	Unit	Day in summer
CHP-plant		
Q_{Gas}	kWh/d	164.6
$Q_{electrical,Generator}$	kWh/d	40.3
$Q_{electrical,net}$	kWh/d	37.6
$Q_{thermal}$	kWh/d	109.5
cos φ	-	0.95
t_{CHP}	h/d	19.1
$g_{thermal,CHP}$	%	66.5
$g_{electrical,CHP,net}$	%	22.9
$g_{electrical,CHP,Generator}$	%	24.5
$g_{overall,CHP}$	%	89.4

References

Mühlbacher, H.; Geiger, B.: Innovative CHP-systems for the energy supply of residential buildings - Progress report Phase II / Ecopower, Institute for Energy Economy and Application Technology, Technical University of Munich, December 2006

IV-6 : Investigation of a Senertec ICE Device at the Catholic University of Leuven[1]

The tests on the Senertec CHP were conducted in 2001, in the framework of an Electrabel[2] research on CO_2-emissions. The Senertec has one thermal and electrical output level, and can therefore only be turned on or off. To gain insight in the performances of the Senertec for residential applications, its transient and stationary behaviour were tested. The aim was to check the efficiencies of the CHP and the overall system (including heat emission and/or storage) starting from different conditions: cold start-up (at least 5 hours shut down), warm start-up (1, 2 and 4 hours shut down before restarting) and steady state (measured after at least one hour on).

Direct coupling with the heat demand often leads to frequent on/off cycling due to fluctuations in the heat demand. Therefore the performances were also tested for use with a storage tank. (For the tests of which the data have been used within Annex 42, the Senertec was coupled directly with the convector.)

Besides temperatures, pressures, flow rates, gas consumption and electricity consumption and production, also the emission of green house gases was measured. The electrical output, as well as the gas consumption are not measured automatically and must be read and written to the file manually. Thermocouples type K measure temperatures at different points. An electromagnetic flow meter is installed on the cold water side. Gas temperatures are measured using a meter fixed to the wall at a certain distance from the set-up. Therefore the error margin on this temperature measurement is rather high.

In order to minimize the errors, thermocouples and flow meters were calibrated. These calibrations were effected by comparing instrument readings to reference instruments and then adjusting offset and slope parameters to adjust the translation of voltage signals to measured quantities.

[1] Authored by Leen Peeters and William D'haeseleer (Catholic University of Leuven)
[2] Electrabel is the main electricity supplier in Belgium

The sample frequency during tests is set equal to 1/min.

The energetic value of natural gas is calculated as:

$$\dot{F} = \dot{q}_{gas} \cdot \frac{p_{gas}}{p_N} \cdot \frac{T_N}{T_{gas}} \cdot LHV$$

$\dot{F}$: the natural gas power [W]
$\dot{q}_{gas}$: the measured flow rate [m³/s]
p_{gas} : the absolute pressure in the gas supply pipes [Pa]
p_N : the pressure in standard atmospheric conditions [101325 Pa and 273,15K]
T_{gas} : the temperature of the gas in the supply pipes [K]
T_N : the temperature in standard atmospheric conditions [101325 Pa and 273,15K]
LHV : the lower heating value of natural gas [J/Nm³]

The natural gas network delivers low caloric gas of which the average composition is given in Table IV-6.1.

Component	Molar fraction [%]
CH_4	83,2
C_2H_6	3,80
C_3H_8	0,839
C_4H_{10}	0,302
C_{4+}	0,1619
N_2	10,28
CO_2	1,400

Table IV-6.1 : composition of L-gas

The corresponding heating value results in 33.7 MJ/Nm³. The pressure in the gas supply pipes is supposed to have a constant value of 104200 Pa.

Uncertainty analysis

As the data is used for the model calibration and validation, the calculation of the derived parameters and their associated uncertainties is described here. However, when using the KULeuven data, care should be taken as the experiments were not performed following the Annex 42 experimental protocol (refer to section II of this report).

As an example the bias and precision errors of the temperatures and flow rates in steady period are calculated here. Bias errors are assigned to primary measurements only. They further propagate, combined with the precision errors, into the derived quantities.

In case of the gas and electricity consumption, as well as the energetic value of the natural gas, additional bias errors were assigned upon judgment. The reason being that for these measurements, the values have to be read from the meter and written to the file. Besides a delay, the introduction of an error is of high risk compared to electronic data reading and writing.

Bias error and precision errors of the flow rates and temperatures measured during a 34 minute steady period, are summarized in Table IV-6.2. The aim of the KULeuven tests was to check the performance on system level; temperatures were therefore measured on the inlet and outlet of the heat production systems.

B indicates the total bias, calculated from the individual bias errors for that sensor, using the root-sum-square method. The precision index S is calculated based on the average value of that parameter during the test and the number of logged readings.

The bias errors and precision indices are combined to express the uncertainty in a measured quantity, $U_{95\%}$, the measured uncertainty at the 95 percent confidence level.

	Total bias B	Precision index S	$U_{95\%}$	Average
T_{in_CHP}	0.1 °C	0.58 °C	0.77 °C	83.32 °C
T_{out_CHP}	0.2 °C	0.54 °C	0.74 °C	36.29 °C
$T_{in\_Convector}$	0.2 °C	0.39 °C	0.55 °C	81.23 °C
$T_{out\_convector}$	0.1 °C	0.24 °C	0.33 °C	37.66 °C
Flow rate	8.7 kg/hr	3.7 kg/hr	9.98 kg/hr	214.19 kg/hr

Table IV-6.2 : bias errors, precision indices, uncertainty at 95% and average value of primary parameters.

T_{in_CHP}, T_{out_CHP} and $T_{in\text{-}convector}$ and $T_{out\_convector}$ represent the inlet and outlet temperatures of CHP and convector respectively.

The estimated error values for gas and electricity consumption/production can be summarized as follows:

- Uncertainty on electricity measurements is 0.1 kWh
- Uncertainty on gas meter measurements is 5 %
- Uncertainty on gas temperature measurement +/- 2°C
- Uncertainty on pressure ‘measurement’ +/- 2%
- Uncertainty on specific heat constant at constant pressure for water is, based on the variation in the values of this constant within the temperature range considered here, 1%

The energetic value of natural gas is calculated, as described above, expressed by:

$$\dot{F} = \dot{q}_{gas} \cdot \frac{p_{gas}}{p_N} \cdot \frac{T_N}{T_{gas}} \cdot LHV$$

And thus the introduced error for this derived quantity results in:

$$\left(\frac{\Delta \dot{F}}{\dot{F}}\right)^2 = \left(\frac{\Delta \dot{q}_{gas}}{\dot{q}_{gas}}\right)^2 + \left(\frac{\Delta p_{gas}}{p_{gas}}\right)^2 + \left(\frac{\Delta T_{gas}}{T_{gas}}\right)^2$$

$$\left(\frac{\Delta \dot{F}}{\dot{F}}\right) = 0.15$$

The uncertainty on the LHV, due to small fluctuations in composition is limited to 2% of the measured value[3].

[3] Personal communication with Fluxys, Belgian gas transmission system operator.

IV-7 : Investigation of a Senertec ICE Device at the Swiss Federal Laboratories for Materials Testing and Research[1]

Introduction

Energy efficiency measurements as well as exhaust gas composition and particle measurements were conducted under stationary as well as cold and warm start conditions on the regular test bench at Empa, in July 2000 and were documented in (Schreiber, 2002). Here, an excerpt from this report, concerning the energy and efficiency measurements, is given in English.

Description of micro-cogeneration unit

The tested micro-cogeneration unit was a heating oil EL driven Dachs HKA H 5.3 ICE unit, manufactured by Senertec, Schweinfurt, Germany. Selected technical manufacturer's data are given in Table IV-7.1.

Summary of results at stationary conditions

The measured power output and efficiency values differ only slightly from manufacturers data, and are within the measurement uncertainties.

[1] Authored by Viktor Dorer and Daniel Schreiber (Swiss Federal Laboratories for Materials Testing and Research)

Table IV-7.1 : Summary of measured data and comparison with manufacturer's data

		Measurements Empa	Manufacturer Data	Deviation
Fuel power input (LHV)	kW	18.5 ±0.2	17.9	+0.6
Heating power output	kW	10.8 ±0.2	10.4	+0.4
Electric power output	kW	5.3 ±0.0	5.3	-0.0
Total useful energy output	kW	16.1 ±0.2	15.7	+0.4
Water circuit efficiency	%	58.5 ±1.2	59	-0.5
Electric efficiency	%	28.6 ±1.0	30	-1.4
Total efficiency	%	87.1 ±1.6	89	-1.9
Radiation losses	%	5.7 ±0.5	-	-
effective exhaust gas loss	%	7.2 ±0.7	-	-
normalized exhaust gas loss (Tu=20°C)	%	7.8 ±0.7	-	-

Experimental set-up

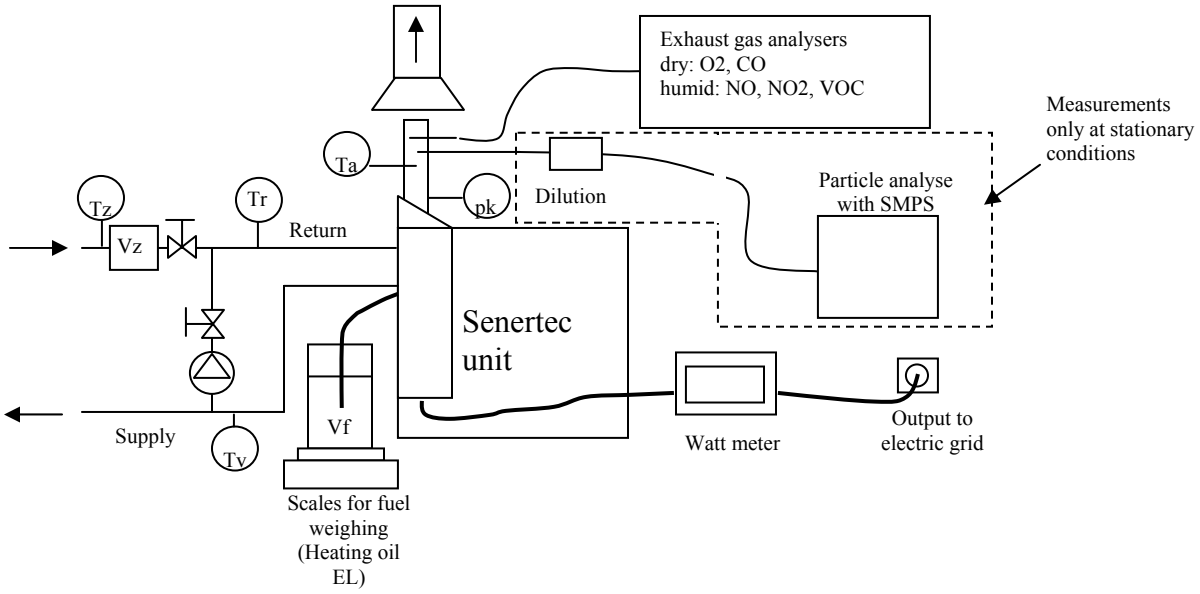

Figure IV-7.1 : Experimental set-up for the measurements on the Senertec cogeneration unit

The following parameter were on-line measured during the tests:

- fuel demand Vf (heating oil extra light), using scales
- delivered electric power
- delivered heating power (calculated from temperature T_V, T_z and water circuit mass flow Vz)
- water return temperature T_r
- water supply temperature T_V
- water circuit inlet temperature T_z
- water circuit inlet mass flow V_z
- exhaust gas temperature T_a

- oil temperature T_{oil}
- ambient temperature T_u
- combustion air temperature T_{air}
- pressure in the exhaust chimney p_k
- exhaust particle size (scans over a period of 2,5 minutes)

The following parameters were not continuously measured during the test.

- carbon particulate matter (soot) / carbon particulate matter during start–up
- air moisture content
- barometric pressure p_u

Experimental procedure

Tests under stationary conditions and tests during cold and warm start-up were conducted. The cogeneration unit has an internal control to keep the internal water temperature high enough, in order to prevent temperature situations endangering the engine block. Therefore, a time lag resulted for the heating power output to the water circuit. It was not possible to influence this temperature hold control from external during the test. The measurements were performed on 27 July, 2000.

Results from measurements

Stationary conditions

Operation parameters:		
Room temperature	25.8	°C
Supply temperature to water circuit	83.8	°C
Return temperature from water circuit	61.7	°C
Oil temperature	32.3	°C

Barometric pressure	965	mbar
Temperature of combustion air	28.5	°C
Rel. humidity of combustion air	47	%
Water content of combustion air	12	g/kg
Stoichiometric air ratio (Lambda)	1.72	-
Input:		
Oil flow rate	1.56	kg/h
Fuel heating power (LHV)	18.50	kW
Output:		
Heating power	10.80	kW
Electric power (AC net)	5.28	kW
Total useful energy output	16.08	kW
Thermal efficiency water circuit (LHV)	58.50	%
Electric efficiency (AC net) (LHV)	28.56	%
Total efficiency (LHV)	87.06	%
Radiation heat loss	5.74	%
Effective exhaust gas loss	7.20	%
Normalized exhaust gas loss (Tu=20°C)	7.80	%
Exhaust gas:		
Exhaust gas temperature	143	°C

Cold start

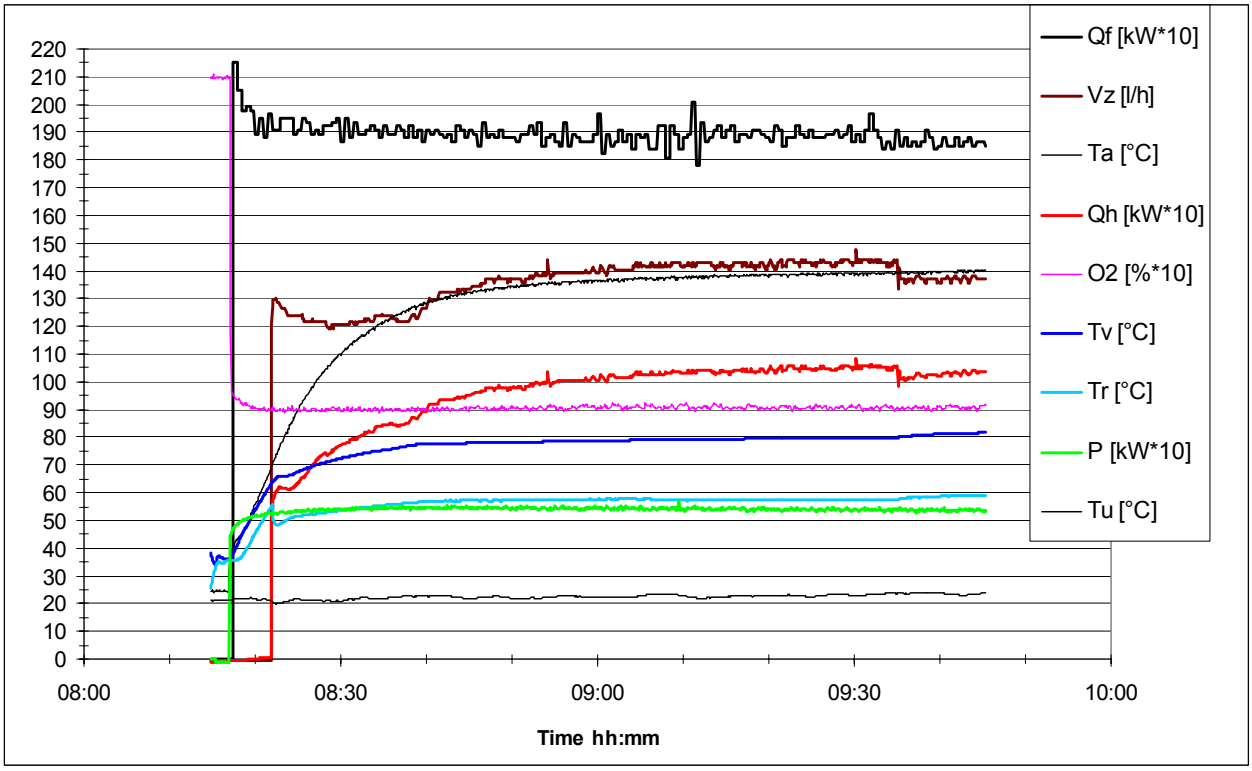

Figure IV-7.2: Results for the cold start-up measurements: temperatures and power

Tu Ambient temperature *Tv Supply temperature* *Qf Fuel power input*
Ta Exhaust gas temperature *Tr Return temperature* *P Electric power output (AC)*
O2 Oxygen content *Qh Heating power output* *Vz Water circuit flow rate*

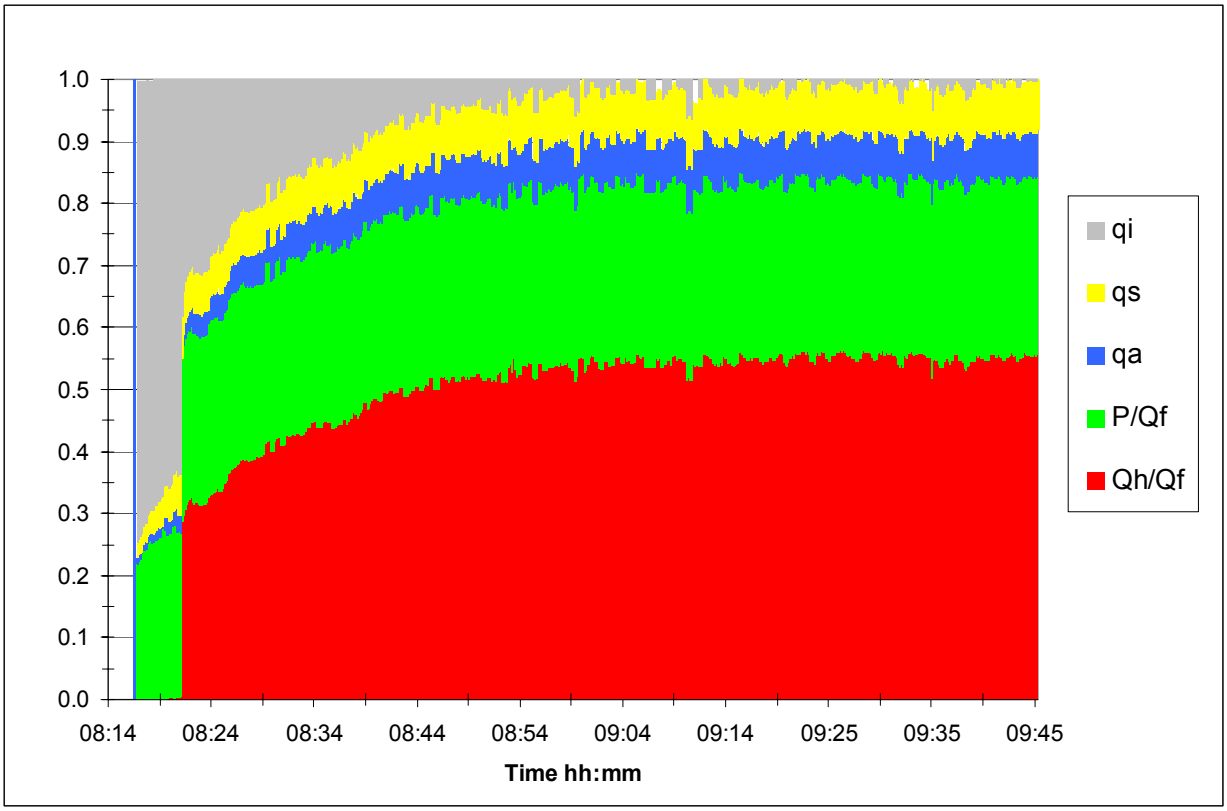

Figure IV-7.3 : Cold start-up measurements: energy losses and electric and thermal efficiencies

qi	*Part for heating up the cogen unit*	*P/Qf*	*Electric efficiency (LHV fuel)*
qs	*Radiation losses*	*qa*	*Exhaus gas loss*
Qh/Qf	*Thermal efficiency (output to water circuit) (LHV fuel)*		

Warm start

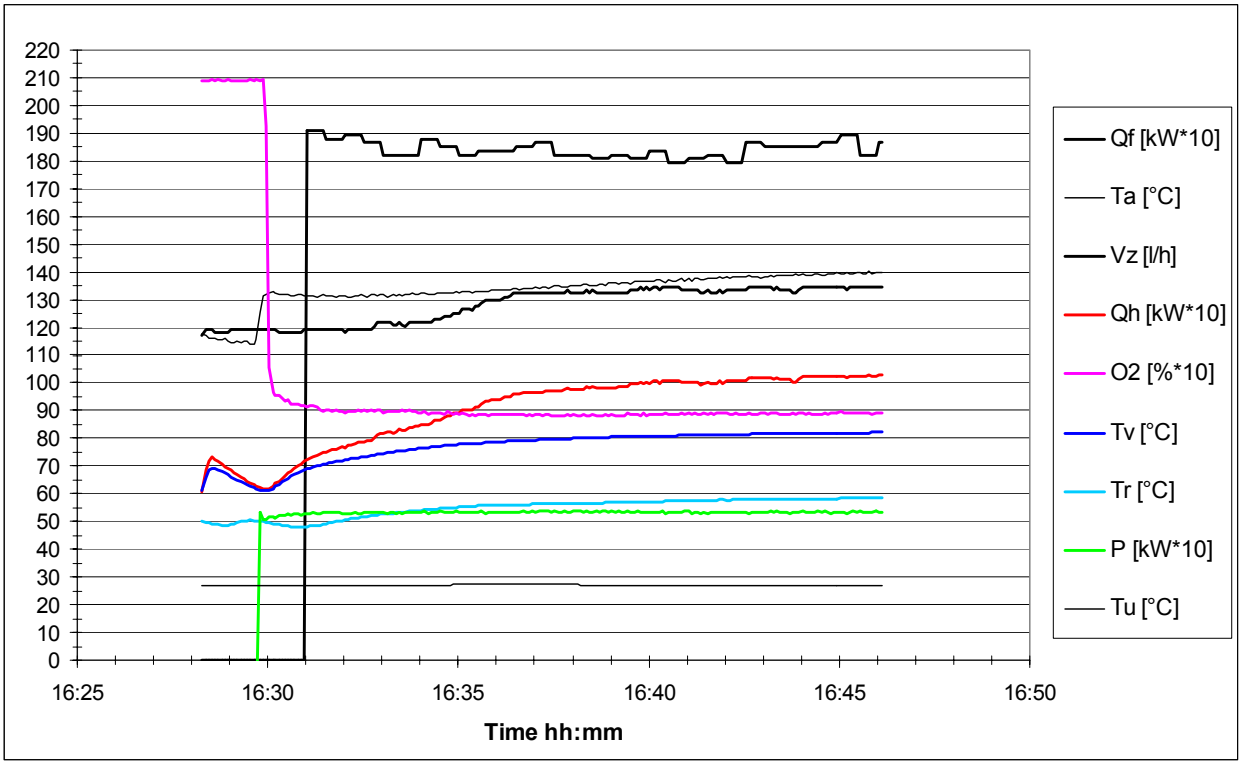

Figure IV-7.4 : Results for the warm start-up measurements: temperatures and power

Tu Ambient temperature Tv Supply temperature Qf Fuel power input
Ta Exhaust gas temperature Tr Return temperature P Electric power output (AC)
O2 Oxygen content Qh Heating power output Vz Water circuit flow rate

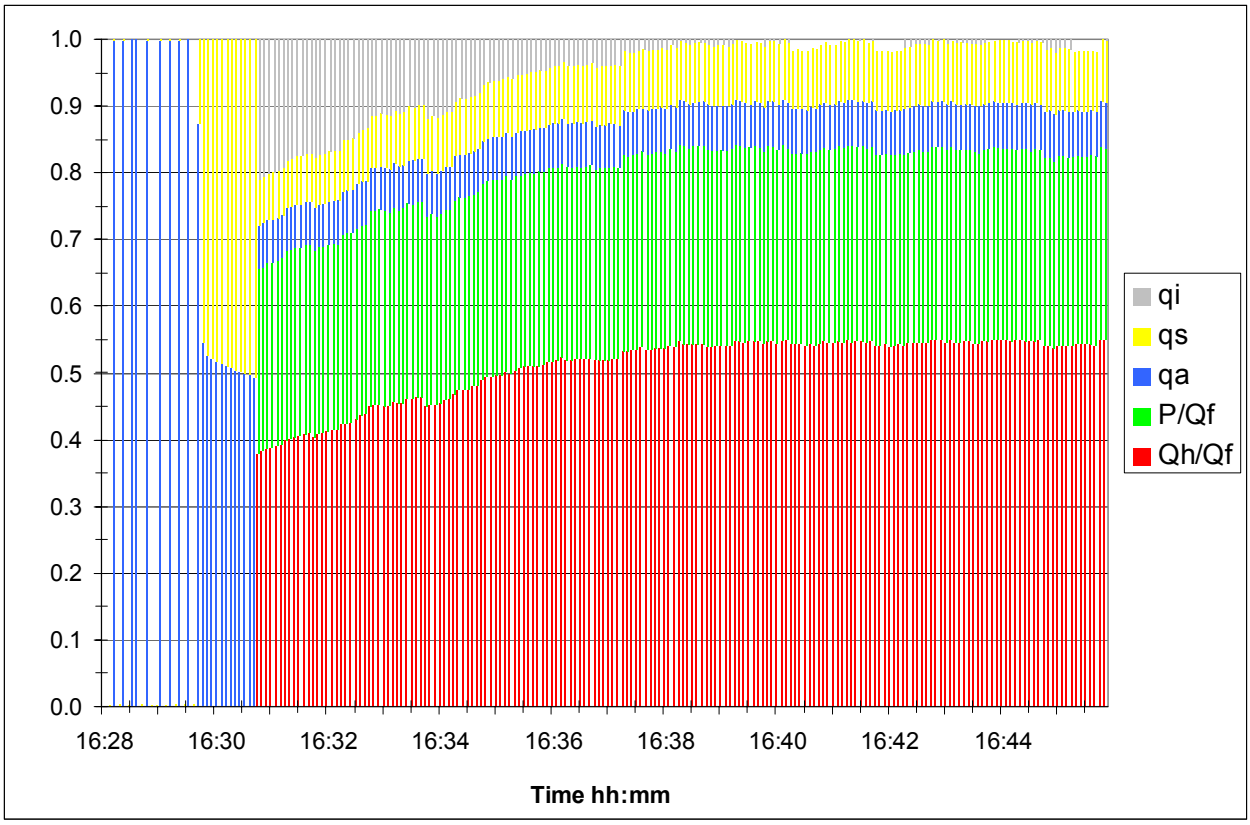

Figure IV-7.5 : Warm start-up measurements: energy losses and electric and thermal efficiencies

qi	*Part for heating up the cogen unit*	*P/Qf*	*Electric efficiency (LHV fuel)*
qs	*Radiation losses*	*qa*	*Exhaust gas loss*
Qh/Qf	*Thermal efficiency (output to water circuit) (LHV fuel)*		

References

Schreiber D. (2002) Emissions- und Wirkungsgradbestimmung am Miniblockheizkraftwerk Senertec H 5.3. Swiss Federal Laboratories for Material Testing and Research (Empa), report 840568, Nov. 2002

IV-8 : Investigation of an AISIN ICE Device at Napoletanagas Experimental Facilities[1]

Experiments were performed on an AISIN-Toyota micro-CHP system based on a four-stroke engine powered by natural gas. The engine is directly coupled to the electric generator, and two heat exchangers recover thermal energy from the engine exhaust gas and by the engine cooling system. The electric and thermal power outputs are 6 kW and 13.5 kW respectfully at nominal operating conditions (rated electric efficiency is 26.5 % and rated thermal efficiency is 59.5 %, based on LHV) with a water flow rate of 0.65 kg/s and a water input-output temperature of 60-65°C.

According to a typical 3-E (Energetic, Economic and Environmental) approach, the performances of the MCHP (the Alternative System) are compared to that of the Conventional System, in this case the electric grid (PP) and a boiler (B). In Figure IV-8.1 the energy flows are shown: alternative and conventional systems can satisfy both the electric power, $\dot{E}_{el,US}$, and the thermal power, $\dot{E}_{th,US}$, requirements for heating and/or domestic hot water production. In the same figure the conversion parameters and primary energy flows are also shown.

[1] Authored by Sergio Sibilio (Second University of Napoli) and Maurizio Sasso (University of Sannio)

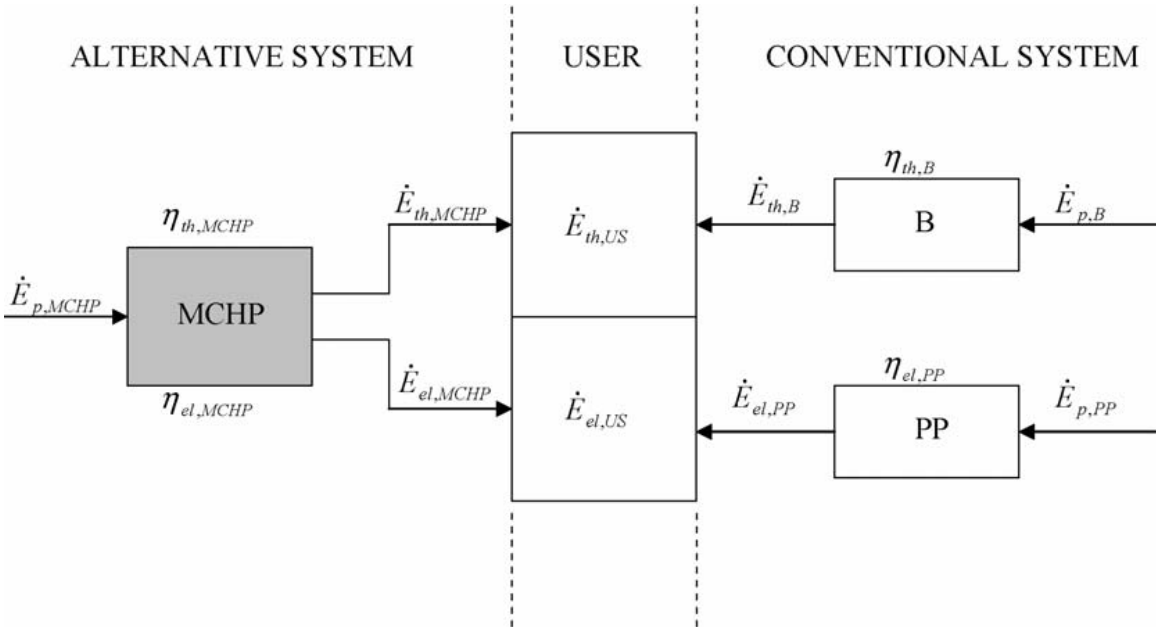

Figure IV-8.1 : Energy flows of alternative (MCHP) and conventional (power plant and boiler) systems

The MCHP has been tested in a wide range of working conditions varying both electric, $\dot{E}_{el,US}$, and thermal, $\dot{E}_{th,US}$, energy supplied to the end-user, and the most important thermodynamic properties have been measured to evaluate the energy and mass flow rates. In order to perform steady state energetic balance (plant and components) the devices considered in the facility have been equipped with measurement sensors for the acquisition of electrical, thermal/cooling and flow quantities needed for first and second law thermodynamic analysis. In Table IV-8.1 are shown thermal and electrical quantities monitored with their main metrological characteristics (M. Sasso, S. Sibilio, L. Vanoli, 2003; R. Possidente, C. Roselli, M. Sasso, S. Sibilio, 2007)..

. The instrumentation for these measurements have the following requirements:

1. accuracy, the instrument must provide measurements with satisfactory metrological performance (in terms of uncertainty, repeatability, stability, etc.);

2. non-intrusiveness, the probe of the measurement instrument must have small dimensions, so as to reduce the unavoidable interference (or modification) with the measured (i.e. the quantity to be measured).

The data acquisition systems are finally composed by:

1. Hydra Data Logger for the acquisition of fuel gas flow rate.

2. Field Point I/O System with one FP-AI-100 module to acquire signals by the tangential turbine and watt-meters, and three FP-RTD-122 modules to acquire signals by the platinum thermal-resistors. Every module has 8 input channels.

These acquisition systems are connected to the central unit equipped with LabView software, a graphical programming language that permits the creation of man machine interface (MMI) to evaluate in real-time unit performance.

Table IV-8.1 : Measurement instruments used in the experimental analysis and main metrological characteristics

Quantità	Sensor/instrument	Measurement field	Accuracy	Data transmission
Electric power	Watt-meter	0-3 [kW_{el}]	± 0.2% at full scale	Analogical output 4-20 mA
Temperature	Platinum RTD thermal ribbon	-60/220 [° C]	± 0.10% a 0° C and 100 Ω	Analogical output with acquisition through Weathstone's bridge
Water flow rate	Tangential turbine	0.03-1.00 [dm^3/s]	± 2% at full scale	Analogical output 4-20 mA
Fuel flow rate	"Positive displacement" meter	[m^3]	± 1%	Low frequency impulses emissions (1 pulses/ m^3)

Many tests have been performed both in steady-state conditions, considering the average values of the acquired parameters in an interval of at least 15 minutes, and considering start warm-up too; initial tests have been carried out considering the Micro-CHP alone (a), then considering some assembly (b) and finally examining a more complex "trigeneration" system.

a) In Figure IV-8.2, in order to remark the optimal operating conditions, $\dot{E}_{th,US}$ and $\dot{E}_{el,US}$, are reported with curves at fixed values of Primary Energy Ratio (iso-PER); this is defined as the ratio of the useful energy output supplied to the end-user to the primary energy consumption. This graph is fundamental to define the domain for an efficient use of the MCHP from an energetic point of view.

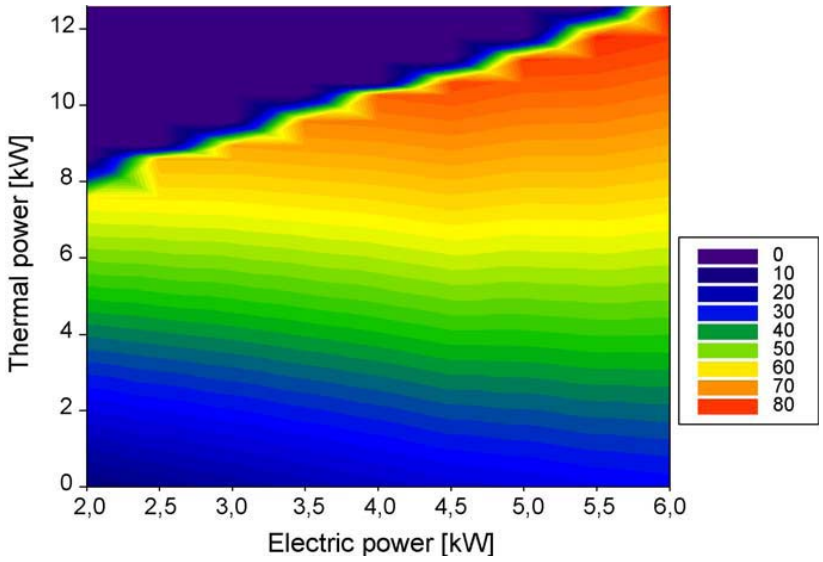

Figure IV-8.2 : Iso-PER curves of MCHP vs. electric and thermal power.

Moreover in Figure IV-8.3 is reported the measured electrical efficiency, η_{el} vs. electric power $\dot{E}_{el}$, that gives the best value of efficiency of around 26% (as declared by manufacturer) for the maximum value of electric power.

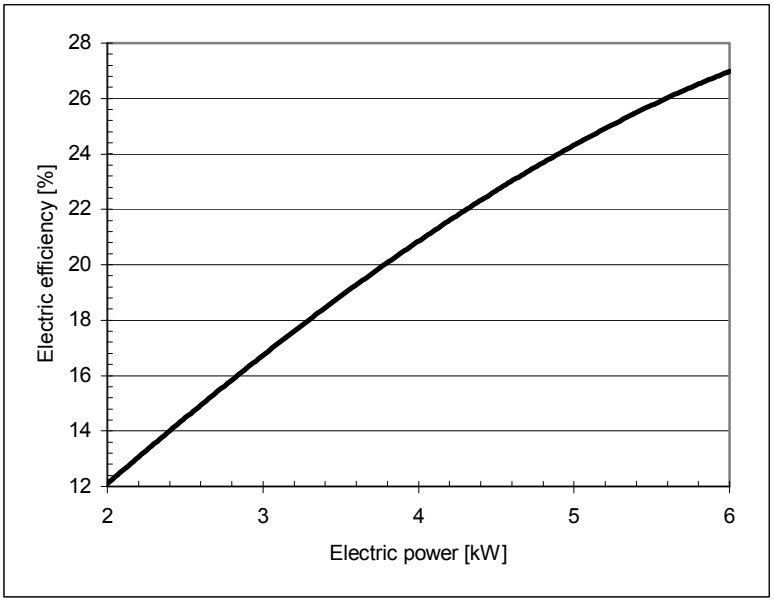

Figure IV-8.3 : Electric efficiency vs supplied electric power.

b) Within several matching, a possible assembly consists of the AISIN MCHP and a 200 L accumulation boiler (MCHP/Heat storage), with electric resistances and internal coil heat exchanger for thermal recovery of the MCHP hot water. In Figure IV-8.4 are reported the results of this analysis considering a cold start-up of the microcogenerator; for each test the electric power supplied to the electric resistances is fixed and the figure

shows the time needed to reach the water temperature of 60 °C in the heat storage.

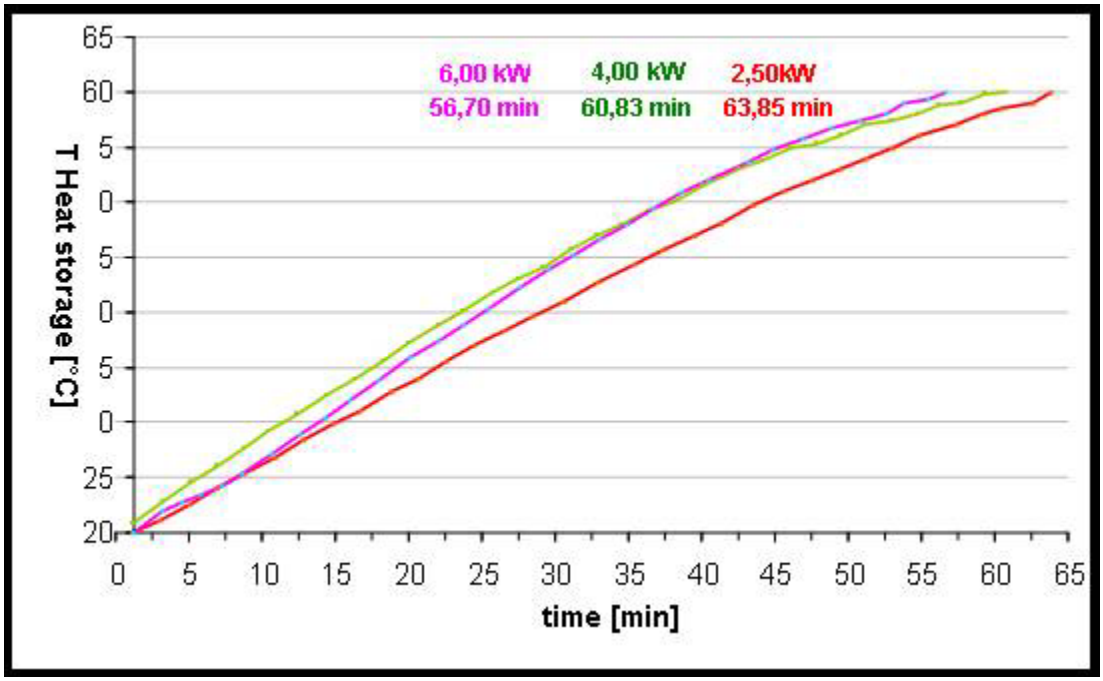

Figure IV-8.4 : Heat storage temperature variation

c) A further analysis on a "trigeneration" system, MCHP/EHP, that consists of a MCHP that drives an electric air/water vapour compression heat pump (EHP), has been performed.

The micro-CHP is coupled with an electric heat pump that supplies in heating mode 6.3 kW with a rated Coefficient Of Performance (COP) = 2.92 and in cooling mode 6.0 kW with a rated COP = 2.94, these values are valid for nominal operating conditions without taking into account the energy consumption of auxiliary devices.

The experimental tests have been performed in steady state conditions, varying the electric power delivered by micro-CHP in the range 2.0–6.0 kW .

Two operating conditions were simulated:

1. “heating mode” with co-production of electric and thermal energy, Figure IV-8.5;

2. “cooling mode” with co-production of electric, thermal (DHW) and cooling energy (tri-generation).

In both MCHP/EHP operating conditions the electric power that exceeds the needs of EHP is supplied to end-user.

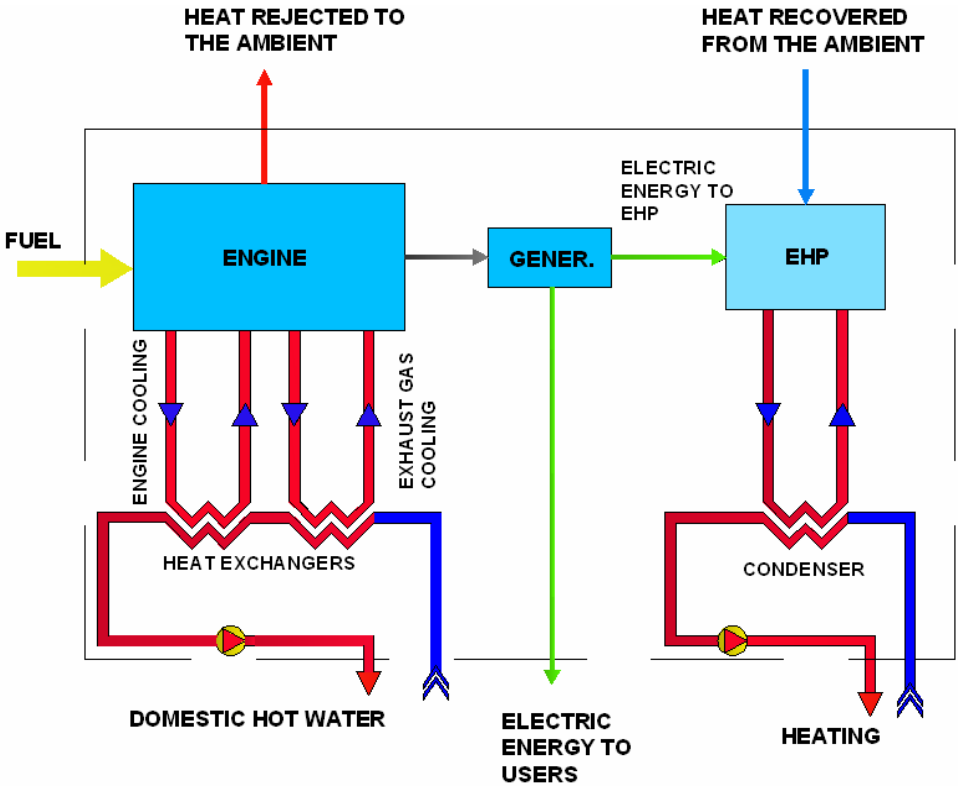

Figure IV-8.5 : MCHP/EHP plant in heating mode.

1. In the “heating mode” has been made experimental tests at two different mass flow-rates of the secondary fluid in the closed circuit, 0.333 kg/s and 0.167 kg/s, that are representative of volumetric requirements of an italian domestic user. The graph in Figure IV-8.6 synthesize the experimental data about total thermal power and the preheating and post-heating shares at the maximum mass flow-rate: we observe that the maximum recovered thermal power goes from 13 to 17 kW; it’s possible, moreover, to observe how, increasing the electric power requested by the user, the preheating share

due to the EHP tends slightly to a diminution, while the post-heating share due to the recovery in the MCHP tends to an increase: this second effect is prevailing on the first, as well as the two shares amount shows an increasing trend, in a logarithmic way.

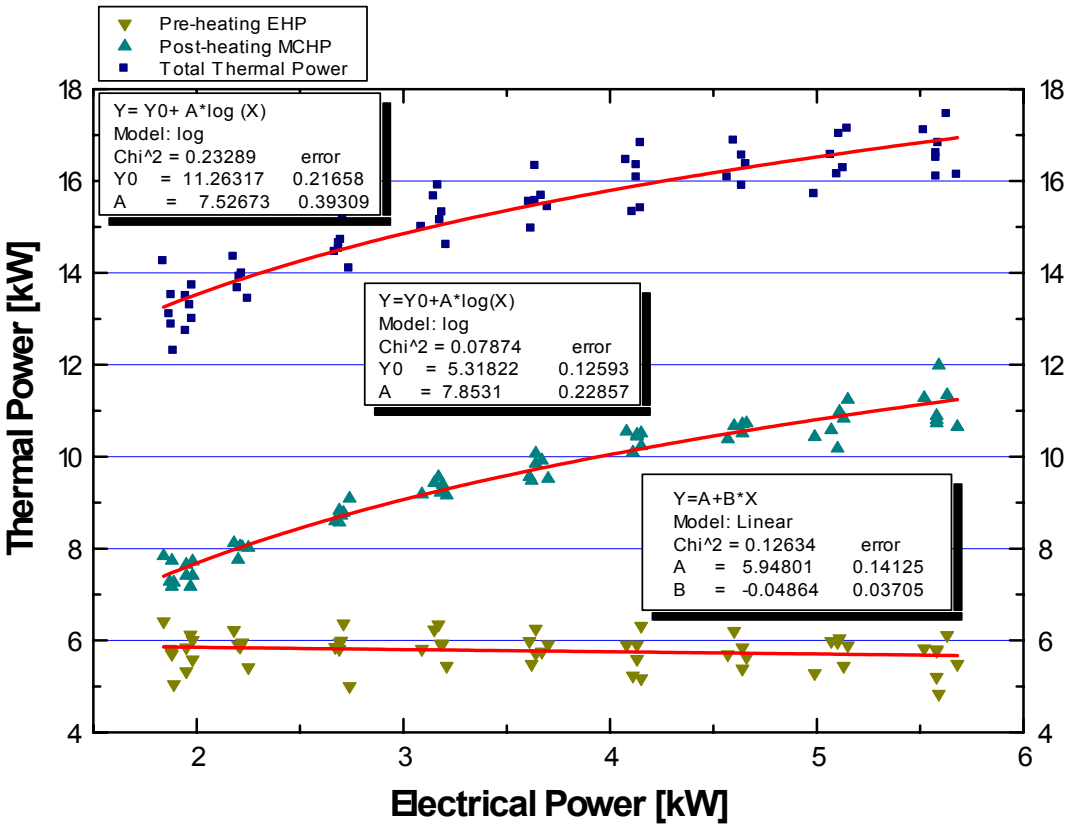

Figure IV-8.6 : Total thermal and preheating power recovered by MCHP/EHP system at the variation of electric power supplied by MCHP (water mass flow-rate 0,333kg/s)

2. As already anticipated in the summer season the MCHP/EHP system is able to satisfy the thermal and cooling needs of a domestic user, over as the production of electric energy, configuring itself as a trigeneration system.

In this operating mode the thermal circuit, recovered by MCHP, and the cooling circuit are separated, so the tests have been made ranging the mass flow-rate of the MCHP thermal recovery to the following values: 0.217 kg/s and 0.108 kg/s; for the cooling

circuit, instead, has been considered a nominal water mass flow-rate of 0.250 kg/s constant.

The graphs in Figure IV-8.7 reports the thermal and cooling power supplied by the system: it's possible to observe that MCHP thermal recovery is practically unvaried related to the values obtained during the heating working mode, covering a range of about 7.5 kW to about 11,5 kW, while for the cooling purpose the power is about 7 kW.

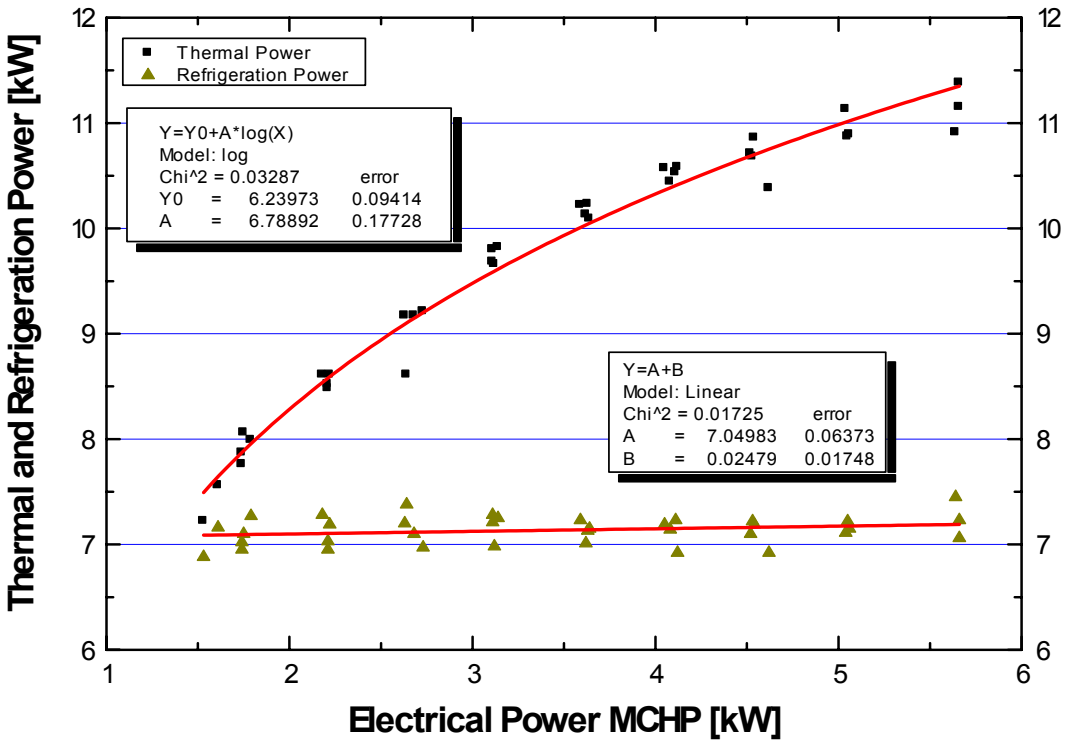

Figure IV-8.7 : Thermal and cooling power trend to the variation of electric power (thermal circuit mass flow-rate 0.108 kg/s , cooling circuit mass flow-rate 0.250 kg/s)

References

M. Sasso, S. Sibilio, L. Vanoli, “Energetic and environmental analysis of a domestic scale heat pump driver by a microcogenerator”, Applied Thermal Engineering 23 (2003) 1247–1259.

R. Possidente, C. Roselli, M. Sasso, S. Sibilio “Assessment of microcogeneration potential for domestic trigeneration”, Int. J. Environmental Technology and Management, Vol. 7, Nos. ½, 2007, pp. 147-164

IV-9 Investigation of a PEMFC (System A) Device at the National Institute of Standards and Technology[1]

A constant power PEMFC device was purchased from a major manufacturer and tested in the NIST facility described in section III-5 of this report. The manufacturer is not identified in this report for confidentiality reasons but rather the device is labelled "System A". A list of the parameters measured during the experiments is provided in Table III-5.2. These data are available upon request.

The PEMFC device

The fuel cell system included a natural gas reformer and an AC inverter for the electrical output. It produced up to 5 kW of AC electrical power and more than 9 kW of thermal power. The system operated at a user-selected electrical output level. Thermal energy was available to customers from on-board heat exchangers, and available thermal energy beyond that which was transferred via these heat exchangers was dissipated to the environment using an automotive-style radiator.

Systematic testing was performed to determine the parameters that affect the electrical and/or thermal performance of the fuel cell system. The influence of the following parameters was evaluated based on steady-state testing (refer to Davis et al. 2005 for further details):

- Electrical power output (expressed as the fraction of the maximum output, i.e. load fraction)
- Ambient temperature
- Ambient relative humidity
- Temperature of fluid entering the fuel cell system for thermal load extraction
- Flow rate of fluid entering the fuel cell system for thermal load extraction

[1] Authored by Mark Davis (National Institute of Standards and Technology)

All steady-state testing was performed according to ASME Performance Test Code 50 (ASME 2002) for fuel cell power systems, which describes the best practices for recording the efficiency of a fuel cell system.

Testing the fuel cell system proved difficult due to the larger than anticipated day-to-day performance degradation. A "bracketing" test sequence was thus employed to avoid confusing the impact of the parametric studies versus the time-dependent degradation. For steady-state testing, one test bracket was set up for each parameter. For instance, to determine the change in performance as a function of the ambient temperature, the fuel cell system performance was first measured at an ambient temperature of 35°C. Holding all other parameters constant, the ambient temperature was then changed to 5°C and the fuel cell's steady-state performance was measured again. Finally, the ambient temperature was returned to 35°C for the last steady-state measurement. The bracket was not considered valid unless the performance measurements for the first and last tests were within the bounds of their respective uncertainties. For each valid bracket, a relative performance index was calculated that shows how the electrical or thermal efficiency, which is reported throughout this section on a higher heating value basis, changed. In tables that include the relative performance index, **bolded** entries indicate a statistically significant change in efficiency.

$$Index = \frac{(\eta_2)}{\frac{(\eta_1 + \eta_3)}{2}}$$

Where η_1, η_2, and η_3 represent efficiency values from the first, second, and third test in the bracket

Test results

Extensive testing of the fuel cell system showed that while the thermal efficiency responded to ambient temperature, electrical load fraction, fluid inlet temperature, and

fluid flow rate, the electrical efficiency was affected by only the electrical load fraction (i.e. the electrical power output) and the life of the system.

Electrical Load Fraction

The electrical performance of the fuel cell system was measured at three power output levels (2.5 kW, 4.0 kW, and 5.0 kW) in both the grid-interconnected and grid-independent modes of operation. A four-test bracket was set up for both modes of operation, and the results are shown in Tables IV-9.1 and IV-9.2. The relative indices for the 50 % and 80 % load fractions were both calculated with respect to the average of the two bracketing 100 % load fraction tests. A value of 1.04, for example, demonstrates that the electrical efficiency is 4 % greater than the 100 % load fraction efficiency.

Table IV-9.1 : Grid-Interconnected electrical efficiency (HHV) four-test bracket

Load Fraction (%)	Electrical Efficiency (%)	Uncertainty (%, k=2)	Index
100	19.4	0.16	
50	20.0	0.17	**1.04**
80	19.8	0.20	**1.03**
100	19.1	0.18	

Table IV-9.2 : Grid-Independent electrical efficiency (HHV) four-test bracket

Load Fraction (%)	Electrical Efficiency (%)	Uncertainty (%, k=2)	Index
100	18.7	0.17	
50	18.8	0.15	1.01
80	19.5	0.15	**1.04**
100	18.7	0.14	

In the grid-interconnected mode of operation, which is the predominant mode, the electrical performance at both 50 % and 80 % load fractions were found to be statistically different than at the 100 % load fraction. However, there was no statistically significant difference between the 50 % and 80 % load fractions.

The electrical efficiency at each load fraction in the grid-independent mode of operation was less than the grid-interconnected mode (compare Tables IV-9.1 and IV-9.2). Additionally, in the grid-independent mode there was no significant difference between the 50 % and 100 % load fraction tests, but the 80 % load fraction was still found to perform better than the 100 % load fraction. The difference in performance between the two modes of operation at the same load fraction cannot be readily explained, but it was found to be repeatable.

Steady-State Thermal Load

An extensive test plan was derived to determine the effects of the thermal load upon the electrical and thermal efficiency of the fuel cell system. Three-test brackets were used. For a given bracket, either the fluid flow rate or fluid inlet temperature was varied between two levels. These brackets were assembled into sets of ten tests that incorporated each possible parameter change. The set of ten tests was performed at two different electrical load fractions and four ambient temperature/relative humidity combinations for a total of 80 tests.

The resulting electrical and thermal efficiencies are shown in Table IV-9.3a and IV-9.3b, respectively. The first three columns in the tables indicate the bracket ID and fluid flow rate/temperature combination of the fluid used to extract the thermal load from the fuel cell. The tests were performed chronologically from top to bottom. The remaining columns are organized first by ambient temperature, then by relative humidity, and finally by electrical load fraction, LF. In both tables, the efficiency and relative performance index are reported for each case. The shaded tests comprise the second test in a three-test bracket, and the surrounding unshaded tests are the first or third tests for the respective bracket. The third tests in brackets I and III are shared with the first tests of brackets II and IV, respectively. Because of the high variability in the unit's performance, only tests within a three-test bracket can be compared, and these comparisons are expressed as relative performance indices.

Table IV-9.3a : Electrical efficiency (HHV) and relative performance index for each steady-state thermal load bracket

ID	Fluid Flow Rate (L/min)	Fluid Inlet Temp (°C)	Ambient Temperature = 35 °C								Ambient Temperature = 11.5 °C							
			Relative Humidity = 40 %				Relative Humidity = 75 %				Relative Humidity = 55 %				Relative Humidity = 25 %			
			LF = 100 %		LF = 50 %		LF = 100 %		LF = 50 %		LF = 100 %		LF = 50 %		LF = 100 %		LF = 50 %	
			η_e	Index	η_e	Index	η_e	Index	η_e	Index	η_e	Index	η_e	Index	η_e	Index	η_e	Index
I	35	55	18.0		20.1		16.8		20.2		18.6		19.5		18.5		19.5	
	5	55	18.1	1.00	20.2	1.00	16.4	0.99	20.1	0.99	18.4	0.99	b		19.0	1.03	b	
II	35	55	18.3		20.2		16.4 19.5		20.4		18.4		19.4		18.4		18.3	
	35	18	18.4	0.99	20.3	1.00	19.2	a	20.4	1.00	18.1	0.99	19.2	0.99	18.7	1.01	18.3	1.01
	35	55	18.8		20.2		17.4		20.2		18.2		19.5		18.7		18.1	
III	5	18	18.7		20.2		18.5		20.7		17.5		19.4		18.4		19.5	
	35	18	18.9	1.00	20.1	1.00	18.6	1.00	20.6	1.00	17.2	0.99	19.6	1.01	18.7	1.01	19.7	a
IV	5	18	19.1		20.1		18.8		20.7		17.4		19.5		18.5		19.9	
	5	55	19.0	1.00	19.9	0.99	17.8	a	20.2	a	17.5	1.02	b		18.3	0.99	b	
	5	18	18.8		20.2		17.0		20.1		17.2		19.8		18.5		19.6	

LF Electrical load fraction

a Invalid bracket

b System would not output steady current due to internal control issues. Data not valid

Table IV-9.3b : Thermal efficiency (HHV) and relative performance index for each steady-state thermal load bracket

Bracket ID	Fluid Flow Rate (L/min)	Fluid Inlet Temp (°C)	Ambient Temperature = 35 °C								Ambient Temperature = 11.5 °C							
			Relative Humidity = 40 %				Relative Humidity = 75 %				Relative Humidity = 55 %				Relative Humidity = 25 %			
			LF = 100 %		LF = 50 %		LF = 100 %		LF = 50 %		LF = 100 %		LF = 50 %		LF = 100 %		LF = 50 %	
			η_{th}	Index	η_{th}	Index	η_{th}	Index	η_{th}	Index	η_{th}	Index	η_{th}	Index	η_{th}	Index	η_{th}	Index
I	35	55	39.2		37.2		36.8		35.9		36.6		28.9		36.8		29.6	
	5	55	10.9	**0.28**	21.5	**0.58**	10.0	**0.28**	21.2	**0.59**	11.5	**0.31**	b		11.6	**0.31**	b	
II	35	55	39.6		37.3		36.0 39.9		36.4		36.4		28.8		37.1		23.5	
	35	18	42.9	**1.08**	42.6	**1.15**	45.9	a	43.7	**1.21**	42.3	**1.16**	34.5	**1.22**	41.2	**1.11**	34.6	**1.48**
	35	55	39.7		36.8		37.8		36.0		36.7		27.8		37.1		23.4	
III	5	18	44.5		44.0		45.9		46.1		43.7		35.5		41.4		36.8	
	35	18	43.6	0.98	42.5	0.96	47.9	1.04	44.3	0.97	44.2	1.03	34.0	0.95	40.6	0.98	35.7	a
IV	5	18	44.8		44.5		46.5		45.6		42.4		35.7		41.6		37.6	
	5	55	11.5	**0.26**	21.4	**0.48**	10.8	a	22.1	a	10.9	**0.25**	b		11.2	**0.27**	b	
	5	18	44.8		45.3		45.6		45.5		44.2		37.3		41.8		38.0	

LF Electrical load fraction

a Invalid bracket

b System would not output steady current due to internal control issues. Data not valid

The relative performance indices are reported for the electrical and thermal efficiency of each of the valid brackets, which are brackets where the efficiency at the first and third test differs by less than the combined measurement uncertainty for both the electrical and thermal efficiency. For example, at an ambient temperature of 35 °C, a relative humidity of 75 %, and an electrical load fraction of 100 %, the electrical efficiencies of the first

and third tests in bracket II differ by more than 2 %, which is greater than the sum of the uncertainties for the electrical efficiency (see Table II-5.2). This three-test bracket is ruled invalid. Bolded indices in the tables indicate parameter changes that resulted in statistically significant changes in performance. An index close to unity for either the electrical or thermal efficiency indicates that the parameter change did not affect the performance.

According to the relative index for electrical efficiency in Table IV-9.3a, changing the thermal load does not affect the electrical performance of the fuel cell system. The thermal efficiency was, understandably, affected by changes in the thermal load, as shown in Table IV-9.3b. Bracket III, which increased the flow rate at a fluid temperature of 18 °C, did not result in a statistically significant performance change. Brackets I, II, and IV did affect the thermal efficiency of the system. Large differences in thermal efficiency were observed in each of the brackets that included the 55 °C – 5 L/min test (brackets I and IV). This combination of a low flow rate and an inlet temperature near the maximum outlet temperature of the fuel cell system (≈ 63°C) prevented the full amount of thermal energy available from the fuel cell system being transferred to the fluid stream. In this case, an integral radiator on the fuel cell system dissipated the remaining thermal energy to the environment. Smaller differences are seen in bracket II, which changed the inlet temperature at the 35 L/min flow rate. These results are consistent over the 8 sets of ambient conditions and electrical load fractions.

Ambient Condition Investigation

Test brackets were set up to determine the effect of ambient temperature and relative humidity on the electrical and thermal efficiency of the fuel cell system. The ambient temperature and relative humidity were varied separately, and each parameter was varied at the 50 % and 100 % electrical load fraction. All tests were performed while extracting thermal energy from the system with the fluid flow rate and inlet temperature constant at 35 L/min and 55 °C, respectively. The test sequence and results are shown in Table IV-9.4.

Table IV-9.4 : Electrical and Thermal Efficiency (HHV) Varying Ambient Environmental Conditions

Load Fraction (%)	Ambient Temperature (°C)	Ambient RH (%)	Electrical Performance		Thermal Performance	
			Efficiency (%)	Relative Index	Efficiency (%)	Relative Index
50	35	40	**18.1**	1.01	**37.0**	1.02
50	35	75	**18.3**		**37.4**	
50	35	40	**18.0**		**36.5**	
50	35	40	**17.8**	1.01	**37.1**	**0.70**
50	5	40	**18.2**		**26.0**	
50	35	40	**18.2**		**37.0**	
100	35	40	**18.3**	1.01	**36.6**	0.99
100	35	75	**18.8**		**36.6**	
100	35	40	**18.9**		**37.0**	
100	35	40	**18.6**	1.02	**36.7**	**0.82**
100	5	40	**18.8**		**29.9**	
100	35	40	**18.4**		**36.2**	

Neither the ambient temperature nor the relative humidity affected the electrical efficiency, but a drop in the ambient temperature from 35 °C to 5 °C did significantly reduce the thermal efficiency. Presumably, this loss in thermal output resulted from the system redirecting thermal energy internally to maintain the proper system temperature. While no change in performance was observed at various relative humidity levels, 75 % is the highest relative humidity attainable in the environmental chamber. Humidity levels closer to saturation may have affected the systems performance.

Thermal Load Extraction Investigation

Test brackets were devised to explicitly determine if the electrical efficiency depended upon whether or not thermal energy was extracted from the system. Brackets for a 50 %, 80 %, and 100 % load fraction were performed at ambient conditions of 11.5 °C and 55 % RH. During tests with thermal extraction, the fluid flow rate and inlet temperature were held constant at 35 L/min and 55 °C, respectively. Table IV-9.5 shows that the electrical performance proved not to be influenced by the presence of a thermal load on the system.

Table IV-9.5 : Electrical Efficiency (HHV) With and Without a Thermal Load

		Efficiency		
Load Fraction	**Thermal Load?**	**Electrical (%)**	**Thermal (%)**	**Overall (%)**
50	Yes	19.8	19.4	39.2
	No	19.7	0.0	19.7
	Yes	19.8	19.3	39.2
80	Yes	20.0	28.1	48.1
	No	20.0	0.0	20.0
	Yes	20.0	28.2	48.2
100	Yes	18.9	32.1	51.0
	No	19.0	0.0	19.0
	Yes	19.0	32.1	51.0

Transient Electrical Load

The transient electrical performance of the fuel cell system was measured in the grid-interconnected and grid-independent mode. No thermal energy was extracted from the system during these tests. The electrical performance was monitored every 5 s, as opposed to a 30 s interval for steady-state tests. In the grid-interconnected mode, the fuel cell system was shifted between power levels in the 6 possible permutations:

- 50 % to 80 %
- 50 % to 100 %
- 80 % to 100 %
- 80 % to 50 %
- 100 % to 80 %
- 100 % to 50 %

In the grid-interconnected mode, the fuel cell system slowly ramps up the power output, as well as the fuel consumption, until the power reaches the setpoint. The system took between 7 min and 18 min to reach steady-state after a shift. Comparing the respective entries from the third and fourth columns of Table IV-9.6, a trend emerges where transitioning to a higher load fraction results in a small dip in electrical efficiency during the transient period whereas the opposite occurs when transitioning to a lower load

Table IV-9.6 : Electrical Efficiency (HHV) During Shifts in Electrical Load Fraction

Steady Electrical Load Fraction	Transition	Grid-Interconnected			Grid-Independent		
		Electrical Efficiency (%)		Duration (min)	Electrical Efficiency (%)		Duration (min)
50		19.4			19.2		
	50 to 100		18.4	18		20.1	18
100		18.7			18.9		
	100 to 80		19.5	9		18.8	6
80		19.6			19.8		
	80 to 50		19.8	8		17.9	6
50		19.8			19.3		
	50 to 80		19.2	7		20.7	9
80		19.8			19.7		
	80 to 100		18.7	9		18.9	10
100		19.2			18.8		
	100 to 50		20.1	18		16.2	7
50		20.2			19.2		

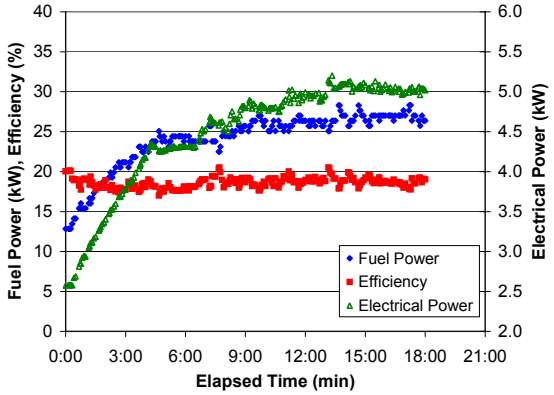

Figure IV-9.1 Performance during a 50 % to 100 % shift in grid-interconnected mode

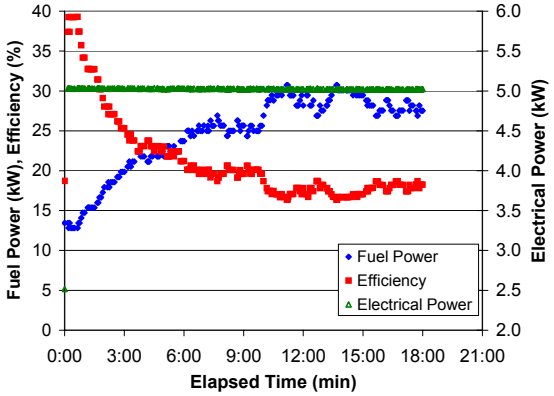

Figure IV-9.2 Performance during a 50 % to 100 % shift in grid-independent mode

fraction. Figures IV-9.1 and 2 show typical traces for the electrical power output, fuel energy consumption, and electrical efficiency during a shift in load fraction.

The same shifts in power were performed in the grid-independent mode. In this mode, the system uses its batteries to immediately meet the power demand and slowly ramps the fuel consumption to meet the need. The time interval required for the fuel consumption to reach steady-state conditions after the electrical load shift, Table IV-9.6, was approximately the same for both the grid-interconnected and grid-independent modes, except for the comparatively faster response time when transitioning from 100 % to 50 % load fractions. Finally, the trend as to the electrical efficiency during the steady-state periods versus the transitioning period, Table IV-9.6 (6th and 7th columns) was opposite

to the trend observed for the grid-interconnected mode. The change in stored energy within the batteries is not taken into account in these calculations.

Quasi-Steady Fluid Inlet Temperature

The thermal performance of the fuel cell system was monitored while the thermal fluid inlet temperature was slowly increased, i.e. "quasi-steady". The fluid temperature increased slowly enough to assume a relatively steady temperature, but the rise in fluid temperature provided a detailed picture of the system's performance as a function of temperature. The fuel cell system was used to heat approximately 1000 L of fluid until the fluid temperature no longer increased. This test was performed at the 50 %, 80 %, and 100 % load fractions at three different fluid flow rates (5 L/min, 20 L/min, and 35 L/min). Figure IV-9.3 shows the results of all these tests. All of the 80 % and 100 % load fraction tests show a dramatic knee in the curve, which results when the fluid outlet temperature reaches its maximum value (~63 °C). At each load fraction, the respective curves for the 20 L/min and 35 L/min tests are nearly identical, and the curves at the 5 L/min tests bend downward earlier than the other tests at the same load fraction.

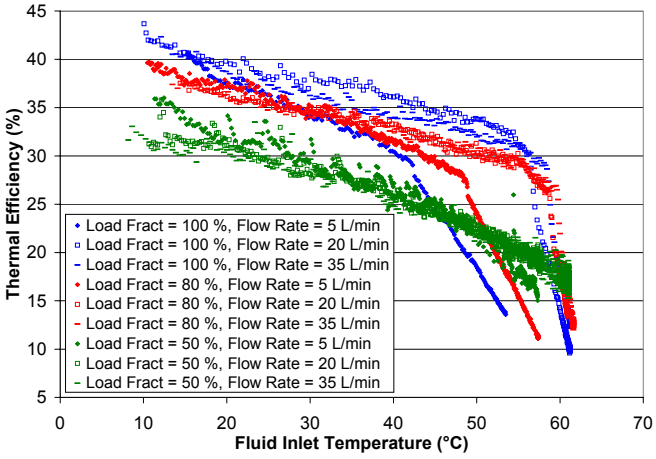

Figure IV-9.3 Quasi-Steady Fluid Inlet Temperature Test

Residential Space and Domestic Hot Water Heating Loads

The fuel cell system was used to heat a thermal storage tank through an internal heat exchanger, as discussed in section III.5. The thermal storage tank was used to supply hot water for a domestic water heater and, separately, thermal energy for space heating loads. The tests simulating domestic hot water usage were performed according to the DOE test procedure for water heaters [3]. The space heating loads are representative of the maximum heating day from a typical single-family home in Atlanta, GA, which was modeled using the building energy simulation program, DOE2 [4].

The test simulating the domestic hot water load showed that this particular fuel cell system's ability to supply thermal energy far exceeds the thermal energy requirements for a typical residential hot water load. The overall efficiencies were approximately 32 % for the 50 % electrical load fraction and only 24 % for the 100 % load fraction, Table IV-9.7. In a field test of a residential fuel cell providing electricity and domestic hot water, Boettner [5] measured an overall efficiency of 29.7 % (LHV).

At an overall efficiency of 43 %, the fuel cell was much more efficient supplying the space heating loads. The heat exchanger in the thermal storage tank did limit the fuel cell system from meeting larger space heating loads. The results from the space heating load test will be used to evaluate the model developed as part of the rating methodology

Table IV-9.7. Real-World Thermal Load Test Efficiencies (Avg of Three 24 h Tests)

	Domestic Hot Water Load		**Space Heating Load**
Efficiency (HHV)	**Load Fraction**		
	50 %	**100 %**	**100 %**
Electrical	18.1	17.2	19.5
Thermal	13.7	6.6	23.6
Overall	31.8	23.8	43.2

Performance Degradation

The electrical and thermal efficiency of the unit changed with cumulative hours of operation. The degradation was significant enough to warrant two stack changes, which were diagnosed by the manufacturer, over the warranty period of the unit. Upon installing the third stack, the manufacturer replaced a reformer catalyst, and the degradation rate was significantly reduced. Figure IV-9.4 shows the electrical efficiency of the unit as a function of the cumulative runtime. Incorporating the performance degradation in the rating methodology will be important until manufacturers extend the lifetime of such units.

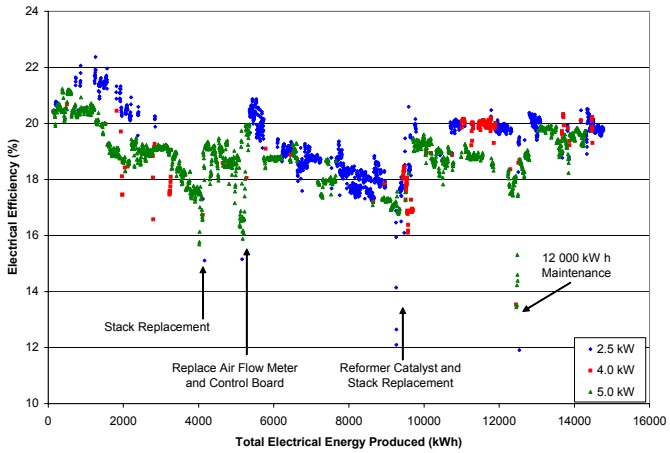

Figure IV-9.4. Electrical Efficiency (HHV) Degradation

References

Davis, M.W., et al, "Parameters Affecting the Performance of a Residential-Scale Fuel Cell System." Proceedings of the 3rd Intl. Conference on Fuel Cell Science, Engineering, and Technology, Ypsilanti, MI, May 23-25, 2005.

ASME PTC 50-2002, "Fuel Cell Power Systems Performance," American Society of Mechanical Engineers, New York, 2002.

U.S. Department of Energy-Office of Energy Efficiency and Renewable Energy, "Energy Conservation Program for Consumer Products: Uniform Test Method for Measuring the Energy Consumption of Water Heaters," 10 CFR Part 430. Appendix E to Subpart B of Part 430, 1998

Gunes, B., Ellis, M., 2003, "Evaluation of Energy, Environmental, and Economic Characteristics of Fuel Cell Combined Heat and Power Systems for Residential Applications," Transactions of the ASME, **125**, pp 208-220.

Boettner, D., Massie, C., and Massie, D., 2004, "Lessons Learned from Residential Experience with Proton Exchange Membrane Fuel Cell Systems for Combined Heat and Power," Proceedings of the ASME Fuel Cell Science, Engineering, and Technology Conference, pp 267-272.

IV-10 Investigation of a PEMFC (System B) Device at the National Institute of Standards and Technology[1]

A thermal load following PEMFC device was purchased from a major manufacturer and tested in the NIST facility described in section III-5 of this report. The manufacturer is not identified in this report for confidentiality reasons but rather the device is labelled "System B". A list of the parameters measured during the experiments is provided in Table III-5.2. These data are available upon request.

The PEMFC device

The proton exchange membrane (PEM) fuel cell unit reforms natural gas to generate a maximum electrical output of 4.6 kW and approximately 8 kW of thermal power. The fuel cell is designed to be installed indoors and is intended to provide domestic hot water and space heating to a residence while supplying electrical power to the utility grid. A typical application would use the fuel cell to heat a thermal storage tank, and water would be drawn from the storage tank for domestic hot water or space heating loads. During periods with little or no thermal loads, the temperature of the storage tank increases, and the fuel cell system scales back its electrical and thermal output. Prolonged intervals of high tank temperatures cause the fuel cell system to enter an “idle” mode of operation until the fluid temperature drops again. The maximum output of the system could also be limited using a graphical interface by adjusting the percentage of maximum fuel input between 0 % and 100 %.

Three types of tests were performed on the fuel cell system. First, steady state tests characterized the thermal and electrical performance of the system under various ambient temperatures, fluid flow rates and temperatures, and electrical outputs. These tests were performed with the system decoupled from the thermal storage tank. A second set of steady state tests were performed with the system coupled to the thermal storage tank.

[1] Authored by Mark Davis (National Institute of Standards and Technology)

Water was withdrawn from the thermal storage tank at a steady rate, which imparted a steady thermal load on the fuel cell system. Finally, the fuel cell system was subjected to simulated domestic hot water and space heating loads.

Decoupled Steady State Tests

The fuel cell system was operated at a steady electrical output by controlling the fuel flow rate setpoint of the system. The ambient temperature, fluid flow rate, and fluid temperature were maintained at the values listed in Table IV-10.1. For each set of conditions listed in the table, individual tests were performed at prescribed electrical output levels. The fuel flow setpoint was adjusted to achieve an electrical load fraction of 100%, 75%, 50%, 25%, and an additional test at 100%. The second test at 100% ensured that the system did not experience any measurable changes in performance of the set of 5 tests. Representative data is shown in Figure IV-10.1 for a flow rate of 20 LPM.

Table IV-10.1 : Conditions for Steady State Tests with Fuel Cell Decoupled from Thermal Storage

Test ID	Ambient Temperature (°C)	Fluid Temperature (°C)	Fluid Flow Rate (LPM)
Steady-1	12	20	10
Steady-2	12	20	20
Steady-3	12	48	10
Steady-4	12	48	20
Steady-5	22	20	10
Steady-6	22	20	20
Steady-7	22	48	10
Steady-8	22	48	20
Steady-9	35	20	10
Steady-10	35	20	20
Steady-11	35	48	10
Steady-12	35	48	20
Steady-13	35	44	10
Steady-14	22	44	10
Steady-15	12	44	10

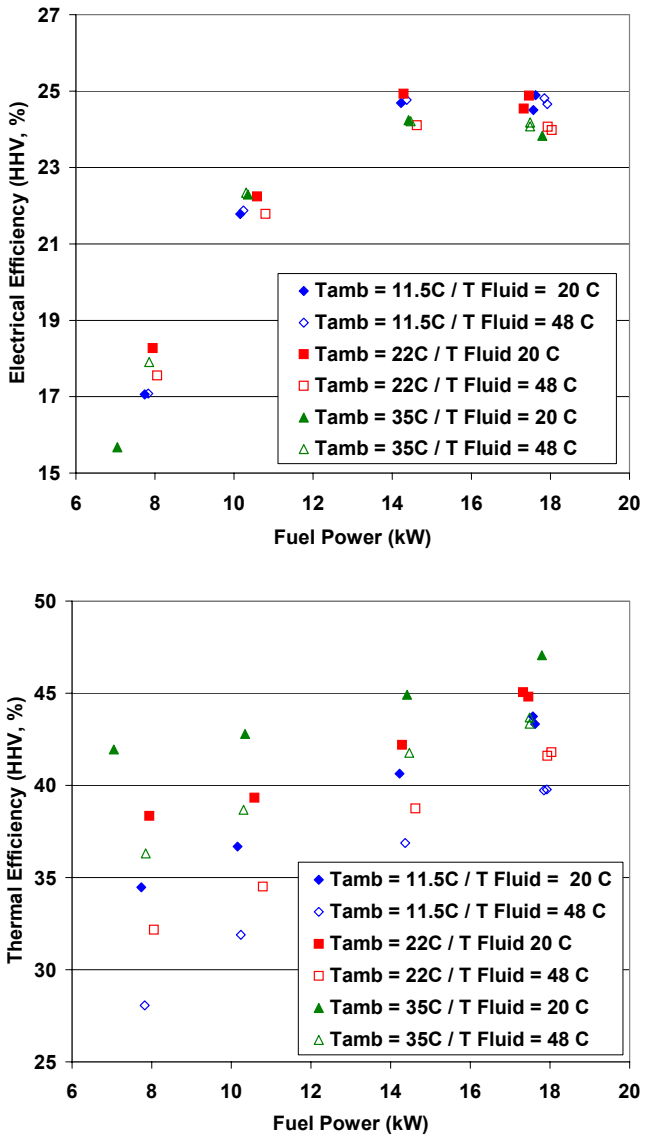

Figure IV-10.1 : Electrical and Thermal Efficiency (HHV) vs. Fuel Power at a Fluid Flow Rate of 20 LPM

Steady State Thermal Load Tests

In contrast to the steady state tests described above, these tests imparted a steady thermal load to the fuel cell, representing a more realistic condition for the fuel cell system. The cogeneration fluid was circulated between the fuel cell system and the integral heat exchanger in the thermal storage tank, and water was removed from the thermal storage tank at a constant flow rate. The fuel cell, which adjusts it output level to maintain an

incoming fluid temperature, modulated its output such that the outgoing fluid temperature was sufficient with respect to the thermal load placed on the storage tank and the various thermal losses to maintain the returning fluid temperature at a steady value In this arrangement, the thermal energy transferred to the fluid by the fuel cell equalled the sum of the thermal energy removed from the thermal storage tank and any losses between the fuel cell and tank. The maximum flow rate for water removal from the tank was determined to be the rate at which the fuel cell system's electrical output was its maximum rated value. All tests were performed at an ambient temperature of 21 °C and a cogeneration fluid flow rate of 20 LPM. The temperature of the fluid returning to the fuel cell system, which was nominally 52 °C, was dictated by the system's control strategy. The electrical output was indirectly controlled by the system as it is proportional to the thermal power output. Table IV-10.2 shows the steady state thermal load tests performed.

Table IV-10.2 : Steady State Thermal Load Tests

Test ID	Electrical Output (kW)	Thermal Output (kW)
THLF-Max	4.5	7.7
THLF -3.0	4.1	6.6
THLF-2.6	4.0	6.3
THLF-2.0	3.2	4.9
THLF-1.4	2.4	3.7
THLF-0.6	1.1	1.6

Simulated Domestic Hot Water and Space Heating Loads

With the fuel cell coupled to thermal storage tank, water was removed from the tank in a manner that represented several simulated residential thermal loads. Specifically, a domestic hot water load was simulated using the US Department of Energy's test method for residential water heaters (US DOE 1998). Space heating loads were calculated using the DOE-2 building simulation program for representative days in several US cities. Tests were performed for a maximum heating day in Atlanta, GA and a representative spring and winter day in Pittsburgh, PA. The space heating loads for the spring and

winter day in Pittsburgh were combined with the domestic hot water loads. The loads are initiated at the beginning of each hour, and each test lasts 24 hours. Table IV-10.3 lists the available tests.

All tests were performed at an ambient temperature of 21 °C and a cogeneration fluid flow rate of 24 LPM.

Table IV-10.3 : Simulated Domestic Hot Water and Space Heating Load Tests

Test ID	Description	Electrical Efficiency (HHV, %)	Thermal Efficiency (HHV, %)
DHW-120305	Domestic hot water load	12.5	22.7
SPC-072205	Space heating load for maximum heating day in Atlanta, GA	23.5	37.8
SPCDHW-WTR	Space and domestic hot water load for winter day in Pittsburgh, PA	25.0	39.2
SPCDHW-SPR	Space and domestic hot water load for spring day in Pittsburgh, PA	22.3	34.2

References

U.S. Department of Energy-Office of Energy Efficiency and Renewable Energy, "Energy Conservation Program for Consumer Products: Uniform Test Method for Measuring the Energy Consumption of Water Heaters," 10 CFR Part 430. Appendix E to Subpart B of Part 430, 1998

IV-11 : Investigation of a Vaillant Fuel Cell Euro 2 at the Technical University of Munich[12]

Technical data and experimental set-up

The tested fuel cell is a prototype (stage of development Euro 2) and manufactured by Vaillant. Prior to testing at the Technical University of Munich, the unit had been tested in a building in the Netherlands over a period from January 2004 to March 2005. For the present study it was operated for about 4000 hours almost without any failure (one incident was reported, which was caused by a leak in the humidification system). The technical data is listed in Table IV-11.1.

Table IV-11.1 :Technical manufacturer data of the Vaillant fuel cell Euro 2

Name	Unit	
Fuel	-	natural gas
Electrical power	kW	1.5 – 4.6
Thermal power	kW	3.0 – 9.1

Figure IV-11.1 gives a schematic drawing of the hydraulic integration and the balance boundary which are needed for balancing.

[1] Edited by Ulli Arndt (Research Institute for Energy Economy, FfE, Munich, Germany)
[2] Deduced appraisements based upon the information presented in this subsection are only allowed to be published with the approval of Vaillant/ecopower. An isolated contemplation of the illustrated results could lead to wrong conclusions.

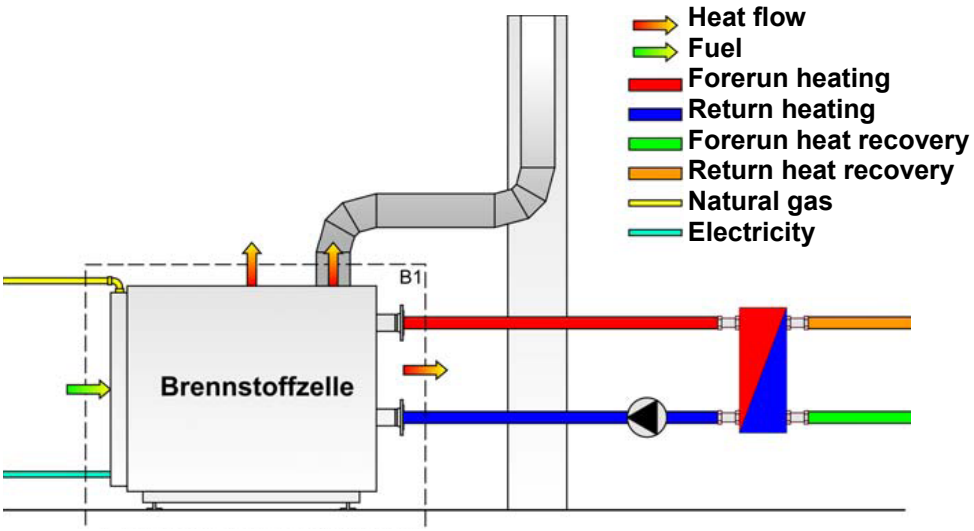

Figure IV-11.1 : Experimental set-up and energy flux of the fuel cell

For the monitoring of the amount of fuel supplied, the dissipated heat flow and the feed-back of electrical energy, the following principles and devices of measurement were used:

Gas input:

The amount of gas used was metered by an experimental gas meter. In addition, air- and gas pressure and the gas temperature were measured simultaneously in order to correct the fuel value relative to standard conditions. The characteristics of the natural gas supplied in Munich are available.

Electrical energy output:

The feed-back of electrical power was monitored by an active energy meter measured as the instantaneous power. With balance times of 15 or 30 minutes this ensures very accurate measurements after a steady state has been reached.

Heat energy output:

The uncoupled thermal energy was metered by a hot water meter with the pulse output and the temperature difference between flow and return. Metering points for the

temperature of the flow and return were calibrated and separate calibration curves were recorded. The maximal error amounts to 0.1 K and results in a measuring error of less than 1.5% when operated under partial load. The heat sink of the uncoupled thermal energy is formed by a counter flow heat exchanger with cold water supply. Depending on the cold water throughput, different flow temperatures are possible, which allows benchmarking of this factor in relation to the electrical and total efficiency factor.

Monitoring of the feed-back of electrical energy:

The feedback of electrical energy was monitored by an active energy meter with pulse output.

Measurements

To assess the energetic behaviour of the fuel cell, the following experiments were carried out, which are described and documented in the following:

- Operation at a steady state with different temperatures of the heating circuit flow
- Warm and cold start
- Operation with load alternation
- Influence of the flow temperature

Steady state experiments

The fuel cell was operated with six different power levels with a range of at least 1.5 kW (electrical) and not more than 4.5 kW (electrical). The flow temperature, as a parametric factor, was changed from 40 °C to 60 °C. The balance times amounted to at least five hours and not more than 20 hours. The results are summarised in Table IV-11.2. Fuel consumption, used pairs of flow and return temperature, monitored thermal and electrical energy input into the grid as well as interesting factors for thermal, electrical and total efficiency factors are shown. All efficiencies are relative to the fuel's LHV.

Table IV-11.2 : Balance results of steady state experiments

Name	Unit	1.5 kW electrical			2.5 kW electrical		
Balance period	h	16.0	16.0	18.0	16.0	12.0	10.0
Forerun temperature	°C	59.8	50.8	39.6	60.1	50.7	39.9
Return temperature	°C	54.1	44.2	32.7	53.0	42.8	31.3
Q_{fuel}	kWh	136.2	136.1	150.3	171.2	128.4	108.9
P_{th}	kW	4.3	5.0	5.3	5.3	6.1	6.7
Q_{th}	kWh	68.1	79.4	96.0	85.3	72.7	66.5
P_{el}	kW	1.5	1.5	1.5	2.5	2.5	2.5
Q_{el}	kWh	24.4	24.4	26.9	40.6	30.5	25.5
η_{th}	**%**	**50.0**	**58.4**	**63.9**	**49.8**	**56.6**	**61.1**
η_{el}	**%**	**17.9**	**18.0**	**17.9**	**23.7**	**23.8**	**23.4**
η_{total}	**%**	**67.9**	**76.3**	**81.8**	**73.5**	**80.4**	**84.5**
Name	**Unit**	**3.0 kW electrical**			**3.5 kW electrical**		
Balance period	h	12.0	6.0	12.0	10.0	14.0	20.0
Forerun temperature	°C	59.7	50.7	40.3	60.1	51.3	40.3
Return temperature	°C	50.1	40.3	29.3	47.8	38.3	26.9
Q_{fuel}	kWh	159.0	79.4	159.1	156.4	218.3	312.3
P_{th}	kW	7.3	8.0	8.6	9.4	10.1	10.7
Q_{th}	kWh	87.3	48.1	103.4	94.1	140.9	213.9
P_{el}	kW	3.0	3.0	3.0	3.5	3.6	3.5
Q_{el}	kWh	36.5	18.2	36.0	35.4	49.8	70.9
η_{th}	**%**	**54.9**	**60.6**	**65.0**	**60.2**	**64.5**	**68.5**
η_{el}	**%**	**23.0**	**23.0**	**22.6**	**22.7**	**22.8**	**22.7**
η_{total}	**%**	**77.9**	**83.6**	**87.6**	**82.8**	**87.4**	**91.2**
Name	**Unit**	**4.0 kW electrical**			**4.5 kW electrical**		
Balance period	h	9.0	12.0	12.0	12.0	8.0	5.0
Forerun temperature	°C	60.6	49.4	39.9	60.5	51.0	39.9
Return temperature	°C	49.8	37.8	28.1	47.4	36.8	25.6
Q_{fuel}	kWh	133.7	178.2	177.4	207.6	140.8	87.6
P_{th}	kW	8.3	9.0	9.3	10.0	10.9	11.4
Q_{th}	kWh	74.5	107.6	112.0	120.4	87.5	57.0
P_{el}	kW	4.0	4.0	4.0	4.5	4.5	4.5
Q_{el}	kWh	36.1	47.8	48.1	54.0	35.8	22.6
η_{th}	**%**	**55.7**	**60.4**	**63.2**	**58.0**	**62.1**	**65.0**
η_{el}	**%**	**27.0**	**26.9**	**27.1**	**26.0**	**25.4**	**25.7**
η_{total}	**%**	**82.7**	**87.2**	**90.3**	**84.0**	**87.5**	**90.8**

Fundamental energy relations, the in-service behaviour, the dependence on the load level and on the temperature of the flow as well as the behaviour of the efficiency factor are shown in Figure IV-11.2.

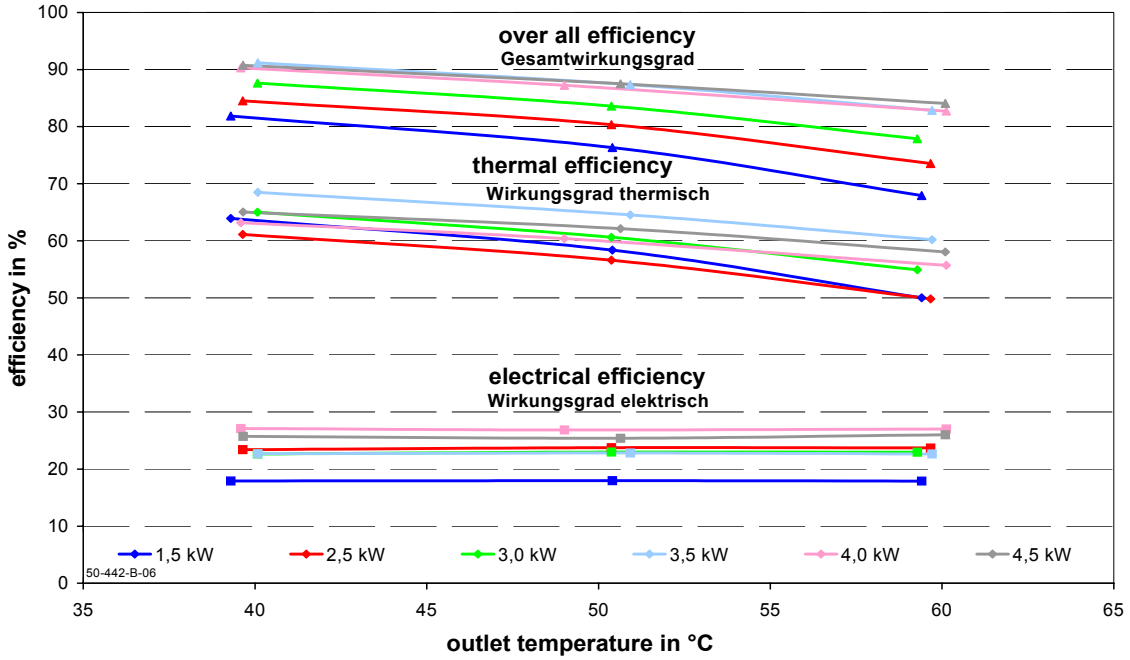

Figure IV-11.2 : Course of the efficiency factor in relation the flow temperature

The steady state behaviour of the fuel cell is summarised as follows:

- η_{el} rises with increasing electrical power independent of the flow temperature
- η_{th} declines with increasing flow temperature and rises parametrically with increasing electrical power output
- η_{total} shows a behaviour comparable to η_{th}: the total efficiency factor decreases with increasing flow temperature, but increases with increasing power.

Cold start experiment

The cold start experiment was initiated after a shutdown period of 23.8 hours. Heating flow and return temperature was set to a constant temperature of 20.7 °C and 21.6 °C. respectively (Figure IV-11.3).

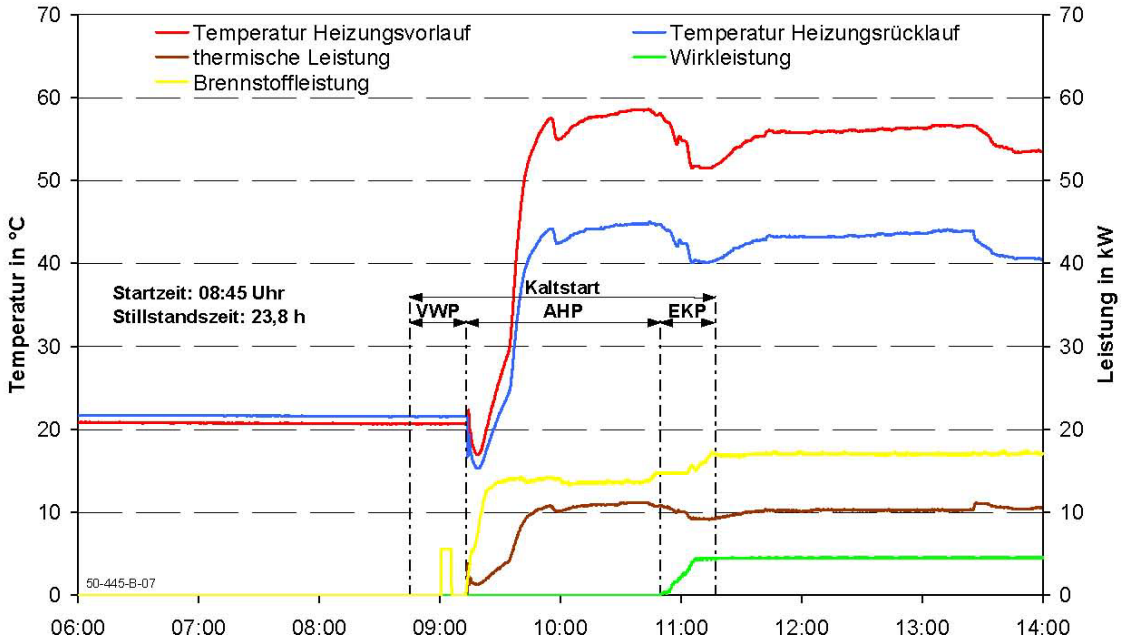

Figure IV-11.3 : Cold start experiment

The experiment was started at 08:45h. For a security check, the gas valve opened 16 minutes after the start at 09:01h for five minutes. The maximum fuel power input was about 6 kW (warm-up period). After a break of six minutes the gas valve reopened and the fuel power increased to 13.5 kW at 09:25h (heat-up phase with a thermal power of about 10 kW). At 10:50h the fuel power continued to increase and reached a steady state at 11:17 at 17.0 kW. The increasing fuel power caused a linear rise of electricity generation, reaching a level of 4.5 kW at 11:09h and remaining at a constant level afterwards. Simultaneously to the starting process, the temperature of flow and return increased to 58 °C and 56 °C. respectively (flow temperature) and 45 °C and 43 °C

(return temperature), respectively. A steady state operation occurs from 11:17h onwards. The cold start can be analysed as follows:

- Pre-heat phase (VWP)
- Heat-up phase (AHP)
- Start of electricity production (EKP)

The balance results of every phase are listed in Table IV-11.3.

Table IV-11.3 : Balance results of the cold start experiment

Name	Unit	
Pre-heat phase (VWP)		
time	-	08:45 – 09:13
period	hh:mm	00:28
fuel consumption	kWh	0.5
heat production	kWh	0.0
electricity production	kWh	0.0
Heat-up phase (AHP)		
time	-	09:13 – 10:50
period	hh:mm	01:37
fuel consumption	kWh	21.4
heat production	kWh	13.8
electricity production	kWh	0.0
Start of electricity production (EKP)		
time	-	10:50 – 11:17
period	hh:mm	00:27
fuel consumption	kWh	7.1
heat production	kWh	4.5
electricity production	kWh	1.4
Entire cold start		
time	-	08:45 – 11:17
period	hh:mm	02:32
fuel consumption	kWh	29.0
heat production	kWh	18.3
electricity production	kWh	1.4

Warm start experiment

During a warm start experiment, the fuel cell is shut down after several hours of steady state operation at rated load.

According to Figure IV-11.4, the shut-down was at 09:06h, subsequently fuel power, thermal and electrical power dropped down to nought within a few minutes. Since the heat sink was continuously operated, the flow and return temperature also decreased exponentially. At 09:10h, four minutes after the shut down was commanded, the fuel cell was restarted. After about 1.5 hours and at a temperature level of around 27 °C, the fuel started operating again. Similar to the cold start, the gas valve was opened for a short time period at 10:37h, subsequently the fuel power was assessed. The thermal power increased to about 10 kW. At 11:02h, the electricity generation was activated. The steady state maximum load of 4.5 kW was reached at 11:22h. Simultaneously, flow and return temperature increased due to heat production.

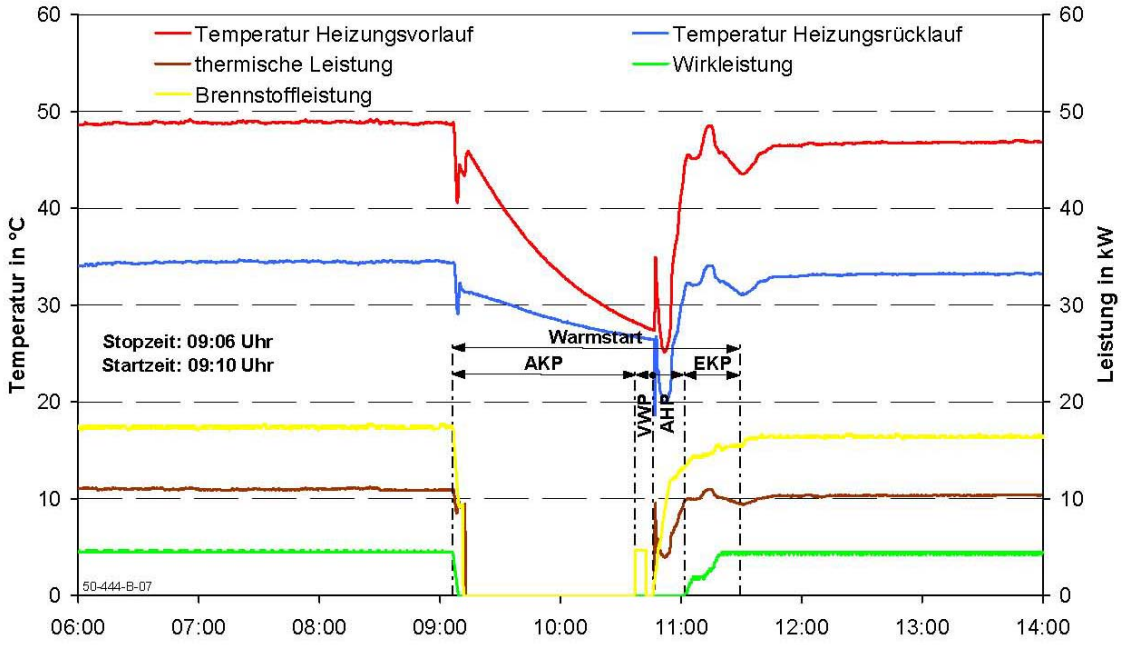

Figure IV-11.4 : Warm start experiment

The warm start can be defined as follows:

- Cool-down phase (AKP)
- Pre-heat phase (VWP)
- Heat-up phase
- Start of electricity production (EKP)

The balance results of the individual phases are listed in Table IV-11.4:

Table IV-11.4 : Balance results warm start experiment

Name	Unit	
Cool-down phase (AKP)		
time	-	09:06 – 10:37
period	hh:mm	01:31
fuel consumption	kWh	1.0
heat production	kWh	1.0
electricity production	kWh	0.1
Pre-heat phase (VWP)		
time	-	10:37 – 10:46
period	hh:mm	00:09
fuel consumption	kWh	0.4
heat production	kWh	0.0
electricity production	kWh	0.0
Heat-up phase (AHP)		
time	-	10:46 – 11:02
period	hh:mm	00:16
fuel consumption	kWh	2.8
heat production	kWh	1.6
electricity production	kWh	0.0
Start of electricity production (EKP)		
time	-	11:02 - 11:29
period	hh:mm	00:27
fuel consumption	kWh	6.8
heat production	kWh	4.7
electricity production	kWh	1.4
Entire warm start		
time	-	09:06 – 11:29
period	hh:mm	02:23
fuel consumption	kWh	11.0
heat production	kWh	7.3
electricity production	kWh	1.5

Alternation of load experiments

Figure IV-11.5 shows the operating performance of the fuel cell during alternation of load. Starting with a steady state operation and a thermal power of around 10 kW and an electrical power of 4.5 kW, an electrical load reduction of 1.5 kW occurs at 19:02h. Within three minutes the reduction of the electrical load is completed. the new load level of 6.5 kW is reached after 20 minutes for the thermal power.

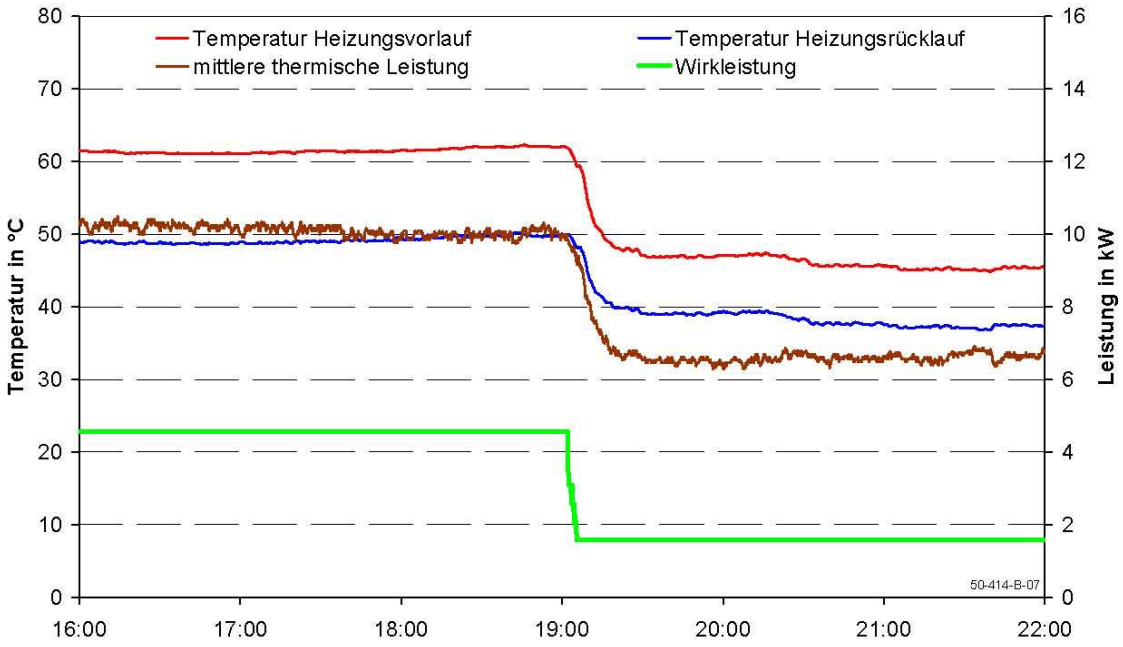

Figure IV-11.5 : Course of temperature and power during an electrical power drop from 4.5 kWel to 1.5 kWel

The fuel shows a very similar behaviour during a load step. The electrical load change from 1.5 kW to 4.5 kW is illustrated in Figure IV-11.6. At 15:20h the electrical power increases within three minutes to 4.5 kW and remains at a constant level afterwards. The thermal power reaches 9.5 kW after 10 minutes. A steady state operation is reached after 30 minutes.

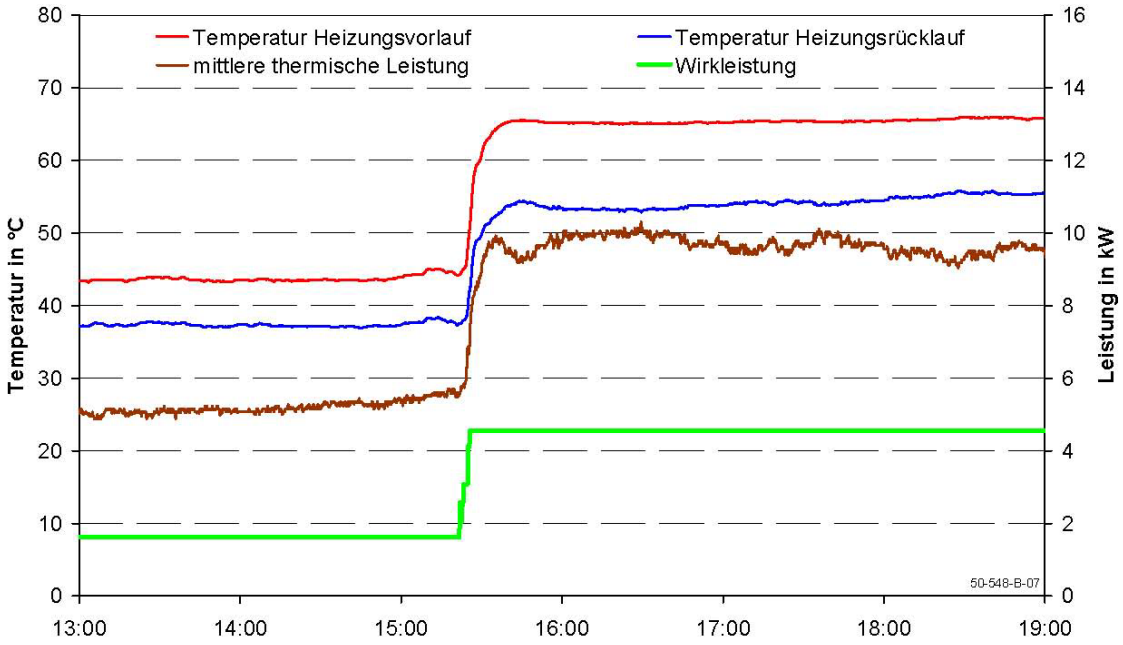

Figure IV-11.6 : Course of temperature and power at an electrical power switch from 1.5 kWel to 4.5 kWel

Influence of the flow temperature

Different flow temperatures cause alterations of the thermal power but do not affect the electrical power. According to Figure IV-11.7 the thermal power increases with declining flow temperature. Based on a flow temperature of 60 °C and thermal power of 10 kW, the thermal power increases to 11.5 kW as long as the flow temperature is reduced to 40 °C. The electrical power remains constant at 4.5 kW throughout the experiment. The small load deviations at 05:50, 22:10 and 07:00h can be explained by internal checks of the fuel cell. which are scheduled to be carried out after 16.5 hours of operation.

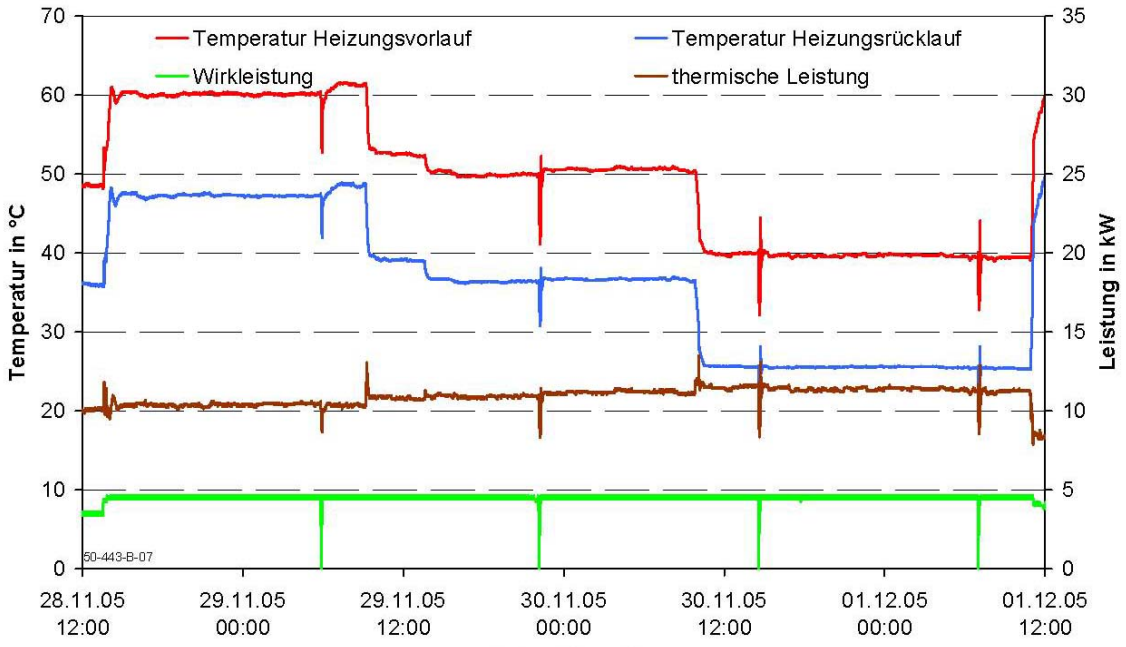

Figure IV-11.7 : Course of temperature and power at different flow temperatures

References

Mühlbacher, H.; Geiger, B.: Innovative CHP-systems for the energy supply of residential buildings - Final report Phase II, Institute for Energy Economy and Application Technology, Technical University of Munich, May 2007

IV-12 : Investigation of a FCT SOFC Device at the Canadian Centre for Housing Technology[1]

SOFC Fuel Cell Field Experiment

A joint project was undertaken by Natural Resources Canada, the Canadian Centre for Housing Technology, and Fuel Cell Technologies Inc. (FCT), a Canadian developer of small solid oxide fuel cells (SOFC) intended for the residential and small commercial market. Development of the FCT product had reached a stage where an installation and test/demonstration in an actual house, such as the highly monitored research house at the Canadian Centre for Housing Technology was possible.

The FCT CHP fuel cell was installed at CCHT in order to:

1. Demonstrate the installation of the First Residential Fuel Cell CHP system in a house in Canada.

2. Demonstrate the performance of the fuel cell CHP system in the residence during different seasons.

3. Examine CHP/residential building integration issues such as HVAC interface, control strategies, grid connection, ability to deal with peak and partial thermal and electrical loads, need for/benefit of thermal storage, amount of electrical export, optimal fuel cell CHP size, etc.

Fuel Cell System Description

FCT's 5kWe nominal fuel cell installed at CCHT operated on natural gas and used tubular solid oxide technology developed by Siemens Westinghouse Power Corporation. This second-generation system featured important improvements from earlier installations including gas-powered heat-up to allow the unit to be started without an

[1] Authored by Mike Swinton and Marianne Manning (National Research Council Canada) and Evgeuniy Entchev and John Gusdorf (Natural Resources Canada)

additional electrical power source; the ability to use low fuel pressures; and the elimination of the purge gas — an expensive gas mixture that was required to protect the cell stacks from oxidation during system startup and shutdown. In addition, the inverter, which converts the fuel-cell energy into AC power that is used by most household appliances, was redesigned to satisfy residential standards. The system also featured improved control of the output power. A block diagram of the fuel cell is shown in Figure IV-12.1.

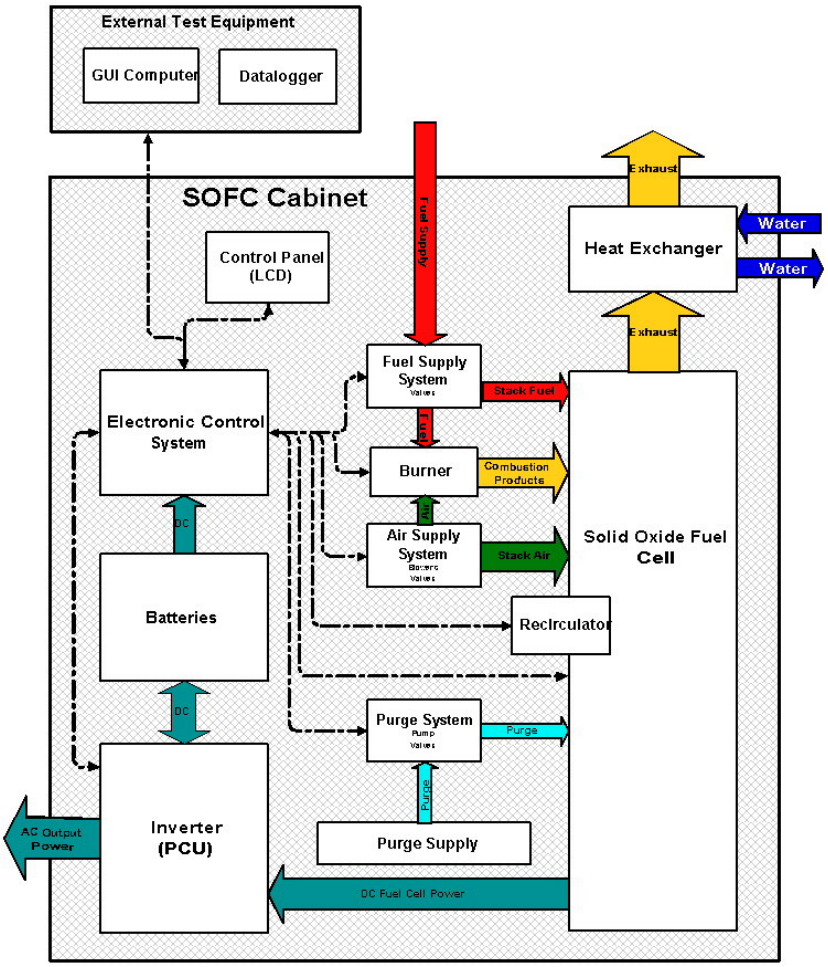

Figure IV-12.1 : Block diagram of the SOFC Fuel Cell

The FCT fuel cell featured in this project was fed by natural gas at 2.2 psig, and incorporates a reformer and all necessary components to supply hydrogen rich reformate

gas to the stack at the appropriate temperature for chemical reaction. Electricity is produced as DC power, and the unit contains a bank of inverters to deliver AC power at the appropriate voltage, ready for use by the house and the grid. Batteries are included in the package, but these were not used to modulate the delivery of electricity according to house demand in these experiments.

The FCT fuel cell balance of plant and controls manage the internal heat flows of the fuel cell to perform the needed reforming and electrochemical processes at the appropriate temperatures, while capturing excess heat in the form of hot water for use outside the fuel cell (used for space and water heating in this application). Effective internal energy management results in the power venting of the products of reaction through a sidewall vent at low temperatures (~50°C), such that a chimney is not needed.

The fuel cell controls are programmed for seamless ramping up to steady-state operating conditions after startup, continual monitoring of internal systems through normal operation, as well as ramp-down and shut-down, while providing the stack with optimal conditions during these three stages of operation, to maximize longevity of the stack.

Fuel Cell Thermal Utilization Module (TUM)

The Thermal Utilization module was designed to capture medium grade heat available from the fuel cell's internal cooling system, and dissipates this heat by supplying it to the house. From the point of view of the fuel cell, the Thermal Utilization Module is part of the cooling system for the fuel cell. In essence, the house is a large radiator in winter that dissipates the heat from the fuel cell. From the house's point of view, the fuel cell is a source of heat, which needs to be captured, stored, and delivered whenever there is a demand for space heating or hot water. From basic design parameters of the house and its performance history, the team knew that it was unlikely that the fuel cell would satisfy all of the house's heating needs in all conditions, so back-up heating provided by a domestic hot water heater was planned in the TUM.

In the shoulder and summer seasons, the house becomes a poor cooling system for the fuel cell, so another means of getting rid of heat was needed. In a fuel cell for residential applications, a by-pass damper would send this heat to the flue without passing through the internal heat exchanger. However, there was a desire in this experiment to meter the quantity of surplus heat generated by the fuel cell that was not needed by the house. So a heat dissipation loop was incorporated into the TUM that would 'kick-in' when the house's heating systems were satisfied. The excess heat was recovered through a heat exchanger to an alternate water/glycol loop, which then transferred that heat to an air stream in an air handler for venting to the outside. This means of metering excess heat allowed the team to identify the quantity of heat that could be usable for other purposes during warmer periods. The strategy also had the advantage of allowing seamless switching between the water loop to the house and the water loop to heat dissipation, while keeping the cooling liquid inside the fuel cell within acceptable temperature ranges.

So the TUM was designed to address all of the fuel cell's cooling needs and considerable portions of the house's heating needs, while also planning for the colder periods of winter, when supplementary heating would be needed.

The Thermal Utilization Module consisted of:

- The hot water tank (HWT) with gas burner, used as a storage tank and for back-up heating
- The air handler (AH)
- The external heat exchanger (HX), belonging to the heat dissipation loop
- The second air handler, belonging to the heat dissipation loop
- A side vent

The schematic diagram of the thermal utilisation module is shown in the Figure IV-12.2.

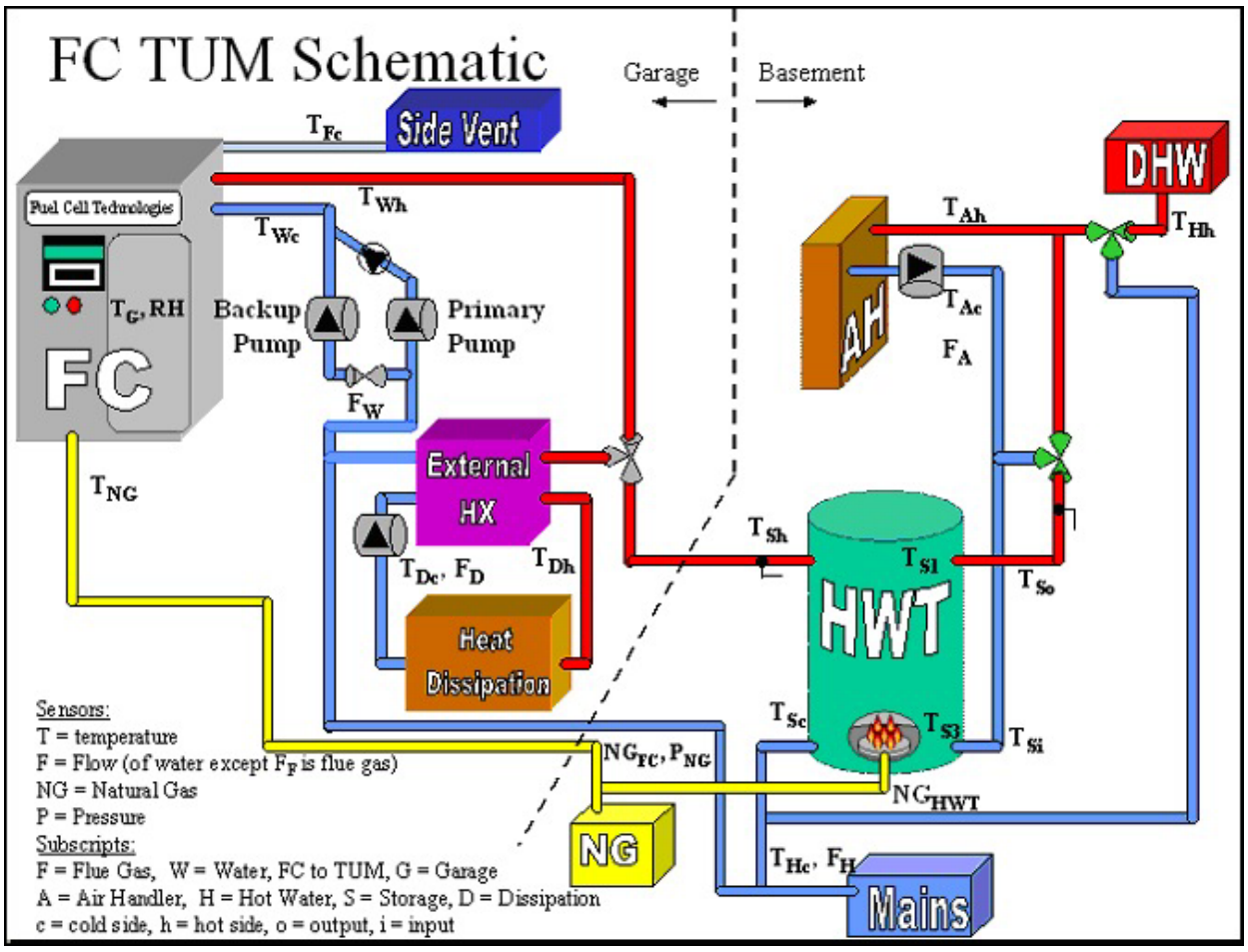

Figure IV-12.2 : Schematic Diagram of the Fuel Cell Thermal Utilization Module and Sensors

The components of the main thermal loop were located in the basement. The existing hot water tank (HWT), as well as the air handler (AH), were already in the test house as a result of a previous experiment. The HWT featured an oversized water storage capacity (284 L), and was already deployed in combo-mode, supplying both domestic hot water and space heating to the house. The hot water line from the fuel cell was connected to the existing tank, thereby providing storage for the excess heat from the fuel cell, and an automatic means of distribution of that heat to the hot water and space heating distribution systems. The burner on the HWT, which was previously the main source of water heating, served as a backup or top-up burner in instances where the fuel cell could

not supply all of the heat requirements, either due to heavy demands or a shut down of the fuel cell.

If the storage tank in the basement was hot, the excess heat from the fuel cell had to be dissipated somewhere. In this event, the system switched to the heat dissipation loop in the garage to dissipate the heat through a second air handler. This loop was filled with glycol in order to prevent the liquid from freezing and the lines from bursting on cold nights. Because of the glycol in this loop, an external heat exchanger was required. A spare air handler was also provided for the heat dissipation loop in case of failure of the primary air handler.

Two pumps, a solenoid, a check valve, a micro-filter, a two way valve, two mixing valves, a glycol reservoir with its pressurized expansion tank and piping connections were specified and installed to complete the Fuel Cell TUM:

- Two pumps maintained the flow. There was a primary pump and a backup pump in case the first one failed.
- A solenoid switched to the backup pump in case of failure.
- A check valve prevented the back flow if the backup pump was working.
- A micro filter removed particles from the water going to the fuel cell.
- A two-way valve allowed the hot water to go either to the house or to the heat dissipation loop.
- Two mixing valves combined hot water (from the HWT) and cold water to control the temperature of the water going to the AH and the domestic hot water
- A glycol reservoir with its own pump belonged to the heat dissipation loop, and was connected to a pressurized expansion tank.

To sum up, there were two thermal configurations: heat storage and heat dissipation.

Electrical Modifications

The modifications were made to accommodate the installation of the 5kW Solid Oxide Fuel Cell (SOFC) system, for either grid-dependent operation (this project), or stand-alone grid-independent operation (possible future projects).

The following wiring changes had already been made to the Test House for pervious CHP connections:

- Three additional bi-directional, pulse generating kilowatt-hour meters, and two power quality meters were added for monitoring purposes.
- A weatherproof padlockable disconnect switch was installed on the exterior of each house to meet requirements of rule 84-028 of the Canadian Electrical Code.
- A four-pole transfer switch was installed to allow various generator configurations without re-wiring.
- A 200-amp disconnect/isolating switch with 20-amp fuses was installed to protect and isolate CHP systems under test.

Only a few wiring changes were specifically made to the Test House to connect the fuel cell:

- A large electrical cable was sized to connect the fuel cell to the electrical circuit. And a hole was drilled through the concrete wall between the garage and the basement to link the fuel cell to the electrical meters and the load panels.
- The safety disconnect characteristics had to be adapted for the FC, so the 20-amp fuses were replaced with 45-amp ones.

The fuel cell has two output lines: one to the house, one to panel 1A (the pony panel) which supplies two heaters, a dissipation air handler, a CO and NG detector, two relays,

two pumps, a two way valve, a solenoid valve, a fluorescent lamp, and a 24v-1.4amps power supply.

A schematic diagram of the integration of these elements to the test house is shown in Figure IV-12.3.

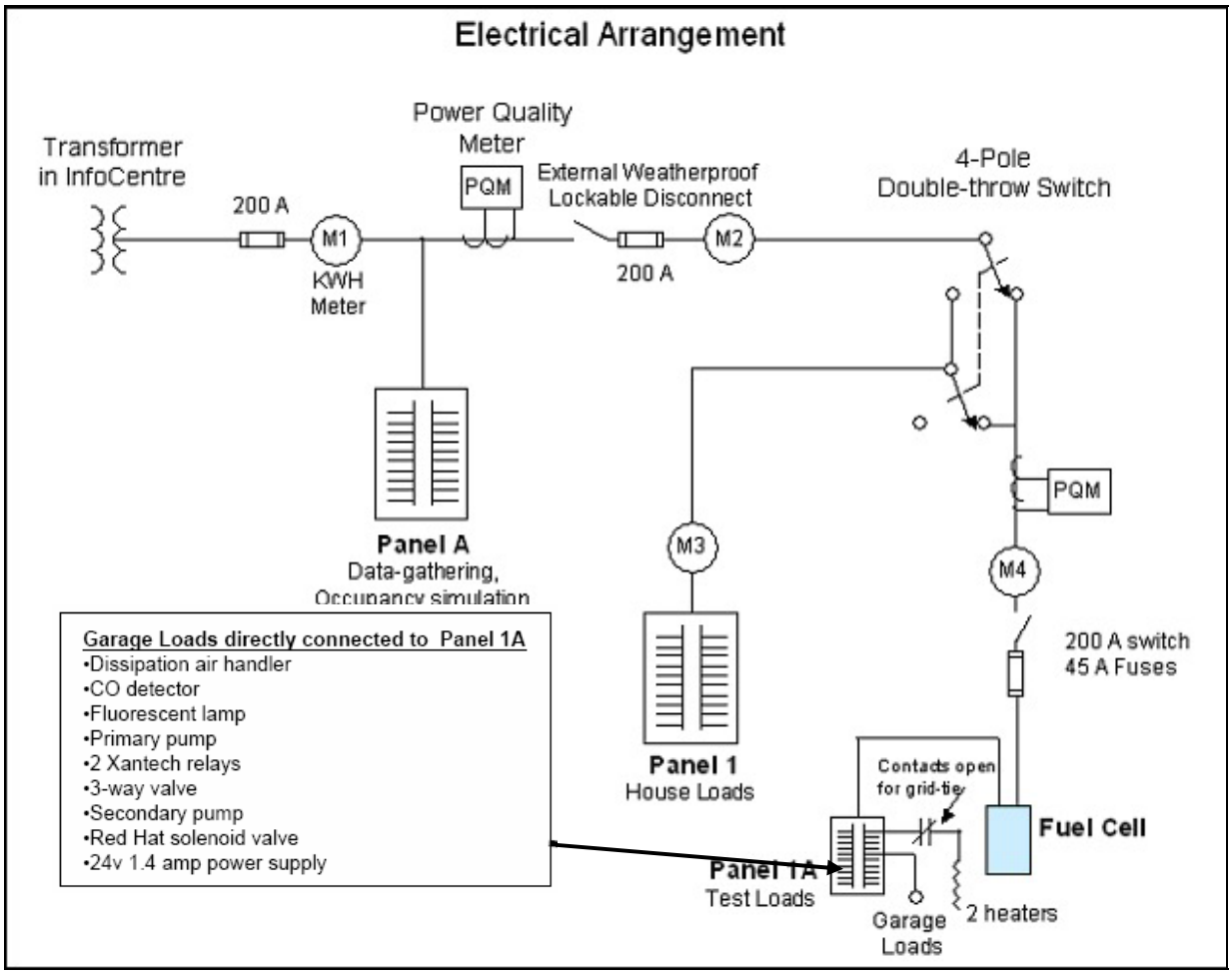

Figure IV-12.3 : Schematic Diagram of the Upgraded Wiring and Metering in the CCHT Test House

There are three possible electrical configurations for different modes of operation:

- Normal operation: Fuel cell not working (no CHP installed or working)
- Test operation 1: Fuel cell grid-tie mode
- Test operation 2: Fuel cell stand-alone mode

Electricity Meters and Link to the Data Logging System

The electric meters and logging system used to account for electricity flows between the CHP, the house and the grid are described below:

- ABB forward and reverse power meters (M1, M2 and M4 in Figure IV-12.3)
- NUDAM pulse counters to interpret the signal generated by the meters and
- An interface between the pulse counters and CCHT's main data acquisition system (HP-VEE based system) to read and record meter output.

Power Quality Meters

- The same two power quality meters used for the Stirling engine experiment (see section IV-2 of this report) were deployed in the SOFC Fuel Cell experiment.

Emergency electrical circuit

In the case of a power failure, the fuel cell would require an emergency load to dissipate the excess electrical energy. To this purpose, two heaters were added to the system in the garage as electrical loads.

Accuracy and Calibration

Both electricity and gas meters were fitted with the NUDAM pulse counters as described above. The resolution of the electricity meters is 0.6 Wh/ pulse. This resolution is 1667

times better than a utility-grade power meter normally used for billing purposes. The gas meter resolution is 0.05 ft^3/pulse.

With this many sensors and meters, benchmarking and calibration are a regular activity at CCHT. For example, as part of the analysis of fuel cell performance, the calibration of an existing meter was checked. During the installation of a dedicated gas line for the fuel cell, a new calibrated meter was installed by the utility. As well, the project team relocated one of its existing gas meters that was hooked up to a NUDAM pulse counters and datalogger. Meter readings were recorded at the start and end of a two-week period, and the datalogger recorded cumulative consumption during that period. The error between the meters over this period was recorded as 0.5% (within the resolution of the original gas meter). The logged error was higher, at 1.7%. The higher error of the logger is associated with a known pulse counting error which shows up randomly in the data set, but which carries a distinctive signature of an additional 257 pulses. A post-processing algorithm has been devised to detect and correct the additional logging errors. Similar exercises over the years have reported differences between existing meters and newly calibrated meters to be of the order of magnitude of a single pulse count – the resolution of the meters.

Monitoring

The experiment featured the management and coordination of 4 separate data collection systems:

1. Fuel Cell Technologies internal monitoring system
2. CCHT's main data collection system
3. Dedicated data logger of the TUM parameters
4. 2 Power quality meters

Each of the CCHT houses has a permanently installed data collection system with over 250 points of temperature, relative humidity, moisture content and flow rates that are read every five minutes and stored every hour. It also has 18 meters for monitoring electricity that were read and stored every five minutes. Three of the kWh meters (two of which are bi-directional) were used in the fuel cell testing.

In addition to the permanent data collection system, a dedicated data logger was installed for the fuel cell. The data logger was a Campbell Scientific CR23X that scanned 26 points every ten seconds and recorded them every minute: These points included 18 temperatures, four flows of water, the relative humidity of the air entering the fuel cell, the natural gas used by the fuel cell and by the hot water tank, and the pressure of natural gas entering the fuel cell. The data logger used water flows and temperature differences to calculate the following heat flows:

1. Heat out of the fuel cell.

2. Heat entering the hot water tank.

3. Heat dissipated.

4. Heat to space heat.

5. Heat to hot water.

These heat flows were calculated every ten seconds and saved every minute.

In addition to data collection, the data logger had several control and alarm functions. It controlled whether the heat from the fuel cell was sent to the hot water tank or to the dissipation air handler. If the primary pump for circulating cooling water through the fuel cell had failed, it would have activated the backup pump, and telephoned an alarm condition to three phone numbers. Telephone alarms would also have been sent if the backup pump had failed, or if the temperature of the dissipation loop had exceeded 75 C.

When the fuel cell was not thermally connected to the house, the third alarm would also have been sent if there were no flow through the heat dissipation loop.

The fuel cell also contains its own data collection system that saves data on a number of internal conditions at least once per minute. FCT sent some of these data to us, and we have used it to determine the direct current (DC) output of the fuel cell, and to compare their natural gas use readings with ours. In the FCT data, natural gas to the burner and to the stack was measured separately. In this report, FCT's data, and results based on it, are always distinguished from CCHT data and results. This is because the FCT data was not collected by an agency that was independent of the fuel cell's manufacturer.

Fuel Cell Experimental Period

Winter season monitoring began on March 5, 2005 with the fuel cell thermally connected to the house. The fuel cell completed its warm-up period and began supplying electricity to the house and grid at 1:15 (am) on March 6th. After some fluctuations, the AC output reached its desired level of approximately 2.5 kW around 20:00 on March 7th. The fuel cell continued to supply both electricity and heat to the house until March 21st, when it was thermally disconnected.

On May 3rd, the fuel cell was thermally connected to the house for shoulder season monitoring. However, two complications affected the shoulder season data collection. First, in order to prevent over-heating of the fuel cell, the dissipation air handler had been switched on constantly in order to ventilate the garage where the fuel cell was located. This need for ventilation was not anticipated by either CCHT or FCT, and had to be dealt with quickly. Second, preliminary data analysis showed that a problem with the 3-way valve was causing a constant dissipation of about 500 W. The constant dissipation was fixed on May 11th. During this same period, remote sensing by FCT of the combustion zone temperatures in the unit indicated a loss of the 3rd of 4 thermocouples. This led FCT to abort further testing rather than risk damage to the unit. This decision was implemented by FCT on May 12th at 7:47 AM.

Although this field experiment does not present the controlled laboratory conditions intended by the Annex 42 experimental protocol (see section II of this report), the project team was mindful of the protocol and integrated as many sensors as possible to address the needs of Annex 42. Nevertheless, key measurements inside the fuel cell could not be collected in this experiment. Subsequent laboratory investigations (see section IV-13 of this report) addressed all requirements of the protocol.

References

Entchev, E., Gusdorf, J., Swinton, M.C., Bell, M., Szadkowski, F., Kalbfleisch, W., Marchand, R.G., "Micro generation technology assessment at the Canadian Centre for Housing Technology," Energy and Buildings, 36, (9), September, pp. 925-931, September 01, 2004 (NRCC-47332)

URL: http://irc.nrc-cnrc.gc.ca/pubs/fulltext/nrcc47332/

DOI: "http://dx.doi.org/10.1016/j.enbuild.2004.03.004"

Bell, M., Swinton, M.C., Manning, M.M., Entchev, E., Gusdorf, J., Szadkowski, F., "Testing a residential fuel cell for combined heat and power," ACEEE Summer Study on Energy Efficiency in Buildings 2006, American Council for an Energy Efficient Economy (Pacific, Grove, CA., U.S.A., August 13, 2006), pp. 1_13-24, August 01, 2006 (NRCC-49220)

Bell M.; Swinton M.; Entchev E.; Gusdorf J.; Szadkowski F.; Kalbfleisch W.; Manning M.; Leban C. Integration of a Residential-sized Fuel Cell to Supply Electricity & Heat to a House at the Canadian Centre for Housing Technology, Final Contract report, pp. 74, November 04, 2005.

Bell, M., Swinton, M.C., Manning, M.M., Entchev, E., Gusdorf, J., Szadkowski, F., "Testing a residential fuel cell for combined heat and power," ACEEE Summer Study on Energy Efficiency in Buildings 2006, American Council for an Energy Efficient

Economy (Pacific, Grove, CA., U.S.A., August 13, 2006), pp. 1_13-24, August 01, 2006 (NRCC-49220)

IV-13 : Experimental Investigation of a FCT SOFC Device at FCT [1]

A prototype SOFC-cogeneration system developed by Fuel Cell Technologies Ltd. was tested according to the Annex 42 experimental protocol in the laboratory facility described in section III-4. The experiments were conducted in March 2007.

Experimental and measurement procedures

The ramp tests described in section II required variation of the electrical output. This was achieved by varying the stack current demanded by the SOFC's internal controller.

The cogeneration device and the water loop were instrumented to record both electrical and thermal conditions throughout the tests. Voltage and current were measured at the points where power flowed to the power conditioning system, to the battery, and to the DC-powered ancillary devices. The AC output from the power conditioning system was also instrumented as were the AC-powered ancillary devices. Voltage taps were placed to measure DC voltage at the stack exit (i.e. at the start of the transmission cable carrying power to the PCU) and at the AC ancillary devices. A current shunt was installed to measure the total ancillary current draw. An watt transducer was used to monitor the AC output to the grid.

The flow rates of fuel supplied to the FCPM's stack and burner (fired to maintain stack temperatures when necessary) were measured independently using two mass flow controllers. Two venturi pressure transducers were used to measure the flow rates of air to the stack and burner.

The flow rate of water through the heat exchanger was measured at its inlet using a turbine water flow meter. Type-T thermocouples were used to measure the temperature of the water at the heat exchanger inlet and outlet. Gas temperatures were measured at the heat exchanger inlet and outlet using type-K thermocouples.

Due to the heat exchanger's design, when water vapour condensed from the exhaust gases the water droplets would drip onto the thermocouple measuring hot gas inlet temperature. This resulted in erroneous temperature readings, a fact that did not hinder model calibration efforts but rather assisted in identifying the onset of condensation. The cogeneration device collects the condensate in an internal reservoir. When full, a float valve triggers a pump to drain this reservoir. A rain gauge tilt bucket was located to collect the pumped condensate to measure its

[1] Authored by Ian Beausoleil-Morrison and Kathleen Siemens (Natural Resources Canada)

volumetric flow rate. This gauge was calibrated to tilt for each accumulation of 8.24 mL.

The cogeneration device is designed such that the cooled gases exiting the heat exchanger are mixed with the dilution air that is drawn through the cabinet to control skin losses to the containing room. The temperature, velocity, and relative humidity of these mixed gases were measured downstream of the mixing point. A velocity probe was used to measure the velocity of this gas stream. Due to the configuration of the cogeneration device's exhaust chimney it was not possible to take these measurements in a region of fully developed flow. Rather, measurements had to be taken close to a 90° bend in the duct. During the exploratory phase of the work, the probe was inserted at numerous locations across the duct and the measured velocity profile examined to choose the most representative location to mount the probe. These limitations resulted in significant uncertainty in the measured flow rate of the combined gas stream.

Finally, the ambient temperature and relative humidity in the test room were measured approximately 1 m above the top of the fuel cell enclosure and approximately 1 m away from the air inlet side of the cogeneration device.

The bias and precision errors from the primary measurements outlined above (e.g. temperatures, flow rates) propagate through into the derived quantities (e.g. the heat exchanger's $(UA)_{eff}$ value). In order to minimize the bias errors, a number of the instruments described above were calibrated. These include the water flow meter, the thermocouples at the heat exchanger's water inlet and outlet, the AC power flow meter, and the natural gas flow meter. These calibrations were effected by comparing instrument readings to reference instruments and then adjusting offset and slope parameters to adjust the translation of voltage signals to measured quantities.

Instantaneous measurements of the FCPM's DC power production, the FCPM's air and fuel supply rates, and the power flow to the battery were taken every second and the averages over the minute were logged to file. All other measurements were taken every 15 seconds and the four values averaged to log the data at each minute. The condensate flow rate was logged at the same frequency, but using a separate data acquisition system. Each of these measurements records the number of times the bucket had been tilted during the preceding minute. The time stamps in each file were used to synchronize the measurements.

Infrared images of the cogeneration device were captured during one test at which the cogeneration device was producing its maximum power. Three of the four side faces and the top of the SOFC enclosure provided unobstructed views for the imaging. These images were used to derive

thermal contour maps by taking into account the surface emissivities.

A gas chromatograph was used to analyze the content of natural gas supply a few days prior to the experiments. This determined the molar fractions of each constituent of the gas supply in order to accurately determine its lower heating value.

Uncertainty analysis

The primary measurements outlined above were used to derive the variables of interest to the model for calibration and validation purposes. The calculation of these derived quantities and their associated uncertainties is detailed here. The methods illustrated here for treating the exhaust-gas-to-water heat exchanger equally apply to other quantities, such as the electrical efficiency of the FCPM, the DC-AC conversion efficiency of the power conditioning system, etc.

The calibration of the exhaust-gas-to-water heat exchanger requires the calculation of the effective product of the heat transfer coefficient and area. This can be derived from five of the primary measurements described in section III-4 as follows,

$$(UA)_{eff} = \frac{(\dot{N}\hat{c}_P)_{w-in} \cdot (T_{w-out} - T_{w-in})}{\left[\frac{(T_{g-in} - T_{w-out}) - (T_{g-out} - T_{w-in})}{\ln\left(\frac{T_{g-in} - T_{w-out}}{T_{g-out} - T_{w-in}}\right)}\right]} \qquad \text{(IV-13-1)}$$

Equation IV-13.1 was evaluated for each minute of recorded data using the four temperature readings (T_{w-in}, T_{w-out}, T_{g-in}, T_{g-out}) and the water flow rate measurement ($\dot{N}_{w-in}$). The heat capacity of the water entering the heat exchanger ($\hat{c}_{P,w-in}$) was calculated from T_{w-in} using a parametric relation (Beausoleil-Morrison, Schatz, and Maréchal, 2006).

The method recommended by the American Society of Mechanical Engineers (described in Abernethy, Benedict, and Dowdell, 1985 and Moffat, 1988) was used to calculate the uncertainties of the measured quantities and to propagate these uncertainties into the derived quantities. With this a bias error was assigned to each primary measurement. These were established based upon the instrumentation specifications, either an absolute error as a percent of full-scale measurement and/or a reading error as a percent of the value measured. Where instruments were calibrated (refer to section III-4) the bias error was established based upon the calibration parameters. In these cases, the bias error was set based upon either the average or maximum deviation

of the corrected measured values to the reference values.

In some cases additional bias errors were assigned based upon judgement. For example, a substantial bias error was assigned to the velocity measurement of the combined exhaust gas stream due to the restrictions on instrument placement, as discussed in section III-4. As another example, an additional bias error was assigned to the condensate flow rate measurement. As described in section III-4, condensate is measured by a rain gauge tilt bucket after it is pumped from an internal reservoir. The time lag between the pumping and measurement actions introduced some uncertainly to the condensate flow rate measurement. Consequently a bias error of 50 mL (the approximate volume of the internal reservoir) was assigned to the measurement of the condensate flow over the duration of each experiment.

The total bias for each measurement point is calculated from the individual bias errors for that sensor using the root-sum-square method,

$$B = \left[B_1^2 + B_2^2 + \cdots + B_k^2 \right]^{1/2} \qquad \text{(IV-13-2)}$$

For each of the tests required by the Annex 42 experimental protocol the desired boundary conditions (e.g. T_{w-in} and $\dot{N}_{w-in}$) were held for a period of time and data logged each minute. The precision index of a single measurement within a given test is calculated based on the average value of the observed parameter during that test and the number of logged readings,

$$S = \left[\frac{\sum_{i=1}^{N} \left(X_i - \bar{X} \right)^2}{N - 1} \right]^{1/2} \qquad \text{(IV-13-3)}$$

Where N is the number of logged readings. It is worth noting that the data were logged at one-minute intervals based upon either one second or 15 second instantaneous readings (refer to section III-4). The X_i values of equation IV-13.3 are the one-minute averaged values since the instantaneous data were not logged. It is also worth noting that S has the same value for each data point within a given test.

The precision index of the average value of a parameter for a given test is lower than that for the individual measurements according to,

$$S_{avg} = \frac{S}{\sqrt{N}} \tag{IV-13-4}$$

Finally, the bias and precision indices are combined to express the uncertainty in a measured quantity,

$$U_{95\%} = \sqrt{B^2 + (t \cdot S)^2} \tag{IV-13-5}$$

$$U_{99\%} = B + t \cdot S \tag{IV-13-6}$$

Where $U_{95\%}$ and $U_{99\%}$ are the measurement uncertainties at the 95 and 99 percent confidence levels, respectively. t is the standard statistical Student t value and is a function of the value of N used in evaluating equation IV-13.3.

The uncertainty of a derived quantity is determined by propagating the bias and precision indices of the measurements that are used to calculate the derived quantity. For example, the bias error for $(UA)_{eff}$ is calculated as follows (refer to equation IV-13.1),

$$B_{(UA)_{eff}} = \left[\left(\frac{\partial (UA)_{eff}}{\partial \dot{N}_{w-in}} \cdot B_{\dot{N}_{w-in}} \right)^2 + \left(\frac{\partial (UA)_{eff}}{\partial T_{w-out}} \cdot B_{T_{w-out}} \right)^2 + \left(\frac{\partial (UA)_{eff}}{\partial T_{w-in}} \cdot B_{T_{w-in}} \right)^2 \right. \tag{IV-13-7}$$

$$\left. + \left(\frac{\partial (UA)_{eff}}{\partial T_{g-in}} \cdot B_{T_{g-in}} \right)^2 + \left(\frac{\partial (UA)_{eff}}{\partial T_{g-out}} \cdot B_{T_{g-out}} \right)^2 \right]^{1/2}$$

The precision index for $(UA)_{eff}$ is determined in a similar manner and the overall uncertainty determined using equations IV-13.5 and IV-13.6.

The propagation of measurement uncertainties into equation IV-13-7 is demonstrated by examining the test that was illustrated in Figure III-4-. The bias errors and precision indices for the four temperature and one water flow rate measurements used in the equation are summarized in Table IV-13.1. The bias errors reported in the table are the average for the 82 measurement points of the test. Likewise, the precision index is that corresponding to each individual measurement, and not the precision index of the set average (i.e. it represents S of equation IV-13.3, not S_{avg} of equation IV-13.4).

measurement	average value over test	B	S	$U_{95\%}$
T_{w-in}	30.60°C	0.10°C	0.58°C	1.17°C
T_{w-out}	43.38°C	0.10°C	0.48°C	0.97°C
T_{g-in}	284.27°C	2.20°C	0.57°C	2.48°C
T_{g-out}	45.04°C	2.20°C	0.36°C	2.32°C
$\dot{N}_w$	$4.0 \cdot 10^{-3} kmol/s$	$7.9 \cdot 10^{-5} kmol/s$	$2.7 \cdot 10^{-5} kmol/s$	$9.3 \cdot 10^{-5} kmol/s$

Table IV-13.1: Uncertainty parameters for test at $T_{w-in} = 30^o C$ and $\dot{N}_w = 0.004 kmol/s$

Table IV-13.1 also lists the average uncertainty at the 95% confidence level of the 82 measurements of each of the five parameters. As can be seen, the precision indices are the predominant determinant of the uncertainty of the water temperature measurements, an observation consistent with the T_{w-in} measurements plotted in Figure . In contrast, the instrument bias errors are the predominant determinants of the uncertainty of the gas temperatures and the water flow rate.

Equation IV-13-1 was applied to calculate the $(UA)_{eff}$ value for each of the 82 measurement points of the test. The procedure outlined in equations IV-13-2, IV-13-3, IV-13-5, and IV-13-7 was then applied to calculate the uncertainty for each of these 82 derived $(UA)_{eff}$ values. Figure IV-13-1 plots these derived values and their uncertainties. The test-averaged $(UA)_{eff}$ value determined from the 82 measurement points and its error bar are also shown in the figure. The uncertainty of the test-averaged $(UA)_{eff}$ value is less than that for individual measurements due to equation IV-13-4.

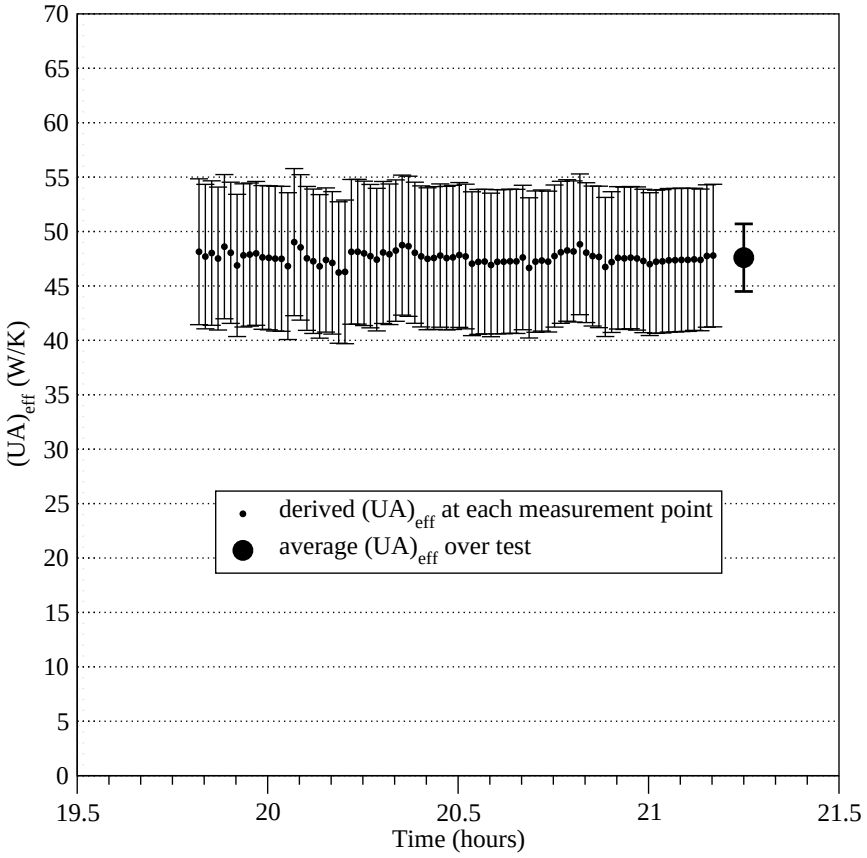

Figure IV-13-1: Derived $(UA)_{eff}$ values and associated 95% error bars for $T_{w-in} = 30^{o}C$ and $\dot{N}_w = 0.004 kmol/s$

References

Abernethy, R.B., Benedict, R.P., and Dowdell, R.B., "ASME Measurement Uncertainty," *Journal of Fluids Engineering* **107**, pp. 161-164 (1985).

Beausoleil-Morrison, I., Schatz, A., and Maréchal, F., "A Model for Simulating the Thermal and Electrical Production of Small-Scale Solid-Oxide Fuel Cell Cogeneration Systems within Building Simulation Programs," *HVAC&R Research Special Issue* **12**(3a), pp. 641-667 (2006).

Moffat, R.J., "Describing the Uncertainties in Experimental Results," *Experimental Thermal and Fluid Science* **1**, pp. 3-17 (1988).

Section V

Calibration of the Annex 42 combustion cogeneration model to the WhisperGen SE device

AUTHORS:

Alex Ferguson (Natural Resources Canada)

WITH INPUT FROM:

Ian Beausoleil-Morrison (Natural Resources Canada)

John Gusdorf (Natural Resources Canada)

Kathleen Siemens (Natural Resources Canada)

Section V Table of Contents

Introduction to this section V-3
Assumptions and sources of uncertainty V-3
Calibration strategy V-8
Static analysis V-10
Quasi-steady state analysis V-11
Dynamic parameter identification V-19
Summary of model inputs V-27
Accuracy of the calibration V-27
References V-38

Introduction to this section

In 2003, the Canadian Centre for Housing Technology integrated a residential Stirling cogeneration unit into a test house and monitored its operation over several months. This section discusses calibration of the Annex 42 combustion cogeneration model using the CCHT Stirling engine data.

Four companion Annex 42 reports are relevant to this work:

- Manning and Swinton provide an overview of the CCHT test facilities in Section III-3 of this report.
- In Section IV-2 of this report, Entchev, Gusdorf, Manning and Swinton describe the Stirling engine tests performed at CCHT, which produced the data for this calibration work.
- A complete description of the Annex 42 combustion cogeneration model is available in Kelly and Beausoleil-Morrison (2007, Section III), hereafter called the *model specification*. The equation references and symbols used in the present section correspond to those in the model specification.
- Portions of the CCHT Stirling engine data were also used to validate the Annex 42 combustion cogeneration model. These activities are described in Beausoleil-Morrison and Ferguson (2007, Section V).

Assumptions and sources of uncertainty

The CCHT experiments were completed in 2003, prior to commencement of Annex 42's working-phase. Thus, the experiments were not designed with Annex 42's goals in mind, and there was no opportunity to modify the testing program to support Annex 42's exper-

imental objectives. As a result, the data collected in the CCHT study are not optimally-suited for calibrating the Annex 42 combustion cogeneration model.

Principle sources of uncertainty associated with using the data collected during the CCHT tests to calibrate the combustion-based cogeneration model include:

Fuel calorific value: The CCHT facility was not equipped to measure the composition or calorific heating value of the natural gas used to fuel the WhisperGen unit. Previous studies at the CCHT facility have assumed a higher heating value of Natural Gas of 37.5 MJ/m^3 under standard temperature and pressure conditions, and this value is deemed representative of the gas available inside the CCHT houses. (Gusdorf, 2006)

The gas meters used at CCHT automatically corrected the reported volumes to standard temperature conditions, but did not account for the gas line pressure. The line pressure at which natural gas is delivered gas also affects its volumetric energy content. Line pressures of 3.45 kPa gauge (0.5 psi) are typical in residential gas delivery in North America. (Gusdorf, 2006)

For the Annex 42 calibration work, the natural gas composition presented in Table V-1 was assumed, which provides a higher heating value of 37.5 MJ/m^3 at standard temperature and pressure conditions. The gas line pressure was also assumed to be 3.45 kPa. Under these conditions, the gas has a lower heating value of 35.16 MJ/m^3 and a higher heating value of 38.98 MJ/m^3.

Air flow measurements: The experiments conducted at CCHT did not include measurement of supply air or exhaust flow rates, which were of limited importance to the CCHT study. Without these data, calibration of the model's air flow correlations is impossible.

Casing temperature measurement: The experiments conducted at CCHT did not characterize the casing temperature of the Stirling cogeneration unit. Without these data, the dynamic thermal model's heat loss coefficient cannot be directly calibrated.

Differing time resolutions: While the fuel flow rate, cooling water flow rate, and inlet and outlet temperatures were measured in one-minute intervals, measurements of the cogeneration unit's electrical output were taken at fifteen-minute intervals. Although comparison with these measurements indicates whether the cogeneration model is accurately predicting the unit's aggregate electrical generation, the data provide no opportunity to explore the cogeneration system's transient response on shorter (approximately one-minute) time scales.

Steady state measurements: The CCHT test facility is designed to replicate real-world conditions inside a residence, and cannot impose steady-state conditions on the combustion cogeneration unit. All of the experiments conducted at CCHT were dynamic tests in which the temperature of the cooling water varied continuously according to conditions in the water tank. Since none of the measurements describe the system under steady-state conditions, the steady-state and dynamic aspects of the engine's response cannot be disaggregated.

Standby behaviour: Without invasive instrumentation, the temperature of the encapsulated cooling water inside the unit's heat exchanger must be measured using a thermocouple located outside the cogeneration unit near the cooling water outlet. The temperature measured at this outlet closely approximates the temperature inside the unit when cooling water flows through the device. But when the flow of cooling water ceases, the temperature measured by the thermocouple does not indicate the actual temperature inside the unit. Therefore, the unit's thermal behaviour during stand-by operation cannot be directly determined.

Instrumentation noise: The rate of fuel consumption was measured using a pulse meter, which notified the logging equipment each time the integrated volume of gas flowing through the meter reaches a discrete multiple of the meter's pre-set pulse resolution. The logging equipment then recorded the number of pulses sent by the meter during each minute of operation.

The resulting data approximate unit's true fuel consumption in discrete steps. During each one-minute interval, the measurements truncate the actual volume of fuel consumed to the nearest multiple of the pulse resolution, and add the remainder to the volume reported during the next minute.

The instrumentation noise introduced by a pulse meters is manageable provided the pulse resolution is much smaller than the volume of fuel flowing through the meter during each measurement interval. But the pulse resolution used in the CCHT WhisperGen tests ($1.42\times10^{3}\,m^3$/pulse) proved too coarse to provide meaningful results over one minute intervals. The rates of fuel consumption reported in the CCHT tests varied from $8.50\times10^{-3}\,m^3$/min (6 pulses per minute) to $1.84\times10^{-3}\,m^3$/min (13 pulses per minute), and the noise introduced by the meter amounts to 7.7%–16.7% of the of the reported reading.

To reduce the uncertainty associated with this instrumentation noise, the fuel consumption data was integrated over ten-minute intervals. Figure V-1 compares the one- and ten-minute integrated average values for the system fuel flow over a two-hour period. While the one-minute data exhibit significant variation from one measurement to the next, the ten-minute integrated values quickly converge towards a constant value, suggesting much of the variation observed over one-minute intervals can be attributed to noise introduced by the pulse meter.

The steady state electrical and thermal efficiency correlations (Equations III-14 and III-15 in the model specification) are sensitive to the power output, cooling water flow rate and cooling water temperature. However, experimental constraints prevented calibration of the terms correlating electrical and thermal efficiency to the power output and cooling water flow rate.

- Since the WhisperGen unit does not modulate its operating point, there is no need to characterize the sensitivity of the electrical and thermal efficiencies to the system

Table V-1: Assumed composition and pressure of natural gas

Constituent	Value	
H_2	0.0	%
CH_4	94.76	%
C_2H_6	2.70	%
C_3H_8	0.23	%
N_2	1.76	%
CO_2	0.55	%
Pressure	3.446	kPa gauge
Lower heating value (LHV)	35.16	MJ/m^3
Higher heating value (HHV)	38.98	MJ/m^3

electrical output. Therefore, terms correlating efficiency to the electrical output were set to zero.

- Similarly, the unit was operated at a single cooling water flow rate and the system's sensitivity to the flow rate of cooling water was not explored. Therefore, terms correlating efficiency to the cooling water flow rate were set to zero.

The CCHT data do describe the WhisperGen unit's performance at a variety of cooling water temperatures. But the dynamic nature of the CCHT experiments ensured that the temperature entering the cogeneration unit was always changing. Under these conditions, variations in performance can be attributed to either i) the engine's sensitivity to cooling water temperature under steady-state conditions; or to ii) the engine's dynamic response to changing conditions in the plant. To ensure the complexity of the parameter identification problem was manageable, the WhisperGen unit's electrical and thermal performance were assumed to be insensitive to cooling water temperature, and terms correlating efficiency to cooling water temperature were set to zero.

For these reasons, most of the terms in the combustion cogeneration model's steady-state efficiency correlations (Equations III-14 and III-15 in the model specification) could not be

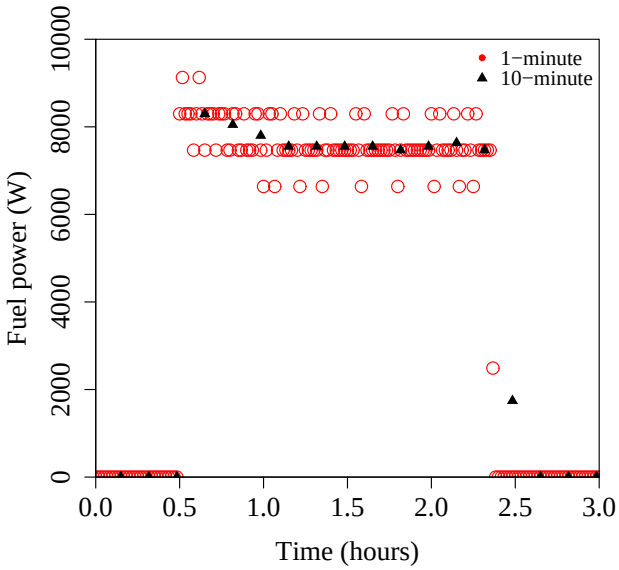

Figure V-1: Comparison of one-minute and 10-minute integrated fuel power.

determined. To reduce the complexity of the calibration problem, the electrical and thermal efficiency correlations were reduced to constant parameters:

$$\eta_e = a_0$$

$$\eta_q = b_0$$

This assumption greatly simplifies the model, and eliminates its sensitivity to the cooling water temperature. However, it is expected that the performance of Stirling-based cogeneration devices, including the WhisperGen unit used in this study, will be sensitive to the cooling water temperature. Should steady-state measurements become available in the future, improved correlations using the functional forms proposed in the model specification would be welcome.

Table V-2: Summary of CCHT WhisperGen calibration data subsets

Subset	Data points	Cycles	Duration (hours)
A	1 734	19	67.2
B	2 395	20	63.4
C	1 013	8	23.4

Calibration strategy

The CCHT WhisperGen data comprise 39 separate monitoring intervals spanning four months. Some of these intervals described summer periods during which the WhisperGen unit operated infrequently. In others, the electrical and thermal data were found to be mismatched by a few minutes, making it difficult to directly compare the units fuel use, electrical and thermal output over short intervals. Finally, the WhisperGen unit failed to operate correctly during three of these intervals.

Within the CCHT WhisperGen dataset, three contiguous periods of data were identified as most suitable for model calibration. These subsets are summarized in Table V-2.

The initial calibration of of the Stirling power system model was performed using subset A. The remaining subsets B and C were used to validate the accuracy of the calibrated model—these efforts are described in Beausoleil-Morrison and Ferguson (2007, Section V).

The Stirling power system model was calibrated using the CCHT data in three steps:

1. *Static analysis:* The WhisperGen Stirling engine and CCHT test documentation were reviewed. Extraneous and redundant model inputs were identified, and inputs pertaining directly to the system configuration determined.

2. *Quasi-steady state analysis:* Portions from the CCHT data, and periods in which the system's fuel flow and net power generation converged towards constant values were identified. Data from these intervals were averaged to derive model inputs.

3. *Dynamic analysis:* The model's remaining parameters were determined using an iterative procedure in which the parameters were first estimated, and then the model's predictions compared with the dynamic measured data.

Static analysis

A review of the CCHT test configuration and WhisperGen documentation determined that several model inputs could be easily identified, have limited impact on the results, or are redundant for the CCHT Stirling cogeneration unit. These are:

Maximum cooling water outlet temperature ($T_{cw,o}$): The WhisperGen cogeneration unit will shutdown if the cooling water temperature at the outlet of the system exceeds 85 °C (Whisper Tech Ltd., 2002). The model's maximum cooling water outlet temperature parameter was set to this value.

Maximum and minimum rate of change in fuel flow ($d\dot{m}_{fuel}/dt$): The Annex 42 combustion cogeneration model provides a facility to limit the rate of change in the fuel flow rate permitted during transient operation (see Section III-2$\dot{5}$ in the model specification). But the WhisperGen cogeneration unit does not modulate its operating point, and this facility was disabled.

Maximum and minimum rate of change in power output (dP_{net}/dt): The model also provides a facility to limit the maximum rate of change in the power delivered by the device during transient operation. But since the WhisperGen cogeneration unit does not modulate its operating point, this limits was disabled.

Cool-down period duration ($t_{cool-down}$): The CCHT heating plant was configured to circulate cooling water through the Stirling engine for 25 minutes after deactivation of the engine. Therefore, the cool-down period duration was set to 1 500 seconds.

Cool-down period mode: The model provides two cool-down configurations: in *Mandatory cool-down mode*, the unit cannot be reactivated during the cool-down period; in *Optional cool-down mode*, the unit can be reactivated at any time during the cool-down period.

The CCHT tests did not reactivate the unit during cool-down operation, and it is not known if the WhisperGen unit can be operated in this manner. This input will not affect predictions during calibration with the CCHT data, and can be adjusted in the future should more information about the WhisperGen unit become available.

Cooling loop configuration: The WhisperGen cogeneration unit is incapable of regulating the flow rate of cooling water. Therefore, the cooling loop configuration was set to *external pump.* In this configuration, the cooling water flow correlation coefficients described in the model specification (c_0–c_8 from Equation III-16) are superfluous.

Combustion air flow correlation coefficients: The CCHT data did not contain sufficient data to calibrate the combustion air flow correlation coefficients (d_0–d_2 from Equation III-17), and they were set to zero during the model calibration.

The combustion air correlation does not affect the model's performance predictions. But in applications where the cogeneration unit draws combustion air from the surrounding enclosure, the combustion air flow will significantly increase rates of infiltration into the building. Unfortunately, the CCHT data afford no opportunity to study these effects.

Quasi-steady state analysis

While the bulk of the CCHT data describe dynamic operating conditions, the observed fuel flow and power output converge towards constant values as the time spent in operation or standby increases. Parameters describing the unit's operation in these modes were determined by extracting and averaging these data.

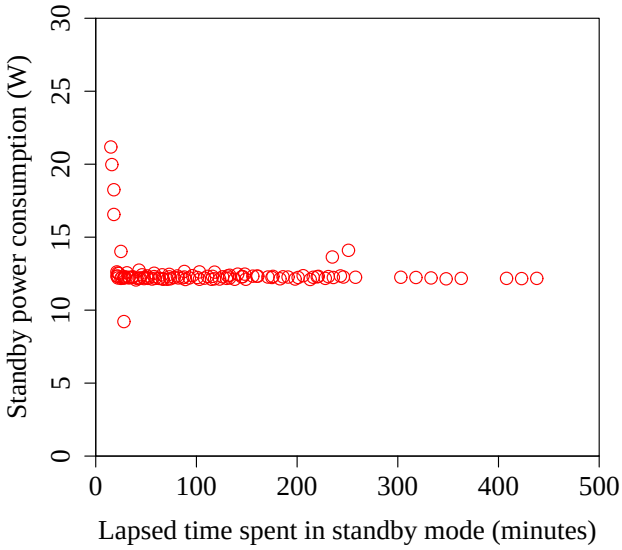

Figure V-2: WhisperGen Stirling cogeneration standby power consumption for all cycles, as a function of lapsed time in standby mode.

Standby operation

When inactive, the WhisperGen Stirling cogeneration unit consumes some electricity. Figure V-2 plots all of the 15-minute averaged electrical consumption measurements taken in standby operation against the time lapsed in this mode when the measurement was taken. Under all conditions, the standby power consumption quickly converges towards a constant value. The mean value of these measurements is -12.5 W, the upper 95% confidence limit is -12.3 W and the lower limit is -12.8 W. Therefore, the model's net standby power generation ($P_{net,standby}$) was set to -12.5 W.

Cool-down operation

During cool-down operation, the WhisperGen cogeneration unit consumes electricity. The electrical power measurements are not optimally suited for characterizing energy use during cool-down operation because the cool-down period is only 25 minutes long, and the electrical generation and consumption measurements were collected over 15-minute intervals. Consequently, only electrical consumption measurements taken during the last 10 minutes of the cool-down period actually pertain exclusively to the cool-down period—measurements taken during the first 15 minutes also reflect the power generated during normal operation, and therefore cannot be used reliably. The measurements taken during the last 10 minutes of each cool-down period, henceforth called the *cool-down period electric data subset*, were used to estimate the WhisperGen unit's power consumption during cool-down operation.

The 25-minute cool down period was divided into 25 one-minute intervals. For each of these intervals, the number of 15-minute averaged measurements from the cool-down period electric data subset that contained the interval were counted. The results, plotted in Figure V-3, suggest the bulk of the measurements pertain to the middle of the cool-down period, and less data are available to describe the energy consumption near the start and end of the cool-down period.

The 15-minute averaged power consumption measurements in the cool-down electric data subset were then decomposed into 1-minute data. For each one-minute interval in the cool down period, all of the 15-minute power consumption observations containing the interval were averaged. The results, plotted in Figure V-4, provides a coarse approximation of the unit's electrical use during cool-down.

These data do not exactly represent the actual power consumption during the cool-down, but provide some insight into the unit's power use. Clearly, the unit's energy consumption during cool-down is highest shortly after deactivation and decreases towards a constant

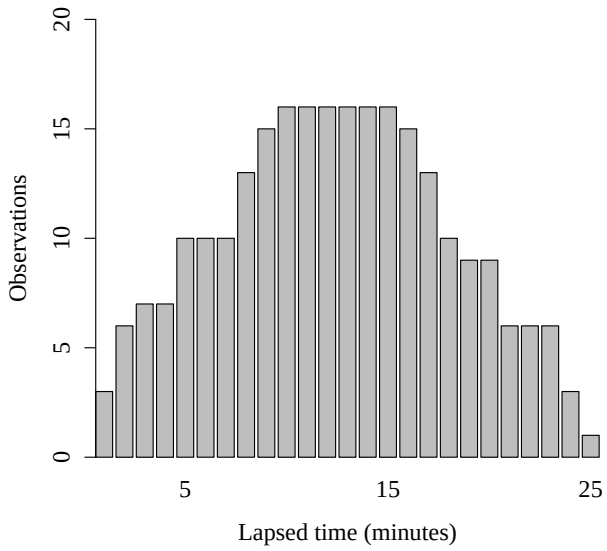

Figure V-3: WhisperGen Stirling cogeneration—number of decomposed power consumption observations for cool-down period, aggregated by lapsed time spent in cool-down operation.

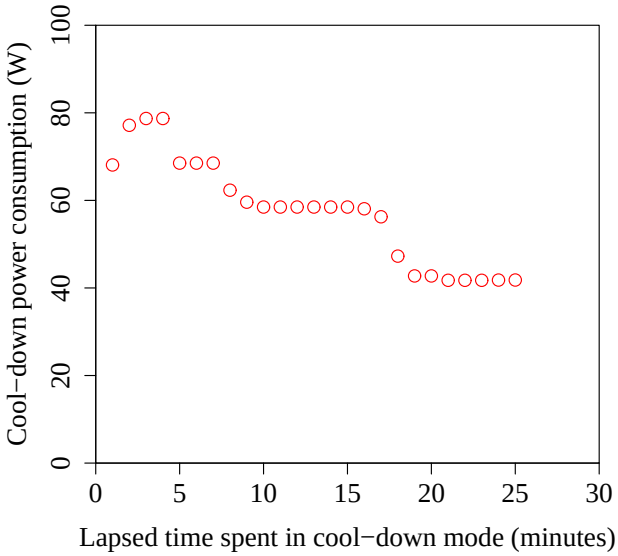

Figure V-4: WhisperGen Stirling cogeneration cool-down decomposed net power generation for all cycles, as a function of lapsed time in cool-down mode.

value near the end of the cool-down period.

The mean value of the 15-minute average net generation measurements taken during cool-down operation is -58.5 W, the 95% upper confidence limit is -48.0 W and the lower limit is -69.0 W. The mean value of the decomposed net generation observations (-57.5 W) agrees well, and better represents the unit's actual power consumption during this period because it weights each observation by the time interval it represents. Accordingly, the model's cool-down power generation ($P_{net,cool-down}$) was set to -57.5 W.

Maximum power

The WhisperGen cogeneration unit is designed for on-off operation, but when the engine is started, its power output is initially much lower than the design value. Figure V-5 plots each power measurement taken during the engine's operation against the lapsed time spent

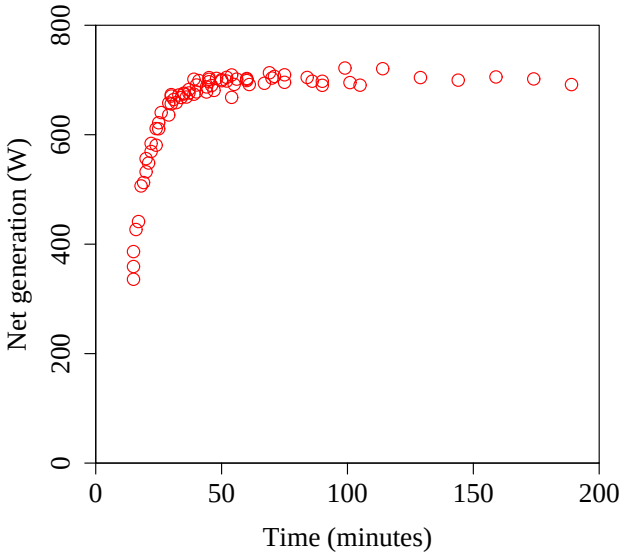

Figure V-5: WhisperGen Stirling cogeneration 15-minute averaged net electric generation for all all cycles, as a function of lapsed time in operation.

in operation when the measurement was collected.

While the data exhibit transient behaviour, the power generation observed after 40 minutes of operation remains relatively constant. The average observed power produced by by the unit after it had been operating for at least 40 minutes was 698.8 W, the 95% upper confidence limit is 702.0 W and the lower limit is 695.5 W. Therefore, the model's maximum power generation parameter ($P_{net,max}$) was set to 698.8 W.

Electrical Efficiency

Like its electrical output, the WhisperGen cogeneration unit's fuel use exhibits transient characteristics during start-up, but then converges towards a constant value as the time spent in operation increases. Figure V-6 plots all of the fuel power measurements observed during the CCHT experiments as a function of the lapsed time spent in operation when

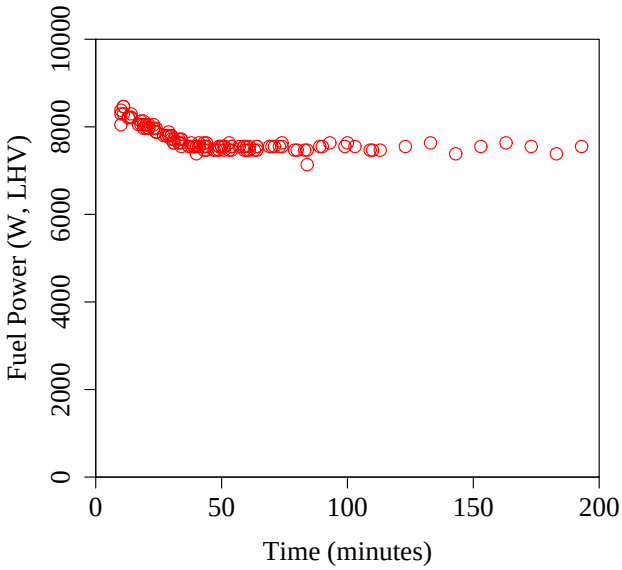

Figure V-6: WhisperGen Stirling cogeneration gross heat input (LHV basis) for all cycles, as a function of lapsed time in operation.

each measurement was collected.

Again, the observed gross heat input to the engine remains reasonably constant after 40 minutes of operation. The mean observed heat input ($\bar{q}_{gross}$, LHV basis) to the engine during this period is 7 523 W, the 95% upper confidence limit is 7 542 W and lower limit is 7 504 W.

The mean observed gross heat input ($\bar{q}_{gross}$) can be combined with the mean maximum net power production ($\bar{P}_{net,max}$) to compute the quasi-steady state electrical efficiency:

$$\bar{\eta}_e = \frac{\bar{P}_{net,max}}{\bar{q}_{gross}} \tag{V-1}$$

where $\bar{\eta}_e$ is the computed average steady-state electrical efficiency during normal operation.

The average gross heat input and net power generation values calculated above yield a quasi-steady state electrical efficiency of 0.092 9 (or 9.29%, LHV basis.) The first coef-

ficient in the model's electrical efficiency equation (a_0) was set to this value, while the remaining coefficients (a_1–a_{26}) were set to zero for the reasons explained earlier.

Sensitivity of electrical output to engine temperature (k_p)

During startup, the combustion cogeneration model's electrical output is correlated to the engine temperature as described by Equation III-25 in the model specification:

$$P_{net,warm-up} = P_{max} k_p \left(\frac{T_{eng} - T_{room}}{T_{eng,nom} - T_{room}} \right)$$

The dimensionless coefficient k_p describes the sensitivity of the power output during warm-up period to the engine temperature. Setting k_p to one causes a direct correlation between the engine temperature (T_{eng}) and the power output, while a value of zero eliminates electrical output during the start-up period.

Figure V-7 plots the combustion-based cogeneration model predictions for k_p values of 0.5 and 1.0, and clearly shows the effect of varying the electrical output sensitivity. Setting k_p to any value other than 1.0 yields discontinuous predictions for power output during start-up.

The actual power output observed in the CCHT tests does not exhibit this discontinuity (see Figure V-5.) Therefore, the electrical output sensitivity parameter (k_p) was set to 1.0.

Maximum fuel flow during start-up ($r_{fuel,warmup}$)

The Annex 42 combustion-based cogeneration model provides a parameter to limit the maximum fuel flow predicted during the start-up period (see Section III-3 in the model specification). Calibration of this input using the CCHT measurements is challenging—the fuel flow meter introduced considerable noise into the measurements (see Figure V-1), and discerning the affects of the unit's fuel flow controller amidst this noise is nearly impossible.

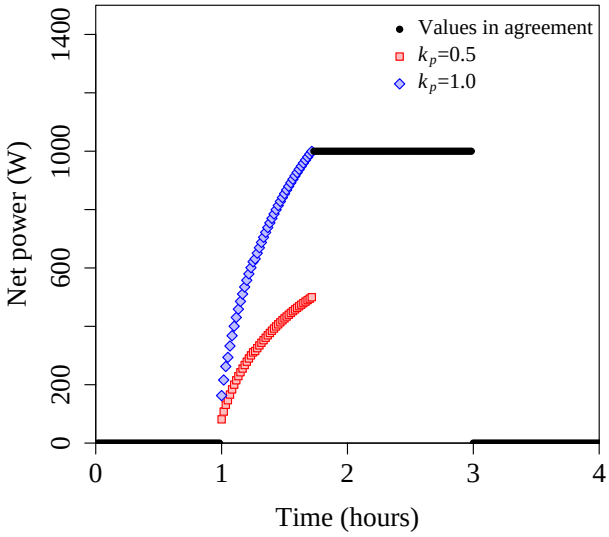

Figure V-7: Effect of varying electric output sensitivity parameter (k_p) on predicted electric power output during start-up period.

Nevertheless, the ten-minute averaged fuel flow measurements plotted in Figure V-6 do not exhibit a discernible limit during the start-up period. Therefore, the start-up fuel flow rate limiting facility was disabled.

Dynamic parameter identification

The dynamic thermal model comprises the following state equations (Equations III-10 and III–11 in the model specification):

$$[MC]_{eng}\frac{dT_{eng}}{dt} = UA_{HX}(T_{cw,o} - T_{eng}) + UA_{loss}(T_{room} - T_{eng}) + q_{gen,ss}$$

$$[MC]_{HX}\frac{dT_{cw,o}}{dt} = [\dot{m}C_p]_{cw}(T_{cw,i} - T_{cw,o}) - UA_{HX}(T_{cw,o} - T_{eng})$$

where:

$[MC]_{eng}$ is the engine control volume heat capacity,

$[MC]_{HX}$ the heat exchanger control volume heat capacity,

UA_{HX} is the coefficient of heat transfer between the engine and cooling water control volumes,

UA_{loss} is the coefficient of heat transfer between the engine control volume and the surroundings,

$q_{gen,ss}$ is the rate of heat generation in the engine,

T_{eng} is the engine control volume temperature,

$T_{cw,i}$ is the cooling water inlet temperature,

$T_{cw,o}$ is the cooling water control volume temperature, and

T_{room} is the temperature of the surrounding enclosure.

These equations contain parameters describing the engine's thermal mass ($[MC]_{eng}$ and $[MC]_{HX}$) and heat transfer (UA_{HX} and UA_{loss}). Other parameters also affect the dynamic thermal model's predictions:

- The heat generation efficiency (η_q) describes the fraction of the gross heat input to the engine that is converted into heat ($q_{gen,ss}$).
- The nominal engine temperature (T_{nom}) affects the length of the unit's warm-up period—higher nominal engine temperatures require additional warm-up time.
- The fuel-flow sensitivity to engine temperature (a_{fuel}) describes additional amounts of fuel consumed during the start-up period

The dynamic nature of the CCHT tests ensured that the inlet temperature of cooling water flowing through the WhisperGen unit's heat exchanger was always changing, and the fuel

use, electrical and thermal output measured during the CCHT tests describe the unit's response to these transient conditions. For this reason, these parameters were estimated using a dynamic parameter identification procedure.

An iterative parameter identification approach was used:

1. A set of input parameters was chosen.
2. The model was subjected to the same cooling water temperature and flow rate, enclosure temperature and control signals as the WhisperGen unit studied in the CCHT tests.
3. The model's predicted outlet temperature, fuel flow rate and power generation were compared to the measured CCHT data
4. The model inputs were adjusted, and steps 2–4 were repeated until the best-possible agreement between model outputs and empirical data was achieved.

To assist in the parameter identification procedure, the *DAKOTA* optimization utility developed by Eldred et al. (2006) was used to identify the parameter set providing the best fit between model predictions and experimental data. DAKOTA automates steps 2–4 of the parameter identification process, and can perform thousands of simulations while searching for the optimal input set. DAKOTA also employs a suite of multi-objective optimization algorithms to quickly converge on these input values.

Plant network and simulation

The combustion-based cogeneration model was integrated into the plant network depicted in Figure V-8. This network permits the following temporal boundary conditions to be specified using an external data file:

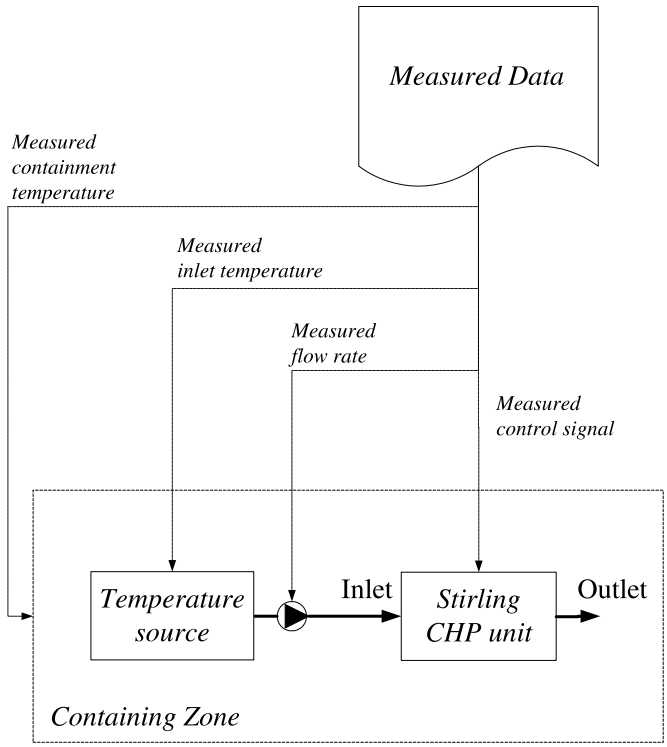

Figure V-8: Plant network employed during dynamic parameter identification

- the containment temperature,
- the cooling water inlet temperature,
- the cooling water inlet flow rate, and
- the WhisperGen control signals.

The plant network imposed boundary conditions corresponding to measurements in subset A on to the combustion-based cogeneration model. Five-day simulations were performed.

Parameter fit optimization methodology

The iterative parameter identification procedure was expedited using the DAKOTA optimization utility. DAKOTA is designed to identify the inputs providing the minimum values

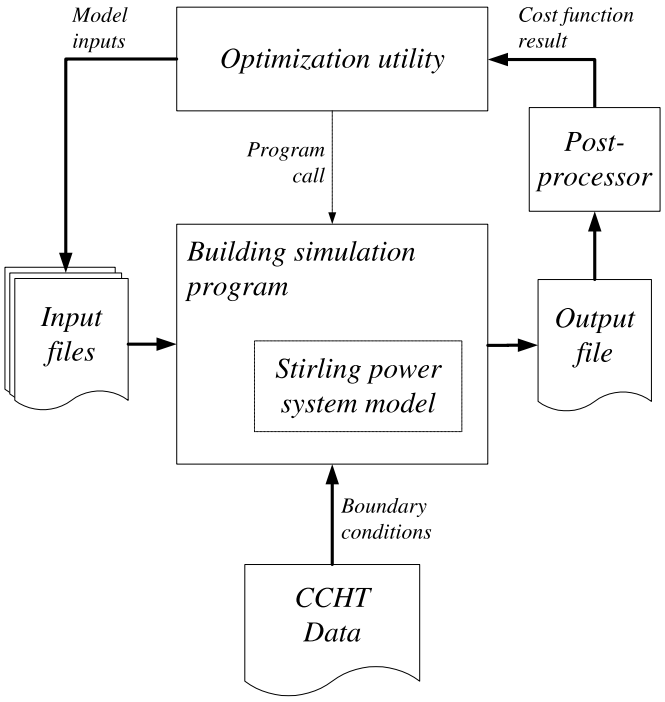

Figure V-9: Coupling between optimization utility and Annex 42 combustion cogeneration model for parameter identification

for a given criteria (called a *cost function*) and supports problems in which the objective functions are calculated by an external program, such as a building simulation program.

The coupling between the optimization utility and the combustion cogeneration model is depicted in Figure V-9. During each iteration, the optimization utility writes the estimated model parameters to the building simulation program's input files. The optimization utility then invokes the building simulation program, which performs a simulation using the parameters described in the input files and the boundary conditions described in the CCHT data. The building simulation program writes the results to an output file, which is post-processed. Finally, the optimization utility interprets the post-processor's output and selects new values for the parameters based on the results of the simulation according to the selected optimization algorithm.

DAKOTA is designed to determine the parameter set providing the the minimum values of specified cost functions. Three cost functions were defined to describe the accuracy of the model's predictions of fuel flow, electrical output and thermal output:

$$\bar{c}_p = \frac{\sum_{i=1}^{n} (P_{net,model} - P_{net,measured})_i^2}{(P_{net,max} - P_{net,min})} \tag{V-2}$$

$$\bar{c}_f = \frac{\sum_{i=1}^{n} (q_{gross,model} - q_{gross,measured})_i^2}{(q_{gross,max} - q_{gross,min})} \tag{V-3}$$

$$\bar{c}_q = \frac{\sum_{i=1}^{n} (q_{recovered,model} - q_{recovered,measured})_i^2}{(q_{recovered,max} - q_{recovered,min})} \tag{V-4}$$

where:

$\bar{c}_p$, $\bar{c}_f$ and $\bar{c}_q$ are cost function results describing the model's predictions of power output, fuel flow and heat recovery, respectively,

$P_{net,model}$ and $P_{net,measured}$ describe the predicted and observed power generation at time step i,

$q_{recovered,model}$ and $q_{recovered,measured}$ describe the predicted and observed rates of heat recovery at time step i,

$q_{gross,model}$ and $q_{gross,measured}$ describe the predicted and observed rates of gross heat input at time step i

$P_{net,max}$ and $P_{net,min}$ describe the maximum and minimum power output observed over the data set,

$q_{recovered,max}$ and $q_{recovered,min}$ describe the maximum and minimum rates of heat recovery observed over the data set, and

$q_{gross,max}$ and $q_{gross,min}$ describe the maximum and minimum rates of gross heat input observed over the data set.

The CCHT experiments did not directly measure the rates of gross heat input (q_{gross}) and heat recovery ($q_{recovered}$), but these values can be easily calculated. The observed rate of gross heat input is as follows:

$$q_{gross,measured} = \dot{m}_{fuel,measured} \cdot LHV_{fuel} \tag{V-5}$$

where:

$\dot{m}_{fuel,measured}$ is the observed fuel flow rate, and

LHV_{fuel} is the lower heating value of the fuel.

And the observed rate of heat recovery is:

$$q_{recovered,measured} = [\dot{m}C_p]_{cw,measured}(T_{cw,o} - T_{cw,i})_{measured} \tag{V-6}$$

$[\dot{m}]_{cw,measured}$ is the measured flow rate of cooling water,

$[C_p]_{cw,measured}$ is the specific heat capacity of the cooling water,

$T_{cw,o,measured}$ is the measured cooling water outlet temperature, and

$T_{cw,i,measured}$ is the measured cooling water inlet temperature.

The denominators in Equations V-2–V-4 reduce the cost functions to dimensionless coefficients of equivalent magnitude. This reduction is important—the magnitudes of the power ($\approx 700\,\mathrm{W}$), heat recovery ($\approx 6\,500\,\mathrm{W}$) and gross heat input ($\approx 7\,500\,\mathrm{W}$) measurements vary widely, and comparison of the unreduced cost-functions would arbitrarily assign more importance to the gross heat input and heat recovery cost functions.

A two-part optimization procedure was used:

- A multi-objective optimization evolutionary algorithm was employed to explore the parameter space. Evolutionary algorithms are well-suited for characterizing cost

function responses over large ranges of input values, and can quickly identify promising solutions. However, evolutionary algorithms may require a disproportionate amount of time to converge on the global minimum.

- A stochastic pattern search algorithm was used to further refine the input parameters. Pattern search algorithms can efficiently identify local minimums, and will locate the global minimum if initialized in its vicinity.

Eldred et al. (2006) provide a detailed overview of these algorithms and their use. The solution nearest to the Pareto-ideal point from the evolutionary algorithm was selected as the starting point for the pattern search. Since DAKOTA's pattern-search algorithm supports only single-objective optimizations, the three cost functions ($\bar{e}_p$, $\bar{e}_f$ and $\bar{e}_q$) were averaged to obtain a single cost function.

Dynamic parameter fit results

The parameter values derived during dynamic calibration of the Annex 42 combustion cogeneration model are presented in Table V-3. While these parameters provide the best agreement between the model predictions and the measurements in the CCHT data subset A, care must be taken in their use and interpretation.

The parameter optimization procedure determined seven parameters using only three criteria to evaluate the suitability of the parameter set. Thus, there may exist multiple sets of parameter inputs that provide the same result, and the set chosen by the parameter optimization procedure may not be the best representation of the actual WhisperGen unit used in the CCHT tests.

Furthermore, the optimization procedure assumes that the combustion cogeneration model is a concise and accurate representation of the test system. If significant disparities exist between the mechanics of the test system and the behaviour of the model, the parameter

Table V-3: Results from dynamic calibration of combustion-based cogeneration model using CCHT data subset A

Parameter		Units	Value
Engine thermal mass	$[MC]_{eng}$	J/°C	18.5×10^3
Heat exchanger thermal mass	$[MC]_{HX}$	J/°C	28.1×10^3
Heat recovery coefficient	UA_{HX}	W/°C	31.8
Heat loss coefficient	UA_{loss}	W/°C	4.64
Nominal engine temperature	T_{nom}	°C	257
Fuel-flow sensitivity	a_{fuel}	–	0.0400
Heat generation efficiency	b_0	–	0.970

optimization procedure will select the model inputs that reduce the effects of these disparities on the error between predicted and measured values. While these values give the best agreement with experimental results, they do not necessarily represent the physical attributes of the test system.

Summary of model inputs

The inputs for the Annex 42 combustion cogeneration model derived from the CCHT WhisperGen measurements are summarized in Table V-4.

Accuracy of the calibration

The success of the calibration procedure was first appraised by comparing the model predictions to the measurements in the calibration data set (subset A). Validation of the calibrated model using the test data subsets B and C is described in Beausoleil-Morrison and Ferguson (2007, Section IV-2)

Table V-4: Summary of input parameters derived from the CCHT WhisperGen cogeneration experiments.

Model parameter		Value	Units
Engine type		*SE*[a]	–
Operating bounds	P_{max}	698	W
	P_{min}	0	W
Maximum outlet temperature	$T_{cw,o_{max}}$	85	°C
Max rate of change in fuel flow	$(d\dot{m}_{fuel}/dt)_{max}$	∞[b]	kg/s^2
Max rate of change in power	$(d\dot{P}_{net}/dt)_{max}$	∞[b]	W/s
Thermal model characteristics	$[MC]_{eng}$	18.5×10^3	J/K
	$[MC]_{HX}$	28.1×10^3	J/K
	UA_{HX}	31.8	W/K
	UA_{loss}	4.64	W/K
Standby mode power use	$P_{net,standby}$	-12.5	W
SE warm-up characteristics[d]	$T_{eng,nom}$	257.3	°C
	k_f	0.0400	–
	k_p	1.0	–
	$r_{fuel,warm-up}$	∞[b]	kg/s
Cool-down characteristics	$P_{net,cool-down}$	-57.5	W
	$t_{cool-down}$	1500.	s
	Cool-down mode	*MC/OC*[c]	–
Electrical efficiency coefficients	a_0	0.0929	–
	a_1–a_{26}	0	–
Thermal efficiency coefficients	b_0	0.970	–
	b_1–b_{26}	0	–
Cooling water mass flow coefficients	c_0–c_8	0	–
Combustion air coefficients	d_0–d_2	0	–

Notes:

[a] *ICE*: internal combustion engine, *SE*: Stirling engine.

[b] The model's rate limiting facilities should be disabled.

[c] *MC*: mandatory cool-down period, *OC*: optional cool-down period. The cool-down configuration can be selected to suite modelling requirements.

Comparison metrics

The accuracy of the calibration was evaluating using metrics quantifying both the instantaneous and cumulative difference in the model predictions. These are:

- the *average absolute error*,
- the *maximum absolute error*,
- the *root mean square error*,
- *Pearson's product-moment correlation coefficient*, and
- the *cumulative error*.

The average absolute error is determined as follows:

$$\bar{e}_{abs} = \frac{1}{n}\sum_{i=1}^{n} |\hat{\theta}_i - \theta_i| \tag{V-7}$$

where:

$\bar{e}_{abs}$ is the average absolute error,

n is the number of measurements, and

$\hat{\theta}_i$ is the measured value at time step i, and θ_i is the predicted value.

The maximum absolute error describes $e_{abs,max}$ the maximum difference between model and predicted values over the course of the simulation:

$$e_{abs,max} = \max\left(\{|\hat{\theta}_i - \theta_i|\}_{i=1}^{n}\right) \tag{V-8}$$

The root mean square error (e_{RMS}) is:

$$e_{RMS} = \sqrt{\frac{1}{n}\sum_{i=1}^{n}(\hat{\theta}_i - \theta_i)^2} \tag{V-9}$$

Pearson's product-moment correlation coefficient is calculated as follows:

$$r^2 = \frac{\sum_{i=1}^{n}\left[\left(\hat{\theta}_i - \bar{\hat{\theta}}\right)\left(\theta_i - \bar{\theta}\right)\right]}{\sqrt{\sum_{i=1}^{n}\left[\left(\hat{\theta}_i - \bar{\hat{\theta}}\right)^2\left(\theta_i - \bar{\theta}\right)^2\right]}} \tag{V-10}$$

$$\bar{\hat{\theta}} = \frac{1}{n}\sum_{i=1}^{n}\hat{\theta}_i \tag{V-11}$$

$$\bar{\theta} = \frac{1}{n}\sum_{i=1}^{n}\theta_i \tag{V-12}$$

Finally, the cumulative error in the fuel consumption, electric output and heat recovery estimates were estimated at the end of the simulation:

$$E_{fuel\ use} = \frac{\sum_{i=1}^{n}(\dot{m}_{fuel,measured} - \dot{m}_{fuel,model})\Delta t}{\sum_{i=1}^{n}\dot{m}_{fuel,measured}\Delta t} \tag{V-13}$$

$$E_{electric\ output} = \frac{\sum_{i=1}^{n}(P_{net,measured} - P_{net,model})\Delta t}{\sum_{i=1}^{n}P_{net,measured}\Delta t} \tag{V-14}$$

$$E_{heat\ recovery} = \frac{\sum_{i=1}^{n}(q_{recovered,measured} - q_{recovered,model})\Delta t}{\sum_{i=1}^{n}q_{recovered,measured}\Delta t} \tag{V-15}$$

where:

$E_{fuel\ use}$ is the cumulative error in the fuel consumption prediction,

$E_{electrical\ output}$ is the cumulative error in power output prediction,

$E_{heat\ recovery}$ is the cumulative error in heat recovery, and

Δt is the time step duration.

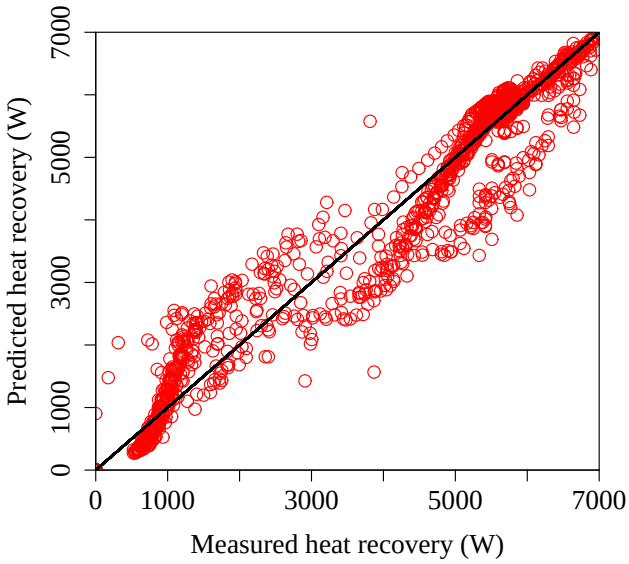

Figure V-10: Comparison of predicted and measured values of heat recovery (CCHT subset A)

Results

Table V-5 quantifies the errors between the model predictions and observations from the calibration data set. The results agree well—the predicted fuel flow correlation coefficient is 1.000, the power generation coefficient is 0.998, and the heat recovery coefficient is 0.994. At the end of the simulation, the predicted cumulative fuel use, electric output and heat recovery all differed from their measured values by less than three percent.

Figures V-10–V-12 plot the correlation between the model predictions and measured values of fuel flow, power output and rate of heat recovery. The predicted fuel flow and power generation agree well with experimental observations while the predicted rates of heat recovery exhibit more variation between measurements and predicted values, with improving agreement at higher rates of heat recovery.

Table V-5: Comparison of Annex 42 combustion cogeneration model predictions with CCHT data (subsets A)

Absolute error, outlet temperature	Average ($\bar{e}_{abs}$)	°C	0.35
	Maximum ($e_{abs,max}$)	°C	3.12
	RMS (e_{RMS})	°C	0.54
	Correlation coeff. (r)	–	0.998
Absolute error, heat recovery	Average ($\bar{e}_{abs}$)	W	78
	Maximum ($e_{abs,max}$)	W	2720
	RMS (e_{RMS})	W	239
	Correlation coeff. (r)	–	0.994
Absolute error, fuel flow	Average ($\bar{e}_{abs}$)	kg/s	0.534×10^{-6}
	Maximum ($e_{abs,max}$)	kg/s	14.0×10^{-6}
	RMS (e_{RMS})	kg/s	171×10^{-6}
	Correlation coeff. (r)	–	1.000
Absolute error, power generation	Average ($\bar{e}_{abs}$)	W	12.0
	Maximum ($e_{abs,max}$)	W	98
	RMS (e_{RMS})	°C	220
	Correlation coeff. (r)	–	0.998
Cumulative heat recovery	Recovered heat	MJ	472
	% error ($E_{heat\ recovery}$)	—	-0.10
Cumulative power production	Power output	MJ	44.8
	% error ($E_{electric\ output}$)	—	2.82
Cumulative fuel use	Fuel use	kg	12.4
	% error ($E_{fuel\ use}$)	—	-0.383

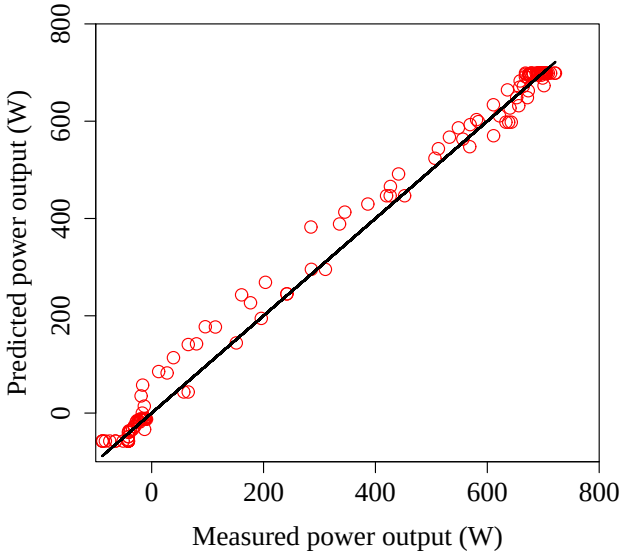

Figure V-11: Comparison of predicted and measured values of power output (CCHT subset A)

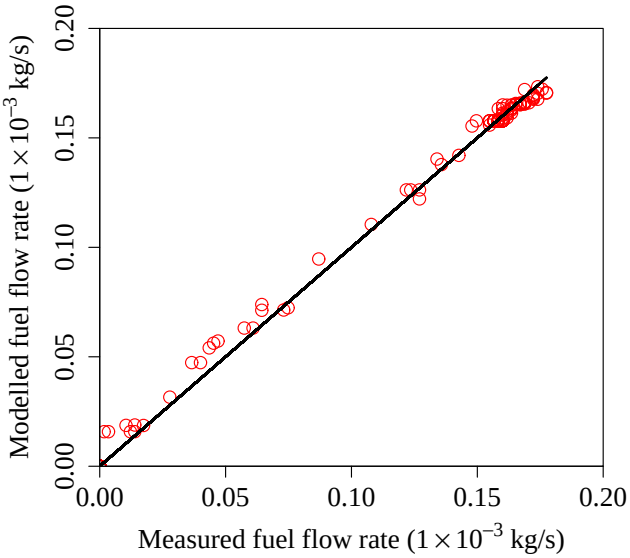

Figure V-12: Comparison of predicted and measured values of fuel flow (CCHT subset A)

The superior agreement achieved in the fuel flow and power output predictions with respect to the heat recovery predictions can be attributed in part to the disparate time frequencies used to collect these data. While the thermal data was collected at one-minute intervals, the electrical data was collected over fifteen-minute intervals, and the one-minute fuel flow data was averaged over ten-minute intervals. Comparing ten- and fifteen-minute averaged data reduces the effects of differences observed between the model's and WhisperGen unit's behaviour over short time scales.

The greater variance between predicted and observed rates of heat recovery may also reflect the WhisperGen unit's sensitivity to cooling water inlet temperature. While coefficients correlating the models heat generation efficiency (η_q) to the cooling water inlet temperature were set to zero in this calibration study, the WhisperGen cogeneration system's electrical and thermal output likely decrease at elevated cooling water inlet temperatures.

Finally, Figures V-13–V-16 plot the predicted fuel flow rate, power generation, outlet temperature and heat production for a five hour period in data subset A. In this particular period, the unit was activated and allowed to operate for nearly two hours, deactivated, and then reactivated one hour later.

These plots illustrate that the calibrated model provides a reasonable approximation of the system behaviour observed in data subset A. However, the ten- and fifteen-minute averaged plots of fuel flow and power output (Figures V-13 and V-14) may conceal disagreement between the calibrated model and physical system at shorter time scales.

Conclusions

In this study, the Annex 42 combustion-based cogeneration model was calibrated using data collected from a WhisperGen Stirling cogeneration unit at CCHT. The CCHT data are not optimally suited for calibration of the combustion-based cogeneration model, and

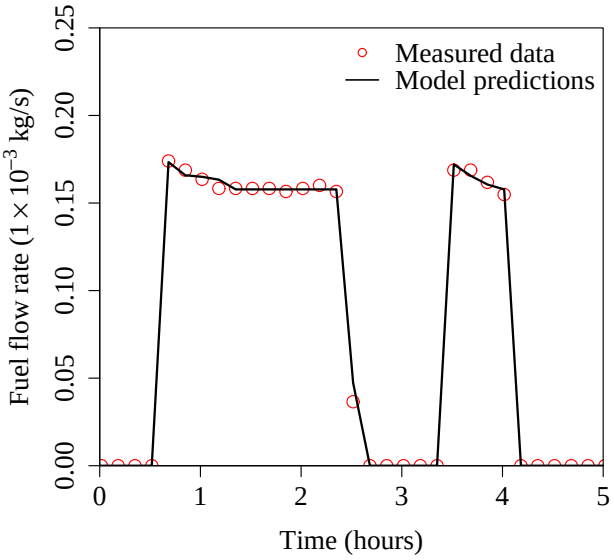

Figure V-13: Comparison between predicted and measured 10-minute averaged fuel flow rate for a five-hour period (CCHT subset A)

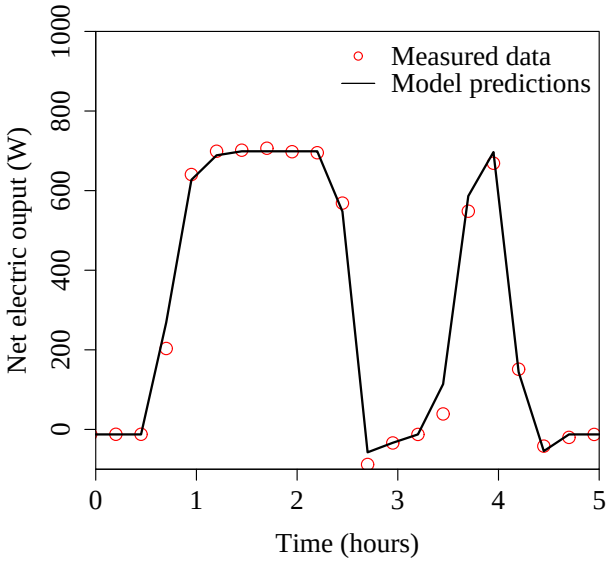

Figure V-14: Comparison between predicted and measured 15-minute averaged net electrical generation for a five-hour period (CCHT subset A)

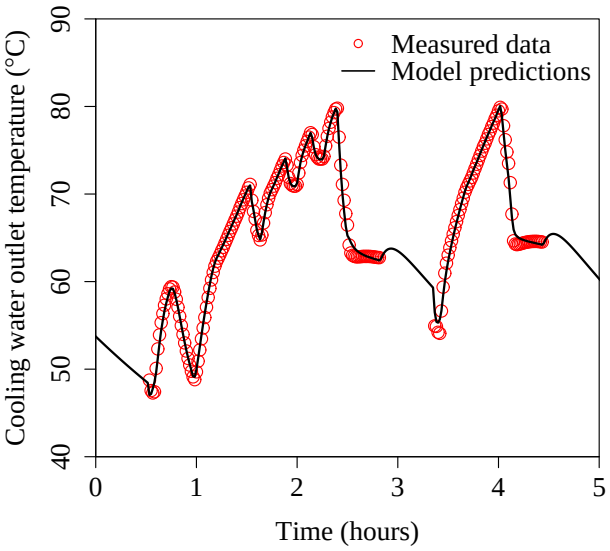

Figure V-15: Comparison between predicted and measured outlet temperatures for a five-hour period (CCHT subset A)

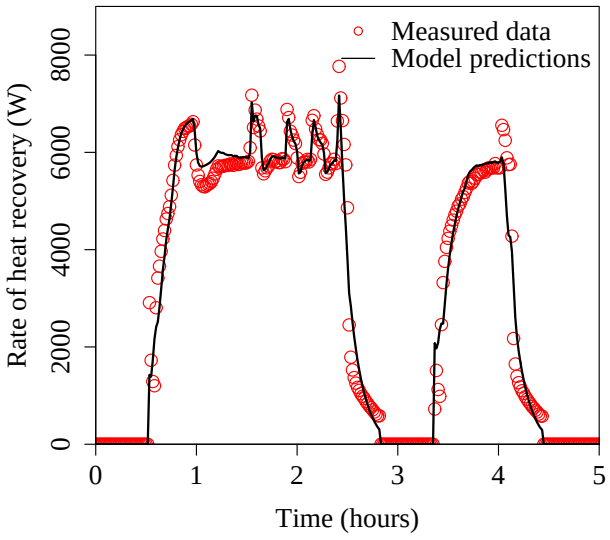

Figure V-16: Comparison between predicted and measured rates of heat recovery for a five-hour period (CCHT subset A)

the model's complexity and corresponding input requirements were reduced to ensure a manageable number of parameters could be derived from limited numbers of experimental measurements.

These simplifications affect the behaviour of the calibrated model. In particular, the calibrated inputs do not describe the affects of cooling water inlet temperature changes on system performance—the calibrated model assumes the electrical and thermal efficiencies are insensitive to the cooling water inlet temperature, but real systems likely exhibit degraded performance at higher inlet temperatures.

Even so, the calibrated model exhibits reasonable agreement when compared with the calibration data set. The predicted fuel use, electric output and heat recovery all differed from observed values by less than 3% over the duration of the data set, and the model provides a good approximation of the observed system behaviour. Therefore, the calibrated model accurately represents the calibration data set.

The calibrated inputs derived in the current study were also used in an empirical validation effort. Validation of the model is described in Beausoleil-Morrison and Ferguson (2007)

This study also illustrates the importance of carefully designing experiments to collect data for calibration and validation exercises. Because the CCHT experiments began prior to Annex 42's working phase, they were not designed with Annex 42's experimental objectives in mind. As the result, tests and measurements that would have been highly useful to Annex 42 were not performed.

References

Beausoleil-Morrison, I. and Ferguson, A., editors (2007). *Inter-model Comparative Testing and Empirical Validation of Annex 42 Models for Residential Cogeneration Devices*. IEA/ECBCS Annex 42 Report. ISBN No. 978-0-662-47562-0.

Eldred, M., Brown, S., Adams, B., Dunlavy, D., Gay, D., Swiler, L., Giunta, A., Hart, W., Watson, J., Eddy, J., Griffin, J., Hough, P., Kolda, T., Martinez-Canales, M., and Williams, P. (2006). *DAKOTA, A Multilevel Parallel Object-Oriented Framework for Design Optimization, Parameter Estimation, Uncertainty Quantifcation, and Sensitivity Analysis: Version 4.0 reference manual*.

Gusdorf, J. (2006). Natural Resources Canada, private communication.

Kelly, N. and Beausoleil-Morrison, I., editors (2007). *Specifications for Modelling Fuel cell and Combustion-Based Residential Cogneration devices within Whole-Building Simulation programs*. IEA/ECBCS Annex 42 Report. ISBN No. 978-0-662-47116-5.

Whisper Tech Ltd. (2002). *WhisperGen Installation Manual: Model PPS24-ACLG*. Whisper Tech Ltd., P.O. Box 13-705, Christchurch New Zealand.

Section VI

Calibration of the Annex 42 Generic Combustion Engine Model to Senertec's 5.5kW ICE-Cogeneration Device

AUTHOR:
Nick Kelly (University of Strathclyde)

Section VI Table of Contents

Acknowledgements VI-3

Introduction to this Section VI-4

Calibration of Performance Maps VI-5

Calibration of Dynamic Characteristics VI-8

Conclusions VI-15

References VI-17

Acknowledgements

The author of this report would like to acknowledge the contributions of the following individuals:

- Ulli Arndt (Forschungsstelle für Energiewirtschaft)
- Leen Peeters (University of Leuven)
- Viktor Dorer (EMPA)

The assistance of the other members of Annex 42 in producing this report is also gratefully acknowledged.

Introduction to this Section

This document describes the calibration of the Annex 42 generic heat engine-based cogeneration model using experimental data from a Senertec 5.5 kW internal-combustion-engine-based (ICE) cogeneration unit. This model is described in detail in Kelly and Beausoleil-Morrison (2007, Section III), which from henceforward will be referred to as the *Model Specifications.*

A two-stage calibration process was adopted. Firstly, the equations describing the steady-state electrical and thermal efficiencies (described in the Model Specifications, Section III) were formulated using data from testing of the unit at different steady-state operating conditions. Secondly, the dynamic characteristics of the model were calibrated using data from the device in thermally transient modes of operation such as warming up or cooling down.

The data for the calibration (and later validation) of the generic cogeneration device model was derived from a set of three experiments conducted by Forschungsstelle für Energiewirtschaft (FFE). The experimental set-up and tests are described in Sections III-1 and IV-4 of this report. These experiments were intended to replicate the loading experienced by the cogeneration unit on a summer, winter and transition day.

Data sets were also available from the University of Leuven (section IV-6 of this report) and EMPA (section IV-7), however these have not been used in this calibration process.

Calibration of Performance Maps

The winter day experimental data was chosen as the data set against which the model was calibrated. This data set includes steady state data along with a complete cold start and cool down cycle, which could be used to determine the dynamic characteristics with regards to operation and cool down (heat loss). The other two FFE data sets were used for validation of the model. The data used in the steady state and calibration processes is shown below in table VI-1.

Table VI-1: data from FFE experiments used in calibration process.

Recorded Data	Units (^oC)	Uncertainty – $U_{95\%}$[1]
ambient temperature	^oC	0.3
exhaust gas temperature	^oC	
coolant temperature (pre-engine jacket)	^oC	0.8
coolant inlet temperature	^oC	0.8
coolant outlet temperature	^oC	0.8
gross electrical power output	kW	0.15
net electrical power output	kW	0.15
coolant flowrate	kg/s	0.05
fuel input power (based on LHV)	kW	0.15
Derived values		
thermal efficiency (based on fuel LHV)	%	-
electrical efficiency (based on net power output)	%	-

Equations of the form shown below could be developed from non-linear regression of the steady state data extracted from the calibration data set.

$$\eta_e = a_0 + a_1 P_{net,ss}^2 + a_2 P_{net,ss} + a_3 \dot{m}_{cw}^2 + a_4 \dot{m}_{cw} + a_5 T_{cw}^2 + a_6 T_{cw} \quad \text{(VI-1)}$$

$$\eta_q = b_0 + b_1 P_{net,ss}^2 + b_2 P_{net,ss} + b_3 \dot{m}_{cw}^2 + b_4 \dot{m}_{cw} + b_5 T_{cw}^2 + b_6 T_{cw} \quad \text{(VI-2)}$$

[1] Unfortunately no direct information is available on uncertainty associated with the data collected. However, information provided by the University of Leuven (refer to Section IV-6) was used to estimate the experimental uncertainty associated with each of the parameters shown in Table VI-1.

The equations describe the electrical and thermal efficiency of the device (η_e and η_q) and a_0 … a_6 are coefficients emerging from the calibration process. As the Senertec device could not modulate its output (other than turning on or off), the equations for both thermal and electrical efficiency need not include the electrical loading variable $P_{net,ss}$. The calibration therefore only used data that featured the device operating at different flow rates ($\dot{m}_{cw}$) and/or coolant temperatures (T_{cw}).

Analysis of this data indicated that there was relatively little influence of the coolant temperature or flow rate on either the electrical or thermal efficiencies (e.g. Figures VI-1a and VI-1b).

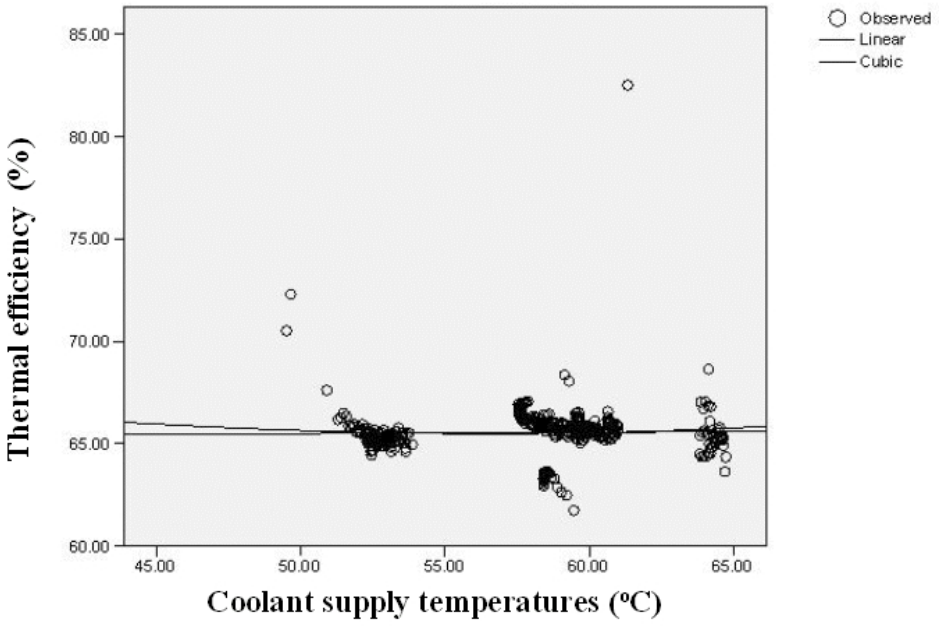

Figure VI-1a: thermal efficiency vs. coolant flow rate

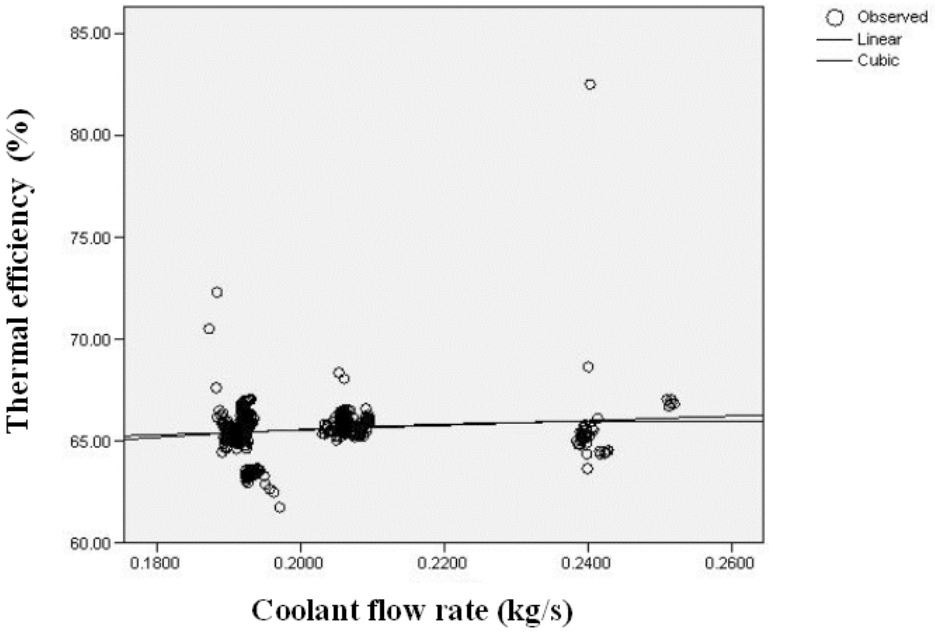

Figure VI-1b: thermal efficiency vs. coolant temperature variation

The insensitivity of efficiency to flow rate and temperature suggested that a fixed thermal and electrical efficiency would be adequate for this particular model instance. Note that lower thermal efficiencies at start up can be accommodated within the model as this is effectively useful heat being absorbed by the engine block thermal mass rather than transmitted to the cooling water.

The following efficiencies emerged from the data analysis and were used in the dynamic calibration process: $\eta_e = 0.27$ and $\eta_q = 0.66$

Calibration of Dynamic Characteristics

Once the performance map characteristics were determined for the device, an iterative process (developed by Ferguson, 2006) was employed, which used the GENOPT software tool and a simplex-search-based approach to determine the model's dynamic parameters. This approach is depicted in Figure VI-2.

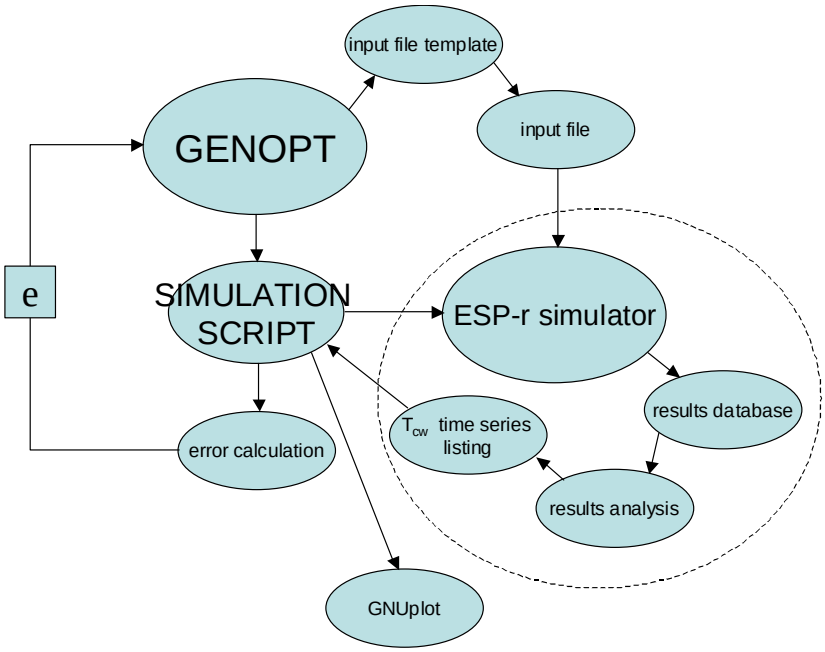

Figure VI-2: operation of the GENOPT-based calibration scheme.

GENOPT drove the simulation software incorporating the cogeneration device model (in this case ESP-r) over multiple simulations. In these simulations the power output required from the generator, the coolant inlet mass flow rate and coolant temperature were derived from experimental data and used as inputs to the simulation model. The calibration was undertaken to determine the values of the following parameters (refer to Model Specifications, Section III):

- UA_{loss} – the heat loss modulus to the environment (W/K)
- UA_{HX} – the heat transfer modulus of the exhaust and jacket heat exchangers (W/K)
- $[MC]_{cw}$ – the thermal capacity of the control volume representing the engine unit and hot side of the heat exchangers (J/K) and

- $[MC]_{eng}$ - the thermal capacity of the control volume representing the cold-side of the heat exchangers (J/K).

At the end of each simulation, the simulated coolant outlet temperature T_s was extracted from the simulation and compared to the experimental value T_{exp} at each time step t. The objective of this process was to minimise the average error e between these two values over the n time steps of the simulation:

$$e = \frac{\sum e_t}{n} \qquad e_t = \left(T_s - T_{\exp}\right)_t \tag{VI-3}$$

The coolant outlet temperature was used as the target for the optimisation as it is the principle, coupling variable between the generic cogeneration model and the systems model into which it would be integrated.

The dataset used in the calibration process was 24 hours long, with measurements taken at a frequency of 1 second. To reduce the computational burden in the iterative calibration simulations, these data sets were modified, with each measurement being averaged over 30 seconds; this allowed simulations to be undertaken with a 30 second rather than 1 second time step resulting in a significant reduction in the computational burden associated with the calibration process.

Figure VI-3 shows some measured temperatures from the winter day experiment. The data used in the dynamic calibration is highlighted. This includes a warm-up of the engine from cold and complete cool down back to ambient conditions.

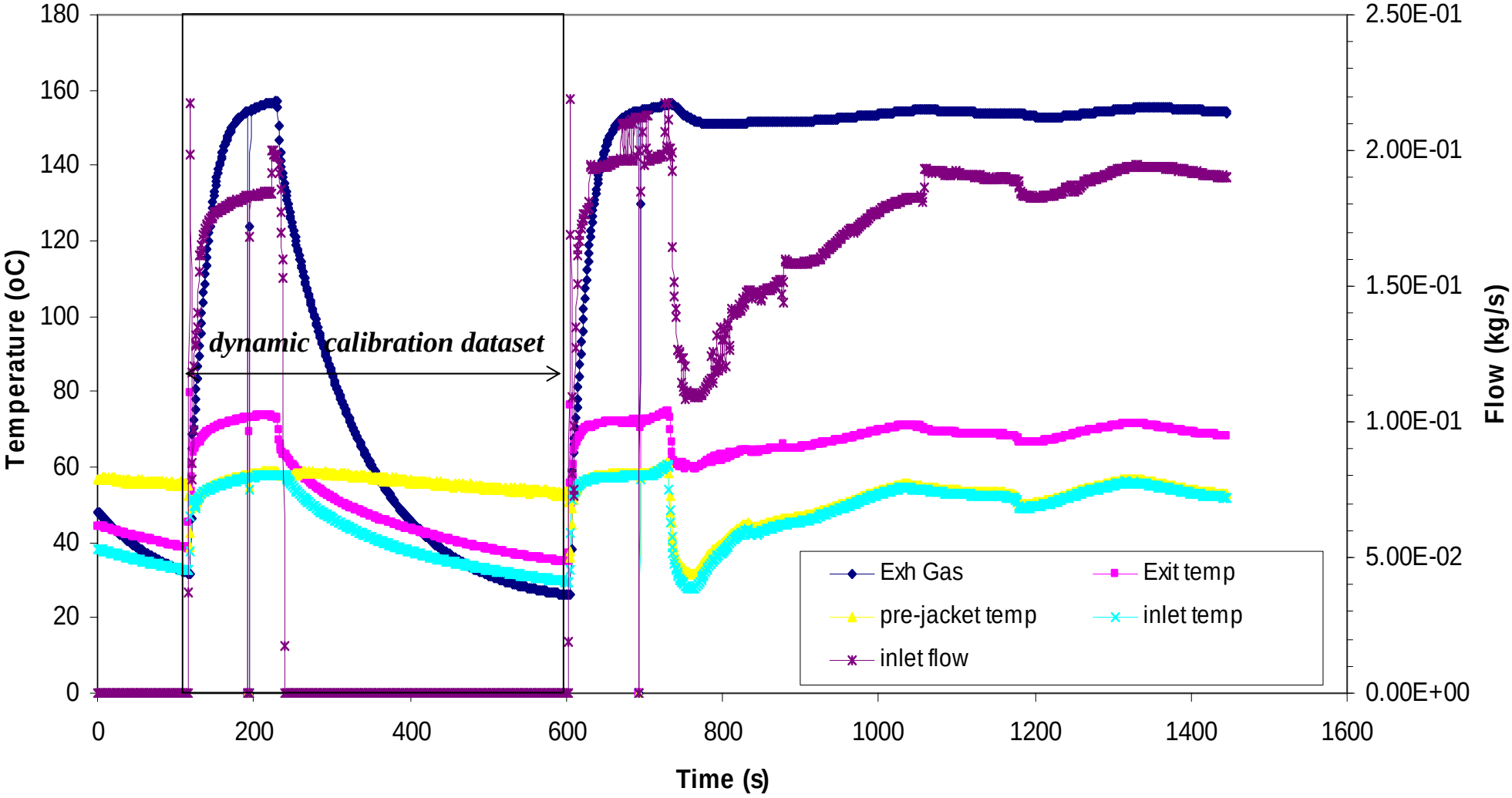

Figure VI-3: excerpt from winter day experimental data

The results from the dynamic calibration are given in Table VI-2.

Figure VI-4 shows the predictions of the calibrated model against the experimental values used in the calibration process.

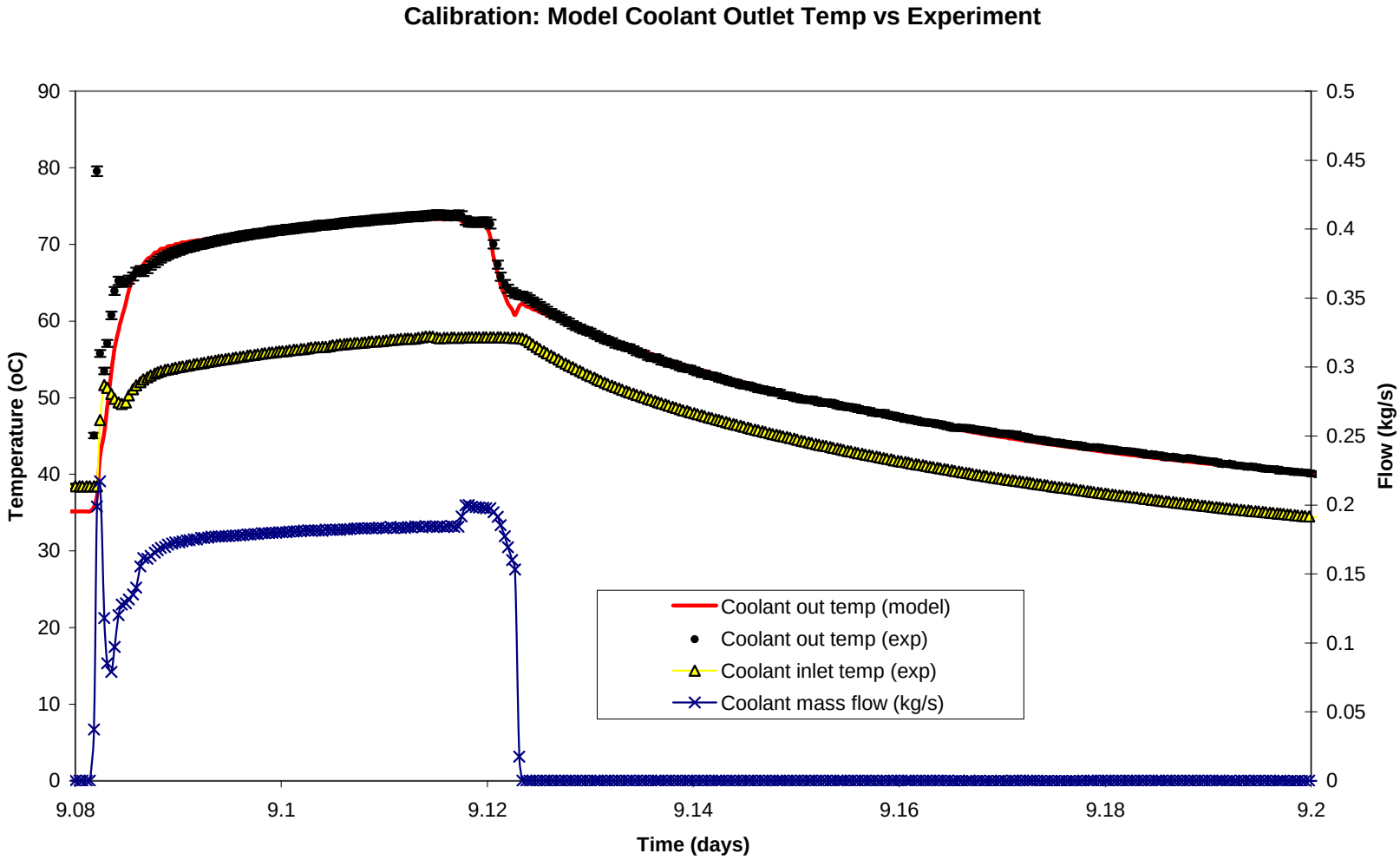

Figure VI-4: model predictions vs. measured values during start-up and cool down cycle

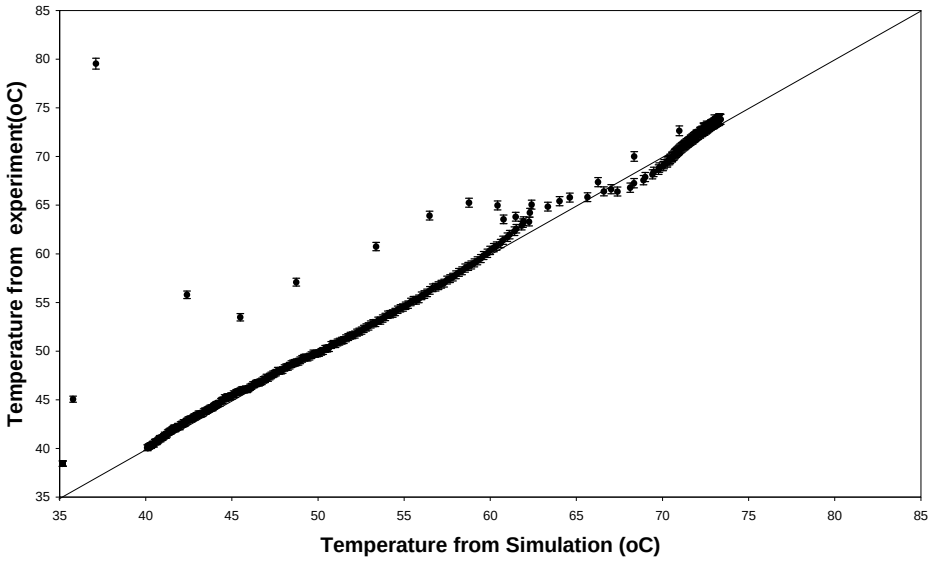

Figure VI-5: comparison of calibrated vs. measured coolant outlet temperature.

Figure VI-4 indicates that the calibrated model accurately reflected the measured data shortly after the engine start up and during the cool down phase. During these periods the model predictions were almost co-incident with the measured data. Figure VI-5 shows that the majority of data points lay along the line of perfect calibration.

The maximum error observed was -42.4^{o}C, which occurred briefly during start up. The mean absolute error in the prediction of the coolant outlet temperature was 0.5^{o}C, which lies within the $U_{95\%}$ uncertainty band for the measurements. The correlation coefficient between the calibrated model output and the experimental data was 0.98.

The deviations between the measured and calibrated results, particularly during start up and obvious point of inflexion between the calibrated and experimental results are discussed below.

Start up Period: there were a small number of points that lay above the line of perfect calibration. These corresponded to points measured during the start up period of the unit and indicate that the model under predicted the rise in temperature of the cogeneration

unit in the first few minutes of operation. Figure VI-4 shows this more clearly, with the measured coolant outlet temperature showed a distinct “spike”, which was not replicated by the model. The reasons for this discrepancy lay in the construction of the model (Section III of the Model Specifications); all of the heat from the combustion process was initially absorbed by control volume 1, which represents the engine block. This resulted in a slow change in temperature of the coolant. In reality hot exhaust gases will quickly enter the exhaust gas heat exchanger, warming an initially stationary “plug” of coolant, resulting in the observed spike in temperature. This effect disappeared after the first 1-2 minutes of operation. Note however, that this shortcoming had relatively little effect on the accuracy of the calibrated model with 96% of predicted coolant outlet temperature values being within 5% of the measured value.

Point of inflexion: Figure VI-5 shows a clear point of inflexion around 67^{o}C. This temperature was roughly equal to the mean temperature of the cooling water during normal operation and deserves further investigation. One explanation could be that the heat transfer characteristics in the heat exchanger changed slightly at this point; with the model as currently configured, it was assumed that heat transfer characteristics of the heat exchanger are constant over the operating temperature range of the unit. However, as is evidenced from figure VI-4, the impact on this assumption with regards to replicating the dynamic performance of the calibrated unit was small.

Conclusions

The following calibrated parameters emerged from the static and dynamic calibration process:

Table VI-2: calibrated parameters for 5.5kW Senertec ICE cogeneration device.

Calibration parameters		
Steady State Parameters		
	a_0	0.27
	$a_1, a_2, a_3, a_4, a_5, a_6$	*all* 0.0
	b_0	0.66
	$b_1, b_2, b_3, b_4, b_5, b_6$	*all* 0.0
Dynamic Parameters		
UA_{loss}	W/K	13.7
UA_{HX}	W/K	741
$[MC]_{cw}$	J/K	1000.7
$[MC]_{eng}$	J/K	63605.6
Validity of Application		
$P_{net,ss}$= 5.5kW or $P_{net,ss}$= 0kW		
$0.0 \leq \dot{m}_{cw} \leq 0.217$ kg/s		
$34.7 \leq T_{cw} \leq 79.5^{o}C$		

The generic cogeneration model developed within Annex 42 has been calibrated using data from a 5.5kW Senertec ICE engine unit using an iterative calibration approach. The following was observed.

- The calibrated model showed good agreement with the initial calibration dataset with 96% of predicted temperatures being within 5% of the experimental value.
- Some excursions from the measured data were identified. These occurred in the few minutes after a cold start: the cause was identified as a shortcoming in the modelling of the heat exchange in the exhaust gas heat exchanger.
- There was also an issue with coolant temperatures around 67^{o}C; around this point the model predictions go through a point of inflexion compared to the line of perfect calibration. The cause of this phenomenon is not clear.
- Using fixed thermal and electrical efficiencies for energy conversion proved more-than-adequate to give a respectable calibration.

Despite the minor problems identified, it can be concluded that the model gives an accurate representation of the ICE unit's dynamic performance in start up and cool down modes.

References

Kelly N. and Beausoleil-Morrison I., editors (2007), *Specifications for Modelling Fuel Cell and Combustion- Based Residential Cogeneration Device within Whole-Building Simulation Programs*, IEA/ECBCS Annex 42 Report, ISBN No. 978-0-662-47116-5.

Ferguson A. and Kelly N. (2006), "Modelling Building-integrated Stirling CHP Systems", Proc. eSim 2006 The Canadian Building Simulation Conference, Toronto, Canada, pp91-98.

Section VII

Calibration of the Annex 42 Fuel Cell Cogeneration Model to Fuel Cell Technologies Ltd.'s SOFC Device

AUTHORS:

Ian Beausoleil-Morrison (Natural Resources Canada)

Kathleen Siemens (Natural Resources Canada)

Section VII Table of Contents

Introduction to this section VII-3
Calibration of gas-to-water heat exchanger VII-4
Calibration of FCPM electrical efficiency VII-9
Calibration of FCPM transient response VII-11
Calibration of FCPM air supply VII-13
Calibration of power conditioning system VII-14
Calibration of dilution air system VII-16
Calibration of FCPM skin losses VII-19
References VII-23
Appendix A : Goodness of fit metrics VII-24

Introduction to this section

Data from 45 of the experiments described in sections III-4 and IV-13 were used to calibrate the Annex 42 fuel cell cogeneration model (FC-cogeneration). This section describes the process used to calibrate each relevant control volume of the model. The reader is referred to Section II of the Annex 42 final report that describes the FC-cogeneration model for details on the model's formulation (Kelly and Beausoleil-Morrison, 2007), which is referred to here as the *model specifications*. Equation symbols used here correspond to those in the model specifications and frequent reference is made to section and equation numbers from that report.

Calibration of gas-to-water heat exchanger

The gas-to-water heat exchanger was calibrated with *method 4* described in section II-7 of the model specifications.

Data from 17 experiments were used to derive the heat exchanger's $(UA)_{eff}$ value at various water ($\dot{N}_{water}$) and gas ($\dot{N}_{aux-mix}$) flow rates and water inlet temperatures ($T_{water,in}$). There was no condensation of water vapour from the exhaust gases during these experiments. The procedure outlined in section IV-13 was applied to each experiment to produce a set of 17 experiment-averaged $(UA)_{eff}$ values at various combinations of $T_{water,in}$, $\dot{N}_{water}$, and $\dot{N}_{aux-mix}$. The $T_{water,in}$ and $\dot{N}_{water}$ values were measured using the instruments described in section IV-13. The $\dot{N}_{aux-mix}$ values were derived from the measured flow rates of the fuel and air supplied to the FCPM with the assumption that these fully reacted and that the $\dot{N}_{aux-mix}$ stream was composed only of these reactants. The $(UA)_{eff}$ values were derived from four temperature and one flow rate measurement, as detailed in equation IV-13-1.

These data represent the calibration data set for equation II-45 of the model specifications and are contained in the accompanying file *FCT_data/gas-to-water-HX-sensible.dat*. This file contains the experiment-averaged values for $\dot{N}_{water}$, $\dot{N}_{aux-mix}$ (kmol/s), $(UA)_{eff}$ (W/K), and the associated $U_{95\%}$ uncertainties (refer to section IV-13).

A non-linear regression method was used to establish the values of the $hx_{s,i}$ coefficients that produced the best fit to equation II-45 of the model specifications. The values of the coefficients determined from this analysis are presented in Table VII-1. This table also presents the ranges of $T_{water,in}$, $\dot{N}_{water}$, and P_{el} (the electrical operating point establishes the value of $\dot{N}_{aux-mix}$) for which the correlation is applicable.

Figure VII-1 compares the $(UA)_{eff}$ determined with model specifications' equation II-45 and the coefficients of Table VII-1 with the $(UA)_{eff}$ values derived from the measurements. The $U_{95\%}$ uncertainty bars are plotted in the figure. The left side of the figure provides a view normal to the $\dot{N}_{aux-mix}$ axis while the right side provides a view normal to the $\dot{N}_{water}$ axis. As can be seen, the functional form of model specifications' equation II-45 well represents the dependency of $(UA)_{eff}$ on the two flow rates. The calibrated values lie within the error bars for each of the 17 data points.

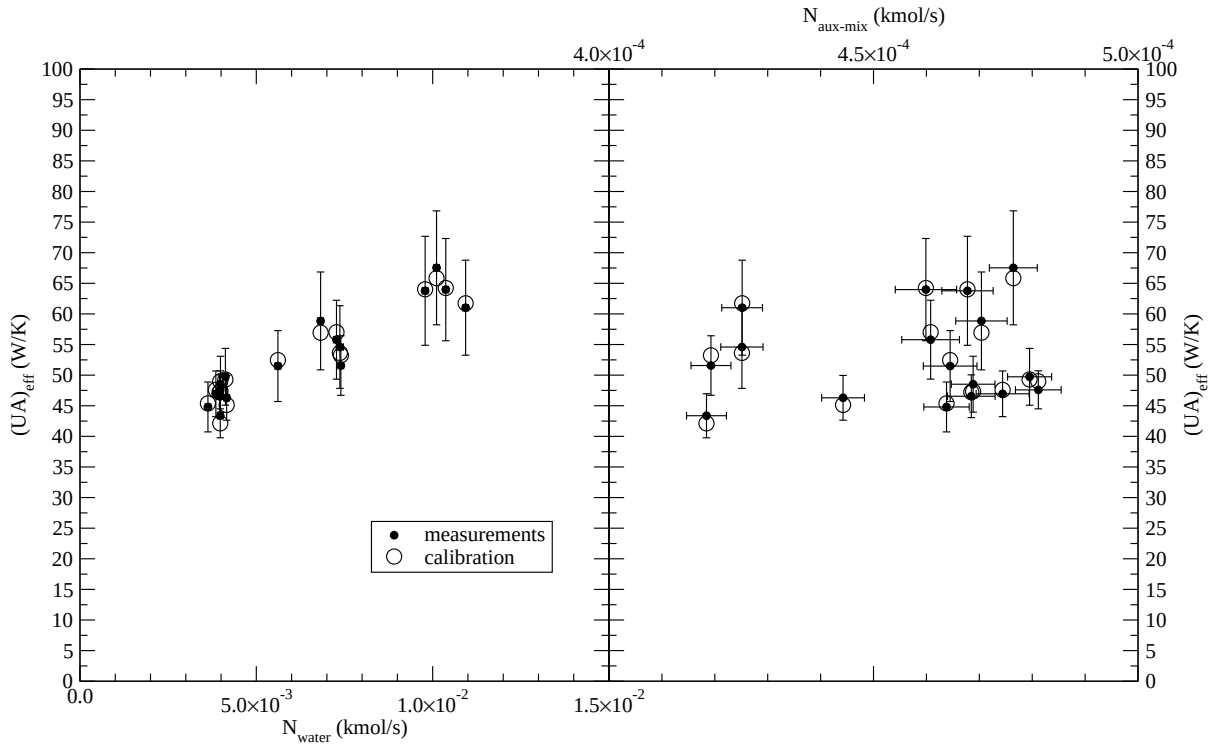

Figure VII-1: Calibrated $(UA)_{eff}$ versus measurements as a function of $\dot{N}_{water}$ (left) and $\dot{N}_{aux-mix}$ (right)

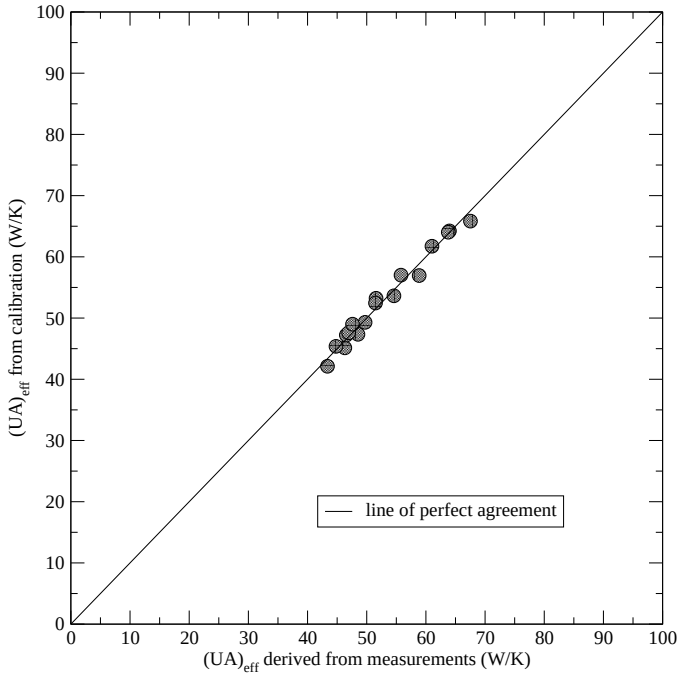

Figure VII-2: Goodness of fit between calibrated and measured $(UA)_{eff}$

Figure VII-2 provides another indication of the goodness of fit between the calibrated $(UA)_{eff}$ values and those derived from measurements. The coefficient of determination (r^2 value) was 0.98. The average error (difference between the calibrated $(UA)_{eff}$ value and that derived from measurements) was 1.0 W/K (1.9%) while the root-mean-square error was 1.1 W/K (2.1%). The maximum error for a single point was 1.9 W/K (3.2%). (The calculation of these metrics is detailed in Appendix A.)

A number of tests, in addition to the 17 described above, were conducted to explore the operation of the heat exchanger under condensing conditions. One of these tests was configured to identify $T_{cond-threshold}$ of the model specifications' equation II-50. This variable represents the threshold of the water inlet temperature above which condensation does not occur. The examination of the tilt bucket readings during preliminary testing indicated an approximate range within which $T_{cond-threshold}$ lay. However, each of these tests was time consuming. As elaborated in section IV-13, the tilt bucket instrument was filled only after the cogeneration device's internal condensate reservoir became filled and was pumped out. Steady conditions had to be held for long periods of time (in some cases many hours) in order to register readings at the tilt bucket.

Section IV-13 explained how the formation of condensation from the exhaust gases led to erroneous $T_{aux-mix}$ thermocouple readings. Advantage was taken of this fact to calibrate $T_{cond-threshold}$. By controlling the water loop illustrated in Figure III-4.1, $T_{water,in}$ was slowly reduced from 33°C, which the preliminary testing had indicated was above $T_{cond-threshold}$. For the FCPM's electrical output exercised in this test, $T_{aux-mix}$ was approximately 280°C. As shown in Figure VII-3 the thermocouple produced reliable data for the first portion of the test. (It should have read approximately 280°C throughout the test.) The thermocouple, however, began producing unreliable readings once $T_{water,in}$ was reduced to 23°C. This event indicated the first formation of liquid water which dripped onto the thermocouple. Even as the inlet water temperature was warmed to 35°C, the thermocouple continued to produce unreliable readings, indicating that condensation continued to form. It took considerable time for the thermocouple readings to stabilize. This tends to indicate that although the onset of condensation requires a low value of $T_{water,in}$, once condensing conditions have been achieved condensation can occur at warmer temperatures. Based upon this test it was decided to set $T_{cond-threshold}$ to 35°C.

The 1-minute averaged data illustrated in Figure VII-3 are contained in the accompanying file *FCT_data/gas-to-water-HX-Tcondthreshold.dat*.

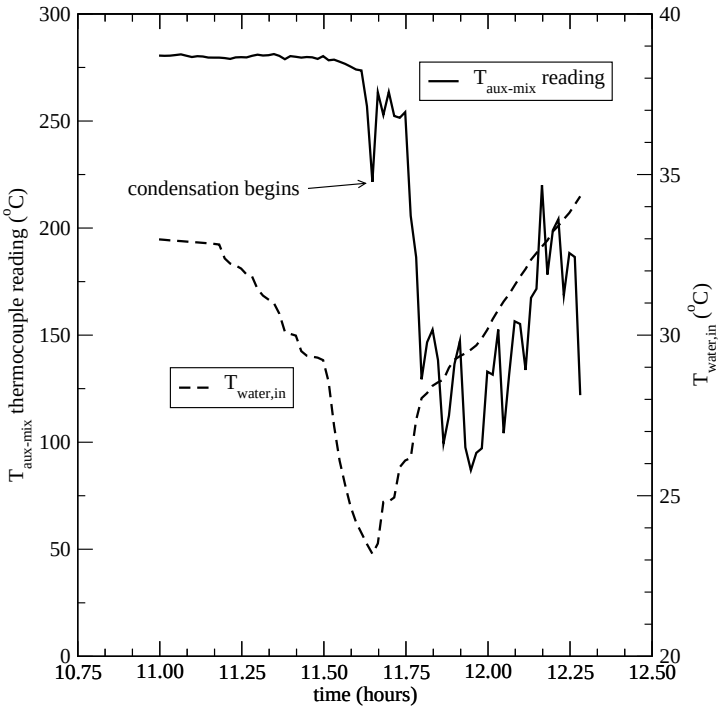

Figure VII-3: Identification of $T_{cond-threshold}$

A series of 7 tests were then conducted at various water flow rates and values of $T_{water,in}$ in order to establish the $hx_{l,i}$ coefficients of the model specifications' equation II-50. Sufficient time was allowed in each test to achieve steady conditions. Due to practical constraints, however, these tests could only be conducted with a nearly constant ratio of water vapour in the exhaust gas stream (refer to $\dot{N}_{H_2O}/\dot{N}_{aux-mix}$ in model specifications' equation II-50).

The data from these 7 experiments are contained in the accompanying file *FCT_data/gas-to-water-HX-latent.dat*. This file contains the experiment-averaged values for $T_{water,in}$, $\dot{N}_{H_2O}/\dot{N}_{aux-mix}$, and $\dot{N}_{H_2O-cond}$, and the associated $U_{95\%}$ uncertainties (refer to section IV-13). The $T_{water,in}$ and $\dot{N}_{H_2O-cond}$ values were measured using the instruments described in section IV-13. The $\dot{N}_{H_2O-cond}$ values were derived from the measured flow rates of the fuel and air supplied to the FCPM with the assumption that these fully reacted and that the $\dot{N}_{aux-mix}$ stream was composed only of these reactants.

A non-linear regression method was used to establish the values of the $hx_{l,i}$ coefficients that produced the best fit of these data to the model specifications' equation II-50. As elaborated above, $T_{cond-threshold}$ was set to 35°C to perform this regression. The values of the coefficients determined from this analysis are presented in Table VII-1. This table also presents the ranges of $T_{water,in}$ and P_{el} (the electrical operating point establishes the value of $\dot{N}_{H_2O}/\dot{N}_{aux-mix}$) for which the correlation is applicable.

Figure VII-4 compares the $\dot{N}_{H_2O-cond}$ determined with the model specifications' equation II-50 and the coefficients of Table VII-1 with the $\dot{N}_{H_2O-cond}$ values derived from the measurements. The coefficient of determination (r^2 value) was 0.96. The average error (difference between calibrated values and those derived from measurements) was 10^{-6} $kmol/s$[1] while the root-mean-square error was $1.2 \cdot 10^{-6}$ $kmol/s$. The maximum error for a single point was $2.1 \cdot 10^{-6}$ $kmol/s$. The uncertainty bars determined in section IV-13 are plotted in the figure. As can be seen, the functional form of the equation reasonably represents the dependency of $\dot{N}_{H_2O-cond}$ upon $T_{water,in}$. The calibrated values lie within the error bars for five of the seven data points. The greatest deviation between measurement and calibration occurs at $T_{water,in} \approx 30^{o}C$ where the condensation flow rate is very small.

[1] To place these numbers in context, a condensation rate of 10^{-6} $kmol/s$ results in approximately 40 W of heat transfer.

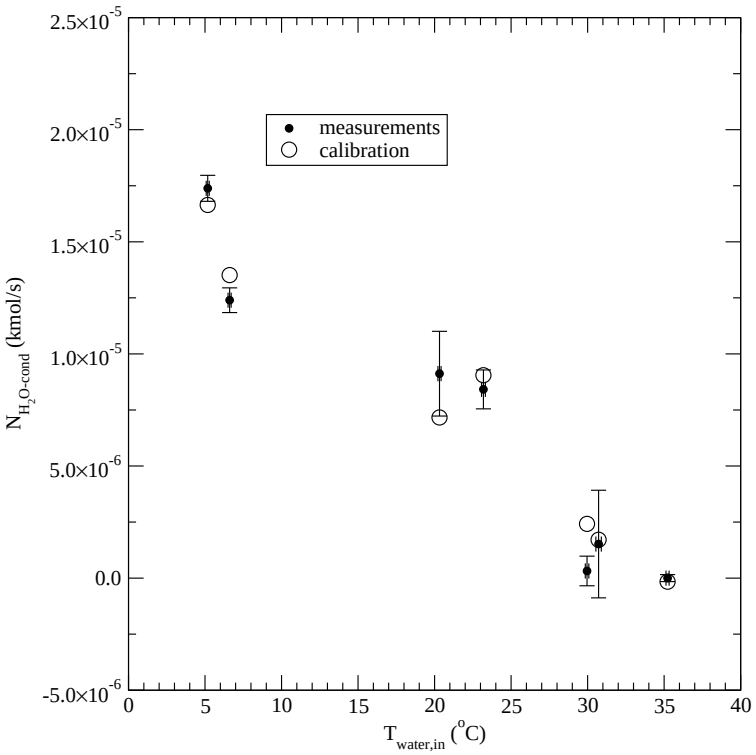

Figure VII-4: Goodness of fit between calibrated and measured $\dot{N}_{H_2O-cond}$

Calibration of FCPM electrical efficiency

Data from 7 experiments were used to calibrate the FCPM electrical efficiency, as treated in section II-2.2 of the model specifications.

Referring to the model specifications' equation II-9, the gross power (P_{gross}) was measured at the power take-offs exiting the fuel cell bundle. The total draw of DC-powered ancillaries ($P_{el,ancillaries-DC}$) was measured and subtracted from P_{gross} to yield the net DC power production of the FCPM (P_{el}). Both the air supply blower (refer to section II-3 of the model specifications) and the dilution air fan (refer to section II-9 of the model specifications) were included in $P_{el,ancillaries-DC}$. Consequently, with this calibration approach the air supply blower control volume is nullified and its performance is aggregated with that of the FCPM. Likewise, the performance of the dilution air fan is aggregated with that of the FCPM, although other aspects of the dilution air system are treated separately, as will be discussed later in this section.

The data from the 7 experiments were used to derive P_{el} values using the model specifications' equation II-9 and to derive the electrical efficiency (ε_{el}) using the model specifications' equation II-10. These data are contained in the accompanying file *FCT_data/FCPM-elec-eff.dat*. This file contains the experiment-averaged values for P_{el}, ε_{el}, and the associated $U_{95\%}$ uncertainties (refer to section IV-13). The P_{el} values were derived from voltage and current measurements described in section IV-13. The ε_{el} values were derived from the derived P_{el} values and the measured fuel supply rate and the fuel's lower heating value, which was calculated using the fuel composition as determined from the measurements outlined in section IV-13.

A non-linear regression method was used to establish the values of the ε_i coefficients that produced the best fit to the model specifications' equation II-8. The values of the coefficients determined from this analysis are presented in Table VII-1. This table also presents the range of P_{el} for which the correlation is applicable. The model specifications' equation II-8 includes coefficients that characterize the FCPM's degradation due to operating time and stop-start cycling. However, the experiments did not examine this aspect of the system's performance. Hence, for the purpose of calibrating equation II-8 the D and L coefficients were set to zero.

Figure VII-5 compares the ε_{el} determined with model specifications' equation II-8 and the coefficients of Table VII-1 with the ε_{el} values derived from the measurements. The $U_{95\%}$ uncertainty bars are plotted in the figure. The coefficient of determination (r^2 value) was 0.58. The average error (difference between the calibrated ε_{el} value and that derived from measurements) was 0.001 (0.4%) while the root-mean-square error was 0.002 (0.6%). The maximum error for a single point was 0.004 (1.2%).

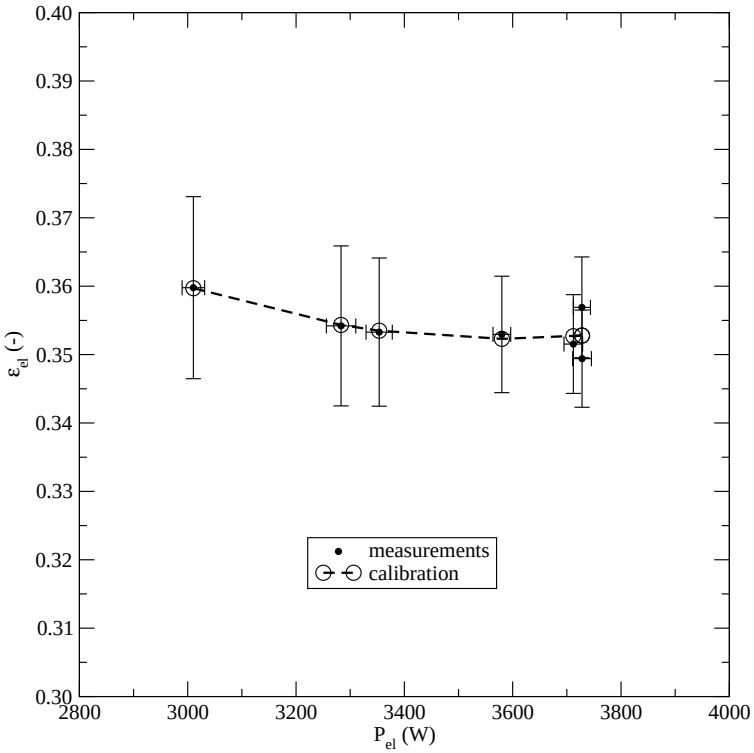

Figure VII-5: Calibrated ε_{el} versus measurements

Calibration of FCPM transient response

Data from a single experiment were used to calibrate the FCPM's transient response, as treated in section II-2.4 of the model specifications.

During this experiment the control system was manually overridden and the stack current demanded from the cogeneration device was reduced from its maximum output by approximately 15%. Three such experiments were conducted. In each case the demanded current was reduced faster than for the preceding experiment. The experiment selected for the calibration had the fastest decrease in demanded current. It is possible that the device can sustain a faster decrease in power output, but experiments were not conducted to determine this.

The data gathered during the transient response experiment are illustrated in Figure VII-6, which plots P_{el} as a function of time. The 1-minute averaged P_{el} illustrated in this figure are contained in the accompanying file *FCT_data/FCPM-transient-response.dat*. The uncertainty estimates are based upon the instrumentation bias errors. The P_{el} values were

derived from voltage and current measurements described in section IV-13.

The 15 minute period indicated in the figure was used to calibrate the transient response for decreasing power and the 2.5 minute period was used to calibrate the transient response for increasing power. The $(dP_{el}/dt)_{\max}$ coefficients presented in Table VII-1 are calculated with the P_{el} and time values at the start and end points of these two periods.

Section II-2.4 of the model specifications also includes parameters to characterize the start-up and cool-down periods. However, no experiments were conducted to examine these aspects of the system's performance.

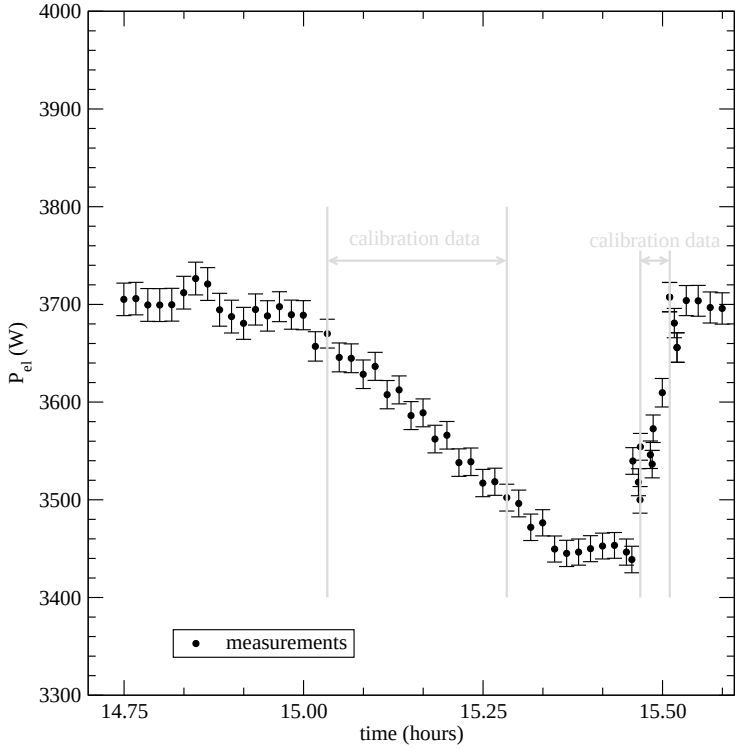

Figure VII-6: Calibration data for FCPM transient response

Calibration of FCPM air supply

Data from 28 experiments were used to calibrate the FCPM air supply. This calibration was performed with *method 2*, as treated in section II-2.6 of the model specifications.

These data are contained in the accompanying file *FCT_data/air-supply.dat*. This file contains the experiment-averaged values for P_{el}, T_{air}, $\dot{N}_{air}$, and the associated $U_{95\%}$ uncertainties (refer to section IV-13). The T_{air} and $\dot{N}_{air}$ values were measured using the instruments described in section IV-13. The P_{el} values were derived from voltage and current measurements described in section IV-13.

A non-linear regression method was used to establish the values of the a_i coefficients that produced the best fit to the model specifications' equation II-16. The values of the coefficients determined from this analysis are presented in Table VII-1. This table also presents the range of P_{el} and T_{air} for which the correlation is applicable.

Figure VII-7 compares the $\dot{N}_{air}$ determined with model specifications' equation II-16 and the coefficients of Table VII-1 with the $\dot{N}_{air}$ values derived from the measurements. The $U_{95\%}$ uncertainty bars are plotted in the figure. The coefficient of determination (r^2 value) was 0.77. The average error (difference between the calibrated $\dot{N}_{air}$ value and that derived from measurements) was $9.7 \cdot 10^{-6}$ kmol/s (2.3%) while the root-mean-square error was $1.2 \cdot 10^{-5}$ kmol/s (2.8%). The maximum error for a single point was $2.3 \cdot 10^{-5}$ (5.6%).

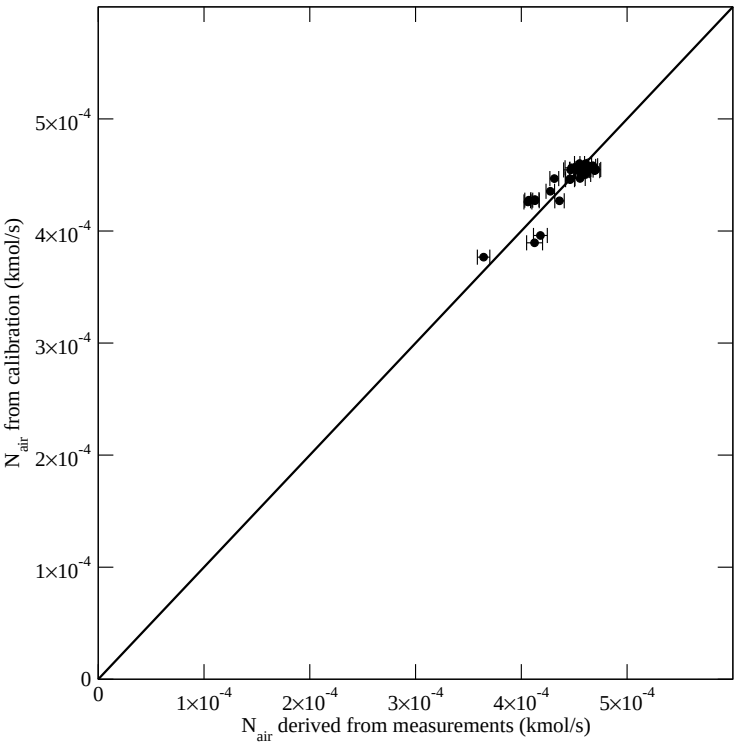

Figure VII-7: Calibrated $\dot{N}_{air}$ versus measurements

Calibration of power conditioning system

Data from 7 experiments were used to calibrate the power conditioning system, as treated in section II-11 of the model specifications.

These data are contained in the accompanying file *FCT_data/power-conditioning.dat*. This file contains the experiment-averaged values for P_{PCU-in} η_{PCU}, and the associated $U_{95\%}$ uncertainties (refer to section IV-13). The measurements indicated that the batteries draw a near-constant trickle of power but experiments were not performed to separately calibrate the battery. Consequently, in this calibration the battery control volume is nullified and its performance is aggregated with that of the power conditioning system. In this way, the DC power flowing into the power conditioning system (P_{PCU-in}) is taken to equal the DC power produced by the FCPM (P_{el}). As previously described, this power flow was derived from voltage and current measurements described in section IV-13. The η_{PCU} values were derived from the derived P_{PCU-in} values and the measured AC output using the model specifications' equation II-76.

A non-linear regression method was used to establish the values of the u_i coefficients that produced the best fit to the model specifications' equation II-77. The values of the coefficients determined from this analysis are presented in Table VII-1. This table also presents the range of P_{el} for which the correlation is applicable.

Figure VII-8 compares the η_{PCU} determined with model specifications' equation II-77 and the coefficients of Table VII-1 with the η_{PCU} values derived from the measurements. The $U_{95\%}$ uncertainty bars are plotted in the figure. The coefficient of determination (r^2 value) was 0.90. The average error (difference between the calibrated η_{PCU} value and that derived from measurements) was 0.001 (0.1%) while the root-mean-square error was 0.001 (0.15%). The maximum error for a single point was 0.002 (0.2%).

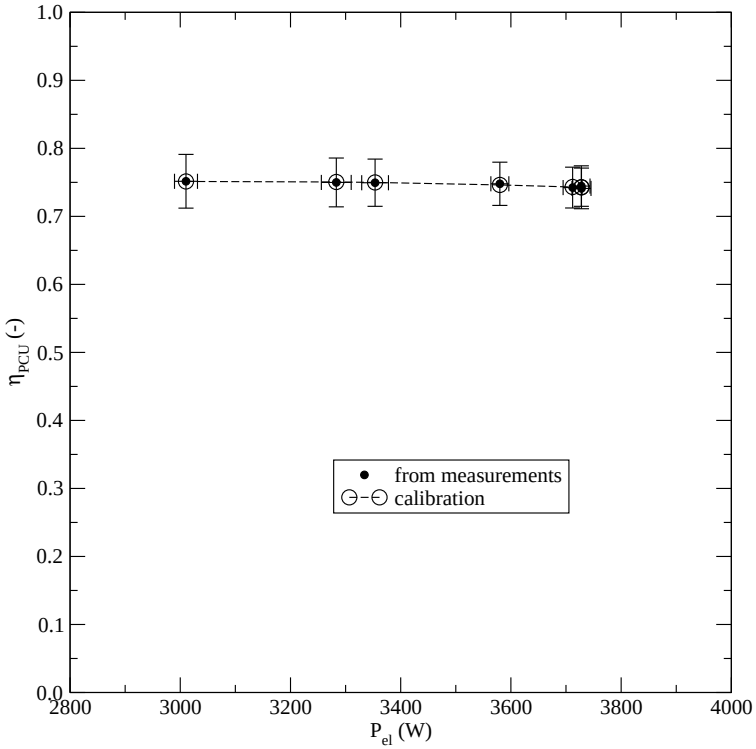

Figure VII-8: Calibrated η_{PCU} versus measurements

Calibration of dilution air system

Data from 7 experiments were used to calibrate the dilution air system, as treated in section II-9 of the model specifications.

The calibration of the dilution air system involves establishing three constant values: the dilution air flow rate ($\dot{N}_{dilution-air}$), the electrical power draw of the dilution fan ($P_{el,dilution-fan}$), and the stack heat loss ($q_{FCPM-to-dilution}$).

As previously elaborated (refer to the section on the calibration of the FCPM electrical efficiency), the performance of the dilution air fan was aggregated with that of the FCPM by including its power draw in the $P_{el,ancillaries-DC}$ term. Consequently, $P_{el,dilution-air}$ is set to zero to avoid double counting this power draw.

The data used to calibrate $\dot{N}_{dilution-air}$ and $q_{FCPM-to-dilution}$ are contained in the accompanying file *FCT_data/dilution-air.dat*. This file contains the experiment-averaged values for P_{el}, $\dot{N}_{dilution-air}$, $q_{FCPM-to-dilution}$ and the associated $U_{95\%}$ uncertainties (refer to section IV-13). The P_{el} values were derived from voltage and current measurements described in section IV-13. The $\dot{N}_{dilution-air}$ values were derived from the measurement of the velocity in the exhaust chimney and the derived $\dot{N}_{aux-mix}$ values using the model specifications' equation II-68. (Note that $\dot{N}_{HX-exh} = \dot{N}_{aux-mix}$.) The $\dot{N}_{aux-mix}$ values were themselves derived from the measured flow rates of the fuel and air supplied to the FCPM with the assumption that these fully reacted and that the $\dot{N}_{aux-mix}$ stream was composed only of these reactants. The $q_{FCPM-to-dilution}$ values were derived from the derived $\dot{N}_{dilution-air}$ values, the derived $\dot{N}_{aux-mix}$ values, the measured temperature of the gas at the heat exchanger's outlet, the measured temperature of the ambient air, the measured temperature in the exhaust chimney, the derived P_{el} values, and the derived η_{PCU} values (the derivation of this quantity is treated in the section on the calibration of the power conditioning efficiency). These derived and measured quantities were used to derive $q_{FCPM-to-dilution}$ using the model specifications' equation II-70 with the assumption that the heat gains from the power conditioning system were added to the dilution air stream.

The value of $\dot{N}_{dilution-air}$ was determined by averaging over the 7 experiments. This value is presented in Table VII-1. Figure VII-9 compares this calibrated value for $\dot{N}_{dilution-air}$ with the values derived from the measurements. The $U_{95\%}$ uncertainty bars are plotted in

the figure. The large uncertainty is due almost entirely to the bias error associated with the placement of the velocity probe in the exhaust chimney, as discussed in section IV-13. The average error (difference between the calibrated $\dot{N}_{dilution-air}$ value and that derived from measurements) was $3.1 \cdot 10^{-5}$ kmol/s (0.5%) while the root-mean-square error was $4.1 \cdot 10^{-5}$ kmol/s (0.7%). The maximum error for a single point was $8.9 \cdot 10^{-5}$ kmol/s (1.4%).

Similarly, the value of $q_{FCPM-to-dilution}$ was determined by averaging over the 7 experiments. This value is presented in Table VII-1. Figure VII-10 compares this calibrated value for $q_{FCPM-to-dilution}$ with the values derived from the measurements. The $U_{95\%}$ uncertainty bars are plotted in the figure. Once again, the large uncertainty is due to the bias error associated with the placement of the velocity probe in the exhaust chimney. The average error (difference between the calibrated $q_{FCPM-to-dilution}$ value and that derived from measurements) was 74 W (3.2%) while the root-mean-square error was 93 W (3.9%). The maximum error for a single point was 193 W (7.7%).

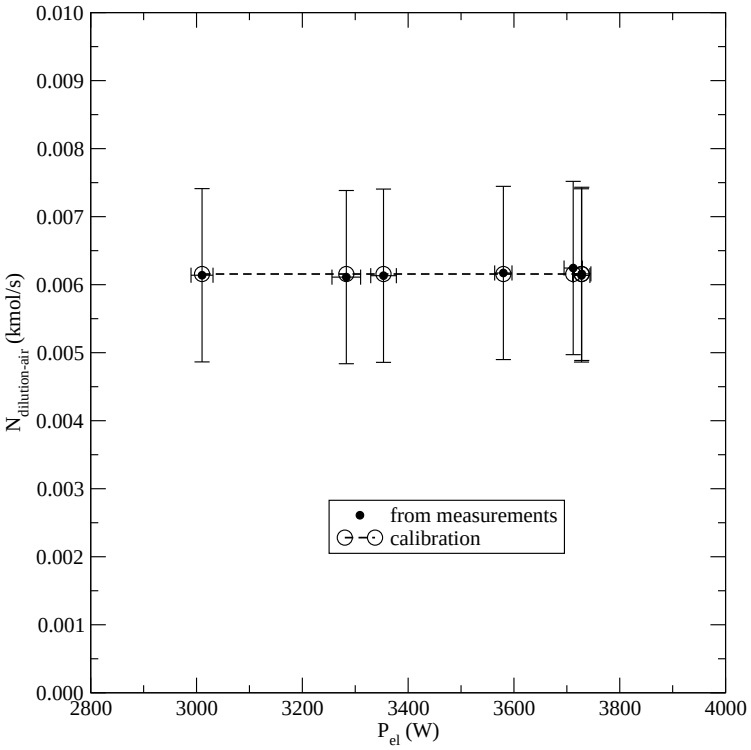

Figure VII-9: Calibrated $\dot{N}_{dilution-air}$ versus measurements

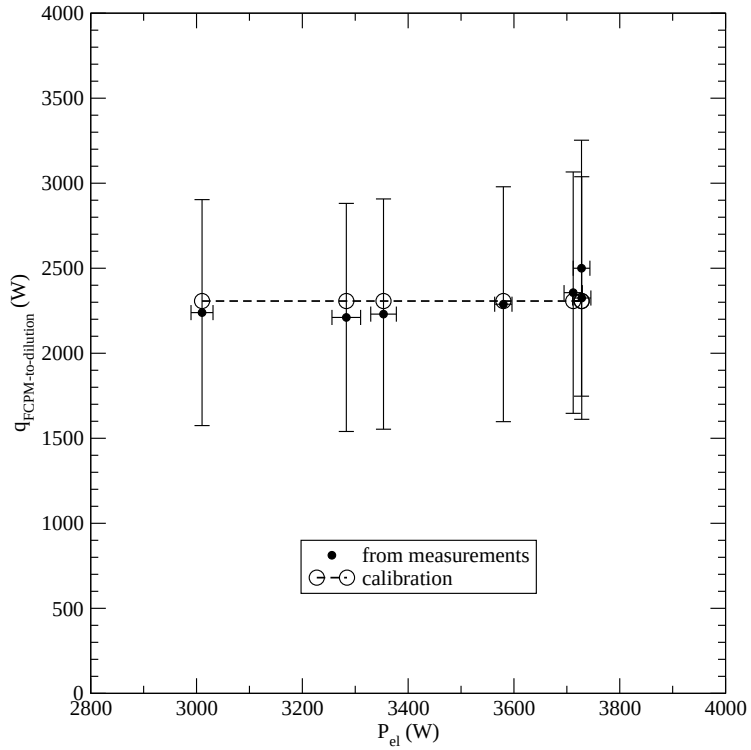

Figure VII-10: Calibrated $q_{FCPM-to-dilution}$ versus measurements

Calibration of FCPM skin losses

Data from a single experiment were used to calibrate the FCPM's skin losses. This calibration was performed with *method 1*, as treated in section II-2.10 of the model specifications. With this method $q_{skin-loss}$ is treated as a constant.

Infrared images of the cogeneration device were captured during this one experiment during which the cogeneration device was producing its maximum power. Three of the four side faces and the top of the SOFC enclosure provided unobstructed views for the imaging. The image from one of the sides is given in Figure VII-11. These images were used to derive thermal contour maps by taking into account the surface emissivities. Average temperatures were then calculated from these thermal contours for each of the four imaged surfaces. The surface-averaged temperatures of the three sides were calculated to be 33.3°C, 25.9°C, and 29.3°C. The surface-averaged temperature for the top was calculated to be 38.2°C.

Figure VII-11: Infrared image of one side of SOFC device

The skin losses from the sides and top of the device were then estimated by calculating the convective and radiative heat transfer from each surface to the surrounding air and the wall surfaces of the laboratory.

To estimate the convective heat transfer, it was assumed that each surface behaved as though it were isothermal at its average temperature and that there was external free convective flow from the surface to the surrounding air. Classical non-dimensional relations were then used to estimate the convective heat transfer rates. For vertical surfaces the heat transfer was calculated using the following relation (Incropera and DeWitt, 1985),

$$\overline{Nu_L} = \left\{ 0.825 + \frac{0.387 Ra_L^{1/6}}{\left[1 + \left(\frac{0.492}{Pr} \right)^{9/16} \right]^{8/27}} \right\}^2 \qquad \text{(VII-1)}$$

Where $\overline{Nu_L}$ is the surface-averaged Nusselt number based upon the length scale L, Ra_L is the Rayleigh number, and Pr is the Prandtl number. The length scale, L, is taken as the height of the cogeneration device, 2.2 m.

Heat transfer from the top surface was determined using the following relation for horizontal surfaces (Incropera and DeWitt, 1985),

$$\overline{Nu_L} = 0.15 \cdot Ra_L^{1/3} \qquad \text{(VII-2)}$$

Where the characteristic length scale, L, is surface area (1.25 m by 0.82 m) divided by the perimeter.

As it was not possible to take an infrared image of one side of the device, it was assumed that the temperature of this surface was equal to its opposite surface (29.3°C). It was further assumed that the bottom surface of the device was adiabatic. The room air temperature was measured at 22°C. Based up this approach, the convective heat transfer from the cogeneration device to the room air was calculated to be 263 W.

The radiative heat transfer was calculated by assuming that each surface acts as a grey body emitter. Due to its large size relative to the cogeneration unit, it is assumed that the laboratory acts as a black body absorber and that the view factor between each surface of the cogeneration system and the laboratory is unity. Further, it is assumed that the

absorbing surfaces of the laboratory are isothermal at T_{room}. Given this, the net radiation leaving each surface can be calculated with,

$$q_{radiation} = A_{surf}\,\varepsilon\sigma\left(T_{surf}^4 - T_{room}^4\right) \tag{VII-3}$$

Where ε is the surface emissivity (assumed to be 0.9), σ is the Stephan-Boltzmann constant, and A_{surf} is the surface area.

Following this approach, the radiative heat transfer from the unit was calculated to be 466 W. Summing the convective and radiative losses gives a total skin loss term of 729 W, as given in Table VII-1. This table also indicates that the applicability of the calibration of the $q_{skin-loss}$ term is limited to containing room temperatures around 22°C, since this calibration was performed with data from a single experiment. This calibration approach does not lend itself to a formal uncertainty analysis. Instead, the impact of the numerous assumptions listed above upon the calculation of $q_{skin-loss}$ was examined. Based upon this sensitivity analysis, it was concluded that the uncertainty associated with this aspect of calibration is approximately 20%.

CALIBRATION PARAMETERS	
gas-to-water heat exchanger	method 4
	$hx_{s,0} = 83.1$; $hx_{s,1} = 4\ 798$; $hx_{s,2} = -138 \cdot 10^{3}$; $hx_{s,3} = -353.8 \cdot 10^{3}$; $hx_{s,4} = 5.15 \cdot 10^{8}$
	$T_{cond-threshold} = 35^{o}C$
	$hx_{l,1} = -1.96 \cdot 10^{-4}$; $hx_{l,2} = 3.1 \cdot 10^{-3}$
FCPM electrical efficiency	$\varepsilon_0 = 0.642388$; $\varepsilon_1 = -1.619 \cdot 10^{-4}$; $\varepsilon_2 = 2.26007 \cdot 10^{-8}$
	$D = 0^{1}$; $L = 0^{1}$
FCPM transient response	$(dP_{el}/dt)_{max,increasing-power}$ = 1.4 (W/s) $(dP_{el}/dt)_{max,decreasing-power}$ = 0.2 (W/s)
air supply to FCPM	method 2
	$a_0 = 1.50976 \cdot 10^{-3}$; $a_1 = -7.76656 \cdot 10^{-7}$; $a_2 = 1.30317 \cdot 10^{-10}$; $a_3 = 2.83507 \cdot 10^{-3}$
FCPM skin losses	method 1
	$q_{skin-loss}$ = 729 W
dilution air	$\dot{N}_{dilution-air}$ = $6.156 \cdot 10^{-3}$ kmol/s $P_{el,dilution-air}$ = 0 W $q_{FCPM-to-dilution}$ = 2 307 W
power conditioning	$u_0 = 0.560717$; $u_1 = 1.24019 \cdot 10^{-4}$; $u_2 = -2.01648 \cdot 10^{-8}$
RANGE OF APPLICABILITY	
5.2 °C ≤ $T_{water,in}$ ≤ 59.8 °C	
$3.63 \cdot 10^{-3}$ $kmol/s \leq \dot{N}_{water} \leq 1.09 \cdot 10^{-2}$ $kmol/s$	
3 010 $W \leq P_{el} \leq$ 3 728 W	
10.0 °C ≤ T_{air} ≤ 24.2 °C	
$T_{room} \approx 22^{o}C$	
NOTES	
[1] Assumed since experiments did not examine degradation.	

Table VII-1: Calibration coefficients for FCT SOFC device

References

Incropera, F.P. and DeWitt, D.P., *Fundamentals of Heat and Mass Transfer, 2nd Edition,* John Wiley & Sons, New York (1985).

Kelly, N. and Beausoleil-Morrison, I. (eds), "Specifications for Modelling Fuel Cell and Combustion-Based Residential Cogeneration Device within Whole-Building Simulation Programs," *IEA/ECBCS Annex 42 Report, ISBN No. 978-0-662-47116-5* (2007).

Appendix A : Goodness of fit metrics

Seven metrics were chosen to assess the goodness of fit of the calibrations:

- The average of the absolute errors, $\bar{e}_{abs}$
- The average of the relative errors, $\bar{e}_{rel}$
- The root-mean-square of the absolute errors, e_{abs}^{RMS}
- The root-mean-square of the relative errors, e_{rel}^{RMS}
- The maximum of the absolute errors, e_{abs}^{MAX}
- The maximum of the relative errors, e_{rel}^{MAX}
- The coefficient of determination, r^2, which is the square of Pearson's product of moment correlation coefficient

These metrics are calculated as follows:

$$\bar{e}_{abs} = \frac{1}{n}\sum_{i=1}^{n}\left|\hat{\theta}_i - \theta_i\right| \tag{VII-4}$$

$$\bar{e}_{rel} = \frac{1}{n}\sum_{i=1}^{n}\frac{\left|\hat{\theta}_i - \theta_i\right|}{\hat{\theta}_i} \tag{VII-5}$$

$$e_{abs}^{RMS} = \sqrt{\frac{1}{n}\sum_{i=1}^{n}\left(\hat{\theta}_i - \theta_i\right)^2} \tag{VII-6}$$

$$e_{rel}^{RMS} = \sqrt{\frac{1}{n}\sum_{i=1}^{n}\left(\frac{\hat{\theta}_i - \theta_i}{\hat{\theta}_i}\right)^2} \tag{VII-7}$$

$$e_{abs}^{MAX} = MAX\left\{\left|\hat{\theta}_i - \theta_i\right|\right\}_{i=1}^{n} \tag{VII-8}$$

$$e_{rel}^{MAX} = MAX\left\{\frac{\left|\hat{\theta}_i - \theta_i\right|}{\hat{\theta}_i}\right\}_{i=1}^{n} \qquad \text{(VII-9)}$$

$$r^2 = \frac{\left[\sum_{i=1}^{n}\left(\hat{\theta}_i - \overline{\hat{\theta}}\right)\cdot\left(\theta_i - \bar{\theta}\right)\right]^2}{\sum_{i=1}^{n}\left(\hat{\theta}_i - \overline{\hat{\theta}}\right)^2 \cdot \left(\theta_i - \bar{\theta}\right)^2} \qquad \text{(VII-10)}$$

Where $\hat{\theta}_i$ is the value derived from measurements at time-step i, θ_i is the calibrated value, and n is the number of measurement points.